NASA/CR-1998- 207054

EXTENDED X-RAY EMISSION AROUND QUASARS AT INTERMEDIATE REDSHIFT

NASA Grant NAG5-2476

Annual Report

For the Period 1 December 1995 through 30 November 1997

Principal Investigator
Dr. Fabrizio Fiore

January 1998

Prepared for:

National Aeronautics and Space Administration
Goddard Space Flight Center
Greenbelt, Maryland 20771

Smithsonian Institution
Astrophysical Observatory
Cambridge, Massachusetts 02138

The Smithsonian Astrophysical Observatory
is a member of the
Harvard-Smithsonian Center for Astrophysics

The NASA Technical Officer for this grant is Dr. Robert Petre, Code 666, Laboratory for High **Energy Astrophysics, Space Sc**ience Directorate, Goddard Space Flight Center, Greenbelt, **Maryland 20771.**

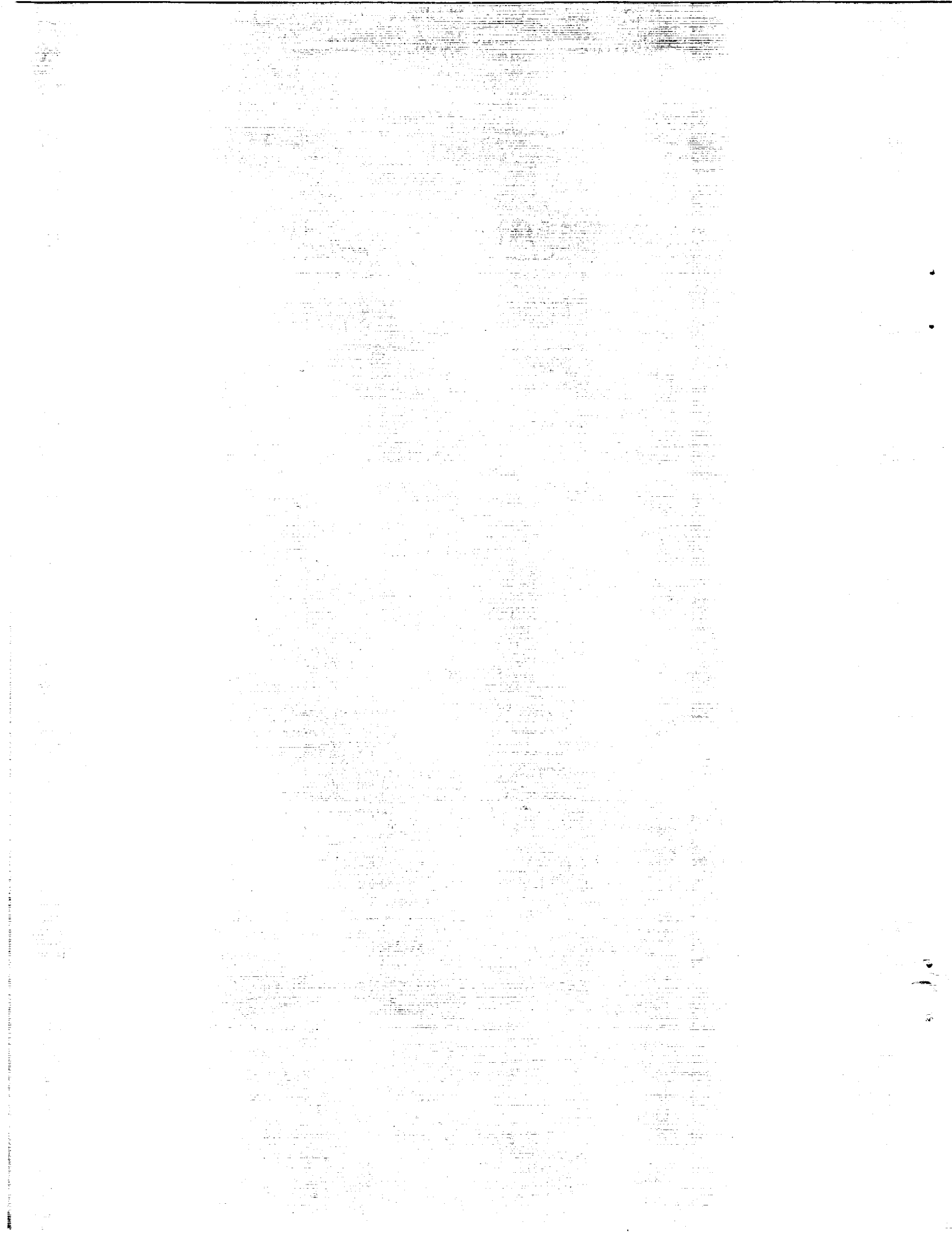

Abstract

We compare the optical to soft X-ray spectral energy distribution (SED) of a sample of bright low-redshift ($0.048<z<0.155$), radio-quiet quasars, with a range of thermal models which have been proposed to explain the optical/UV/soft X-ray quasar emission: (a) optically thin emission from an ionized plasma, (b) optically thick emission from the innermost regions of an accretion disk in Schwarzschild and Kerr geometries. We presented ROSAT PSPC observations of these quasars in an earlier paper. Here our goals are to search for the signature of thermal emission in the quasar SED, and to investigate whether a single component is dominating at different frequencies.

We find that isothermal optically thin plasma models can explain the observed soft X-ray color and the mean OUV color. However, they predict an ultraviolet (1325Å) luminosity a factor of 3 to 10 times lower than observed. Pure disk models, even in a Kerr geometry, do not have the necessary flexibility to account for the observed OUV and soft X-ray luminosities. Additional components are needed both in the optical and in the soft X-rays (e.g. a hot corona can explain the soft X-ray color). The most constrained modification of pure disk models, is the assumption of an underlying power law component extending from the infrared ($3\mu m$) to the X-ray. This can explain both the OUV and soft X-ray colors and luminosities and does not exceed the $3\mu m$ luminosity, where a contribution from hot dust is likely to be important. We also discuss the possibility that the observed soft X-ray color and luminosity are dominated by reflection from the ionized surface of the accretion disk.

While modifications of both optically thin plasma models and pure disk models might account for the observed SED, we do not find any strong evidence that the OUV bump and soft X-ray emission are one and the same component. Likewise, we do not find any strong argument which definitely argues in favor of thermal models.

Subject headings: Quasars - X-ray: Spectra

1.INTRODUCTION

The most striking property of the continuum of unbeamed quasars (simply quasars hereinafter) is the fact that it extends over at least seven decades in frequency, from 100 μm to 100 keV, maintaining a similar luminosity per decade. The most prominent feature of a quasar's spectral energy distribution (SED) is the blue bump which dominates the optical/ultra-violet (OUV) emission and contains $\gtrsim 50\%$ of the energy output. The blue bump could have a broad maximum in the 1300–1000Å range, as suggested by Malkan (1988), or could extend into the so far unobserved extreme UV region, if some intrinsic reddening is present. The observed soft X-ray flux is in most cases lower than that predicted by extrapolating the UV flux with the typical spectral indices measured at wavelengths longer than $\sim$ 1000Å. This requires a sharp drop in the extreme UV region. The soft X-ray flux ($\lesssim$1 keV), however, is higher than the extrapolation of the higher energy (2-10 keV) power law. This low energy X-ray turn-up, commonly known as the soft X-ray excess, is generally interpreted as the high energy tail of the blue bump. Although such a connection is suggestive given that both components increase into the unobservable extreme UV, no direct evidence yet exists. However it is clear that the combination of OUV and soft X-ray data will provide invaluable constraints on models which seek to explain both components, such as thermal emission from an accretion disk (e.g. Shields 1978, Malkan & Sargent 1982, Czerny & Elvis 1987, Sun & Malkan 1989, Laor 1990, on the OUV side, and Turner et al 1988, Elvis et al 1991, from the X-ray side), and optically thin free-free (see Barvainis 1993 for a review).

The soft X-ray excess was recognized as a distinct and common component below 1 keV of the X-ray spectra of Seyfert 1 galaxies and quasars in both EXOSAT and *Einstein* data (Turner & Pounds 1989, Wilkes & Elvis 1987, Masnou et al 1992). However, the poor energy resolution of both instruments at these energies resulted in little or no information about the spectral form. The softer energy band and improved resolution of the ROSAT (Trümper 1983) PSPC (Pfeffermann et al 1987) provides us with our first opportunity to study the spectrum of the soft excess and thus to realize its full potential as a constraint on models for the OUV/X-ray continuum.

We observed a sample of low-redshift, radio-quiet quasars selected to be the brightest with known soft excesses, to acquire high signal-to-noise ($> 100\sigma$) spectra with the PSPC. The analysis of these X-ray observations is reported in a companion paper (Fiore et al 1994, hereinafter Paper I). The main results from this paper are:

1. The PSPC spectra span a broad range of slopes ($1.3 < \alpha_E < 2.3$, where $F_\nu \propto \nu^{-\alpha_E}$) and are steeper than at higher energies (typically 2-10 keV) by $\Delta\alpha_E = 0.5 - 1$. They are dominated by the soft X-ray excess.

2. The deviations from a single power law model in the 0.2-2 keV band are small but still significant. The "break point" between the hard and soft components

The following papers have been written using this grant as well as Grant NAG5-3039 (copies attached):

The complex optical to soft X-ray spectrum of low redshift radio-quiet quasars II: comparison with free-free and accretion disk models. F. Fiore, M. Elvis, A. Siemiginowska, B. Wilkes, J. McDowell, and S. Mathur, 1994, ApJ, 449, 74.

The X-ray and ultraviolet absorbing outflow in 3C351. S. Mathur, F. Fiore, M. Elvis, and B.J. Wilkes, 1994, ApJ, 433, 234.

Testing the ionized disc reprocessing model for the soft X-ray emission of quasars F. Fiore, G. Matt, and F. Nicastro, 1997, MNRAS, 284, 731

The soft X-ray properties of a complete sample of optically selected quasars II. Final results A. Laor, F. Fiore, M. Elvis, B. J. Wilkes, J. C. McDowell, 1997, ApJ, 477, 93

X-ray spectral survey of WGACAT quasars: I Spectral evolution and low energy cut-offs. F. Fiore, M. Elvis, P. Giommi and P. Padovani, 1997, ApJ, in press

X-ray spectral survey of WGACAT quasars, II: Radio and optical properties of quasars with low energy cut-off M. Elvis, F. Fiore, P. Giommi and P. Padovani, 1997, ApJ, in press

Ionized absorbers in AGN: the role of collisional ionization and time-evolving photoionization F. Nicastro, F. Fiore, M. Elvis, and G.C. Perola, 1997, ApJ, submitted

The variability of X-ray steep and flat quasars F. Fiore, A. Laor, M. Elvis, F. Nicastro and E. Giallongo, 1997, ApJ, submitted

The ASCA view of steep soft X-ray quasars F. Fiore, G. Matt, M. Cappi, M. Elvis, K.M. Leighly, F. Nicastro, L. Piro, A. Siemiginowska, B.J. Wilkes, 1997, MNRAS, submitted

The equilibrium photoionized absorber in 3C351 F. Nicastro, F. Fiore, G.C. Perola, M. Elvis, 1997, ApJ, in preparation

Detection of a resonant absorption line in the ASCA spectrum of NGC985 F. Nicastro, F. Fiore, N. Brandt, C. S. Reynolds, 1997, proc. of the symposium "The Active Sky", Rome 21-24 Oct 1997

The X-ray variability properties of PG quasars: new ROSAT/HRI results F. Fiore, A. Laor, M. Elvis, F. Nicastro and E. Giallongo, 1997, Proceedings of the Wise Observatory 25th Anniversary Symposium on Astronomical Time Series, eds. D. Maoz, Kluwer Academic Publishers

Extended X-ray emission around GPS quasars L.A. Antonelli and F. Fiore, 1997, Proceedings of the II National Meeting on AGNs "From Micro to Mega Parsec" A. Comastri, T. Venturi, M. Bellazzini eds., Mem. Soc. Astr. It. (Journal of the Italian Astron. Society) vol. 68 - 1997, in press.

THE COMPLEX OPTICAL TO SOFT X-RAY SPECTRUM OF LOW-REDSHIFT RADIO-QUIET QUASARS[1] II: COMPARISON WITH FREE-FREE AND ACCRETION DISK MODELS

Fabrizio Fiore*, Martin Elvis, Aneta Siemiginowska, Belinda J. Wilkes
Jonathan C. McDowell and Smita Mathur
Harvard-Smithsonian Center for Astrophysics
60 Garden St, Cambridge MA 02138
* Present address: Osservatorio Astronomico di Roma
via dell'Osservatorio 5, Monteporzio-Catone (RM), I00040 Italy

January 26, 1998

[1]This paper is based in part on data obtained on the Multiple Mirror Telescope (MMT), a joint facility of the Smithsonian Institution and the University of Arizona.

is in all cases above 0.7 keV. The PSPC spectra exclude "narrow" models, such as a single line or a black body, for the soft X-ray component.

3. The strength of any line emission feature in the soft X-ray band is small (less that 10-20 % of the counts in each channel), unless the continuum is complicated.

Here we present the optical to soft X-ray SED of the quasars and compare them with the predictions of a wide range of thermal models which have been proposed to explain the OUV/soft X-ray quasar emission: (a) optically thin plasma emission, (b) optically thick thermal emission from the innermost regions of an accretion disk in Schwarzschild and Kerr geometries. Our aims are to search for the signature of thermal emission in the quasar SED and to investigate whether a single component is dominating at different frequencies or rather if the quasar SED are best reproduced by the superposition of different components.

2. THE SOFT X-RAY COMPONENT AND THE BIG BLUE BUMP

A longstanding question in quasar research is whether the soft X-ray emission and the OUV blue bump are one and the same component. The most direct way to verify this is to search for simultaneous/correlated variations in both the UV and soft X-ray emission. Unfortunately simultaneous UV and soft X-ray observations of longer than a few hours are difficult to schedule with ROSAT and IUE and have so far been performed only for a few, very bright objects like the BL Lacertae object PKS2155-304 (Edelson et al 1994).

A number of quasars have been observed nearly simultaneously by IUE and ROSAT during the ROSAT all sky survey (Walter et al 1994). These authors found that in six out of eight cases the shape of the UV to soft X-ray component is similar, while the relative strength of the UV emission compared to the hard X-ray power law varies by a factor of ten over the sample.

A more indirect method is through the statistical properties of the UV and soft X-ray emission of a sample of quasars. Walter & Fink (1993) have reported a strong correlation between the soft X-ray (PSPC) spectral indices and the ratio between the flux at 1350Å and that at 2 keV in a sample of about 50 quasars. Under the assumption that the PSPC spectral index is a good indicator of the strength of the soft excess, this was interpreted as evidence that the soft X-ray emission and OUV emission are part of the same component: a O-UV-X-ray bump. There are some concerns about this analysis. We note that: (a) the Walter & Fink sample is soft X-ray selected, since it includes only the brightest quasars in the ROSAT All Sky Survey. Then, the PSPC spectral index and the 2 keV flux are strongly correlated quantities, since 2 keV is the upper end of the PSPC band: in a flux limited soft X-ray survey a source with a low 2 keV flux is likely to have also a steep PSPC spectral index. (b)

The Walter & Fink sample is very heteregeneous. It contains: low luminosity Seyfert galaxies and high luminosity, high redshift quasars, sources with strong and faint blue bump; radio-loud and radio-quiet objects; strongly absorbed and unabsorbed sources. The correlations between these properties and the luminosity in the optical, UV and soft X-ray bands are all complicated and could drive, at least in part, the Walter & Fink correlation.

Laor et al (1994) report a result similar to the Walter & Fink correlation. They found a significant correlation between the PSPC spectral index and the optical (3000Å) to X-ray (2 keV) rest frame spectral index α_{OX} in a sample of 10 optically selected, z< 0.4 (<z>=0.22), $M_B < -23$ quasars (three of which are radio-loud). Being optically selected, this small sample does not suffer from the selection bias mentioned above.

As an example we plot in Fig. 1 α_{OX} [1] as a function of the PSPC best fit single power law energy index α_E. We include the Laor et al (1994) radio quiet objects, the sample presented in Paper I (4 objects are PG quasars and the remaining two, NAB0205+024 and MKN205 have a comparably strong blue bump), and all the radio-quiet PG quasars in the Walter & Fink sample which have small Galactic N_H and z< 0.4. The combined sample consists of 22 objects, all radio-quiet, with a strong blue bump, without significant intrinsic absorption and spanning a large range in optical luminosity ($-26 < M_B < -21$). We estimate that a spread in α_{OX} of ± 0.1 is introduced by the fact that the observations in OUV and X-rays are not simultaneous (from the data in Table 1 and 2, see below). It is not clear whether or not the amplitude of the long term UV variability is correlated with the luminosity. O'Brien et al (1988) found some evidence for an inverse correlation, but their sample of high luminosity objects was small. For the sample presented in this paper there is no evidence for a correlation between the amplitude of the UV variability and luminosity. We therefore assume that the spread in α_{OX} is roughly similar at all luminosities. For the objects in the sample presented in this paper the optical luminosity has been corrected for the contribution from the host galaxy, while the objects in the Laor et al and Walter & Fink samples were not so corrected. We note however that the contribution of the host galaxy should be small even in low luminosity objects at 3000 Å (see the galaxy template in Elvis et al 1994a), thus affecting α_{OX} only slightly.

The correlation between α_E and α_{OX} is quite good for the high optical luminosity objects (11 objects with $M_B < -23.5$, linear correlation coefficient equal to 0.855 corresponding to a probability of 99.95 %). The linear correlation coefficient for the whole sample is lower (r=0.60, corresponding to a probability of 99.6 %). In fact, the four points which deviate most from the correlation are all lower optical luminosity sources. Two of these sources, PG1440+356 (MKN478) and PG1244+026 have a very steep PSPC slope but their soft X-ray luminosity is comparable or even higher than

[1] $\alpha_{OX} = \frac{log(L(2500\mathring{A})/L(2keV))}{2.6057}$

their UV luminosity, unlike all the other sources in the sample. PG1440+356 is one of the few quasars detected at ~ 0.1 keV by the ROSAT Wide Field Camera (Pounds et al 1993). Another Wide Field Camera source (RE1034+398) has a very steep PSPC spectrum (Puchnarewicz et al 1995), flat α_{OX} and soft X-ray luminosity higher than the UV luminosity. Pounds (1994) and Fiore & Elvis (1994) suggested that these sources could belong to a separate class of quasars, sources that emit the most of the power in soft X-rays, unlike the majority of optically selected quasars. Fiore & Elvis (1994) suggested that these source could resemble Galactic Black Hole Candidates in the high (and soft) state.

Assuming that the PSPC spectrum of radio-quiet, strong blue bump sources, is made up of two distinct components, a steep one dominating below $\sim 1-2$ keV and a hard one dominating at higher energies, the correlation in Fig. 1 can be interpreted in two ways. Either, (a) the intensity of the soft component is more or less the same in all sources while that of the hard one varies over a broad range. Or, (b) the intensity of the soft component varies over a broad range in these sources while that of the hard one is more or less the same. The significantly larger scatter in the 2 keV luminosity found by Laor et al (1994) with respect to that in the 0.3 keV luminosity, argues for the first case. This suggests that, in high optical luminosity sources at least, a correlation between the blue bump and the soft X-ray component, does indeed exist. However, this does not prove that the luminosity in different frequency band arises from the same emission component. In the following sections we test the single component hypothesis by discussing the ability of various models to reproduce both X-ray and OUV data.

3. OBSERVATIONAL DATA

3.1 X-ray data

The numerical results of the spectral fitting from Paper I are given in Table 1. Table 1 lists the soft X-ray monochromatic luminosities νL_ν at 0.4 keV and 1 keV (soft component only), the soft component energy index ($F_\nu \propto \nu^{-\alpha_{ES}}$), and 2 keV monochromatic luminosity (soft plus hard components) for the quasars in our sample. They are from Paper I and were obtained by fitting to the PSPC data a two power law model, or a power law plus thermal bremsstrahlung model, with low energy absorption (N_H was limited to values greater than the Galactic column along the line of sight). The power law plus thermal bremsstrahlung model gives a fit of quality comparable to the two power law model in all sources but PG1426+015, where it produces a significantly worse χ^2 (see Paper I). Errors on the luminosities represent 1 σ confidence intervals for four interesting parameters.

In Paper I we compared the PSPC results concerning the soft component intensity with those obtained with previous satellites, finding that they always agree within the errors. In spite of the low energy resolution of the EXOSAT LE and the *Einstein* IPC several authors estimated the shape of the soft X-ray component

in a number of quasars. In particular, Comastri et al (1992) fitted the EXOSAT ME/LE data with a two power law model (with N_H fixed to the galactic value) for a sample of six quasars, three of which are in common with our sample. They found a soft component energy index α_{ES} of $3.33^{+0.66}_{-0.42}$ in PG1211+143, $3.32^{+1.20}_{-0.67}$ in TON1542 (PG1229+204), and $2.66^{+1.09}_{-0.49}$ in PG1426+015. For each source the EXOSAT indices and PSPC indices in Table 1 are consistent with each other, within the rather large errors. However, the EXOSAT best fit spectral indices are in all cases steeper by $\Delta\alpha \sim 1$ than the PSPC best fit indices, and the break energy of ~ 0.6 keV estimated by Comastri et al. (1992) falls short than the typical break energy of 1 keV found in Paper I. There could therefore be a systematic offset between the EXOSAT and the PSPC measurements. We note that the Comastri et al indices were obtained by fitting the data from two distinct experiments (the ME and the LE). Since the ME starts to be sensitive only above 1 keV, while the peak of the LE sensitivity is below this energy, the best fit parameters could be largely affected by inaccuracies in the relative calibration of the two instruments. For example a soft component slope steeper than the actual one would be easily obtained if, given the same incident spectrum, the normalization in the LE were systematically higher than that in the ME (also see the discussions on the relative calibration of two instruments in Masnou et al, 1992, and in Paper I). On the other hand, the energy band and resolution of the PSPC allow a quite accurate determination of the shape of the soft component of bright quasars. In Paper I we showed that calibration uncertainties currently limit this ability and forced us to adopt very conservative errors on the parameters describing the soft X-ray component. We remark here that the offset between the EXOSAT and PSPC results is in all cases smaller than the statistical+systematic uncertainties.

Masnou et al (1992) fitted the IPC/MPC data with a broken power law model (with N_H fixed to the galactic value) for a sample of 7 quasars, two of which are in common with the present sample. For these two quasars they found a low energy slope of $\alpha_{ES} = 2.6$ (NAB0205+024) and $\alpha_{ES} = 1.47$ (MKN 205). These slopes are consistent with the ones obtained from our analysis (see Table 1).

Saxton et al. (1993) fitting the EXOSAT ME/LE data of a sample of 12 quasars parameterized the soft excess as a thermal bremsstrahlung model with a fixed temperature of 0.2 keV, close to the best fit temperature obtained fitting this model to the composite spectrum of the six quasars in our sample in Paper I.

3.2 IR-optical-UV data

Table 2 gives the infrared (3 μm), optical (5500 Å), and UV (2500 Å and 1325 Å) monochromatic luminosities (νL_ν). When more than one infrared, optical or UV observation is available we report the maximum and minimum observed luminosities including errors, the number of observations and their date span. As a reference we also give in Table 2 the average α_{OX} of these quasars. The mean α_{OX} in the sample is 1.47, slightly lower than the mean value of 1.525 found by Laor et al (1994) for a

complete sample of optically selected, low-redshift, radio-quiet quasars (a difference of 0.06 in α_{OX} corresponds to a 40 % difference in the optical to X-ray luminosity ratio). When available, the infrared, optical and UV luminosities were extracted from the "Atlas of Quasar Energy Distributions" (Elvis et al 1994a). Additional optical spectrophotometric data were included for NAB0205+024 and PG1244+026 (see below). The data from TON1542 include optical data from Neugebauer et al (1987), IR data from Rudy, Levan and Rodriguez (1982) and archival IUE spectra.

The IUE data were corrected for the reduction in the efficiency of the cameras with the time (Bohlin & Grillmar 1988). Following the procedures in Elvis et al (1994a), the data were corrected for reddening, shifted to the rest frame and corrected for the contribution of the host galaxy using the galaxy template given in Table 16 of Elvis et al (1994a). These authors showed that the contribution of the host galaxy can be important ($\gtrsim$20%) for $M_V < -25$ ($\nu L_\nu(5500\AA) < 2 \times 10^{45}$). Direct measurements of the host galaxy were used in two cases (NAB0205+024 and PG1211+143). In two cases (MKN205 and PG1426+015) we used the H band mean luminosity of the host galaxy in the Elvis et al. sample (logL(H)=$44.6^{+0.3}_{-0.6}$, but note that in MKN205 we modified the upper error bar, so as not to overpredict the total H band luminosity). In the remaining two cases the observed H band luminosity is lower than the mean host galaxy luminosity in Elvis et al. (1994a), and we assumed therefore that the host galaxy luminosity in these objects is a little lower than the observed H luminosity. In all cases we used highly conservative error bars on the host galaxy luminosity. Table 2 lists the host galaxy normalization in the H band for each quasar. MKN205 was quoted as a "weak bump quasar" by McDowell et al (1989), showing a very steep optical to UV slope, but this slope turns out to be consistent with the quasar average slope ($f_\nu \sim -0.1$) if the contribution from the host galaxy is close to the mean value in Elvis et al (1994a). The errors on the host galaxy luminosity have been propogated to find the uncertainties on the luminosity at optical and UV frequencies.

Optical spectrophotometry was obtained for two of the quasars: NAB0205+024 and PG1244+026; on the Multiple Mirror Telescope (MMT) using the MMT spectrograph and the red channel on 1991 September 15 and 1991 May 17 respectively (the PSPC observations of these quasars were performed in 1992 January and 1991 December, respectively). On both dates conditions were photometric. Two spectra were obtained, the first through a wide slit ($5'' \times 180''$) to ensure photometric accuracy and the second through a narrow slit ($1.5'' \times 180''$) for improved spectral-resolution ($\sim$ 20Å) and signal-to-noise. The 150 lpm grating was used yielding a wavelength range of $\sim 3800 - 7600$Å. The spectra were reduced in the standard manner using IRAF. The wide slit observation was flux calibrated with reference to a nearby standard star observed sequentially with the quasar. The continuum shape and level of the narrow slit spectrum were then normalized to agree with this flux calibrated spectrum. Continuum fluxes at 5500Å measured from these spectra are presented in Table 2. The spectra will be presented in a later paper.

The errors contain the evaluated uncertainty on all the above corrections, in addition to the statistical uncertainty. In the case of the IUE data a further 3 % systematic uncertainty is folded into the errors (Bohlin 1980). The data in different bands are not simultaneous. Variations of a factor ~ 2 were recorded for these quasars in optical and UV and of a factor 5 in X-ray. The uncertainty due to source variability is generally larger than the quoted (statistical+systematic) errors.

4. MODELING THE IR-TO-SOFT-X-RAY SED OF QUASARS

4.1 Optically Thin Plasma Models

4.1.1 The model

Thermal bremsstrahlung at temperatures of $10^5 - 10^7$ K emitted by an optically thin gas cloud is a candidate mechanism to produce the OUV/soft-X-ray bump in quasar spectra (Barvainis 1993). We calculate the free-free contribution for a spherical and isothermal cloud assuming that the cloud has radius (R) and density (n_e) consistent with an optical depth less than 1 ($\tau_{eff} = (\tau_\nu(\tau_\nu + \tau_{es}))^{1/2} < 1$; where τ_ν are the free-free and τ_{es} the electron scattering optical depths). The bremsstrahlung luminosity is calculated using (Rybicki & Lightman, 1979):

$$L_\nu = 9.5 \times 10^{-38} (\frac{4}{3}\pi R^3) n_e^2 T^{-1/2} exp(-\frac{h\nu}{kT}) g_{ff} \text{ erg s}^{-1} \text{ Hz}^{-1},$$

where g_{ff} is the Gaunt factor calculated using an approximation given by Gronenschild and Mewe (1978).

In the soft X-ray band the free-free emission from the ionized plasma represents only part of the total emission, since recombination, 2-photon, and line emission from the same plasma can also be important, depending on the temperature (Raymond & Smith 1977). We calculated the 2-photon and recombination continua as in Raymond & Smith (1977). We do not include line emission in our modeling but we discuss in the next sections how it can affect the spectral shape and intensity.

4.1.2 Comparison with the data

We plot in Fig. 2 the $3\mu m - 2$ keV SED of the six quasars, galaxy subtracted and including only the soft X-ray component. On the upper panel we also plot free-free models, for $T = 10^6$ and $T = 3 \times 10^6$, that roughly encompass the observed SED. On the lower panel we plot the free-free, 2-photon and recombination continua, as well as the sum of these continua, for T=10^6 K. At this temperature free-free emission dominates the OUV part of the spectrum but the harder recombination continuum dominates the soft X-ray part of the spectrum. Note the numerous, rather deep edges present in the total continuum.

Rather than attempt a formal fit of these models to the data, we make use of color diagrams to evaluate their flexibility and to evaluate the range of the parameters for which they are able to reproduce the data (also see Siemiginowska et al 1995).

In Fig. 3 we plot the soft X-ray color ($\nu L_\nu(1keV)/\nu L_\nu(0.4keV)$, soft component only), against the OUV color ($\nu L_\nu(1325\AA)/\nu L_\nu(5500\AA)$) for the six quasars. The soft X-ray color is calculated using the X-ray monochromatic luminosities in Table 2. The dotted line with open squares shows the predictions of pure bremsstrahlung models with temperatures in the range $10^6 - 10^7$ K. The additional contribution of recombination and 2-photon continua would increase by a factor 6 the continuum at 0.4 keV and by a factor 30 the continuum at 1 keV for $T = 10^6$ K thus increasing the soft X-ray color by a factor of five. For $T = 10^7$ K the contribution of recombination and 2-photon continua would increase the flux at 0.4 keV by a factor 1.2 and the flux at 1 keV by a factor 1.4, thus increasing the X-ray color by 9 %. Filled squares show soft X-ray color predicted in these two cases.

The bremsstrahlung model can reproduce the observed soft X-ray color for temperatures in the range $2 - 5 \times 10^6$ K (0.15–0.4 keV). Including the contribution of 2-photon and recombination continua yields a lower limit of $\sim 1.5 \times 10^6$ K on the temperature. These models can also reproduce the observed OUV color.

In Table 1 we also list the upper limits on the 1325Å predicted luminosity calculated by extrapolating the best X-ray fit (for the power law plus thermal bremsstrahlung model) into the UV. Because of the large extrapolation and the uncertainty on the contribution of the recombination and 2-photon continua in the X-ray band (which would lower the best fit temperature and raise the normalization, and hence produce higher UV luminosity), we assumed as upper limit on the predicted UV luminosity twice the best fit value. In Fig. 4 we plot the observed 1325Å luminosities versus the predicted ones. When more than one IUE observation is available we used the smallest observed 1325 Å luminosity. Fig. 4 shows that the model underpredicts the 1325Å luminosity by a factor 3 to 10.

4.1.3 Discussion

Optically thin plasma models can reproduce the observed soft X-ray color for temperatures in the range $1.5 - 5 \times 10^6$ K (0.13-0.4 keV). At these temperatures line emission can also be important in the X-ray band. The main emission lines, assuming collisional equilibrium, for temperatures $10^6 < T < 5 \times 10^6$ K, are the iron L complex at about 0.9 keV and the O VII and O VIII Kα lines at 0.57 and 0.65 keV. However, the ionization state of the soft X-ray emitting gas in quasar nuclei is unlikely to be controlled by collisions only, and photoionization is likely to be important, especially in the innermost regions close to the hard X-ray source. This strong radiation field could reduce the line emission intensities. Recent calculations by Kriss et al (1994) show that in the case of plasma in photoionization equilibrium the OVII and OVIII

Kα lines are still very strong. Paper I limits the amount of line emission in the six quasars in the 0.5–1 keV energy range (in most cases there is a deficit of counts with respect to a power law model rather than an excess, see Figures 1, 3 in Paper I). It should be said however that emission features have been seen in the *Einstein* SSS spectra of some other quasars (Turner et al 1991). In particular features, interpreted as oxygen lines in the framework of an ionized absorber model, have been recently seen in the X-ray spectrum of the Seyfert galaxy NGC3783 (George et al 1995). The lack of strong line emission in the quasars discussed in this paper argues against emission from isothermal optically thin ionized gas as the main contributor to the soft X-ray spectrum of these sources (see Paper I sections 3.5 and 3.6), unless the soft X-ray emission lines are optically thick while the continuum is optically thin. Since at temperatures of interest ($T < 10^7$ K) most of the cooling is in the emission lines, this requires high plasma densities. In some free-free models the assumed gas density is very high ($\sim 10^{15}$ cm^{-3}, case 2 in Barvainis, 1993). Whether such a density is high enough to suppress line emission efficiently should be investigated in detail.

Optically thin plasma models predict OUV colors consistent with the observed ones (taking into account the large uncertainties due to source variability and the fact that the observations were not simultaneous). This color, however, is not very sensitive to temperature for $T \gtrsim 5 \times 10^5$ K, i.e. in the range for which the models can explain the soft X-ray color ($\sim$15% change in the OUV color). Therefore, these models would not be able to produce the soft X-ray color higher than ~ 0.001 and at the same time give a spread in the OUV color. Detecting, through *simultaneous* observations in optical and UV, a large spread in the OUV color in a sample of quasars with strong soft excesses and soft X-ray color higher than ~ 0.001 would therefore be a critical test for the single temperature free-free models.

The best fit power law plus free-free model to the PSPC data underpredicts the UV luminosity of the six quasars. The reason is that the fit forces a high temperature, locating the maximum of the emission in the soft X-rays, while the highest luminosities are actually observed in the UV band. Fitting the X-ray data with the power law plus free-free model while requiring that the predicted 1325Å luminosity matches the observed value, yields χ^2 much worse than in the previous cases (by $\Delta\chi^2 = 20$ to 100) and temperatures between 0.05 and 0.13 keV (the best fit temperature in the fits with free thermal component normalization is between 0.15 and 0.3 keV in all cases). As mentioned before, for $T < 10^7$ K the contribution of the recombination continuum would significantly harden the spectrum, but still not enough to explain the soft X-ray color for the temperatures which would fit the OUV part of the spectrum.

In summary, the single temperature optically thin plasma models are probably too simple to explain both the OUV and soft X-ray component of these quasars *simultaneously*. The strong constraints posed by the present data could be relaxed by dropping the hypothesis that the OUV and soft X-ray emission are dominated by a single component. Optically thin plasma at increasing temperatures could dominate

the optical to soft X-ray quasar SED. This conclusion is somewhat ironic, since one of the most celebrated results of optically thin plasma models for the quasar blue bump (see e.g. Barvainis 1993) is the natural explanation of the simultaneous variations at different wavelenght, observed in a few, typically low luminosity ($L_{bol} < 10^{45}$ erg s^{-1}) quasars, due to a single physical component dominating the OUV emission.

Different frequencies dominated by components at different temperature is the distinguishing feature of another large class of models: the accretion disk models, which we discuss in turn.

4.2 Accretion disk models

4.2.1 The models

We consider emission from a geometrically thin accretion disk (outer radius of 1000 Schwarzschild radii) around a supermassive ($10^6 - 10^8 M_\odot$) black hole with accretion rates ($\dot{m}$) corresponding to 0.01 - 0.8 L_{Edd} (the Eddington luminosity), assuming that the locally generated flux is emitted in the vertical direction only. Laor & Netzer (1989) pointed out that this assumption could be unsafe for $\dot{m} > 0.3$. In fact, for such high accretion rates disks become slim (Abramowicz et al 1988), and additional cooling processes should be included (advective transport of energy in the radial direction). However, Szuszkiewicz et al (1994) show that the spectra of thin and slim accretion disks differ significantly only when accretion rates are much higher than the critical one. We limited ourselves to the sub-Eddington regime only. The error introduced using our approach instead of the above more detailed calculations for $\dot{m} > 0.3$ should be smaller than all other uncertainties present in this analysis.

The efficiency of converting the potential energy into radiation is assumed to be equal to 0.08 for a non-rotating (Schwarzschild) and to 0.324 (Laor & Netzer 1989) for a maximally rotating (Kerr) black hole. Equations for the disk structure are taken from Novikov & Thorne (1973) and Page & Thorne (1974). We calculated the spectrum using the method described by Czerny & Elvis (1987, taking into account comments of Maraschi & Molendi 1990, see also Czerny et al 1993) which includes electron scattering and Comptonization. For disk temperatures $< 10^6$ K free-bound transitions are important and the electron scattering and Compton effects correspondingly less significant. It is difficult to estimate this contribution, since free-bound opacities depend on the ionization state of matter and on a large number of transitions of many different ions. Ross et al (1992) calculated spectra emitted by a radiation dominated disk (in the Schwarzschild geometry) including free-bound processes from hydrogen and helium. However, at high frequency free-bound opacities from metals may be more important and may influence the final spectra strongly and should be taken into account. This has not been accomplished yet. Since we are interested in the general shape of the soft X-ray spectra we use the free-bound

approximation of Maraschi & Molendi (1990). For rotating black holes we use the general relativistic transfer function of Laor, Netzer & Piran (1990).

Pure accretion disk models in a Schwarzschild geometry systematically underpredict the soft X-ray emission for any choice of parameters that reproduces the OUV observed luminosity so we will no longer consider these models.

We consider also two modifications of the pure accretion disk model, namely inclusion of an underlying power law, and inclusion of a hot corona above the disk (Czerny & Elvis 1987).

4.2.1.1 An IR-to-X-ray underlying power law.

It is well known that accretion disk models are too steeply falling to long wavelengths in the optical region. Many previous modeling attempts (Malkan & Sargent 1982, Sun & Malkan 1989, Laor 1990) have invoked an additional component in the form of an 'underlying power law' that props up the disk flux in the optical and extends into the IR beneath the lumps clearly due to thermal dust emission (Clavel et al 1989, Barvainis 1992). The normalization of this power law would be such that it extrapolates quite well into the X-ray region (Carleton et al 1987, Elvis et al 1986).

Independent evidence for such a power-law is weak and even contradictory (c.f. McAlary & Rieke 1988, Green et al 1992) and in at least one quasar (NGC4051, Done et al 1990) there is a strong evidence *against* a power law component representing the majority of the emission in IR and X-rays (even if the IR-to-X-ray SED of NGC4051 actually resembles a power law, see Fig. 6 in Done et al 1990). Nevertheless, since we need additional flux in both the optical and the soft X-ray bands, the minimal assumption is to add the same component to each, and the simplest form to assume is a power-law. This adds two additional parameters (slope and normalization of the power-law), but because the model cannot overpredict either the 3 micron or hard X-ray luminosities it is also more constrained than a simple disk model, and so has predictive power.

4.2.1.2 Comptonization in a corona above the disk

A hot corona above a relatively cool accretion disk been discussed by many authors (e.g. Liang & Price 1977; Begelman, McKee & Shields 1983; Begelman & McKee 1983; White & Lightman 1989). The vertical thickness of the corona is small compared to its horizontal dimension. The corona is optically thin ($\tau_{es} < 0.8$) and has a high temperature (T_{cor}, 10 keV$-$50 keV) compared to that of the photons emitted by the disk. These photons are upscattered by the hot electrons, and the primary disk emission is modified in that a power law is produced at frequencies $\nu_0 \ll \nu < kT_{cor}/h$ (with an exponential tail $\sim \nu^3 \exp(-h\nu/kT_{cor})$ for $\nu > kT_{cor}/h$; Sunyaev & Titarchuk 1985, Górecki & Wilczewski 1984, Zdziarski 1985). In the above expression ν_0 is the

typical frequency of the soft photons. We follow the simplified description of the process given by Sikora & Zbyszewska (1986) (see also Czerny & Zbyszewska 1991) in the Schwarzschild geometry to find the modified OUV-to-soft-X-ray disk spectrum.

The energy index of the power law of the Comptonized spectrum depends on the optical depth, temperature and geometry of the corona (Sunyaev & Titarchuk 1985). In Fig. 5 we plot the energy index of the power law of the Comptonized spectrum as a function of the corona temperature for three values of τ_{es}. The temperature dependence is rapid: for kT_{cor} = 50 keV τ_{es} =0.25 and 0.5 the power law energy index is 2.0 and 1.5 respectively. When kT_{cor} = 10 keV and τ_{es} = 0.5 the power law energy index is about 5. Corona models with low τ_{es} and $kT_{cor} < 50$ keV cannot explain the hard (2-10 keV) spectrum of quasars, but only that below $\approx$ 2 keV. The hard X-ray spectrum requires high τ_{es} and high temperatures.

4.2.2 Comparison with the data.

Disk models in a Kerr geometry for two choices of black hole masses ($10^7 M_\odot$ and $10^8 M_\odot$), accretion rates (Fig. 6a; $\dot{m}$=0.1, 0.8) and inclination angles (Fig. 6b; $\mu = cos\theta$ = 0.25, 1) are compared with the six quasar SED in Fig. 6. The models roughly encompass the observed SED.

In Fig. 3 we plot the predicted soft X-ray and OUV colors for four families of the Kerr disk models spanning a typical range of parameters. Pure Kerr disk models cannot reproduce the OUV color for the range of parameters for which they can match the observed soft X-ray color (with the exception of PG1426+015): they are too "blue". Only high inclination (μ =0.25), high accretion rate ($\dot{m}$=0.8) models can reproduce the observed soft X-ray color.

In Fig. 7 we plot the 0.4 keV soft X-ray component luminosity as a function of the 1325 Å luminosity for pure Kerr disk models. The $M = 10^7 M_\odot$ models underpredict the 1325 Å luminosity. The $M = 10^8 M_\odot$ models that could account for the soft X-ray color tend to overpredict the soft X-ray luminosity.

We study the effects of the inclusion of an underlying power law from IR to X-rays by using again the soft X-ray and the OUV colors. Fig. 8 shows these colors with a set of models for two black hole masses ($10^7 M_\odot$ and $10^8 M_\odot$), $\dot{m}$ = 0.3 and μ = 0.5, α_{IRX} = 1.25 and three normalizations of the power law component. The model can reproduce both the soft X-ray and the OUV colors with typical disk parameters. The $3\mu m$ luminosity predicted by the above models is within the observed range (Fig. 9). Finally in Fig. 10 we plot the 0.4 keV soft X-ray component luminosity as a function of the 1325 Å luminosity. Also here in most cases the predicted luminosity match that observed. We stress again that these models make use of a fixed accretion rate and a fixed inclination.

To study the effects of the inclusion of a hot corona we use the soft X-ray and OUV colors. These are plotted in Fig. 11 along with the expectation of accretion disk

plus corona models for two black hole masses, three accretion rates, 0.1, 0.3 and 0.8 $\dot{m}$, $T_{cor} = 10 - 50$ keV and $\tau_{es} = 0.25 - 0.5$. These models are able to reproduce the observed soft X-ray and OUV colors but they introduce two additional parameters with respect to the pure disk models.

4.2.3 Discussion

Accretion disk models have been widely used in the past to model the quasar blue bump. In spite of their popularity a clear proof that the majority of the OUV emission in the blue bump actually originates from a disk is still lacking. On the one hand there is both theoretical (e.g. Czerny 1993) and observational (e.g. double-peaked H-α lines in radio-galaxies, Eracleous & Halpern 1994, the broad iron K_α lines reportedly seen by ASCA in a number of Seyfert 1 galaxies, Mushotzky et al 1995, especially the double-peaked iron K_α line in MCG-5-23-16 reported by Weaver, 1995) support to the idea that disks do exist in the innermost regions of quasars. On the other hand the UV spectra of quasars do not show characteristic signatures predicted by simple accretion disk models (e.g. the review of Kinney 1993).

We find that pure accretion disk models are not able to reproduce the observed optical to soft X-ray SED for the blue bump and soft X-ray component simultaneously. Even to fit just three points (the luminosity at 1325Å 0.4 keV and 1 keV), some fine tuning seems unavoidable. Furthermore the range of parameters which give reasonable predictions is particularly narrow and extreme: high inclination, high accretion rate and a black hole mass $\sim 10^8 M_\odot$. The reason for this apparent lack of flexibility of Kerr disk models is that to account for the strength and shape of the soft X-ray component the luminosity of the spectrum must peak in the soft X-ray region rather than a decade lower $\sim 10^{16}$ Hz as the data suggest. On the other hand, pure accretion disk models capable of reproducing the observed quasar UV luminosity are steeper in the soft X-ray region than the observed spectra.

Adding an IR-to-X-ray power law to the disk models readily produces colors and luminosities in the observed range of soft-X-ray and OUV simultaneously. Furthermore this combination does not violate the 3μm or hard X-ray constraints. This success certainly does not prove the existence of an underlying power-law, but does raise the possibility of its existence again.

A more physically based additional component is a hot corona above the disk. The inclusion of this component, not surprisingly, help in hardening the spectra and in reproducing the soft X-ray color and luminosity.

Recently, Haardt & Maraschi (1993) presented a model for the X-ray spectrum of quasars based on Comptonization of soft photons by a population of thermal electrons in a hot corona above a layer of cold reflecting matter. Their models reproduce well the 2-10 keV spectrum of radio-quiet quasars, as well as the sharp steepening above $\sim 50 - 100$ keV found by SIGMA, OSSE and ASCA in the spectra

of a number of quasars (Jourdain et al 1992, Maisack et al 1993, Cameron et al 1993, Elvis et al 1994b). The soft X-ray spectrum, as inferred from Fig. 4 and 5 in Haardt & Maraschi (1993), breaks sharply around a characteristic energy that depends mainly on the temperature of the cold reflecting layer, which in turns depends on the physical parameters of the system (the mass of the central object, the size of the emitting region, and the luminosity in units of L_{Edd}). For a black hole mass of $10^6 M_\odot$, L=L_{Edd}, and a size for the X-ray emitting region of 7 R_S, the temperature is $\sim$ 50 eV and the break energy is around 1 keV. The slopes below and above the break energy depend on the temperature of the corona, its optical depth and the inclination of the system to the line of sight. For low optical depth ($\tau = 0.01$) the $\Delta\alpha_E$ between the soft and hard slopes is very large for any inclination ($\sim$ 5-6). For greater optical depths ($\tau = 0.05 - 0.2$), $\Delta\alpha_E$ depends mainly on the inclination: it is large (5-6) for face on systems and reduces to zero in the case of $\tau = 0.2$ and nearly edge-on systems. Our analysis (see Paper I) suggests a break energy at $\approx$ 1 keV and a $\Delta\alpha_E = 0.5 - 1$. To reproduce our observations the Haardt & Maraschi models would then require a small black hole mass and a peculiar inclination. It appears therefore that these models suffer from problems similar to those of pure disk models.

Another possible mechanism for hardening the soft X-ray spectrum from an accretion disk is via irradiation of its surface by an external X-ray source. Irradiation of the disk not only modifies the ionization state of the disk surface and produces an additional soft X-ray component (Ross & Fabian 1993, Matt, Ross & Fabian 1993, Życki et al 1994), but also affects the vertical structure of the disk. In addition, the outer parts of the disk will also be influenced by external irradiation (by the X-rays and by the UV spectrum generated at small radii, if the fractional disk thickness increases outwards and/or if relativistic deflection of the light is important, as in disks around a rotating black hole (Cunningham 1976). This may modify the OUV slope (Malkan 1991), and irradiation may be the cause for the flattening of the spectrum in the OUV band with respect to pure disk models and of the wide range of observed OUV slopes.

Ross & Fabian calculated the reflection spectrum from a slab of gas at $R = 7R_S$ under the assumption that the illuminating hard X-ray flux is equal to the soft flux locally produced in the slab. They found that the ionization parameter of the gas determines the emerging X-ray spectrum. In their model the ionization parameter ξ is directly linked to the accretion rate ($\xi \propto \dot{m}^3$). Most recently Matt, Fabian & Ross (1993) generalized this approach calculating the UV and X-ray spectrum from an accretion disk illuminated by a central X-ray source. In the models of Ross & Fabian the spectrum flattens by about $\Delta\alpha_E \approx 0.4$ from the 0.3-2 keV region to the 2-20 keV region, for $0.15 < f < 0.3$ and for a black hole mass of $10^8 - 10^9 M_\odot$. A similar result is inferred from Fig. 4 and 12 in Matt et al (1993) for an illuminated accretion disk in a Schwarzschild geometry with a black hole mass of $10^9 M_\odot$ and $\dot{m} \lesssim 0.4$.

The average PSPC spectral index of low optical luminosity ($M_B > -23$),

radio-quiet quasars without strong absorption (28 objects in the Walter & Fink, 1993, sample) is 1.44, which implies a $\Delta\alpha_E$ with respect to the 2-10 keV spectrum similar to that predicted by Ross & Fabian. On the other hand in the same sample the average spectral index of the radio-quiet quasars with $M_B < -23$ (17 objects) is 1.64 (similar to the average slope of the radio-quiet quasars in Laor et al 1994), steeper than in lower optical luminosity sources. Furthermore, in 30 % of these objects and in half of the sources of the sample presented in this paper $\alpha_E > 2$ (e.g. NAB0205+025, PG1211+143, PG1244+026, see Paper I). If the 2-10 keV spectrum of these quasars has a slope close to the mean *Ginga* slope in Williams et al (1992), then a $\Delta\alpha_E \sim 1$ is implied, significantly larger than predicted by reflection. The reason is that the integrated intensity of the reflected spectrum in the soft X-ray band cannot be much greater than the intensity of the ionizing X-ray continuum at the same energies (unless the X-ray source is obscured in part, or strongly beamed toward the disk). Reflection might account for the soft component of low optical luminosity quasar, but probably it does not dominate the soft component of the high optical luminosity quasars in the sample presented in this paper. The luminosity locally generated (not reprocessed) is likely be a non-negligible part of the total soft X-ray luminosity in these sources. PSPC calibration uncertainties presently limit the strength of this result.

5. CONCLUSIONS

We have compared the observed OUV to soft X-ray SED of six radio-quiet, low-redshift quasars with the predictions of several competing thermal models. Our main results are as follows:

1. Isothermal optically thin continuum emission from an ionized plasma cannot explain simultaneously the soft X-ray color and the luminosity in the optical and UV of the six quasars. A distribution of temperatures would help in relaxing the strong constraints posed by the present data. While this is not inconceivable, this assumption is not justified by the model itself but represents an "a posteriori" tuning.

2. On the other hand, accretion disk models naturally predict that components at different temperature dominate different frequencies. However, we find that pure disk models, even in a Kerr geometry, cannot account for the observed OUV and soft X-ray colors and luminosities. The rather flat soft X-ray component slope found by the PSPC requires high inclinations and high accretion rates, which in turn overestimate the soft X-ray luminosity, when producing the correct UV luminosity.

3. The soft X-ray color can be explained if the soft X-ray emission is dominated by an additional component. The assumption of an underlying power law component extending from the infrared ($3\mu m$) to the X-ray, can explain both

the OUV and, soft X-ray colors and luminosities, while it does not overpredict the observed $3\mu m$ luminosity. The presence of an optically thin hot ($T \lesssim 50$ keV) corona around the accretion disk can explain the soft X-ray color and luminosity.

4. A promising physical model is one involving reflection from an ionized accretion disk. This might explain the observed soft X-ray spectrum and luminosity of quasars with a soft X-ray component not much stronger than the primary component. However, it can not readily explain the large soft excesses found in at least half of the quasars in this sample.

The present analysis, and the absence of strong line features in the PSPC spectra noted in Paper I, argue against single temperature, solar metal abundance, optically thin emission as the only contributor to the OUV-to-soft-X-ray SED of the quasars in the sample presented in this paper. Pure disk models also fail to describe the quasar SED. While modifications of both optically thin plasma models and pure disk models might account for the observed SED, we do not find any strong evidence that the OUV bump and the soft X-ray emission are one and the same component, and that this component is thermal in origin. The observed SED could be produced by different components dominating different wavelenghts, or by non-thermal emission mechanisms.

ACKNOWLEDGMENTS

We thank Ari Laor for kindly providing us with the transfer function code for the Kerr geometry and for many useful discussions, Bożena Czerny, Magda Zbyszewska and Giorgio Matt for discussions about comptonization, disk emission and reflection. We also thank the referee, Richard Barvainis, for his comments that contributed to improve the paper. This work was supported by NASA grants NAGW-2201 (LTSARP), NAG5-1872, NAG5-1883 and NAG5-1536 (ROSAT), and NASA contracts NAS5-30934 (RSSDC), NAS5-30751 (HEAO-2) and NAS8-39073 (ASC).

REFERENCES

Abramowicz, M.A., Czerny, B., Lasota, J.P., & Szuszkiewicz, E. 1988, ApJ, 332, 646

Barvainis, R. 1992, in "Testing the AGN Paradigm", S.S. Holt, S.G. Neff and C.M. Urry eds., AIP 254, p. 129

Barvainis, R. 1993, ApJ, 412, 513

Begelman, M.C., McKee, C.F., & Shields, G.A. 1983, ApJ, 271, 70

Begelman, M.C., & McKee, C.F. 1983, ApJ, 271, 89

Bohlin, R.C. 1980, A&A 85, 1

Bohlin, R.C., & Grillmar, C.J. 1988, ApJS, 68, 487

Carleton, N.P., Elvis, M., Fabbiano, G., Willner, S.P., Lawrence, A., & Ward, M. 1987, ApJ, 318, 595

Comastri, A., Setti, G., Zamorani, G., Elvis, M., Giommi, P., Wilkes, B.J., & McDowell, J.C.M. 1992, ApJ, 384, 62.

Cameron, R.A., et al 1993, in Proc. Compton Symposium, St. Louis, MO, ed N. Gehrels

Clavel, J., Wamsteker, W., & Glass, I.S. 1989, ApJ, 337, 236

Cunningham, C.T. 1976, ApJ, 208, 534

Czerny, B., & Elvis, M. 1987, ApJ, 321, 305

Czerny, B., & Zbyszewska, M. 1991, MNRAS, 249, 634

Czerny, B. 1993, in "Multi-wavelength Continuum Emission of AGN", 159th IAU Symposium, Courvoisier & Blecha eds., (Kluwer: Dordrecht), p. 261

Czerny, B., Jaroszyński, M., & Czerny, M. 1994, MNRAS, 268, 135

Done, C., et al 1990, MNRAS, 243, 713

Elvis, M., Green, R.F., Bechtold, J., Schmidt, M., Neugebauer, B.T., Soifer, B.T., Matthews, K., & Fabbiano, G. 1986, ApJ, 310, 291

Elvis, M., Giommi, P., Wilkes, B.J., & McDowell, J.C. 1991, ApJ, 378, 537

Elvis, M., Wilkes, B.J., McDowell, J.C., Green, R.F., Bechtold, J., Willner, S.P., Polomski, E. & Cutri, R. 1994a, ApJS, 95, 1

Elvis, M., Matsuoka, M., Siemiginowska, A., Fiore, F., Mihara, T., & Brinkmann, W. 1994b, ApJL, 436, L55

Edelson, R., et al 1994, ApJ, submitted

Eracleous, M. & Halpern, J.P. 1994, ApJS, 90, 1.

Fiore, F., Elvis, M., McDowell, J.C., Siemiginowska, A., & Wilkes, B.J., 1994, ApJ, 431, 515.

Fiore, F., & Elvis, M. 1994, in "High Energy Radiation from Galactic and Extragalactic Black Holes", 30th COSPAR Meeting, Hamburg, Germany

George, I., Turner, T.J., & Netzer, H. 1995, ApJL, 438, L37

Górecki, A., & Wilczewski, W. 1984, Acta Astron., 34, 141

Green, P.J., Anderson, S.F., & Ward, M.J. 1992, MNRAS, 254, 30

Haardt, F., & Maraschi, L. 1993, ApJ, 413, 507

Kinney, A.L. 1993, in "The Physics of Active Galaxies", Camberra, Australia

Jourdain, E, et al 1992, A&A, 256, L38

Kriss, G.A. 1994, BAAS, vol26, No.2, p.879.
Laor, A., & Netzer, H. 1989, MNRAS, 238, 897
Laor, A., Netzer, H., & Piran, T. 1990, MNRAS, 242, 560
Laor, A., 1990, MNRAS, 246, 396
Laor, A., Fiore, F. Elvis, E., Wilkes, B.J., & McDowell, J.C. 1994, ApJ, 435, 611
Liang, E.P.T., & Price, R.H. 1977, ApJ, 218, 249
Maisak, M., et al 1993, ApJ, 407, L61
Malkan, M.A., & Sargent, W.L.W. 1982, ApJ, 254, 22
Malkan, M.A. 1988, Adv. Space res., Vol. 8, No. 2-3, p. (2)49
Malkan, M.A. 1991, in "Structure and Emission Properties of Accretion Disks", C. Bertout, S. Collin, J-P. Lasota & J. Tran Than Van eds. (Frontieres: Gif sur Yvette Cedex), p. 165
Maraschi, L. & Molendi, S. 1988, ApJ, 353, 452
Masnou, J.-L., Wilkes, B.J., Elvis, M., McDowell, J.C., & Arnaud K.A. 1992, A&A, 253, 35
Matt, G., Fabian, A.C., & Ross, R.R. 1993, MNRAS, 264, 839
McAlary, C.W., & Rieke, G.H. 1988, ApJ, 333, 1
McDowell, J.C., Elvis, M., Wilkes, B.J., Willner, S.P., Oey, M.S., Polomski, E., Bechtold, J., & Green, R.F. 1989, ApJ, 345, L13
Mushotzky, R., et al 1995, MNRAS, in press
Neugebauer, G., Green, R.F., Matthews, K., Schmidt, B.T., Soifer, B.T., & Bennet, J. 1987, ApJS, 63, 615
Novikov, I.D., & Thorne, K.S. 1973, in "Black Holes" De Witt C. De Witt B. eds. (Gordon & Breach: New York)
O'Brien, P.T., Gondhalekar, P.M., & Wilson, R. 1988, MNRAS, 233, 845
Page, D.N., & Thorne, K.S. 1974, ApJ, 191, 499
Pfefferman, E., et al 1987, Proc SPIE, 733, 519
Pounds, K.A, et al. 1993, MNRAS, 260, 77
Pounds, K.A., 1994, in "New Horizons in X-ray Astronomy", Tokyo, Japan
Puchnarewicz, E. et al 1995, in preparation
Raymond, J.C., & Smith, B.W. 1977, ApJS, 35, 419
Ross, R.R., Fabian, A.C., & Mineshige, S. 1992, MNRAS, 258, 189
Ross, R.R., & Fabian, A.C. 1993, MNRAS, 261, 74
Rudy, R. J., LeVan, P. D., & Rodriguez-Espinosa, J. M. 1982 AJ, 87, 598
Rybicki, G.B., & Lightman, A.P. 1979, "Radiative Processes in Astrophysics" John Wiley & Sons, New York
Saxton, R.D., Turner, M.J.L., Williams O.R., Stewart, G.C., Ohashi, T. & Kii, T. 1993, MNRAS, 262, 63
Shields, G.A. 1978, Nat, 272, 706
Siemiginowska, A., Kuhn, O., Elvis, M., Fiore, F., McDowell, J.C., & Wilkes, B.J. 1994, ApJ, submitted
Sikora, M., & Zbyszewska, M. 1986, Acta Astron., 36, 255

Sun, W.-H., & Malkan, M.A. 1989, ApJ, 346, 68
Sunyaev, R.,A., & Titarchuk, L.G. 1985, A&A, 143, 374
Szuszkiewicz, E. et al 1994, in preparation
Trümper, J. 1983, Adv. Space Res., 2, No. 4, 241
Turner, T. J., & Pounds, K. A. 1988, MNRAS, 232, 463
Turner, T. J., & Pounds, K. A. 1989, MNRAS, 240, 833
Turner, T.J., Weaver, K.A., Mushotzky, R.F., Holt, S.S., & Madejsky, G.M. 1991, ApJ, 381, 85
Walter, R., & Fink, H.H. 1993, A&A, 274, 105
Walter, R., Orr, A., Courvoisier, T.J.-L., Fink, H.H., Makino, F., Otani, C., & Wamsteker, W. 1994, A&A, in press
Weaver, K. 1995, 185^{th} AAS Meeting, Tuscon, AZ, Jan. 1995.
White, T.R., & Lightman, A.P. 1989, ApJ, 340, 1024
Wilkes, B.J., & Elvis. M. 1987, ApJ, 323, 243
Williams, O.R., et al 1992, ApJ, 389, 157
Zdziarski, A.A. 1985, ApJ, 289, 514
Życki, P.T., Krolik, J.H., Zdziarski, A.A., & Kallman, T.R. 1994, ApJ, 437, 597

Figure Captions

Figure 1. The PSPC energy index plotted against the OUV to X-ray energy index α_{OX} for the quasars of the sample presented in this paper (squares), the radio-quiet quasars in the Laor et al (1994) sample (circles), and the PG objects in the sample of Walter & Fink (1993) with z< 0.4 (triangles). Open symbols identify high luminosity quasars ($M_B < -23.5$), filled symbols identify low luminosity quasars ($M_B > -23.5$).

Figure 2. The IR–soft X-ray Spectral Energy Distributions of the six quasars, (after the subtraction of the galaxy contribution and of the high energy X-ray power law): NAB0205+024: open triangles, PG1211+143: filled squares, MKN205: filled circles; TON1542: filled triangles, PG1244+026: open squares, PG1426+015: open circles. Upper panel: the solid lines represent the free-free continuum for $T = 3 \times 10^6$ K and two normalizations; the dashed line represents the free-free continuum for $T = 10^6$ K. Lower panel: the solid line represents the sum of the continua from an optically thin plasma with $T = 10^6$ K; the short-dashed line is the free-free continuum; the long-dashed line is the recombination continuum; the dot-dashed line is the two-photon continuum.

Figure 3. The Soft X-ray color ($\nu L_\nu(1keV)/\nu L_\nu(0.4keV)$, soft component only), plotted against the OUV color ($\nu L_\nu(1325\AA)/\nu L_\nu(5500\AA)$) . Filled and open circles with error bars identify the six quasars, the dashed error bars indicate the error resulting from a power law plus free-free fit (Paper 1). In three cases (open circles) (PG1211+143, MKN205, and PG1426+015) the quasars have been observed by IUE more than once and we plot the OUV color obtained using both the maximum and minimum optical and UV flux. The dotted line identifies the prediction of a pure free-free model as a function of temperature with open boxes indicating: 1, 2, 3, 5, 10 $\times 10^6$ K (soft X-ray color increases with temperature). The filled boxes indicate the soft X-ray color predicted including the contribution of 2-photon and recombination continua for $T = 10^6$ and $T = 10^7$ K. Dashed lines identify accretion disk models in a Kerr geometry. Filled hexagons and triangles indicate five disk inclinations, $\mu = \cos\theta = 1, 0.75, 0.5, 0.2, 0.1$ (soft X-ray color increases with inclination) with $M = 10^8 M_\odot$ and accretion rates 0.3 L_{Edd} and 0.8 L_{Edd}. Open hexagons and triangles identify disk models with $M = 10^7 M_\odot$ for the same inclinations and accretion rates.

Figure 4. The observed 1325Å luminosity plotted against that predicted by the best fit power law plus thermal bremsstrahlung model for the X-ray spectrum of the six quasars. The predicted luminosity upper limits are twice the best fit luminosity from X-ray spectral fitting.

Figure 5. The spectral energy index of Comptonized spectrum in the corona model as a funcion of the temperature for three values of the optical depth.

Figure 6. The IR–soft X-ray Spectral Energy Distributions of the six quasars, (after the subtraction of the galaxy contribution and of the high energy X-ray power law): NAB0205+024: open triangles, PG1211+143: filled squares, MKN205: filled circles; TON1542: filled triangles, PG1244+026: open squares, PG1426+015: open circles. Solid lines in figure a) represent accretion disk models in a Kerr geometry with $M = 10^8 M_\odot$, inclination $\mu = 0.5$, and two accretion rates ($\dot{m} = 0.1, 0.8$). Dashed lines identify Kerr disk models with $M = 10^7 M_\odot$ for the same accretion rates and inclinations. Solid lines in figure b) represents Kerr disk models with $M = 10^8 M_\odot$, accretion rate 0.8 the critical one and three disk inclinations, $\mu = 1, 0.5, 0.2$. Dashed lines identify disk models with $M = 10^7 M_\odot$ for the same accretion rates and inclinations.

Figure 7. The 0.4 keV luminosity plotted against the 1325Å luminosity. Filled hexagons and triangles identify accretion disk models in a Kerr geometry with $M = 10^8 M_\odot$, $\dot{m} = 0.3, 0.8$, and five disk inclinations from $\mu = 1$ to $\mu = 0.1$. Open hexagons and triangles identify disk models with $M = 10^7 M_\odot$ for the same accretion rates and inclinations.

Figure 8. The Soft X-ray color plotted against the OUV color as in Fig. 3. Filled triangles identify disk plus power law models with $M = 10^8 M_\odot$, $\dot{m} = 0.3$, disk inclination $\mu = 0.5$, and three values of the power law normalization. The power law spectral index is fixed at 1.25. Open triangles identify disk models with $M = 10^7 M_\odot$ for the same accretion rate, inclination, power law spectral index and normalizations as in the previous case.

Figure 9. The soft X-ray color plotted against the $3\mu m$ luminosity. Filled triangles identify disk plus power law models with $M = 10^8 M_\odot$, $\dot{m} = 0.3$, disk inclination $\mu = 0.5$, and three values of the power law normalization. The power law energy index is fixed at 1.25. Open triangles identify disk models with $M = 10^7 M_\odot$ for the same accretion rate, inclination, and power law slope and normalizations as in the previous case.

Figure 10. The 0.4 keV luminosity plotted against the 1325Å luminosity. Filled triangles identify disk plus power law models with $M = 10^8 M_\odot$, $\dot{m} = 0.3$, disk inclination $\mu = 0.5$, and three values of the power law normalization. The power law slope is fixed at 1.25. Open triangles identify disk models with $M = 10^7 M_\odot$ for the same accretion rate, inclination, and power law slope and normalizations as in the previous case.

Figure 11. The Soft X-ray color plotted against the OUV color as in Fig. 3. Filled hexagons identify accretion disk models in a Schwarzschild geometry with a hot corona with parameters: $M = 10^8 M_\odot$, $\dot{m} = 0.1, 0.3, 0.8$, kT=50 keV and $\tau = 0.5$. Filled squares identify models with kT=50 keV and $\tau = 0.25$ and filled triangles models with kT=10 keV and $\tau = 0.5$. Open symbols identify the same models but with $M = 10^7 M_\odot$. Higher accretion rates result in a higher UV to optical color.

TABLE 1: X-ray Observations

name	$\nu L_\nu^{a,b}(0.4keV)$	$\nu L_\nu^{a,b}(1keV)$	$\alpha_{ES}^{b,c}$	$\nu L_\nu^{a,d}(2keV)$	$\nu L_\nu^{a,b}(1325\AA)$
NAB0205+024[e]	$8.07^{+1.79}_{-2.09}$	$1.60^{+0.33}_{-0.63}$	2.8 ± 0.5	$1.07^{+0.07}_{-0.12}$	
[f]	$5.53^{+1.49}_{-0.60}$	$0.78^{+0.30}_{-0.30}$		$1.18^{+0.09}_{-0.09}$	2.2
PG1211+143[e]	$2.46^{+0.90}_{-0.65}$	$0.74^{+0.33}_{-0.41}$	$2.3^{+1.1}_{-0.3}$	$0.56^{+0.10}_{-0.06}$	
[f]	$1.64^{+0.74}_{-0.25}$	$0.25^{+0.19}_{-0.10}$		$0.62^{+0.08}_{-0.07}$	0.6
MKN205[e]	$1.15^{+0.62}_{-0.20}$	$0.31^{+0.35}_{-0.10}$	$2.3^{+1.1}_{-0.7}$	$0.92^{+0.05}_{-0.04}$	
[f]	$0.77^{+0.34}_{-0.28}$	$0.124^{+0.16}_{-0.065}$		$0.94^{+0.06}_{-0.06}$	0.3
TON1542[e]	$0.71^{+0.43}_{-0.25}$	$0.135^{+0.225}_{-0.076}$	$2.4^{+1.6}_{-0.7}$	$0.44^{+0.02}_{-0.02}$	
[f]	$0.41^{+0.20}_{-0.07}$	$0.005^{+0.009}_{-0.003}$		$0.45^{+0.07}_{-0.07}$	0.8
PG1244+026[e]	$0.72^{+0.12}_{-0.09}$	$0.22^{+0.013}_{-0.062}$	$2.3^{+0.4}_{-0.6}$	$0.088^{+0.012}_{-0.004}$	
[f]	$0.49^{+0.16}_{-0.04}$	$0.090^{+0.050}_{-0.032}$		$0.099^{+0.019}_{-0.015}$	0.2
PG1426+015[e]	$3.21^{+0.49}_{-0.58}$	$1.69^{+0.29}_{-0.66}$	$1.8^{+0.4}_{-0.3}$	$1.43^{+0.12}_{-0.09}$	
[f]	$2.22^{+0.54}_{-0.25}$	$0.144^{+0.115}_{-0.034}$		$1.56^{+0.14}_{-0.14}$	0.7

[a] in units of 10^{44} erg s^{-1}; [b] soft X-ray component;

[c] $F_\nu \propto \nu^{-\alpha_{ES}}$; [d] total X-ray luminosity;

[e] 2 power law fit; [f] power law + thermal bremsstrahlung fit.

TABLE 2: Infrared – Ultraviolet Observations

Name	Redshift	$\log \nu L(H)^a$ of Galaxy	$\nu L_\nu^a(3\nu m)$ No.; Dates	$\nu L_\nu^a(5500\mathring{A})$ No.; Dates	$\nu L_\nu^a(2500\mathring{A})$ No.; Dates	$\nu L_\nu^a(1325\mathring{A})$ No.; Dates	α_{OX}^b
NAB0205+024	0.155	44.19 ± 0.04	$9.4^{+1.0}_{-0.9}$ 1; 85/9	8.1-11.5 3; 78/2-91/9	33 ± 1 1; 82/12	31 ± 4 1; 82/12	1.57
PG1211+143	0.085	$43.36^{+0.04}_{-0.23}$	10.9–14.7 5; 81/5–88/4	9.7–16.6 6; 80/6–88/9	23.4–27.8 2; 85/12–87/2	19.1–31.3 2 83/12–85/2	1.64
MKN205	0.070	$44.60^{+0.1c}_{-0.6}$	1.7–4.2 3; 76/6–85/6	$1.6^{+1.5}_{-0.6}$ 1; 72/5	1.8–7.3 2; 78/7–83/2	3.3–6.1 2; 78/7–83/2	1.27
TON1542	0.064	$44.48^{+0.1d}_{-0.6}$	$3.17^{+0.63}_{-0.38}$ 1; 81/5	$2.61^{+0.75}_{-0.31}$ 1; 80/11	7.5 ± 0.2 1; 82/5	10.2 ± 0.3 1; 82/5	1.47
PG1244+026	0.048	$43.76^{+0.1d}_{-0.6}$	$0.39^{+0.07}_{-0.04}$ 1; 83/2	0.53-0.92 2; 7/80-5/91	1.06 ± 0.05 1; 83/2	1.06 ± 0.05 1; 83/2	1.41
PG1426+015	0.086	$44.60^{+0.3c}_{-0.6}$	5.9–12.1 5; 81/7–88/5	2.6–7.3 6; 80/7–88/9	22.3–28.4 2; 83/2–85/5	24.9–42.8 2; 83/2–85/5	1.48

[a] in units of 10^{44} erg s^{-1};

[b] $\alpha_{OX} = \frac{log(L(2500\mathring{A})/L(2keV))}{2.6057}$;

[c] Galaxy subtraction for TON1542 used the mean values given in Elvis et al 1994: $L_H = 4^{+4}_{-3} \times 10^{44}$erg s^{-1}; $r_e = 10^{+3}_{-6}$ kpc;

[d] Galaxy normalization chosen to match the restframe H luminosity.

The X-ray and Ultraviolet Absorbing Outflow in 3C351

Smita Mathur, Belinda Wilkes, Martin Elvis and Fabrizio Fiore
Harvard-Smithsonian Center for Astrophysics
60 Garden St, Cambridge MA 02138
Internet: smita@cfa.harvard.edu

December 5, 1997

Abstract

3C351 (z=0.371), an X-ray 'quiet' quasar, is one of the few quasars showing signs of a 'warm absorber' in its X-ray spectrum; i.e. partially ionized absorbing material in the line of sight whose opacity depends on its ionization structure. The main feature in the X-ray spectrum is a K-edge due to OVII or OVIII. 3C351 also shows unusually strong, blueshifted, associated, absorption lines in the ultraviolet (Bahcall et al 1993) including OVI ($\lambda\lambda 1031, 1037$). This high ionization state strongly suggests an identification with the X-ray absorber and a site within the active nucleus.

In this paper we demonstrate that the X-ray and UV absorption is due to the same material. This is the first confirmed UV/X-ray absorber. Physical conditions of the absorber are determined through the combination of constraints derived from both the X-ray and UV analysis. This highly ionized, outflowing, low density, high column density absorber situated outside the broad emission line region (BELR) is a previously unknown component of nuclear material.

The effect of the X-ray quietness and IR upturn in 3C351 spectral energy distribution (SED) on the BELR is also investigated. The strengths of the high ionization lines of CIV $\lambda 1549$ and OVI $\lambda 1034$ with respect to Lyα are systematically lower (up to a factor of 10) with the 3C351 SED as compared to those produced by the 'standard' continuum, the strongest effect being on the strength of OVI $\lambda 1034$. We find that for a 3C351 like SED CIII] $\lambda 1909$ ceases to be a density indicator.

1 Introduction

A minority of AGN show optical and ultraviolet absorption lines within the profiles of their broad emission lines (Ulrich 1988). While this ionized absorbing material must be associated with the active nucleus, there is no accepted model for it (see, e.g. Kolman et al 1993). Similarly, many AGN, mostly Seyfert galaxies, exhibit strong low energy X-ray cutoffs (e.g. Turner & Pounds 1989) due to 'cold' material in their nuclei, also with no accepted identification. The possibility of linking two types of absorbers has not seemed promising to date (Ulrich 1988). However, recent observations of X-ray 'warm absorbers' promise to change this situation. 3C351 provides a particularly good opportunity.

3C351 (z=0.371) is one of the few quasars showing signs of a 'warm absorber' in its X-ray spectrum; i.e. a partially ionized absorbing material in the line of sight whose opacity depends on its ionization structure (Fiore et al 1993; hereafter Paper I). The main feature in the X-ray spectrum is a K-edge due to OVII or OVIII. 3C351 also shows unusually strong, associated, absorption lines in the ultraviolet (Bahcall et al 1993) including OVI ($\lambda\lambda 1031, 1037$), strongly suggesting an identification with the X-ray absorber, and a site within the active nucleus.

In this paper we search for, and find, a model for the absorber which is consistent with both the X-ray and UV data. We re-analyze the X-ray and UV data with this aim in mind (section 2). In order to produce self consistent models, we find that use of the observed (ionizing) continuum of 3C351, rather than a generic quasar continuum is critical (section 3). We find that the UV absorption line clouds (section 4), but not the broad emission line region (BELR) clouds (section 3), can cause the X-ray absorption. Finally we derive the physical characteristics of this outflowing material (section 4) and consider why a previous similar attempt to identify an X-ray absorber with a strong UV absorber in a different AGN was not successful (section 5).

2 X-ray, Ultraviolet and Optical Data

2.1 X-ray Spectrum

The details of the X-ray observations, extraction of the source pulse height spectrum, and its analysis are presented in Paper I which showed the presence of an ionized absorber. The input spectrum to the ionized absorber used in Paper I was a simple power law. However, the inferred parameters of the ionized absorber depend critically on the input spectrum. To investigate this dependence, we refitted the X-ray spectrum with the observed 3C351 SED as the input to a warm absorber, changing the energy at which the X-ray spectrum turns up to meet the ultraviolet using a broken power law. The break energy was varied from the unobserved EUV range to well within the PSPC range: 0.07 keV, 0.37 keV, and 0.7 keV. The slope ($f_\nu \propto \nu^{-\alpha}$) in the soft energy range (α_1) is fixed by the observed flux in the UV at one end and the break energy at the other. The slope, α_2, above the break energy was fixed at 1, typical for lobe dominated radio loud quasars (Shastri et al 1993). The resulting parameters are given in Table 1 and the best fit spectrum is shown in Figure 1. The fits gave χ^2= 24.7, 29.8, and 31.7 respectively for the three models for 27 degrees of freedom. A χ^2 of 31.7 is unacceptably large (probability of 25%) so a break at a lower energy (0.37 keV or less) is preferred. We will only discuss models with lower break

energies in the rest of the paper unless otherwise noted. The difference in the break energy in the three models results in small differences in the best fit values of the absorbing column density (N_H=1–2 $\times 10^{22} atoms\ cm^{-2}$), and larger differences in the ionization parameter U of the warm absorber (U=6–12). U here is defined as the dimentionless ratio of ionizing photon to baryon density. The best fit ionization parameter differs significantly from that for a single power law (U=0.1–0.2) while the column density is similar (N_H=1–4 $\times 10^{22} atoms\ cm^{-2}$) (Paper I).

2.2 Ultraviolet and Optical Spectra

3C351 was also observed by HST as a part of the Quasar Absorption Lines Key Project (Bahcall et al 1993). By a fortunate coincidence, the HST ultraviolet observations were quasi-simultaneous with the X-ray observations (ROSAT: October 28–30, 1991; HST: October 22, 1991). An unusually strong metal line absorption system (Figure 2a–d) is observed at z=0.3646 (Bahcall et al 1993). This system was previously noted in the co-added IUE spectrum by Kinney et al(1992). The system contains the high excitation doublets of OVI, NV and CIV and the Lyman series Lyα, Lyβ, Lyγ (blended with another Lyα line at z=0.92) and Lyδ. Bahcall et al (1993) suggested that an associated cluster of galaxies is responsible for the UV absorber. However, the deep image of this field by Ellingson et al (1994) shows that there are no associated galaxies. We conclude that the UV absorber is associated with the quasar itself.

Table 2 lists the published equivalent widths (EW), and full width at half maximum (FWHM), of the absorption lines in the z=0.3646 system given by Bahcall et al. There are two important exceptions, CIV and NV. In both cases we have modified the values from Bahcall et al. The broad (FWHM = 8.58 Å), strong (EW=3.09 Å) absorption line at 2114.5 Å within the CIV line was not identified by Bahcall et al. The automatic algorithm used by Bahcall et al to identify the absorption lines finds a weak CIV doublet at 2112.8 and 2116.6 Å (EW= 0.26 Å and 0.12 Å respectively) but leaves the broad line unidentified. Inspection of the spectrum (Figure 2c) shows that the CIV absorption doublet is not clearly resolved. This is not surprising given the typical FWHM of absorption lines in this system. If we assume that the whole absorption for this broad system (FWHM= 8.58 Å) at 2114 Å is due to an unresolved CIV line (1549.1 Å), the redshift is then 0.3646, in agreement with the rest of the system. We use this larger EW in our modeling.

The position of the NV absorption doublet, between the emission line peaks of the heavily blended lines of Lyα and NV (figure 2b), results in a large uncertainty in the continuum level and in the resulting equivalent widths. The published values of the NV ($\lambda\lambda$1238, 1242) EWs are 1.60 Å and 1.63 Å . For the HST data, Schneider et al (1993) defined a continuum by a cubic spline fit to a number of discrete continuum points. This approach does not allow for the blue wing of the NV emission line suppressed by the absorption lines. Thus the true continuum around 1695 Å is likely to be higher than that fitted by the cubic spline method. This is significant since the error in the continuum determination results in $\sim$ 40% change in the EW so the NV EWs may be as high as 2.2 Å and 2.3 Å respectively. These uncertainties are taken into account in our modeling.

The Lyα absorption line (z=0.3646) is blended with another Lyα absorption line (z=0.3621) resulting in significant uncertainty in its equivalent width. The values in Table 2 assume $\sim$ 40% error.

The FWHM of these absorption lines in the z=0.3646 system ranges from 2.85 Å to 8.58 Å .

This implies a maximum value of the velocity spread parameter 'b' to be $< 600 - 1200$ km s^{-1}.

No lines from the low excitation ions of CII, NI, NII, OI, SiII, AlII, and FeII are present (equivalent widths $\lesssim 0.4\AA$). Also, ground-based observations by Boiss'e et al (1992) showed no z=0.3646 MgII absorption doublet, giving an upper limit of 0.1 Å to its equivalent width.

Bahcall et al (1993) do not report emission line strengths. In order to see whether the high ionization emission line clouds could produce the X-ray absorption, the spectra were obtained from the HST archive and analyzed using IRAF. Equivalent widths and fluxes were measured for lines of Lyman α, CIV λ1549, CIII] λ1909, and OVI λ1034 using local continuum estimates and the results are given in Table 2. As discussed above, the spectral lines show strong absorption features. Lyman α is also blended with emission lines of SiII λ1260, and NV λ1240, and the SiII λ1537, NeV λ1575 features are superposed on the CIV λ1549 emission line. Apart from NV λ1240, which is a strong contaminant, these lines are weak and not expected to exceed $\sim$ 10% of the line. We thus estimate our errors at the 10% level. Since NV cannot be deblended from Lyman α without introducing large additional uncertainties, we modeled the two emission lines together. In addition, the weaker lines were included in the line strengths predicted by photoionization models so that a proper comparison with observed lines could be made. The emission line fluxes were corrected for the absorption line systems using the EWs in Table 2.

3C351 was also observed in the ultraviolet by IUE. Kinney et al(1991) have published an optimally extracted, "co-added" spectrum of 3C351. As a consistency check, the co-added spectrum of 3C351 was also obtained from the IUE archive and analyzed to measure the strengths of the emission lines. The equivalent widths of the lines were found to be consistent with those measured from the HST spectra.

2.3 Observed Energy Distribution of 3C351

3C351 was observed by us with ROSAT because it was known to be X-ray 'quiet', i.e. it has a factor of $\sim$ 5 lower X-ray flux than the average radio loud quasar. The X-ray to optical flux ratio α_{OX} for 3C351 is 1.6, as compared to α_{OX}=1.3 for an average radio loud quasar (Wilkes et al 1994). Soft X-rays affect the ionization within the emission line clouds and influence the production of the high ionization lines, hence it is important to use the spectral energy distribution (SED) of 3C351 in photoionization modeling rather than using an "average" one, as is generally used (Mathews and Ferland 1987). Figure 3 shows the observed SED of 3C351 (Elvis et al 1994) The short dashed line is the AGN continuum defined in CLOUDY (Ferland 1991) which we shall call the 'standard continuum'. This standard continuum is similar to that used by Mathews and Ferland (1987) with the exception that the spectral index ($f_\nu \propto \nu^\alpha$) is changed from -1 to $+5/2$ for frequencies below the mm break. The solid line is the best fit interpolation to the observed SED of 3C351. The X-ray slope is not well constrained due to the presence of the ionized absorber. We use two extreme values of α for radio loud quasars (0.0 – 1.0) (Wilkes and Elvis 1987) to investigate its effect on the resulting line strengths (Figure 3). All the continua are normalized to match the observations in the optical/UV. We have extrapolated our best fit spectrum into the submillimeter region with α=2.5 (appropriate for synchrotron self-absorption) and the core radio component is smoothly joined onto it. The exact point where the two components join is not well defined but small differences here do not change our results significantly.

The observed SED and the standard spectrum differ significantly in the X-ray, IR and radio

regions. The weak flux in the X-ray is not due to X-ray variability or to the effect of the ionized absorber (Paper I). 3C351 also shows a clear upturn in the IR at $\sim 1\mu m$, turning over again at $\sim 25\mu m$. IR and radio emission can produce large amounts of free-free heating which can influence the relative strength of emission lines (Ferland & Persson 1989). The 1.3mm observations by Antonucci and Barvainis (1993) are critical to the photoionization balance since they strongly limit the extrapolation of the IR continuum. If the IR points are smoothly joined onto the radio, then the resulting continuum produces a large amount of free-free heating. This is unphysical because it produces unacceptably large emission of CIV λ1549 relative to Lyα. If instead the 1.3mm observations are used, the slope in the submillimeter region is constrained to +5/2, similar to the radio quiet quasars. This provides another argument in favor of the Antonucci and Barvainis hypothesis that the IR and radio cores are two distinct components and must arise at different locations thus relaxing the requirement that they smoothly connect. In the following section we investigate the effect of using the 3C351 SED on the physical conditions in photoionized gas clouds and so on the resulting line strengths.

3 Photoionization Models

Until recently models for the BELR had typical values of the ionization parameter U in the line emitting clouds of $\sim 10^{-2}$ (Davidson and Netzer 1978). The value of U for the ionized absorber in 3C351 is 100– 1000 times larger (Table 1). The line ratio CIII] λ1909/ CIV λ1549 is a sensitive function of U and such large values would produce unusually low values for CIII] / CIV ($<< 0.3$) and thus it appeared unlikely that a BELR cloud was responsible for the X-ray absorption.

Reverberation studies have now revealed that BELR clouds, at least those emitting the high ionization lines, are closer to the continuum source and so are exposed to a far more intense radiation field than previously thought (Peterson, 1993) with an ionization parameter of ~ 3. This is in the range required by the X-ray absorber. These studies have also shown that the CIII] λ 1909 line, previously used to deduce $n_e \geq 10^9 cm^{-3}$, is formed at a larger distance, $\sim 3-4$ light weeks, (Clavel et al 1991) and so is produced in different clouds. Thus, there is no clear density indicator for the Lyman α - CIV region. Several implications of this intense radiation at the BELR inner radius are discussed in detail by Ferland and Persson (1989). Of particular relevance to the present study are:

1. Free-free heating is more important for higher fluxes or ionization parameters.

2. The strongest effect of the SED is upon the higher ionization lines which are formed near the illuminated face of a cloud.

3. The ratio of CIV λ1549 to Lyα is an increasing function of density because of both the increased free-free heating and the decreased efficiency of Lyα emission.

4. The OVI λ1034 line increases in strength with increasing ionization parameter.

Since the importance of free-free heating increases with the intensity of the incident radiation field, a knowledge of the complete IR–X-ray energy distribution (SED) is needed to understand and model the high ionization emission lines. We have attempted to fit the OVI, CIV and Lyα/NV emission line EW with the conditions determined for the X-ray absorber using the

quasar's observed SED. The input spectrum, ionization parameter, hydrogen density and the column density of a cloud are the physical parameters which uniquely determine the strengths of the emission lines. We have explored a wide range of this parameter space: the hydrogen density was varied between 10^8 – $10^{11} cm^{-3}$; Lyman continuum optical depth: 10^4 – 10^6; and the ionization parameter: 0.01 – 10.0; in each case both the standard continuum and the 3C351 SED were considered as the input spectrum. In the following section we discuss the results. All the calculations were done using G. Ferland's CLOUDY software.

3.1 The effect of the SED on the emission lines

The dependence of the emission line strengths measured relative to Lyman α on the ionization parameter (U), hydrogen density (n_H) for both input spectra is shown in figures 4 and 5. The effect of the Lyman continuum optical depth on the line ratios was small (< 10%) for optical depths between 10^4 and 10^6. One effect that stands out is that of using the observed SED of 3C351 instead of the standard SED. The emission line strengths change significantly (up to a factor of ten) as the input spectrum is changed from the standard continuum to the 3C351 SED.

3.1.1 The relation between the SED and the ionization parameter

The two extreme wavelength intervals in the 3C351 SED, the X-ray and IR-radio, act competitively with opposite effects on the strengths of the emission lines of interest. In figure 4a, CIV, CIII] and OVI line strengths relative to Lyα are plotted as a function of U for log(n_H)=11. A larger IR-radio flux increases the line ratios due to increased free-free heating. Smaller X-ray flux produces lower numbers of ions and decreases the line ratios. For lower values of U, the low X-ray flux level in the 3C351 SED dominates and the line ratios are systematically lower than those produced by the standard continuum. Above some $U_{critical}$ the effect due to free-free heating dominates. The value of $U_{critical}$ is higher for ions with higher ionization potentials and increases with decreasing n_H. For low n_H (log(n_H)=9), $U_{critical}$ for OVI is sufficiently high that free-free heating is negligible for almost the entire range of U (Figure 4b).

The strongest effect of the low X-ray flux in 3C351 is on the strength of the OVI line. This is not surprising since the ionization potential of OV is 0.11 keV. The strength of the OVI line is lower by a factor of ~ 10 with an input spectrum which is X-ray quiet ($\alpha_{ox} = 1.6$).

Use of the standard quasar continuum instead of the observed, X-ray quiet one, to model the 3C351 emission lines would lead to a value of the ionization parameter lower by a factor of 2.5. The IR upturn and radio loudness have the opposite effect, but this is significant only when both U and n_H are high ($U \gtrsim 0.1$, $n_H \sim 10^{11}$ cm^{-3}).

3.1.2 The relation between the SED and the density

When U is low, the shape of the input continuum makes no significant difference to the strength of the CIV and CIII] lines but it always has a significant effect on the strength of OVI. For the standard continuum, the strength of CIII] λ1909 drops rapidly for densities higher than the critical density for collisional de-excitation ($10^9 cm^{-3}$) (Figure 4c) and so CIII] is normally used to put an upper limit on the BELR cloud densities. This effect vanishes using the 3C351 SED for values of U (> 0.1). This is due to increased free-free heating, which produces heating without

ionization. Thus, for X-ray quiet, IR-radio loud SED, *CIII]* λ1909 *ceases to be a density indicator* for U > 0.1.

Kwan (1984) pointed out that uncertainty in the dielectronic recombination rates and the strong dependence of CIII] λ1909/CIV λ1549 on U compromised its role as a density indicator. Our results show a second cause to discount the value of CIII] as a density diagnostic. We conclude that, even without variability information to confirm CIII]'s origin in different gas, it is not a good indicator of density in the high-ionization Lyα-CIV emitting region.

3.2 A High Ionization BELR as the Warm Absorber?

We compared the photoionization models described above with the observed UV emission lines CIII], CIV, OVI and Lyα. The predicted intensities of blended lines of $NV\lambda1240$, $NeV\lambda1575$ and $SiIII\lambda1895$ were added to those of $Ly\alpha$, $CIV\lambda1548$ and $CIII]\lambda1909$ respectively (Figure 5). The observed strength of $CIII]\lambda1909$ (= 0.1 relative to Lyα) is used only as an upper limit since, as already noted, reverberation studies show it originates from a separate, larger region. This constraint requires $\log(n_H) > 9$ for the entire range of U (Figure 4b). For the observed ratio of $CIII]\lambda1909/CIV\lambda1548 \leq 0.2$, a density $n_H \geq 10^{10.5}$ is preferred. Figure 4a compares the results for $\log(n_H)$=11. The 3C351 SED as the input produces large amounts of CIV with respect to $Ly\alpha$. This results from additional free-free heating due mainly to the IR upturn. The CIII] line constraint is now satisfied only for $logU < -1.2$; lower than that required for OVI production.

If this IR flux is produced by the thermal emission from dust at larger distances from the nucleus, the BELR clouds would not see the same continuum as we do. In that case we need to compare the observed line ratios with those predicted by the 3C351 SED without the IR upturn. The CIII] line constraint is now satisfied for the range of U relevant for CIV-OVI clouds (Figure 5). The inferred value of ionization parameter for CIV-$Ly\alpha$ producing clouds is then log U= -1.5 ± 0.2 for n_H=$10^{11} cm^{-3}$. The inferred value for OVIλ1034 is much larger being log U=-0.6 ± 0.1 implying that OVI is produced even closer to the ionizing continuum than the CIV-$Ly\alpha$ clouds.

It is interesting to observe that only when the input continuum spectrum is the 3C351 SED without the IR upturn, is the CIII] constraint satisfied for the entire range of U relevant for CIV-Lyα clouds. Thus, if CIII] is produced at a distance larger than the CIV-$Ly\alpha$ clouds, the IR upturn is necessarily produced beyond the BELR clouds. This provides an argument in favor of a dust model for the IR emission (Sanders et al 1989, Barvainis 1993)

Even though the ionization parameter inferred for the OVI emission line is much larger than the standard value (0.3 as compared to 0.01) (Figure 5) it is still much lower than that required for the X-ray absorber (6–12). Thus, we rule out the possibility of identifying the X-ray absorber as a BELR cloud.

4 The X-ray Absorber as The UV Absorber

Table 2a gives the EW and FWHM of the absorption lines in the z=0.3646 system. The existence of highly ionized OVI lines is particularly intriguing given the OVII absorption edge seen in soft X-rays (section 2). If the two absorbers are identical then the X-ray observations provide strong

constraints on the total N_H (Table 1) which allow us to solve for a consistent model for both the UV lines and the X-ray absorber.

The photoionization models predict f_{OVI}, the fraction of oxygen in the OVI state of ionization. Assuming a solar abundance of oxygen relative to hydrogen (8.51×10^{-4}, Grevesse and Anders 1989) and using the total N_H from the X-ray analysis, the column density of OVI, N_{OVI}, can be derived; $N_{OVI} = 3 \times 10^{17} cm^{-2}$. N_{ion} for the other ions has been derived similarly. These model values are listed in Table 3.

A measured column density for each ion of the UV absorber was derived from the line EW with a standard curve-of-growth analysis (e.g. Spitzer 1978). Figure 6 shows curves of growth for 'b' values ranging from 80 to 130 km s^{-1} where 'b' is the velocity spread parameter. Abscissa is log(Nλf) where Nλ has the dimension cm^{-1}. f is the oscillator strength of the transition. Values of f are taken from Wiese et al (1966). The lower limit to the column density of an ion is obtained from the linear part of the curve of growth. For OVI doublet transition $N_{OVI} > 1.7 \times 10^{15} cm^{-2}$. Small values of 'b' imply unacceptably large column densities ('b' $= 4km\ s^{-1}$ gives $N_{OVI} \sim 10^{27} cm^{-2}$); making the absorbing material optically thick to Thompson scattering. The maximum value of b is $\sim$ 600 - 1200 km s^{-1} given by the observed line widths (see section 2.2). High resolution data are needed to allow b and N_{ion} to be fitted independently. A value of b $\sim$ 105 - 115 km s^{-1} gives consistent solutions to the X-ray and UV line constraints. We shall use b = 110 $km\ s^{-1}$. The measured column density is then $N_{OVI} = 3 \times 10^{17} cm^{-2}$. A consistent solution was obtained for all the UV lines: OVI, CIV, NV and Lyα (figure 6).

Table 3 compares the column densities of each ion derived from the UV line analysis to those predicted by the photoionization models for different values of X-ray spectral break energy. The match provided by the models is good to better than 5% for CIV and OVI and consistent for NV. As noted in section 2, the heavy blending of Lyα and NV, results in a large uncertainty in the continuum level and so in the resulting equivalent width of NV. Thus the inferred range of N_{NV} is large (15.3 - 15.8).

In a highly ionized system such as this, hydrogen is mostly ionized with $\log f_{HI} = -6.5$. Given total hydrogen column density of $1.4 \times 10^{22} cm^{-2}$, the predicted Ly$\alpha$ EW is $W_{\lambda\ obs.} = 2.38$ (Figure 6) while the observed (Bahcall et al 1993) $W_{\lambda\ obs.} = 3.54$. This would imply that roughly 70% of the Lyα absorption attributed to the z=0.3646 absorber takes place in the highly ionized absorber . However, as noted earlier, Lyα (z=0.3646) is blended with Lyα (z=0.3621); thus, given the large uncertainties in the equivalent width due to de-blending, *all* the Lyα absorption could in fact come from the X-ray absorber.

Given the high ionization of this absorption system, magnesium is highly ionized (MgVI and higher) leaving no magnesium in the MgII state ($\log f_{MgII} < -30$) and thus MgII absorption should not occur. The same is also true for the low ionization ions of CII, NI, NII, OI, SiII, AlII, and FeII. This is consistent with the observations (see section 2).

For the X-ray model with break energy at 0.7 keV, the inferred parameters for the UV absorber are inconsistent with the parameters of the X-ray absorber (Table 3). If the X-ray absorber is indeed the UV absorber, for which the above evidence is compelling, then the break in the X-ray power law must be at lower energies. We note that this model also has the highest χ^2 (31.66 for 27 dof) among all the three models (section 2) and the X-ray fit is unacceptable. A break at lower energies ($\sim$0.37 keV or less) is thus preferred by both X-ray and UV data.

We conclude that in 3C351 the X-ray and UV absorbers are one and the same.

4.1 The Physical Characteristics of the Absorber

Since the X-ray absorber is strongly identified with the UV absorber, constraints from both UV and X-ray data can be combined to derive its physical properties. These properties describe a component of nuclear material not previously recognized. We have already shown that the absorber has high N_H (1–1.8$\times 10^{22} cm^{-2}$), and high U (6.7–12). Changes in density from 10^3 to $10^{11} cm^{-3}$ in the photoionization models result in no significant change in the values of fractional ionization, so the density is not constrained directly.

The absorption lines are blueshifted with respect to the high ionization emission lines by $\sim 2000 km\ s^{-1}$. The high ionization lines themselves generally show blueshifts of 1000–2000 $km\ s^{-1}$ (Espey et al 1989) relative to the Balmer lines, implying an outflow velocity for the absorber of $\sim$ 3000–4000$km\ s^{-1}$ in the quasar rest frame.

The UV absorption troughs extend through the emission lines down below the continuum level (Figure 2) requiring that both the continuum emitting region and the BELR are at least partially covered by the absorber. This places the absorber outside the BELR. Scaling from the reverberation mapping of NGC 5548 (Clavel et al 1991) by the square root of 3C351 luminosity ($L_{3C351} = 2 \times 10^3\ L_{N5548}$, r_{5548}= 10 lt. days) gives r $\gtrsim 1/3pc$ from the central continuum. The larger ionization parameter and larger radial distance compared to the BELR imply a lower density for the absorber. The radial distance of the ionized absorber is $r_{abs} = (Q/4\pi U n_H c)^{1/2}$ where Q is the number of ionizing photons. For the best fit parameters of the warm absorber this gives $r_{abs} = 5 \times 10^{19} n_5^{-1/2} cm$ where n_5 is the number density in the units of $10^5 cm^{-3}$. Hence the density of the absorber must be $\lesssim 5 \times 10^7 cm^{-3}$. This low density in combination with the large column density (1–2 $\times 10^{22} cm^{-2}$) implies a depth for the absorber, $\gtrsim 2 \times 10^{14} cm$.

The depth of the Lyα absorption line ($2.06 \times 10^{-14} ergs^{-1} cm^{-2} \AA^{-1}$) exceeds the continuum level ($0.77 \times 10^{-14} ergs^{-1} cm^{-2} \AA^{-1}$) (Figure 2b) implying that the absorber covers most ($\gtrsim$60%) of the BELR. However we note that the different lines indicate different percentages of the emission lines being covered, e.g. for OVI it could be 100% with the continuum covered $\gtrsim$80%. Thus the ionized absorber covers a large fraction, possibly all, of the BELR and the continuum along the line of sight and so must also have a diameter $\gtrsim 1/3pc$. The mass of the absorber is then $\gtrsim 10^3 M_\odot$

Further constraints come from the fact that a cloud with these physical properties exposed to the quasar continuum radiation would necessarily emit line radiation. For the contribution of the absorber to the broad emission lines to be negligible (line flux $< 10\%$ of continuum flux) the covering factor of such clouds must be low (< 0.01). Since the absorption lines lie within the profiles of their broad emission lines, upper limits to the emission by the absorber could be large. Covering factor may then be higher. Similar arguments have been used before to constrain the covering factor of the absorbing clouds in the broad absorption line quasars (BALQSOs) (Turnshek 1988).

The radiation pressure experienced by the warm absorber is easily sufficient to accelerate it to outflow velocities of a few thousand km s^{-1}, as shown by Turner et al (1993). The effective Eddington limit for the warm absorber gas is given by $L_{Edd}^{eff} = L_{Edd} \times \sigma_T/\sigma_{eff}$ where σ_T is Thomson cross section and σ_{eff} is the effective cross section including photoelectric absorption. σ_{eff} is defined such that

$$e^{-\sigma_{eff} N_H} \int_E f(E) dE = \int_E f(E) e^{-\sigma(E) N_H} dE$$

where f(E) is the transmitted flux at energy E and $\sigma(E)$, the absorption cross section at energy E,

is $\sum_{ion} \sigma_{ion}(E) f_{ion} A(atom/H)$. σ_{eff} is $\sim 1.4 \times 10^{-23}$ for a break energy of 0.37 keV. Thus $L_{Edd}^{eff} = 4.7 \times 10^{-2} L_{Edd}$. A quasar (or a Seyfert galaxy) emitting not too far below its Eddington luminosity must thus necessarily accelerate a warm absorber outwards due to its radiation pressure. This is consistent with the blueshift seen in the UV absorber. Turner et al (1993) applied this to the ionized absorber in NGC3783, although their constraint on the velocity (v< $1000 km\ s^{-1}$) depended on their assumption of a covering factor of unity which is unlikely to be applicable to 3C351 where the covering factor is $\sim 1\%$ (see above). Even for NGC3783, a covering factor of $\sim 1\%$ would allow for outflow velocities of 3000 – 4000 km s^{-1}.

The corresponding mass loss rate is $0.05 < \dot{M} < 5\ M_{\odot}\ yr^{-1}$ for covering factors between 1% and unity. This is comparable to the accretion rate needed to power the central continuum source, $\dot{M}_{accretion}$ = 2 kinetic luminosity of $(0.06 - -6) \times 10^{42} erg\ s^{-1}$, which is only 10^{-5}–10^{-3} of the radiative luminosity of the quasar.

Variations in the continuum will change the ionization state of the absorbing gas resulting in corresponding changes in the column densities of individual lines. However, the absorption lines lie on the flat portion of the curve-of-growth; so a large change in column density would result in a small change in equivalent width of the lines. Thus the model predicts no significant correlation between variations in the continuum and the EW of the UV absorption lines. But the change in X-ray opacity would change the effective value of U and would change its signature at the oxygen absorption edge in the X-ray spectrum.

5 Discussion

Strong associated metal line absorption has been observed before in other AGN with soft X-ray absorption. However, in no case was the UV absorber identified with the X-ray absorber as the physical parameters of the two were found to be very different. Our results for 3C351 show that there are five reasons for these apparently discrepant conditions:

1. The MgII ion is not produced in enough abundance until column densities are high (Kwan and Krolik 1981). So the absence of MgII absorption in a high ionization absorption system was interpreted as due to a low ($N_H < 10^{20.5}$) column density. However, the column densities inferred from the X-ray data were some two orders of magnitude higher ($N_H \sim 10^{22}$–10^{23}). Our analysis shows that the reason for the lack of MgII absorption may instead be that the material is highly ionized. In this case large column densities are allowed despite the the absence of MgII absorption.

2. A second consequence of the assumed low column densities for the UV absorbers would be that the absorbing gas is fully ionized. In our analysis the column densities are large enough to allow partial ionization.

3. The key high ionization line OVI λ1034 is not easily observed in AGN with IUE. It can only be seen for $z \gtrsim 0.2$ and few AGN at such redshift are bright enough to be studied with IUE. CIV was thus the most commonly observed high ionization absorption line. For optically thin, AGN-photoionized gas, CIV is the dominant carbon ionization state when $U \sim 5 \times 10^{-3}$ (Donahue & Shull, 1991). Since strong CIV absorption was observed, such values were assumed to be appropriate for the UV absorber. This is much lower than

that required for a warm absorber. However the combination of CIV and OVI absorption in 3C351 demonstrates that this assumption does not apply. In the present model the ionization parameter of the absorber is high (U $\sim$ 6), and CVI rather than CIV is the dominant state of ionization.

4. Early X-ray observations constrained only the total absorbing column density along the line of sight due to either a lack of sensitivity below the 0.6 keV oxygen edge, or of resolution to detect the edge. Absorption as seen in the X-rays was assumed to be due to neutral, 'cold' gas because 'hot' gas would be transparent to X-rays. There was no observational constraint on the actual ionization structure of the absorber. The higher spectral resolution of ROSAT constrains the ionization state of the absorber providing clear evidence for partially ionized gas.

5. The physical conditions of the absorbing gas are poorly determined from absorption line studies in the UV alone (Lanzetta et al 1991) because only a few lines are measured (NVλ1240, CIVλ1549 and possibly MgIIλ2798 or OVIλ1034) yielding column density estimates of a few ions but no information on the ionization state. Since the X-ray absorption cross-section is relatively insensitive to ionization and depletion (Morrison and McCammon 1983), X-ray measurements give a total column density. Thus the combination of UV and X-ray provides information on the ionization state of the gas and hence the physical conditions.

The case of the Seyfert galaxy NGC 3516 (z=0.009) is instructive. Kolman et al (1993) present simultaneous X-ray and UV observations of NGC 3516 with absorption features seen in the UV spectrum and the signature of a warm absorber in the X-ray spectrum. The authors rule out a common origin of the UV and X-ray absorption.

The X-ray observations were made with *Ginga* which has its response at higher energies (1–20 keV) than ROSAT (0.1–2 keV). The warm absorber in NGC 3516 has an absorption edge in the range 7.4–8.3 keV, which includes ionization stages from Fe^{+12} to Fe^{+21}. A simple warm absorber model was constructed by introducing an additional absorption edge in to the model; a physical warm absorber was not constructed and thus U could not be constrained. The UV spectrum from IUE contains absorption lines of CIV, NV and SiIV and the low ionization line MgII. U was deduced by assuming that the fractional abundance of CIV is a maximum yielding a low value of U (log U= -2.18 - -0.83 for $\log N_H = 20 - 22$). In the warm absorber, iron is at least 12 times ionized, which is consistent with C^{+5} and higher stages of ionization. Therefore, such matter is probably too highly ionized to produce the observed UV absorption lines, especially MgII. However, the evidence for MgII absorption in NGC3516 is rather weak (Kolman et al 1993). If this line is not confirmed (e.g. in an HST spectrum), then highly ionized matter similar to that in 3C351 is a possibility. It may then be possible to reconcile the ionization states of the UV and X-ray absorbers in NGC3516.

The identification of the UV and X-ray absorbers in 3C351 with the same absorbing gas opens up new possibilities for studying the physical conditions not only of warm absorbers but also of other high column density systems such as 'cold' absorbers and BALQSOs through combined X-ray and UV analysis. BALQSOs typically have $N_H \sim 10^{21-22} cm^{-2}$, are highly ionized and have a complex velocity structure. Initial results from ROSAT (Kopko et al 1993) imply that they are relatively faint in soft X-rays, suggestive of strong absorption, and another UV/X-ray

absorber connection. Once again the combination of UV and X-ray data would result in strong constraints on the physical conditions of the absorber.

6 Conclusions

In this paper we have shown that the X-ray and UV absorbers in 3C351 are highly likely to be one and the same. The physical conditions of the absorber are determined through the combination of constraints derived from both the X-ray and UV analysis. The absorber is found to be highly ionized (U= 6–12), outflowing with a velocity $\sim$ 2000–4000$km\ s^{-1}$, having high column density (N_H = 1–2 $\times\ 10^{22} cm^{-2}$), low density ($n \lesssim 10^7 cm^{-3}$); probably a low covering factor ($\sim$ 1%) and situated outside the BELR. These properties describe a component of the active nucleus not previously recognized.

This is the first confirmed X-ray/UV absorber. We have shown that the previous attempts to identify an UV absorber with a X-ray absorber were unsuccessful because of the lack of high quality data which forced assumptions to be made in photoionization modeling. These led to incompatible conditions being derived for the UV and X-ray absorbers. The identification of the UV and X-ray absorbers in 3C351 with the same absorbing gas opens up new possibilities for studying the physical conditions in other UV and X-ray absorbers. We have demonstrated the great advantage in determining the properties of the absorber that is afforded by the combination of UV and X-ray data .

We have also investigated the effect of the 3C351 SED on emission line strengths. We demonstrate that it is important to use the observed SED rather than a standard one, to derive the physical parameters in the BELR self-consistently. The 3C351 SED differs significantly from the standard continuum in that it is X-ray quiet, radio loud and has an upturn in the IR. The strongest effect of the low X-ray flux is on the strength of OVI λ1034. The strengths of the high ionization lines of CIV λ1549 and OVI λ1034 with respect to Lyα are systematically lower (up to a factor of 10) with the 3C351 SED as compared to those produced by the standard continuum for U $<$ $U_{critical}$. This is mainly due to the weak X-ray flux. Free-free heating was found to be dominant for large values of the ionization parameter (U $>$ 0.1) and higher densities ($n \sim 10^{11} cm^{-3}$). We find that for a 3C351- like SED, CIII] λ1909 ceases to be a density indicator.

3C351 was observed by us with ROSAT because it was known to be X-ray quiet, as a part of our program to observe quasars with extreme continuum properties. Our expectation was that they would produce new insights into the underlying physical processes. This strategy indeed seems to be fruitful.

Acknowledgements

We thank the Quasar Absorption Line Key Project team for making the Hubble Space Telescope observations available. We acknowledge the Data Management Facility/ Data Archiving and Distributing System (DMF/DADS) at STScI for making the archived IUE Quasar Atlas available. We thank T. Kallman and H. Netzer for useful discussion, B. Jannuzi for the help with HST spectra and G. Ferland for providing us with the photoionization code CLOUDY. It is our pleasure to thank our colleagues A. Dobrzycki and J. McDowell for their help.

This work was supported by NASA grants NAGW-2201 (LTSARP), NAS5-30934 (RSDC) and NAG5-1883 (ROSAT).

Table 1. ROSAT 2-power Law Spectral Fits

Break Energy keV (Fixed)	α_1 (Fixed)	α_2 (Fixed)	χ^{2a}	N_H^b $10^{22}cm^{-2}$	U^b
0.07	4.7	1	24.73	$1.8^{+0.4}_{-0.3}$	12^{+4}_{-2}
0.37	2.45	1	29.82	1.4 ± 0.3	$6.7^{+2.3}_{-1.2}$
0.7	2.16	1	31.66	$1.0^{+0.4}_{-0.2}$	$1.1^{+0.7}_{-0.3}$

a. for 21 degrees of freedom.

b. errors are 1σ for two degrees of freedom.

Table 2. UV Emission and z=0.3646 Absorption Line Parameters

Line Identification	λ_{obs} ($\AA$)	EW^b_{obs} ($\AA$)	FWHM ($\AA$)
a)Absorption[a]			
CIV 1549	2113	3.09	8.58
NV 1238	1690.74	1.60[c]	3.22
NV 1242	1695.67	1.63[c]	3.44
Lyα	1658.92	3.54[c]	4.46
OVI 1031	1408.34	2.73	3.09
OVI 1037	1416.39	1.99	2.85
b)Emission			
CIII] 1909	2614.6	18.5	25.0
CIV 1549	2121.98	68.2	32.2
Lyα/NV	1664.11	60.5	31.6
OVI 1031,1037	1426.14	6.8	23.0

a. from Bahcall et al (1993) except for the uncertainties in EWs

b. uncertainties are $\sim$ 10% except where noted

c. uncertainties are estimated to be $\sim$ 40%

Table 3. Comparison of Column Densities in Model and Data

Ion	log N_{ion} (Measured)[a]	log N_{ion} (Model)		
		E_{Break} = 0.07 keV	E_{Break} = 0.37 keV	E_{Break} = 0.7 keV
OVI	17.5 – 18.0	17.5	17.5	18.3
NV	15.3 – 15.8	15.7	15.8	16.8
CIV	15.9 – 16.1	15.9	15.9	17.3
HI (Lyα)	15.4 – 17.4	15.3	15.6	16.5

a. assuming b= 110 km s^{-1}

Figure Captions

Figure 1: The best fit X-ray spectrum. (E_{break}= 0.37 keV, $N_H = 1.4 \times 10^{22} cm^{-2}$, U=6.7)

Figure 2: The HST UV spectrum. a) OVI b) Ly_α/NV c) CIV d) CIII]. The dotted line is the continuum defined in Bahcall et al (1993). The prominent emission lines are labeled. The absorption lines in z=0.3646 system are marked above the spectrum and the galactic absorption lines are marked below the spectrum.

Figure 3: The 3C351 SED. Solid line: the best fit SED, dashed line: 'standard' continuum and dotted line: average X-ray continuum for radio loud quasars. The bow shows limits to the X-ray slope (see text).

Figure 4: Photoionization models. Line strengths as a function of (a) U for $\log n_H = 11$ (b) for $\log n_H = 9$ (c) as a function of n_H for $\log U = -1.0$ using the complete SED. Observed values are shown by horizontal lines.

Figure 5: Comparison with observations; line strengths as a function of U for $\log n_H = 11$. SED here is without either the IR upturn or radio. Observed values are shown by horizontal lines.

Figure 6: (a) The curve of growth for 'b' values ranging from 80 to 130 in steps of 10. Nλ has the dimension cm^{-1}. (b) a part of (a) expanded. Observed values of W_λ/λ for OVI λ1031, CIVλ1549 and NVλ1242 are marked by the horizontal lines.

Mon. Not. R. Astron. Soc. 000, 000–000 (0000) Printed 5 December 1997

Testing the ionized disc reprocessing model for the soft X-ray emission of quasars

Fabrizio Fiore[1,2,3], Giorgio Matt[4,5] and Fabrizio Nicastro[1,3]

[1] *Osservatorio Astronomico di Roma, Via dell'Osservatorio, I-00044 Monteporzio-Catone, Italy.*
[2] *SAX Science Data Center, via Corcolle 19, I-00131 Roma, Italy*
[3] *Harvard Smithsonian Center for Astrophysics*
[4] *Istituto di Astrofisica Spaziale, C.N.R., Via Enrico Fermi 21, I-00044 Frascati, Italy*
[5] *Dipartimento di Fisica, Università degli studi "Roma Tre", Via della Vasca Navale 84, I-00146 Roma, Italy.*

5 December 1997

ABSTRACT

One of the current explanations for the soft X–ray emission of AGN is reprocessing of the hard X–rays by partially ionized, optically thick matter. This idea is very appealing because it would explain the shape of the AGN soft X-ray spectrum in terms of atomic physics. While at present the reflection model correctly describes the soft X-ray spectra of a few low luminosity Seyfert galaxies, it is not clear whether it can be applied to higher luminosity quasars. To investigate this issue quantitatively, we have fitted the high signal–to–noise PSPC spectra of 11 AGN of different luminosities with a model consisting of a direct hard X-ray component, reflection from the ionized surface of an accretion disc and the direct thermal emission of the disc. We find that the AGN with an acceptable fit are a minority, and have all a low optical (and bolometric) luminosity, flat α_{PSPC} and the flattest α_{OX} of the sample, while those with the worst fit have all high optical (and bolometric) luminosity, steep α_{PSPC} and the steepest α_{OX} of the sample. We conclude that either the reprocessing model is not correct and the form of the soft X-ray spectrum of AGN cannot be simply explained in terms of characteristic atomic features (i.e. highly ionized oxygen K–edges), or the origin of the soft X-ray emission of AGN is not "universal".

1 INTRODUCTION

About 50 percent of luminous, low redshift quasars (Wilkes & Elvis 1987) and Seyfert galaxies (Turner & Pounds 1989) observed by *Einstein* and EXOSAT showed some sort of "soft excess" above the extrapolation of their 2-10 keV power law ("hard component" hereinafter). This low energy X-ray turn-up is often interpreted as the high energy tail of the UV bump, although no direct evidence of such a connection yet exists. Other types of soft excess are known including emission associated with an extended component in low luminosity AGN (e.g. NGC4151, Elvis et al. 1990, Perola et al. 1986; NGC1068, Wilson et al. 1992; NGC4388, Matt et al. 1994); emission line features in the 0.7-1 keV band (Turner et al. 1991); the recovery of the spectrum below the oxygen edge in "warm absorber" sources (e.g. Nandra & Pounds 1992; Fiore et al. 1993; Fabian et al. 1994).

ROSAT (Trümper 1983) PSPC (Pfeffermann et al. 1987) observations greatly improved our knowledge of the 0.2-2 keV spectrum of low redshift quasars and Seyfert galaxies (simply quasars hereinafter). They were able to:

(i) distinguish between different types of soft excess, for example between warm absorber sources and quasars with a genuine soft component.

(ii) Show that the number of quasars having a strong soft component is greater than thought in the past.

(iii) Show that in many cases the soft component dominates the PSPC band. This means that the "break point" between hard and soft components must be located in the

Table 1. Quasar sample

Name	Redshift	log A(z)[a]	$\log(\nu L_\nu(3000\AA))$	α_{OX}	α_{OS}
Mark 1152	0.052	54.777	43.70	1.08	1.00
Mark 590	0.027	54.203	44.00	1.25	1.14
Mark 1044	0.016	53.746	43.45	1.40	1.15
Mark 110	0.036	54.454	43.55	1.00	0.84
Mark 205	0.070	55.039	44.25	1.23	1.18
Mark 290	0.030	54.295	43.75	1.38	1.49
NAB 0205+024	0.155	55.746	45.10	1.55	1.24
PG 1116+215	0.177	55.865	45.60	1.61	1.56
PG 1211+143	0.085	55.211	44.95	1.57	1.39
TON 1542	0.064	54.960	44.40	1.42	1.29
Mark 478	0.070	55.039	44.50	1.48	1.10

[a] $A(z) = \nu L_\nu / \nu f_\nu = 4\pi[2c/H_0(1+z-\sqrt{1+z})]^2$, assuming H_0=70 km s^{-1} and $q_0 = 0.5$,

(1994); and two (PG 1116+215 and Mark478) by Laor et al. (1995). We used the spectra obtained for those papers. Data for the other 4 quasars were taken from the ROSAT public archive and reduced following Fiore et al. (1994). Table 2 gives for the 11 quasars the observation date, duration, and count rate.

When more than one observation was available for each quasar (Mark 110, Mark 205, Mark 290, and TON1542) we verified that the spectral shape in each observation were consistent with each other. We did not find any significant spectral variability in front of up to factor of 2 changes in intensity. We then added together the spectra of each source with multiple observations to increase the signal to noise ratio. Each PSPC spectrum used has a signal to noise $\gtrsim 30$. PI channels 1 and 2 (of the standard division to 34 PI channels, E<0.11 keV) were ignored in the following spectral analysis. PSPC spectra were rebinned in order to have at least 20 counts per bin to allow the use of χ^2 statistics.

Table 3 gives for each of the 11 quasars the best fit parameters, obtained fitting to the data a single power law with low energy absorption model, along with the Galactic N_H, the 0.3 keV and the 2 keV luminosity ($\log\nu L_\nu$).

4 THE MODEL

The model is basically that described in Matt, Fabian & Ross (1993), which in turn is an extension and generalization of the reprocessing model of Ross & Fabian (1993). Here we summarize the main features of the model, referring the reader to the above mentioned papers for more details.

A radiation–pressure dominated Shakura–Sunyaev (1973) accretion disc is supposed to be illuminated by a central, point–like source of X-ray photons, located at 20 $r_g = (GM/c^2)^{1/2}$. The luminosity of this central source, L_h, between 1 Rydberg and 100 keV (where the spectrum is assumed to have a cutoff) is equal to $\eta_h \dot{m} L_{Edd}$, where $\dot{m}$ is the accretion rate in the disc, in units of the critical one. The spectral shape of the hard component is assumed to be a power law with energy spectral index of 1, consistent with the finding of Nandra & Pounds (1994), Comastri et al (1992) and Williams et al. (1992) for the 2-10 keV spectrum of both low and high luminosity quasars. The disc conversion efficiency is set to 0.06, as for a Schwarzschild black hole, while the viscosity parameter α (Shakura & Sunyaev 1973) is assumed equal to 0.1.

The disc emits primarily by converting viscous dissipation into radiation energy. However, its uppermost layer can be significantly affected by the external illumination, especially in the inner regions, where the ionization parameter

Table 2. PSPC Observations

Name	exposure	count rate[a]	Date
Mark 1152	3223	1.81	1992 July 11
Mark 590	3484	5.00	1993 Jan 14
Mark 1044	2836	2.07	1992 Aug 9
Mark 110	10285	5.95	1991 Nov 1-1992 Apr 22
Mark 205	13891	1.00	1991 Nov 10-1992 Apr 15
Mark 290	6997	0.72	1992 Aug 20-1992 Dec 9
NAB 0205+024	14070	0.69	1992 Jan 18-23
PG 1116+215	24942	0.97	1991 May 29-30
PG 1211+143	3877	1.01	1991 Dec 17-24
TON 1542	12000	1.28	1991 Dec 13-1992 Jul 6
Mark 478	2393	2.06	1992 Jan 17

[a] in counts seconds^{-1}

Table 3. Power law fit

Name	Galactic N_H^a	N_H^a	α_E	F(1)[b]	χ^2/dof	$\log(\nu L_\nu(0.3keV)^c)$	$\log(\nu L_\nu(2keV)^c)$
Mark 1152	1.67[d]	1.73 ± 0.22	1.32 ± 0.10	4.06 ± 0.10	28.62/27	43.73	43.48
Mark 590	3.07[d]	2.70 ± 0.16	1.41 ± 0.06	13.8 ± 0.30	25.88/29	43.74	43.41
Mark 1044	3.0[e]	3.93 ± 0.33	1.99 ± 0.12	5.38 ± 0.19	30.37/29	43.18	42.38
Mark 110	1.5[e]	1.36 ± 0.06	1.38 ± 0.03	10.9 ± 0.10	58.57/29	43.87	43.57
Mark 205	2.74[d]	3.30 ± 0.19	1.36 ± 0.06	3.32 ± 0.06	29.48/28	43.92	43.63
Mark 290	2.32[d]	2.11 ± 0.30	1.17 ± 0.12	2.01 ± 0.07	41.33/24	42.85	42.73
NAB 0205+024	2.99[d]	3.41 ± 0.25	2.26 ± 0.10	1.16 ± 0.04	34.70/27	44.67	43.65
PG 1116+215	1.44[d]	1.43 ± 0.10	1.73 ± 0.05	1.31 ± 0.03	38.13/29	44.53	43.94
PG 1211+143	2.83[d]	3.25 ± 0.36	2.00 ± 0.14	2.05 ± 0.09	39.64/27	44.23	43.42
TON 1542	2.58[d]	2.02 ± 0.14	1.71 ± 0.06	2.24 ± 0.05	30.38/28	43.87	43.29
Mark 478	0.97[f]	1.49 ± 0.22	2.38 ± 0.13	1.92 ± 0.15	20.53/24	44.32	43.31

[a] in cm^{-2}; [b] in 10^{-3} photons cm^{-2} s^{-1} keV^{-1}, at 1 keV; [c] Log of monocromatic luminosity in erg s^{-1}; [d] Elvis, Lockman & Wilkes (1989); [e] Stark et al. (1992); [f] Lockman, private communication.

ξ, defined as $4\pi F_h/n_H$ (where n_H is the hydrogen number density) is the greatest for geometrical reasons. In this case the matter can be significantly ionized, and the disc can become highly reflective; moreover, the surface temperature is higher than without illumination, so giving extra thermal radiation. Emission lines, mainly due to recombination from He–like and H–like carbon and oxygen atoms, can also appear. The calculations of the ionization structure and the angle–averaged spectra have been performed using the Ross & Fabian (1993) code whenever possible, with the angular distribution of the emissivity calculated by integrating numerically the radiative transfer equations (see Matt et al. 1993 for further details). The code makes use of the diffusion approximation and therefore it fails for ξ lower than a few tens erg cm s^{-1}. This occurs in the outermost disc regions for every $\dot{m}$, and everywhere for values of $\dot{m}$ lower than about 0.1–0.2 (remember that $\xi \propto \dot{m}^3$), depending on the black hole mass. In the regions where the photoionization code breaks down, we have assumed neutral matter and simple black–body thermal emission, with the temperature simply calculated by means of the Shakura–Sunyaev (1973) formulae. In such cases the reflected spectra were calculated following Lightman & White (1988).

After calculating the local emissivity as above described, we have integrated the contributions from each point over the whole disc, taking into account the relativistic effects in the Schwarzschild metric by means of the fully relativistic treatment described in Fabian et al. (1989), Chen & Eardley (1991) and Matt et al. (1993). As shown in Matt et al. (1993), these effects mainly consist in broadening the features and in flattening the continuum; both effects increase with the inclination angle. It must be stressed that,

to build–up the model to be fitted, the overall disc spectrum has been calculated only when at least one zone out of the 10 in which the disc has been divided for calculation purposes is significantly ionized, i.e. the Ross & Fabian (1993) code can be used. This in practice restricts the possible values of $\dot{m}$ to a relatively narrow range (from ~0.2 to 0.6, the maximum adopted value as for greater values the thin disc approximation breaks down).

To summarize, the parameters of the model are: a) $\dot{m}$, the mass accretion rate; b) the mass of the black hole, M_8 (in the following in units of 10^8 solar masses); c) the disc inclination angle, i; d) $\eta_{\rm h}$, i.e the fraction of hard and disc powers. To allow for a different relation between the fraction of $L_{\rm h}$ illuminating the disc and that toward the observer we introduce an additional parameter $a = L_{\rm h\ ill}/L_{\rm h\ dir}$. We note that the model is not fully self-consistent for values of a much different from 1. In fact, the ionization status of the disc (hence the spectra produced) is not exactly the same if the emission pattern of the central source is different (as changes the radial dependence of the flux incident on the disc).

In this situation the power law normalization is not a free parameter but it is given by:

$$Norm = \frac{2\eta_{\rm h}}{(1+a)}\frac{\dot{m}M_8}{Int}\frac{8\times10^{54}}{A(z)} = \frac{\eta_{\rm h}}{(1+a)}\dot{m}M_8\frac{1.8\times10^{54}}{A(z)} \quad (1)$$

where $A(z)$ is the distance modulus, and $Int = \int_{1Ryd}^{100keV} E^{-\alpha_E}dE = 8.903$, for $\alpha_E = 1$.

This equation might be used to roughly estimate the value of $\frac{\eta_{\rm h}}{(1+a)}$ appropriate to the quasars in our sample. In fact, $\dot{m}M_8$ can be related to the observed 3000 Å luminosity (reported in Table 1, together with the distance modulus $A(z)$) and the power law normalization is approximately given by the 1 keV flux F(1) in Table 3, after subtraction of the contribution at this energy of the reprocessed radiation. This contribution varies between 5 % and 40 % of the total flux at 1 keV for the range of parameter values explored (see next section). If in the estimate of $\dot{m}M_8$ from the 3000 Å luminosity we neglect the extra optical-UV flux produced by the irradiation of the disc by the X-ray power law, $\frac{\eta_{\rm h}}{(1+a)}$ for our sample of quasars should be in the range 0.002-0.5. However, the extra optical-UV flux produced by the irradiation can be large: following Siemiginowska et al (1995), the wavelength at which the flux generated in the disc equals the extra flux produced by irradiation is approximatively given by

$$\lambda_{crit} \approx 4065 M_8^{1/4}\dot{m}^{-1/4}f_{irr}^{-3/4}\ \mathring{A} \quad (2)$$

where f_{irr} describes the efficiency with which the disc is illuminated by the X-ray source, and it is therefore close to $\frac{\eta_{\rm h}}{(1+a)}$. For $\dot{m} = 0.3$, $M_8 = 1$ and $f_{irr} = 1$, this wavelength is 5500 Å , while for $M_8 = 0.1$ $\lambda_{crit} = 3100$ Å . For $f_{irr} = 0.1$ these wavelengths increase by a factor 5.6 and therefore the extra flux at 3000 Å should be negligible. The relationship between the 3000 Å and 1 keV luminosities and $\frac{\eta_{\rm h}}{(1+a)}$ becomes therefore complex. Roughly speaking, the lower limit found above should not change, while the upper limit might increase. We then decided to explore two regions of the parameter space which are far off one from the other (i.e. $\eta_{\rm h} = 1$ and $\eta_{\rm h} = 0.1$), to try to encompass a large number of cases.

5 RESULTS

We generated two grid of models, one for $\eta_h = 1$ and the other for $\eta_h = 0.1$. In the first case the range of $\dot{m}$ investigated is 0.2–0.4, while in the second case it is 0.4–0.6. These ranges ensure in both cases that the ionization of the innermost disc regions is enough for the diffusion approximation to be valid. The ranges of M_8 and i investigated are 0.01-10 and 0-80 degrees respectively. We then run spectral fits

Figure 1. PSPC spectra with their best fit models for the ionized disc model assuming η_h=1 and a=1 (upper panels) and the ratio between the data and the best fit models (lower panels): a) Mark 590; b) Mark 110; c) NAB0205+024.

interpolating on these grids and allowing for low energy photoelectric absorption. The results of the fits are summarized in Table 4 ($\eta_h = 1$) and Table 5 ($\eta_h = 0.1$). The fits have been performed letting the absorbing column density to be free to vary and with the parameter a either fixed to 1 or kept free. The number of free parameters is 4 and 5 in the two cases. When a fit is highly statistically unacceptable we give in Tables 4 and 5 the best fit value of the parameters and the χ^2 only. In the other cases we also give the 1σ uncertainty on the best fit parameter for 3 (Table 4) and 4 (Table 5) interesting parameters.

5.1 $\eta_h = 1$ and a fixed to 1

In this case, the fit is statistically acceptable for three out of 11 sources, namely Mark 1152, Mark 590 and Mark 205. For Mark 205 the χ^2 is similar to the one obtained fitting a single power law (Table 3), while for Mark 1152 the reduction in χ^2 is significant at the 97 % confidence level (by using the F test). For Mark 590 the χ^2 is worse than that obtained fitting a power law by 4.6. For the latter source Fig. 1a shows the PSPC spectrum with the best fit model and the ratio between the data and the best fit model. Fig. 2 shows the best fit emission model (not convolved with the PSPC response) to the spectrum of Mark 1152 (thin line).

For Mark 110 the fit is statistically unacceptable (probability of 1.9 %). The PSPC spectrum with the best fit model and their ratio is shown in Fig. 1b. The deviations between the data and the model are at most of 5 percent. Their amplitude is therefore similar or smaller than the uncertainties on the knowledge of the PSPC response matrix (Fiore et al. 1994). The largest deviations are at energies below the Carbon edge (0.28 keV). Excluding from the fit the first two points (PI channels 3 and 4, E<0.2 keV), where the systematic uncertainties are larger due to the presence of the so called "electronic ghost images" (Hasinger et al. 1992), the fit with the reprocessing model becomes acceptable (χ^2=35.6, 26 dof, probability of 10 %). The best fit parameters are very similar to those in Table 4. Note that the χ^2 for a simple power law model does not improve ignoring channels 3 and 4.

Figure 2. Best fit emission model to the spectrum of Mark 1152 (thin line) and NAB0205+024 (thick line). The dashed line represents the X-ray power law illuminating the disc. the model spectra are normalized to have the same flux at 2.4 keV to show the different behaviour at lower energies.

The reduction in χ^2 adopting the reprocessing model in comparison to the power law model is significant at the 99 % confidence level (using the spectrum in 32 channels) and at better than 99.9 % (when ignoring channels 3 and 4). We therefore consider in this case "acceptable" the fit with the reprocessing model.

For Mark 290 the fit is marginally acceptable (probability of 6.8 %). The deviation between the data and the model are of the order of 5-15 %. The largest deviations are present between 0.5 and 1 keV and suggest the presence of emission and/or absorption structure, like those expected in the case of an ionized absorber along the line of sight. Fitting the data with a power law model plus one absorption edge

gives an acceptable χ^2 of 27.23 (22 dof). The edge energy is 0.70 ± 0.1, consistent with the OVII edge, and the edge depth is $\tau = 0.65 \pm 0.35$. Since in this case there is a probably large contribution of complex absorption to the detected spectral features, the test of the reprocessing model is weak and not conclusive.

For Mark1044 the fit is marginally acceptable (probability of 6.1 %). The deviation between the data and the model are of the order of 5-15 % also in this case. The largest deviation is an excess around 0.9 keV.

In three cases (NAB0205+024, PG1116+215 and PG1116+215) the fit is completely unacceptable and the deviations between model and data are of the order of 20 % or higher. In all three cases the largest deviations are an excess of counts between 0.5 and 0.9 keV and a deficit of counts above 1.5 keV. Fig. 1c shows the PSPC spectrum of NAB0205+024 with the best fit model and their ratio The best fit emission model (not convoluted with the PSPC response) is shown in Fig. 2 (thick line). This is normalized at the the same flux of the best fit model of Mark1152 at 2.4 keV. The NAB0205+024 best fit model is significantly steeper than that of Mark1152 below 0.4 keV only, where the contribution of the direct disc emission can be significant. From Fig. 1c it is clear that the reflection model is flatter than the measured spectrum between 0.4 and 2 keV, where the spectrum, in the case $a = 1$, is dominated by the reprocessed radiation and by the direct X-ray emission, and therefore where the average slope of the spectrum is steeper than that of the direct X-ray emission by a limited amount (see the Introdution).

In the other 2 cases (TON 1542 and Mark 478 the fit is statistically unacceptable and the deviations between model and data are the order of 10-15 %. In these two cases the fit with a single power law produces a χ^2 significantly smaller than the reprocessing model.

The 4 sources with "acceptable" fit have all $\dot{m}$ close to our lower bound of 0.2, and black hole mass between 2 and 3×10^7 $M_\odot$. The inclination angle is small in Mark 590 and Mark 110, intermediate but poorly constrained in Mark 205, and high in Mark 1152.

5.2 $\eta_h = 1$ and a free

As the fits with a fixed to 1 are acceptable only for a small sub-sample, we have tried to fit to the data the model with a as a free parameter. As discussed above, strictly speaking this can be done only for values of a not too different from unity, the model otherwise losing its self-consistency. However, in the fit procedure we have not bounded this parameter (apart of course from being positive), as also values much different than one can say something about the real emission.

Among the four sources for which the model with a=1 already gives an "acceptable" fit, letting a to be free to vary produces a significant reduction in χ^2 in Mark 205 (at the 97.8 % confidence level) and a marginal reduction in χ^2 in Mark 110. In the first case a is poorly constrained while in the second case a value for a slighly less than 1 (0.5-1) appears to be favoured by the fit.

For Mark 1044 and Mark 290 letting a to vary does not improve the fit and in fact the best fit of a is in these cases close to 1.

For the three sources with completely unacceptable fits with $a = 1$, there is a great improvement in χ^2 letting a to assume very large values (which means, by assuming a pure reflection model), but the fits remain unacceptable.

For TON 1542 and Mark 478 there is a significant improvement in χ^2 (at better than 99.999 % and 99.8 % con-

fidence level respectively) but the best fit value of a is in both cases high, in a region of the parameter space where the model is no longer self–consistent. a smaller than ~ 5 are still excluded in both cases.

5.3 $\eta_h = 0.1$

We have also tested the case $\eta_h = 0.1$ where the total luminosity of the X-ray source is only one tenth of the disc luminosity. These model of course have stronger intrinsic disc emission and smaller reflection component in comparison with the models with $\eta_h = 1$. They are generally steeper than the $\eta_h = 1$ models going toward the low energies.

With this model the fits were in all cases worse or at most similar to the fits with $\eta_h = 1$. The best fit values for the N_H were systematically higher than the Galactic values and than the case with $\eta_h = 1$, indicating that these models are generally too steep going toward low energies. This result is not surprising, since pure thin accretion disc spectra (either in a Schwartzschild or Kerr metrics) are known not to fit the soft X-ray data of quasars (e.g. Fiore et al 1995) because they are generally too steep in soft X-rays. This result further excludes a strong pure disc emission in the soft X-ray spectrum of quasars.

6 DISCUSSION

The results presented in the previous section show that reprocessing from an ionized disc is, in general, not a good model for the soft X–ray spectrum of quasars, being "acceptable" only for a few sources.

The situation is not significantly improved by allowing a reasonable anisotropy in the X-ray emission (i.e. $a \neq 1$). In one case only, the fit becomes acceptable letting a to assume values of 10 or higher. Smaller values results in unacceptable fits. It is worth stressing that a=10 exceeds the maximum values expected from anisotropic inverse Compton (Ghisellini et al. 1991).

Using the best fit values of M_8 and $\dot{m}$ in Table 4 (case $\eta_h = 1$) it is possible to roughly estimate the model disc luminosity at 3000 Å (using a disc emission model in the Schwarzschild metric). If the extra optical-UV flux produced by the irradiation of the disc by the X-ray power law is neglected, 3000 Å luminosities similar or smaller up to a factor of 10 of the observed ones (reported in Table 1), are obtained. However, for small black hole masses the extra 3000 Å luminosity produced by irradiation can be similar or even higher than the intrinsic disc luminosity (see eq. 2), thus reducing, and in some cases eliminating altogether, the inconsistency between predicted and observed luminosities. The inconsistency remains for the quasars with a large black hole mass best fit value.

We also fitted the data assuming a disc intrinsic luminosity ten times higher than the X-ray source luminosity, i.e. $\eta_h = 0.1$ (see Table 5). The results were not satisfactory: all quasars with an unacceptable fit in the case $\eta_h = 1$ have an unacceptable fit with $\eta_h = 0.1$ too, and only in one case, out of the four quasars with an acceptable fit in the case $\eta_h = 1$, the fit remains acceptable with $\eta_h = 0.1$. Intermediate situations with $0.1 < \eta_h < 1$ have not been tested and could in principle produce an acceptable fit in some cases. However, this would require an unpalatable fine tuning of this parameter.

Interestingly, the four quasars with an "acceptable" fit have all a small best fit black hole mass ($0.1 < M_8 < 0.3$), low optical luminosity, flat α_{PSPC} and the flattest α_{OX} of the sample, while the three quasars with the worst fits have all high optical luminosity, steep α_{PSPC} and the steepest α_{OX} of the sample (see Tables 1 and 3). In the following we discuss briefly the implications of these findings.

Table 4. Fits with the reflection model ($\eta_h = 1$)

Name	N_H^a	M_8	$\dot{m}$	i	a	χ^2/dof
Mark 1152	$2.7^{+0.5}_{-0.3}$	$0.19^{+0.05}_{-0.07}$	$0.23^{+0.07}_{-0.03}$	$80-14$	1 FIXED	23.40/26
	$2.5^{+1.0}_{-0.6}$	$0.12^{+0.26}_{-0.06}$	$0.24^{+0.10}_{-0.04}$	$80-35$	$0.23^{+3.9}_{-0.22}$	23.09/25
Mark 590	$4.2^{+0.3}_{-0.1}$	$0.20^{+0.01}_{-0.02}$	$0.20+0.01$	<33	1 FIXED	36.78/28
	$4.4^{+0.6}_{-0.3}$	$0.26^{+0.04}_{-0.07}$	$0.21+0.01$	<31	$2.2^{+0.6}_{-1.3}$	33.00/27
Mark 1044	$3.4^{+0.3}_{-0.2}$	0.013 ± 0.002	0.31 ± 0.02	$80-4$	1 FIXED	36.71/25
	$3.4^{+0.6}_{-0.3}$	$0.013^{+0.007}_{-0.003}$	$0.32^{+0.03}_{-0.07}$	$80-10$	$1.1^{+1.9}_{-0.9}$	36.69/24
Mark 110	2.5 ± 0.1	$0.27^{+0.01}_{-0.02}$	$0.20+0.01$	<6	1 FIXED	45.70/28
	2.4 ± 0.2	$0.23^{+0.04}_{-0.01}$	$0.20+0.01$	<9	$0.66^{+0.35}_{-0.13}$	41.84/27
Mark 205	$4.7^{+0.4}_{-0.6}$	0.27 ± 0.06	$0.22+0.02$	28 ± 25	1 FIXED	29.17/28
	5.3 ± 1.0	0.31 ± 0.08	$0.28^{+0.06}_{-0.02}$	<41	>1.1	23.94/27
Mark 290	$3.0^{+0.6}_{-0.2}$	$0.026^{+0.004}_{-0.003}$	$0.29^{+0.02}_{-0.04}$	$80-4$	1 FIXED	33.89/23
	3.2 ± 0.1	$0.029^{+0.014}_{-0.008}$	0.30 ± 0.02	<64	$1.3^{+1.3}_{-0.5}$	33.03/22
NAB 0205+024	2.7	0.22	0.4	60	1 FIXED	304/26
	$2.3^{+0.1}_{-0.3}$	2.47 ± 0.25	0.21 ± 0.01	<6	>30	46.27/25
PG 1116+215	1.7	0.37	0.37	60	1 FIXED	184.3/28
	1.8	1.35	0.32	60	>100	77.5/27
PG 1211+143	3.9	0.10	0.4	60	1 FIXED	92.26/26
	3.5 ± 0.4	0.66 ± 0.18	0.24 ± 0.03	37^{+28}_{-37}	>12	44.72/25
TON 1542	$2.8^{+0.2}_{-0.1}$	$0.18^{+0.01}_{-0.03}$	$0.20+0.02$	30^{+20}_{-10}	1 FIXED	43.84/27
	$3.3^{+0.4}_{-0.3}$	$0.30^{+0.01}_{-0.07}$	0.23 ± 0.03	<44	$9.1^{+70}_{-6.1}$	17.79/26
Mark 478	1.3 ± 0.2	$0.068^{+0.019}_{-0.005}$	$0.4-0.06$	60^{+6}_{-13}	1 FIXED	38.62/23
	1.8 ± 0.5	0.36 ± 0.10	$0.26^{+0.05}_{-0.03}$	60^{+10}_{-40}	>16	28.64/22

The model adopted in this paper is based on the work of Matt et al. (1993) and is valid only when the innermost disc regions are significantly ionized. On the other hand, reprocessing could in principle occur in a disc which is neutral or mildly ionized even in the vicinity of the black hole (this would actually be the case for $\dot{m} \lesssim 0.1$). The reason why we find so many unacceptable fits could then be that we are investigating a too small interval of $\dot{m}$. However, we find that the quasars with an acceptable fit with the reprocessing model have all a low optical luminosity, while those with the worst fits have all high optical luminosity. It seems unlikely the latter sources would all have accretion rates significantly smaller than the previous ones. If the disc is only mildly ionized the reflection would occur basically below the carbon edges (0.285-0.498 keV) while the typical energy break in the sources analysed here is often significantly greater (Fiore et al. 1994, Laor et al. 1994). Furthermore, Nandra et al. (1996) recently found in PG1116+215 evidence for a iron Kα line from highly ionized ions, which might indicate a highly ionized accretion disc. Therefore, we conclude that the small range of $\dot{m}$ investigated is not the main cause of the negative result.

The spectral shape of the hard X-ray component was assumed to be a power law with $\alpha_E = 1$. This assumption is certainly justified in low luminosity Seyfert galaxies but may be wrong in higher luminosity sources. Among the five high optical luminosity quasars in our sample only PG1211+143 (Yaqoob et al. 1994), and PG1116+215 (Nan-

Table 5. Fits with the reflection model ($\eta_h = 0.1$)

Name	N_H	M_8	$\dot{m}$	i	a	χ^2/dof
Mark 1152	$4.4^{+0.9}_{-0.3}$	$1.2^{+0.1}_{-0.2}$	0.40 + 0.20	< 18	1 FIXED	25.18/26
	$4.5^{+0.8}_{-0.5}$	$1.2^{+0.6}_{-0.5}$	0.44 + 0.08	< 30	$1.3^{+2.1}_{-1.3}$	24.83/25
Mark 590	5.6	1.1	0.4	11.0	1 FIXED	92.55/28
	$5.5^{+0.6}_{-0.4}$	$1.8^{+0.3}_{-0.2}$	$0.45^{+0.03}_{-0.05}$	< 18	$3.9^{+1.5}_{-1.2}$	41.94/27
Mark 1044	8.1	0.14	0.4	80	1 FIXED	138.9/25
	$9.4^{+0.6}_{-0.1}$	$0.64^{+0.08}_{-0.09}$	0.4 + 0.04	< 10	$19^{+23}_{-6.9}$	50.24/24
Mark 110	3.5	1.5	0.40	14.5	1 FIXED	80.68/28
	3.6 ± 0.2	1.9 ± 0.2	0.44 ± 0.03	< 16	$2.1^{+0.6}_{-0.6}$	60.23/27
Mark 205	$5.4^{+0.7}_{-0.4}$	$1.7^{+0.1}_{-0.3}$	0.40 + 0.08	32^{+13}_{-12}	1 FIXED	51.94/28
	$6.2^{+0.9}_{-0.8}$	$2.1^{+0.4}_{-0.3}$	$0.56^{+0.04}_{-0.09}$	< 44	$4.0^{+4.8}_{-2.0}$	33.25/27
Mark 290	$9.3^{+0.4}_{-0.1}$	$0.22^{+0.01}_{-0.01}$	0.40 + 0.03	< 6	1 FIXED	56.35/23
	$9.3^{+0.8}_{-0.1}$	$0.22^{+0.08}_{-0.08}$	0.40 + 0.02	< 6	$1.0^{+3.2}_{-1.0}$	56.11/22
NAB 0205+024	3.6	1.8	0.6	59	1 FIXED	352/26
	2.5	7.9	0.6	5	34	147.4/25
PG 1116+205	2.4	2.75	0.6	60	1 FIXED	321.8/28
	2.4	1.76	0.6	60	0.1	241/27
PG 1211+143	5.9	0.72	0.59	30	1 FIXED	86.63/26
	$5.9^{+0.6}_{-1.8}$	$2.1^{+1.0}_{-0.6}$	0.60 − 0.10	29 ± 26	>8	43.06/25
TON 1542	4.3	1.0	0.40	30	1 FIXED	98.27/27
	$4.7^{+0.3}_{-0.2}$	1.8 ± 0.4	$0.54^{+0.03}_{-0.14}$	< 45	$11^{+3.5}_{-1.8}$	24.45/26
Mark 478	$2.9^{+0.3}_{-0.4}$	$0.62^{+0.48}_{-0.05}$	0.57 ± 0.03	< 68	1 FIXED	54.80/23
	$3.0^{+0.4}_{-0.2}$	$2.7^{+2.6}_{-1.3}$	$0.56^{+0.04}_{-0.10}$	36^{+42}_{-26}	> 9	29.73/22

dra et al. 1996) have a published high quality spectrum (measured by ASCA) above 2 keV. Lower quality spectra from the EXOSAT ME and the *Einstein* MPC have been published by Comastri et al. (1992) and Masnou et al. (1992) for TON1542 and NAB0205+024 respectively. In all cases the X-ray energy index measured between 2 and 10 keV is consistent with our assumption.

The model details depends on several other parameters. Some of them have been fixed in a more or less arbitrary way. For instance, the parameter α, which should describe the viscosity effects in the disc, is in some sense arbitrary in its very nature. It is difficult to predict what could be a reasonable value for α; our choice (0.1) is a common one, but not for this reason less arbitrary. We have also assumed a Schwarzschild black hole. This has two consequences: the gravitational energy conversion factor has been fixed to 0.06 (while for a rotating black hole it can be as high as 0.4); the relativistic corrections on the spectral shapes are less extreme than for a rotating black hole, mainly due to the fact that the last stable orbit for a Kerr black hole can approach the gravitational radius, while it is $6r_g$ for a Schwarzschild black hole (e.g. Bardeen et al. 1972; Kojima 1991). Having used those values for α and the energy conversion factor should not represent, however, a serious problem in fitting the data. The major consequence should be to miscalculate some of the other parameters rather than to make the fits

unacceptable. The use of the Schwarzschild instead of the Kerr metric, on the other hand, could have a not negligible effect to the spectral shape. Unfortunately, the numerical code for calculations in Kerr metric presently available to us (Laor 1991) makes use of an angular dependence of the disc emission which is very much different from that appropriate in the physical case under consideration (Matt et al. 1993); such a code is therefore of little use for our purposes. We have started developing a more general code to treat radiative transfer in the Kerr matric (Martocchia & Matt, in preparation), but such a treatment is well beyond the scope of this paper.

Even considering the limitations of our reprocessing model just outlined, the present results further confirm the contradiction mentioned in the Introduction. Either the reprocessing model is not correct altogether, and therefore the form of the soft excess cannot be simply explained in terms of characteristics atomic features, like the oxygen K-edges, or the form of the soft excess is not "universal", being the soft X-ray spectrum of low optical luminosity and flat α_{OX} quasars well described by the reprocessing model while that of higher luminosity and steeper α_{OX} quasars is not.

If the second possibility is the right one, then our results indicate that direct disc emission at soft X-ray energies (at least in the form we parametrized it) does not dominate the spectrum of neither low or high optical luminosity quasars. The observed soft X-ray spectrum of high luminosity, steep α_{PSPC} quasars could be due to an optically thin hot ($T \lesssim 50$ keV) corona surrounding the accretion disc (Czerny & Elvis 1987, Fiore et al 1995, Laor et al 1996) or might be produced by non-thermal emission mechanisms.

To study in a greater detail the soft X-ray emission of quasars we have to await for measurements with a spectral resolution in the 0.1-1 keV energy range higher than that of the ROSAT PSPC, and with a wider band, like those that will be performed in the near future by the Low Energy and the Medium Energy Concentrator Spectrometers on board the SAX satellite (Scarsi 1993, Parmar et al. 1996, Boella et al 1996).

ACKNOWLEDGMENTS

We wish to thank Randy Ross for allowing us the free use of his radiative transfer code. We also thank Cesare Perola and Aneta Siemiginowska for usefull discussions. This research has made use of the NASA/IPAC Extragalactic Database (NED) which is operated by the Jet Propulsion Laboratory, California Institute of Technology, under contract with the National Aeronautics and Space Administration. F.F. acknowledges support by NASA grant NAG8-290.

REFERENCES

Bardeen J.M., Press W.H., Teukolsky S.A., 1972, ApJ, 178, 347
Boella G. et al, 1996, A&A, submitted
Chen K., Eardley D.M., 1991, ApJ, 382, 125
Comastri A., et al., 1992, ApJ, 384, 62
Courvoisier T.J-L., Paltani S., 1992, "IUE - Uniform Low Dispersion Archive, AGN", esa SP 1153 A
Czerny B., Elvis M., 1987, ApJ, 321, 305
Czerny B., Życki, P., 1994, ApJL, 431 L5
Elvis M., Lockman F.J., Wilkes B.J., 1989, AJ, 97, 777
Elvis, M., Fassnacht, C., Wilson, A.S., Briel, U., 1990, ApJ, 361 459
Fabian A.C., Rees M.J., Stella L., White N.E., 1989, MNRAS, 238, 729
Fabian A.C., et al., 1994, PASJ, 46, L59
Fiore F., Elvis M., Mathur S., Wilkes B., McDowell J., 1993, ApJ, 415, 129
Fiore, F., Elvis, M., 1995, in proceedings of the 30th COSPAR meeting "High energy radiation from Galactic and extragalactic black holes"
Fiore, F., Elvis, M., McDowell, J. C., Siemiginowska, A., Wilkes, B. J., 1994, ApJ, 431, 515
Fiore F., Elvis E., Siemiginowska A., Wilkes B.J., McDowell J.C., Mathur S., 1995, ApJ, 449, 74
Ghisellini G., George I.M., Fabian A.C., Done C., 1991, MNRAS, 248, 14
Hasinger G. et al., 1992, Legacy, 2, 77, OGIP MEMO, CAL/ROS/92-001
Kojima Y, 1991, MNRAS, 250, 629
Laor A., 1991, ApJ, 376, 90
Laor A., Fiore F., Elvis E., Wilkes B.J., McDowell J.C., 1994, ApJ, 435, 611
Laor A., Fiore F. Elvis E., Wilkes B.J., McDowell J.C., 1996, ApJ, submitted
Lightman A.P., White T.R., 1988, ApJ, 335, 57

Masnou J.-L., Wilkes B.J., Elvis M., McDowell J.C., Arnaud K.A., 1992, A&A, 253, 35
Martocchia A., Matt G., 1996, in preparation
Matt G., Fabian A.C., Ross R.R., 1993, MNRAS, 264, 839
Matt G., Piro L., Antonelli L.A., Fink H.H., Meurs E.J.A., Perola G.C., 1994, A&A, 292, L13
Nandra K., Pounds K.A., 1992, Nat, 359, 215
Nandra K., Pounds K.A., 1994, MNRAS, 268, 405
Nandra K. et al, 1996, ApJ, 459, 542
Parmar A. et al, 1996, A&A, submitted
Perola G.C., et al., 1986, ApJ, 306, 508
Pfefferman E., et al., 1987, Proc SPIE, 733, 519
Ross R.R., Fabian A.C., 1993, MNRAS, 261, 74
Siemiginowska A., Kuhn O., Elvis M., Fiore F., McDowell J.C., Wilkes, B.J., 1995, ApJ, 454, 77
Scarsi L., 1993, A&AS, 97, 371
Shakura N.I., Sunyaev R.A., 1973, A&A, 24, 337
Stark A.A., Gammie C.F., Wilson R.W., Bally J., Linke R.A., Heiles C., Hurwitz M., 1992, ApJS, 79, 77
Trümper J., 1983, Adv. Space Res., 2, No. 4, 241
Turner T.J., Pounds K. A., 1989, MNRAS, 240, 833
Turner T.J., Weaver, K.A., Mushotzky, R.F., Holt, S.S., Madejsky, G.M. 1991, ApJ, 381, 85
Walter R., Fink H.H., A&A, 274, 105
Walter R., et al., 1994, A&A, 285, 119
Wilkes B.J. Elvis M., 1987, ApJ, 323, 243
Williams O.R., et al., 1992, ApJ, 389, 157
Wilson A.S., Elvis M., Lawrence A., Bland–Hawthorn J., 1992, ApJ, 391, L75
Yaqoob T. et al, 1994, PASJ, 46,
Życki P.T., Krolik J.H., Zdziarski A.A., Kallman T.R., 1994, ApJ, 437, 597

THE SOFT X-RAY PROPERTIES OF A COMPLETE SAMPLE OF OPTICALLY SELECTED QUASARS II. FINAL RESULTS

Ari Laor[1,2], *Fabrizio Fiore*[3,4], *Martin Elvis*[4],
Belinda J. Wilkes[4] *and Jonathan C. McDowell*[4]

[1]Theoretical Astrophysics,Caltech 130-33, Pasadena, CA 91125
[2]Current address: Physics Department, Technion, Haifa 32000, Israel
email: laor@physics.technion.ac.il

[3]Osservatorio Astronomico di Roma, via dell'Osservatorio 5, Monteporzio-Catone (RM), 00040,
and SAX Scientific Data Center, via corcolle 19 I-00131 Roma, Italy
email: fiore@susy.mporzio.astro.it

[4]Harvard-Smithsonian Center for Astrophysics, 60 Garden Street, Cambridge, MA 02138
emails: elvis@cfa.harvard.edu, belinda@cfa.harvard.edu, mcdowell@cfa.harvard.edu

ABSTRACT

We present the final results of a *ROSAT* PSPC program to study the soft X-ray emission properties of a complete sample of of low z quasars. This sample includes all 23 quasars from the Bright Quasar Survey with $z \leq 0.400$, and $N_{\rm H\ I}^{\rm Gal} < 1.9 \times 10^{20}$ cm^{-2}. Pointed *ROSAT* PSPC observations were made for all quasars, yielding high S/N spectra for most objects which allowed an accurate determination of the spectral shape. The following main results were obtained:

1. The spectra of 22 of the 23 quasars are consistent, to within $\sim 30\%$, with a single power-law model at rest-frame $0.2-2$ keV. There is no evidence for significant soft excess emission with respect to the best fit power-law. We place a limit of $\sim 5\times10^{19}$ cm^{-2} on the amount of excess foreground absorption by cold gas for most of our quasars. The limits are $\sim 1 \times 10^{19}$ cm^{-2} in the two highest S/N spectra.

2. X-ray absorption by partially ionized gas ("warm absorber") in quasars is rather rare, occurring for $\lesssim 5\%$ of the population, which is in sharp contrast to lower luminosity Active Galactic Nuclei (AGNs), where absorption probably occurs for $\sim 50\%$ of the population.

3. Extensive correlation analysis of the X-ray continuum emission parameters with optical emission line parameters indicates that the strongest correlation is between the spectral slope α_x, and the Hβ FWHM. A possible explanation for this remarkably strong correlation is a dependence of α_x on $L/L_{\rm Edd}$, as seen in Galactic black hole candidates.

4. The strong correlations between α_x, and $L_{\rm [O\ III]}$, Fe II/Hβ, and the peak [O III] to Hβ flux ratio are verified. The physical origin of these correlations is still not understood.

5. There appears to be a distinct class of "X-ray weak" quasars, which form $\sim 10\%$ of the population (3 out of 23), where the X-ray emission is smaller by a factor of 10-30 than expected based on their luminosity at other bands, and on their Hβ luminosity. These may be quasars where the direct X-ray source is obscured, and only scattered X-rays are observed.

6. Thin accretion disk models cannot reproduce the observed 0.2-2 keV spectral shape, and they also cannot reproduce the tight correlation between the optical and soft X-ray emission. An as yet unknown physical mechanism must be maintaining a strong correlation between the optical and soft X-ray emission.

7. The H I/He I ratio in the high Galactic latitudes ISM must be within 20%, and possibly within 5%, of the total H/He ratio of 10, which indicates that He in the diffuse H II gas component of the interstellar medium is mostly ionized to He II or He III.

We finally note the intriguing possibillty that although the average α_x in radio-loud quasars (-1.15 ± 0.14) is significantly flatter than in radio-quiet quasars (-1.72 ± 0.09) the X-ray emission may not be related to the presence of radio emission. The different average α_x may result from the strong α_x vs. Hβ FWHM correlation and the tendency of radio-loud quasars to have broader lines.

Subject headings: galaxies: nuclei—quasars: general— X-rays: spectra—interstellar: matter

1 INTRODUCTION

Quasars emit most of their power in the UV to soft X-ray regime. The PSPC detector aboard *ROSAT* allowed a significantly improved study of the soft X-ray emission of quasars compared with earlier missions (some of which were not sensitive below 2 keV), such as *HEAO-1, EINSTEIN, EXOSAT*, and *GINGA* (e.g. Mushotzky 1984; Wilkes & Elvis 1987; Canizares & White 1989; Comastri *et al.* 1992; Lawson *et al.* 1992; Williams *et al.* 1992; and a recent review by Mushotzky, Done, & Pounds 1993). These earlier studies indicated that the X-ray emission above 1-2 keV is well described by a power law with a spectral slope $\alpha_x = d\ln f_\nu / d\ln\nu$ of about -0.5 for radio loud quasars and about -1.0 for radio quiet quasars. Large heterogeneous samples of AGNs were recently studied using the *ROSAT* PSPC by Walter & Fink (1993) and by Wang, & Brinkmann, & Bergeron (1996). However, the objects studied in the papers mentioned above do not form a complete sample, and the available results may be biased by various selection effects which were not well defined a priori. In particular, most of the studied objects are nearby, intrinsically X-ray bright AGNs.

To overcome the potential biases in existing studies we initiated a *ROSAT* PSPC program to make an accurate determination of the soft X-ray properties of a well defined and complete sample of quasars. This program was designed to address the following questions:

1. What are the soft X-ray spectral properties of the low redshift quasar population?

2. Are simple thin accretion disk models (e.g. Laor 1990) able to fit the observed optical/UV/soft X-ray continuum? are other modifying mechanisms, such as a hot corona (e.g. Czerny & Elvis 1987) required? Are models invoking optically thin free-free emission possible (e.g. Ferland, Korista & Peterson, 1990; Barvainis 1993)?

3. Do the observed soft X-ray properties display any significant correlations with other properties of these quasars? Are these correlations compatible with various models for the continuum and line emission mechanisms?

Our sample includes all 23 quasars from the BQS sample (Schmidt & Green 1983) with $z \leq 0.400$, and $N_{\rm H\,I}^{\rm Gal} < 1.9 \times 10^{20}$ cm^{-2}, where $N_{\rm H\,I}^{\rm Gal}$ is the H I Galactic column density as measured at 21 cm. These selection criteria allow optimal study of soft X-ray emission at the lowest possible energy. The additional advantages of the BQS sample are that it has been extensively explored at other wavelengths (see Paper I for further details), and that it includes only bright quasars, thus allowing high S/N X-ray spectra for most objects. The sample selection criteria are independent of the quasar's X-ray properties, and we thus expect our sample to be representative of the low-redshift, optically-selected quasar population.

Preliminary results from the analysis of the first 10 quasars available to us were described by Laor et al. (1994, hereafter Paper I). Here we report the analysis of the complete sample which allows us to address the three questions posed above. The outline of the paper is as follows. In §2 we describe the observations and the analysis of the spectra. §3 describes the analysis of correlations between the soft X-ray properties and other continuum and emission line properties. In §4 we compare our results with other soft X-ray observations and discuss some of the implications. We conclude in §5 with answers to the questions raised above, and with some new questions to be addressed in future studies.

2 THE OBSERVATIONS AND ANALYSIS OF THE SPECTRA

The complete sample of 23 quasars is listed in Table 1 together with their redshifts, m_B and M_B magnitudes (calculated for $H_0 = 50$ km s^{-1}, q=0.5), R, the radio to optical flux ratio, and $N_{\rm H\,I}^{\rm Gal}$. The redshifts, m_B, and M_B magnitudes are taken from Schmidt & Green (1983), R is taken from Kellerman *et al.* (1989). Note that 4 of the 23 quasars in our sample are radio loud (defined here as $R \geq 10$).

The Galaxy becomes optically thick below 0.2 keV for the typical high Galactic column of 3×10^{20} cm^{-2} (Dickey & Lockman 1990; Morrison & McCammon 1983), and accurate values of $N_{\rm H\,I}^{\rm Gal}$ are therefore crucial even for our low $N_{\rm H\,I}^{\rm Gal}$ sample. The $N_{\rm H\,I}^{\rm Gal}$ values given in column 7 of Table 1 are taken from Elvis, Lockman & Wilkes (1989), Savage et al. (1993), Lockman & Savage (1995), and the recent extensive measurements by Murphy et al (1996). All these measurements of $N_{\rm H\,I}^{\rm Gal}$ were made with the 140 foot telescope of the NRAO at Green Bank, WV, using the "bootstrapping" stray radiation correction method described by Lockman, Jahoda, & McCammon (1986), which provides an angular resolution of 21', and an uncertainty of $\Delta N_{\rm H\,I}^{\rm Gal} = 1 \times 10^{19}$ cm^{-2} (and possibly lower for our low $N_{\rm H}$ quasars). This uncertainty introduces a flux error of 10% at 0.2 keV, 30% at 0.15 keV, and nearly a factor of 2 at 0.1 keV. Thus, reasonably accurate fluxes can be obtained down to $\sim$ 0.15 keV. Note that Murphy et al. (1996) includes accurate $N_{\rm H\,I}^{\rm Gal}$ measurements for about 220 AGNs, including most AGNs observed by *ROSAT*, which would

be very useful for eliminating the significant systematic uncertainty in the PSPC spectral slope which must be present when a low accuracy $N_{\rm H\,I}^{\rm Gal}$ is used.

Table 2 lists the PSPC observations of all the quasars. For the sake of completeness we include also the 10 quasars already reported in Paper I. All sources were detected, and their net source counts range from 93 to 38,015, with a median value of about 1900 counts. The PROS software package was used to extract the source counts. Table 2 includes the exposure times, the dates of the observations, the net number of counts and their statistical error, the count rate, the radius of the circular aperture used to extract the source counts, the offset of the X-ray position from the optical position, the *ROSAT* sequence identification number, and the SASS version used for the calibration of the data. All objects, except one, are typically within 15″ of the center of the PSPC field of view, so all the identifications are secure. The one exception is PG 1440+356 which is offset by 40′, but since this object is very bright in the *ROSAT* band (Gondhalekar et al. 1994), and in the extreme UV (Marshall et al. 1996), its identification is quite secure. Note that the exposure times are uncertain by about 4% due to a number of possible systematic errors, as described by Fiore *et al.* (1994). The typically large number of counts for each object allows an accurate determination of the spectral slope for most objects, as described below.

Model fits to the extracted number of source counts per pulse invariant (PI) channel, $N_{\rm ch}^{\rm ob}$, were carried out using the XSPEC software package. PI channels 1-12 of the original 256 channels spectra ($E < 0.11$ keV), were ignored since they are not well calibrated and are inherently uncertain due to the large Galactic optical depth. The January 1993 PSPC calibration matrix was used for observations made after 1991 Oct. 14, and earlier observations were fit with the March 1992 calibration matrix. The best fit model parameters are obtained by χ^2 minimization. Nearby channels were merged when $N_{\rm ch}^{\rm ob} < 10$. A 1% error was added in quadrature to the statistical error in $N_{\rm ch}^{\rm ob}$, to take into account possible systematic calibration errors (see Paper I).

2.1 *A Single Power-Law*

As in Paper I, we fit each spectrum with a single power-law of the form $f_E = e^{-N_{\rm H}\sigma_E} f_0 E^{\alpha_x}$, where f_E is the flux density, σ_E is the absorption cross section per H atom (Morrison & McCammon 1983), f_0 is the flux density at 1 keV, and E is in units of keV. We make three different fits for each object, with: 1. $N_{\rm H}$ a free parameter, 2. $N_{\rm H}$=$N_{\rm H\,I}^{\rm Gal}$. 3. $N_{\rm H}$=$N_{\rm H\,I}^{\rm Gal}$, and $0.47 \leq E \leq 2.5$ keV, i.e. using only the hard ROSAT band (channels 12 – 34 of the rebinned 34 channels spectra). A comparison of fits 1 and 2 allows us to determine whether there is evidence for a significant intrinsic absorption excess or emission excess relative to a single power-law fit with $N_{\rm H}$=$N_{\rm H\,I}^{\rm Gal}$. This comparison also allows us, as further shown in §5.3.3, to determine whether the 21 cm measurement of $N_{\rm H\,I}^{\rm Gal}$ is a reliable measure of the Galactic soft X-ray opacity. A comparison of fits 2

and 3 allows us to look for a dependence of the power-law slope on energy.

Table 3 provides the results of fits 1-3 described above. The table includes the 13 objects not reported in Paper I, and 6 objects from paper I for which we only now have the accurate $N_{\rm H\,I}^{\rm Gal}$ values. For each fit we give the best fitting spectral slope α_x, the normalization of the power-law flux at 1 keV (f_0), the best fitting $N_{\rm H}$, the χ^2 of the fit ($\chi^2_{\rm fit}$), the number of degrees of freedom (dof), and the probability for $\chi^2 \geq \chi^2_{\rm fit}$. The errors $\Delta\alpha_x$ and $\Delta N_{\rm H}$ in fit 1 were calculated by making a grid search for models with $\Delta\chi^2 = 2.30$, as appropriate for 1 σ confidence level for two interesting parameters (e.g. Press *et al.* 1989). The error on the slope $\Delta\alpha_x$ in fits 2 and 3 is calculated by requiring $\Delta\chi^2 = 1.0$ (i.e. 68% for one interesting parameter). We neglect the effect of $\Delta N_{\rm H\,I}^{\rm Gal}$ on $\Delta\alpha_x$ in fits 2 and 3 since we use accurate $N_{\rm H\,I}^{\rm Gal}$ for all objects.

The observed and best fit spectra for the 13 quasars not reported in paper I are displayed in Figure 1. There are 3 panels for each object. The upper panel displays the observed count rate per keV as a function of channel energy, the histogram represents the expected rate from the best fit power-law model, $N_{\rm ch}^{\rm ob}$, with $N_{\rm H}$ a free parameter (fit 1). The middle panel displays Δ/σ, where $\Delta = N_{\rm ch}^{\rm ob} - N_{\rm ch}^{\rm mod}$, and σ is the standard error in $N_{\rm ch}^{\rm ob}$. This plot helps indicate what features in the spectrum are significant. The lower panel displays the fractional deviations from the expected flux, or equivalently $\Delta/N_{\rm ch}^{\rm mod}$, which indicates the fractional amplitude of the observed features.

As shown in Table 3, in all 13 objects the simple power-law model with $N_{\rm H\,I}^{\rm Gal}$ (fit 2) provides an acceptable fit (i.e. $\Pr(\chi^2 \geq \chi^2_{\rm fit}) > 0.01$). Note in particular the spectrum of PG 1116+215, which despite the very high S/N available (24,272 net counts), shows no deviations from a simple power law above a level of $\lesssim 10\%$. In Paper I a simple power-law model could not provide an acceptable fit to three of the 10 quasars, though in two of them the apparent features could not be fit with a simple physical model, and in one of them this may be due to calibration errors (see §4.1).

As mentioned above, a comparison of the free $N_{\rm H}$ fit (fit 1) with the $N_{\rm H\,I}^{\rm Gal}$ fit (fit 2) allows us to look for evidence for an absorption or an emission excess. We measure the statistical significance of the reduction in $\chi^2_{\rm fit}$ with the addition of $N_{\rm H}$ as a free parameter using the F test (Bevington 1969). In PG 1440+356 we find a significant reduction with Pr= 7.5×10^{-4} (F=12.98 for 26 dof), where Pr is the probability that the reduction in χ^2 is not statistically significant (calculated using the FTEST routine in Press *et al.* 1989). The $N_{\rm H}$ obtained in fit 1 suggests intrinsic absorption of about 5×10^{19} cm^{-2} above the Galactic absorption. However, unlike all other objects, PG 1440+356 was observed significantly off axis (see Table 2), and some small systematic calibration errors may be present there. Note also that the $\chi^2_{\rm fit}$ of the fit with $N_{\rm H\,I}^{\rm Gal}$ (Pr=0.05) is still acceptable. We therefore cannot conclude that an extra absorber must be present in PG 1440+356. Marshall et al. (1996) found a very steep slope ($\alpha = -4.7 \pm 0.65$) in

PG 1440+35 at 0.1-0.15 keV (80-120Å) using the Extreme UV Explorer. There is no indication for such a component in the PSPC spectrum below 0.15 keV (Fig.1c). However, given the very low sensitivity of the PSPC below 0.15 keV, such a steep soft component may still be consistent with the PSPC spectrum. In the other 12 objects the free $N_{\rm H}$ fit does not provide a significant improvement (i.e. Pr$>$ 0.01), and thus there is no clear evidence for either intrinsic absorption, or low energy excess emission above a simple power-law.

Figure 2 compares the Galactic $N_{\rm H}$ deduced from the accurate 21 cm measurements with the best fit X-ray column deduced using the free $N_{\rm H}$ fit. The straight line represents equal columns. The χ^2 of the $N_{\rm H}$(21 cm)=$N_{\rm H}$(X-ray) model is 31.9 for 22 dof (PG 1001+054 was not included because of the low S/N), which is acceptable at the 8% level. This result demonstrates that there is no significant excess absorption over the Galactic value in any of our objects. It is interesting to note that in our highest S/N spectra, PG 1116+215 and PG 1226+023, $N_{\rm H}$(X-ray) is determined to a level of $0.8 - 1 \times 10^{19}$ cm^2, and is still consistent with $N_{\rm H}$(21 cm), indicating that both methods agree to better than 10%.

The average hard *ROSAT* band (0.5-2 keV) slope for the complete sample is -1.59 ± 0.08 (excluding PG 1114+445 which is affected by a warm absorber, and PG 1001+054 and PG 1425+267 where the S/N is very low). This slope is not significantly different from the average slope for the full *ROSAT* band, -1.63 ± 0.07.

Spectral fits to the PSPC spectra of some of the objects in our complete sample were already reported by Gondhalekar et al. (1994), Ulrich & Molendi (1996), Rachen, Mannheim, & Biermann (1996), and Wang, Brinkmann, & Bergeron (1996). The results of the single power-law fit with a free $N_{\rm H}$ in these papers are all consistent with our results for the overlapping objects. The only discrepancy is with PG 1444+407 were both us and Wang et al. find a similar slope but Wang et al. find evidence for absorption, while we find no such evidence. For a simple power-law fit to PG 1444+407 Wang et al. find $\chi^2 = 26$ for 20 dof which is acceptable only at the 17% level ($\sim 1.4\sigma$ level), while we find for such a fit $\chi^2 = 14.7$ for 20 dof, which is acceptable at the 80% level.

As discussed in paper I (§5.1.3), the difference in spectral slopes at hard and soft X-rays raises the possibility that α_x may be changing within the PSPC band itself. The individual spectra are well fit by a simple power law, and thus any spectral curvature must be consistent with zero. Stronger constraints on the spectral curvature may be obtained by measuring the average curvature parameter (β, defined in Paper I) for the complete sample since the random error in the mean is smaller by $\sqrt{N} \sim 5$ than the random error for individual objects. Unfortunately, the PSPC calibration uncertainty at low energy, discussed in Paper I, introduces a systematic error in β (which obviously does not cancel out as $\sqrt{N}$), and as shown in paper I, does not allow a reliable determination of the curvature parameter. We therefore did not try to constrain the

spectral curvature parameter in this paper.

3 CORRELATION ANALYSIS

Table 4 presents 8 of the 12 rest-frame continuum parameters and 7 of the 18 emission line parameters used for the correlation analysis. The definitions of the spectral slopes are as in Paper I. The X-ray continuum parameters are from fit 2, and from Paper I. The near IR and optical continuum parameters are taken from Neugebauer *et al.* (1987). The emission line parameters were taken from Boroson & Green (1992). Luminosities were calculated assuming H_0=50 km s^{-1} and $q_0 = 0.5$.

The four additional continuum parameters not presented in Table 5 for the sake of brevity are $\alpha_{\rm irx}$, $\alpha_{\rm irs}$ (defined in Paper I), radio luminosity (Kellerman et al. 1989), and 1 μm luminosity (Neugebauer et al. 1987). The 11 emission line parameters not detailed in Table 5 are: [O III] EW, Fe II EW, Hβ EW, He II EW, [O III]/Hβ and He II/Hβ flux ratio, [O III] peak flux to Hβ peak flux ratio, radio to optical flux ratio, and the Hβ assymetry, shape, and shift parameters. All these 11 parameters are listed in Table 2 of Boroson & Green (1992).

The significance of the correlations was tested using the Spearman rank-order correlation coefficient (r_S) which is sensitive to any monotonic relation between the two variables. A summary of the main correlation coefficients and their significance is given in Table 5.

3.1 *The Significance Level*

In Paper I the correlation analysis was carried out using 10 objects, and only relatively strong correlations ($r_S \geq 0.76$) could be detected at the required significance level (Pr$\leq$ 0.01). Here, with 23 objects, a Pr$\leq$ 0.01 corresponds to $r_S \geq 0.52$, and we can thus test for the presence of weaker correlations, and check whether the correlations suggested in Paper I remain significant. We have searched for correlations among the 12 continuum emission parameters, and between these 12 parameters and the 18 emission line parameters listed above, which gives a total of 294 different correlations. One thus expects about 1 spurious correlation with Pr$\leq 3.4 \times 10^{-3}$ in our analysis, and for a significance level of 1% one would now have to go to Pr$\leq 3.4 \times 10^{-5}$, rather than Pr$\leq 1 \times 10^{-2}$. However, we find that there are actually 42 correlations with Pr$\leq 3.4 \times 10^{-3}$, rather than just one, in our sample. Thus, the probability that any one of them is the spurious one is only 2.4%, and the significance level of these correlations is reduced by a factor of 7 (= 0.024/0.0034), rather than a factor of 300. Below we assume that correlations with Pr$\leq 1 \times 10^{-3}$ are significant at the 1% level (there are 30 correlations with Pr$\leq 1 \times 10^{-3}$, versus an expected number of 0.3). Thus, given the large number of correlations we looked at, we can only test reliably for correlations with $r_S \geq 0.64$ (which corresponds to Pr$\leq 1 \times 10^{-3}$ for 23 data points).

3.2 *The Near IR to X-Ray Energy Distribution*

A comparison of the rest-frame spectral energy distributions of all 23 quasars is shown in Figure 3. The 3-0.3 μm continuum is from Neugebauer et al. (1987), and the 0.2-2 keV continuum is from paper I and from this paper. The upper panel shows the absolute luminosities, and the lower 2 panels the luminosity normalized to unity at $\log \nu = 14.25$ for radio quiet quasars and for radio loud quasars. Note the relatively small dispersion in the normalized 0.3 keV ($\log \nu = 16.861$) luminosity. The outlying objects are labeled. PG 1626+554 is the only object where a steep α_x is clearly associated with a strong soft excess (relative to the near IR flux). In other objects a steep α_x tends to be associated with a low 2 keV flux. This trend is also suggested by the presence of a marginally significant correlation between α_x and α_{ox} ($r_S = 0.533$, Pr= 0.0089, see below), and the absence of a significant correlation between α_x and α_{os} ($r_S = -0.201$, Pr= 0.36).

The X-ray luminosity distribution appears to be bimodal with two quasars, PG 1001+054 and PG 1411+442, being a factor of 30 weaker than the mean radio quiet quasar. These two quasars appear to form a distinct group of 'X-ray weak quasars'. The statistics for the radio loud quasars (RLQ) are much poorer, and there is no well defined mean, but PG 1425+267 may be a similar X-ray weak RLQ.

3.3 *Correlations with Emission Line Properties*

Figure 4 presents the correlations between the hard X-ray luminosity, $L_{2\ \mathrm{keV}}$ ($\log \nu = 17.685$), or the soft X-ray luminosity, $L_{0.3\ \mathrm{keV}}$, with the luminosities of Hβ, [O III], He II, or Fe II. The value of r_S and the two sided significance level (Pr) of r_S are indicated above each panel. Upper limits were not included in the correlations. Thus, the actual correlations for He II, where there are 5 upper limits, are likely to be smaller than found here (there is only one upper limit for [O III] and Fe II, and none for Hβ). Excluding He II, the X-ray luminosity is most strongly correlated with $L_{\mathrm{H}\beta}$ ($r_S = 0.734$, Pr= 6.6×10^{-5}). We note in passing that $L_{\mathrm{H}\beta}$ has an even stronger correlation with the luminosity at 3000 Å($r_S = 0.866$, Pr= 9×10^{-8}) and with the near IR luminosity at 1 μm ($r_S = 0.810$, Pr= 2.7×10^{-6}).

The position of the X-ray weak quasars is marked in Fig.4. Both PG 1001+054 and PG 1411+442 appear to have an X-ray luminosity weaker by a factor of about 30 compared to other quasars with similar $L_{\mathrm{H}\beta}$. PG 1425+267 is also weaker by a factor of ~ 10 compared with the other RLQ. These ratios are the same as those found above in §3.2, based on the spectral energy distribution.

Figures 5a-d displays various emission parameters which correlate with α_x (as obtained with $N_{\mathrm{H}}=N_{\mathrm{H\ I}}^{\mathrm{Gal}}$). The FWHM of H$\beta$, $L_{[\mathrm{O\ III}]}$, the Fe II/Hβ flux ratio, and the ratio of [O III] peak flux to Hβ peak flux (as defined by Boroson & Green) are the emission line parameters which

correlate most strongly with α_x. As found in Paper I, all the α_x versus emission line correlations become significantly weaker when we use α_x obtained with the free $N_{\rm H}$ fit.

The X-ray weak quasars are labeled in the $\alpha_{\rm ox}$ vs. α_x correlation in Figure 5e. As expected they have a steeper than expected $\alpha_{\rm ox}$ for their α_x. The last parameter shown in Figure 5f is $1.5L_{14.25}^{1/2}\Delta v^{-2}$, where Δv =Hβ FWHM. This parameter is related, under some assumptions, to the luminosity in Eddington units, as further discussed in §4.7.

4 DISCUSSION

4.1 *The Soft X-Ray Spectral Shape*

We find an average spectral index $\langle\alpha_x\rangle = -1.62 \pm 0.09$ for the complete sample of 23 quasars, where the error here and below is the uncertainty in the mean. This slope is consistent with the mean slope $\langle\alpha_x\rangle = -1.57 \pm 0.06$ which we found for the subsample of 24 quasars out of the 58 AGNs analyzed by Walter & Fink (1993, the other 34 AGNs in their sample are Seyfert galaxies (as defined by Véron-Cetty & Véron 1991). A similar average slope of -1.65 ± 0.07 was found by Schartel et al. (1996) for 72 quasars from the LBQS sample detected in the *ROSAT* all sky survey (RASS). Puchnarewicz et al. (1996) find a significantly flatter mean slope, $\langle\alpha_x\rangle = -1.07 \pm 0.06$, in a large sample of 108 soft X-ray selected AGNs. The reason for this dramatic difference is not entirely clear, but it may be related to intrinsic absorption, as suggested by Puchnarewicz et al. (see §4.2).

RLQ are known to have a flatter α_x than radio quiet quasars (RQQ) at energies above the PSPC band (e.g. Wilkes & Elvis 1987, Lawson et al. 1992). We find $\langle\alpha_x\rangle = -1.72 \pm 0.09$ for the 19 RQQ, and $\langle\alpha_x\rangle = -1.15 \pm 0.14$ for the 4 RLQ in our sample. We find a similar trend using the Walter & Fink quasar data, where $\langle\alpha_x\rangle = -1.61 \pm 0.08$ for the RQQ and $\langle\alpha_x\rangle = -1.36 \pm 0.08$ for the RLQ. We therefore find that the trend observed at harder X-rays also extends down to the 0.2-2 keV band. Schartel et al. (1995) stacked PSPC images of 147 RQQ and 32 RLQ finding for the sum images $\langle\alpha_x\rangle = -1.65 \pm 0.18$ for RQQ and $\langle\alpha_x\rangle = -1.00 \pm 0.28$ for the RLQ. However, the mean redshift of their objects is ~ 1.3 and thus their results apply to the $\sim 0.45 - 4.5$ keV band.

As discussed in Paper I, the *ROSAT* PSPC indicates a significantly different soft X-ray spectral shape for quasars compared with earlier results obtained by the *EINSTEIN* IPC and *EXOSAT* LE+ME detectors (e.g. Wilkes & Elvis, 1987; Masnou et al. 1992; Comastri et al. 1992; Saxton et al. 1993; Turner & Pounds 1989; Kruper, Urry & Canizares 1990). In particular, earlier missions suggested that the hard X-ray slope (Lawson et al. 1992; Williams et al. 1992) extends down to ~ 0.5 keV with a steep rise at lower energy. Here we find that the 0.2-2 keV spectrum is fit

well by a single power-law with Galactic absorption. This indicates that: 1). the break between the soft and hard X-ray slope must occur well above 0.5 keV, 2) the break must be gradual, and 3) there is no steep soft component with significant flux down to $\sim$ 0.2 keV. As mentioned in Paper I, the different *EINSTEIN* IPC and *EXOSAT* LE+ME results may be traced back to the combined effect of the lower sensitivity of these instruments below $\sim$ 0.5 keV, and possibly some calibration errors. Small systematic errors in the PSPC response function appear to be present below 0.2 keV (Fiore *et al.* 1994), and this instrument is thought to be significantly better calibrated than earlier instruments at low energy.

No significant spectral features are present in the PSPC spectra of all 13 additional quasars reported here, indicating that intrinsic features must have an amplitude of less than 10-20%. Note, in particular the high S/N spectrum of PG 1116+215, where the number of counts is about 12 times the median sample counts, yet this spectrum is still consistent with a simple power-law. For the complete sample we find that only 1 quasar, PG 1114+445, has a significant physical feature which is well described by a warm absorber model. In two other quasars, PG 1226+023 and PG 1512+370, there are significant features below 0.5 keV (paper I). In the case of PG 1512+370 the features are at a level of $\sim$ 30%, and in PG 1226+023 they are at a level $\lesssim$10% and may well be due to small calibration errors. This result is consistent with the result of Fiore et al. (1994) who found that a simple power-law provides an acceptable fit to the individual spectra of six high S/N PSPC quasar spectra.

A composite optical to hard X-ray spectral energy distribution for RLQ and RQQ is displayed in Figure 6. To construct it we used the mean $L_{14.25}$ (Table 5), the mean α_o, the mean α_x, and the mean α_{ox} in our sample. We excluded from the mean the three X-ray weak quasars, and PG 1114+445, where α_x is highly uncertain due to the presence of a warm absorber. The mean spectra were extended above 2 keV assuming a slope of -1 for RQQ and -0.7 for RLQ. The Mathews & Ferland (1987, hereafter MF) quasar energy distribution is also displayed for the purpose of comparison. The MF shape assumes a steep soft component with a break to the hard X-ray slope above 0.3 keV, and it therefore significantly underestimates the soft X-ray flux at $\sim 0.2 - 1$ keV.

RLQ tend to be somewhat stronger hard X-ray sources than RQQ. This trend, together with the flatter X-ray slope of RLQ was interpreted by Wilkes & Elvis (1987) as possible evidence for a two component model. In this interpretation RLQ have the same hard X-ray component with $\alpha_x \sim -1$, as in RQQ, with an additional contribution from a flatter $\alpha_x \sim -0.5$ component, making their overall X-ray emission flatter and brighter. The additional X-ray component in RLQ could be related to the radio jet, e.g. through inverse Compton scattering. The composite spectrum suggests that although RLQ are brighter at 2 keV, they may actually be fainter at lower energy because of their flatter α_x. The RLQ composite is based only on four objects and

is therefore rather uncertain. In addition, the results of Sanders et al. (1989 §III.c) suggest that RLQ in the PG sample are about twice as bright at 2 keV compared with RQQ of similar optical luminosity, rather than the $\sim 30\%$ found for the composite, thus the difference in PSPC α_x would imply a smaller difference at 0.2 keV than shown in the composite. If RLQ are indeed weaker than RQQ at 0.2 keV then the two component model suggested above would not be valid, and RLQ need to have a different X-ray emission process, rather than just an additional component.

The difference between RLQ and RQQ may actually be unrelated to the radio emission properties, as discussed in §4.4.

Figure 6 also displays a simple cutoff power-law model of the form $L_\nu \propto \nu^{\alpha_o} e^{-h\nu/kT_{\rm cut}}$ with $\alpha_o = -0.3$ and $T_{\rm cut} = 5.4 \times 10^5$ K. This is an alternative way to interpolate between the UV and soft X-ray emission, and it is also a reasonable approximation for an optically thick thermal component. The lack of a very steep low energy component down to 0.2 keV allows us to set an upper limit on $T_{\rm cut}$. The upper limit is set using α_o and $\alpha_{os'}$ the slope from 3000 Å to rest frame $0.15(1+z)$ keV (the lowest energy were the Galactic absorption correction error$\lesssim 30\%$), given by

$$\alpha_{os'} = [2.685\alpha_{ox} - (17.685 - \log\nu_{s'})\alpha_x]/\log(\nu_{s'}/10^{15}), \quad \text{where} \quad \log\nu_{s'} = 16.560 + \log(1+z).$$

The upper limit on the cutoff temperature $T_{\rm cut}^{\rm ul}$ is related to the spectral slopes by

$$T_{\rm cut}^{\rm ul} = \frac{4.8 \times 10^{-11}(\nu_{s'} - 10^{15})\log e}{(\alpha_o - \alpha_{os'})\log(\nu_{s'}/10^{15})} \ {\rm K}.$$

We find a rather small dispersion in $T_{\rm cut}^{\rm ul}$ with $\langle T_{\rm cut}^{\rm ul}\rangle = (5.5 \pm 2.6) \times 10^5$ K, averaged over the complete sample (Table 4), which corresponds to a cutoff energy of 47 eV, or about 3.5 Ryd. This value of $T_{\rm cut}^{\rm ul}$ corresponds very closely to the far UV continuum shape assumed by MF (see Fig.6).

Walter et al. (1994) fit such a cutoff model directly to six quasars and Seyfert galaxies finding $\langle E_{\rm cut}\rangle = 63 \pm 12$ eV, or $\langle T_{\rm cut}\rangle = (7.3 \pm 1.4) \times 10^5$ K, while Rachen, Mannheim & Biermann (1996) find using such a model $\langle T_{\rm cut}\rangle = (6.3 \pm 2.3) \times 10^5$ K for 7 quasars and Seyfert galaxies. These values are consistent with our results. The small dispersion in $T_{\rm cut}$ reflects the small dispersion in $\alpha_{\rm os}$ in our sample, which is in marked contradiction with the dispersion predicted by thin accretion disk models, as further discussed in §4.5.

4.2 *Intrinsic Absorption*

As shown in Fig.2, the H I column deduced from our accurate 21 cm measurements is consistent for all objects with the best fit X-ray column. It is quite remarkable that even in our highest S/N spectra the 21 cm and X-ray columns agree to a level of about 1×10^{19} cm^{-2}, or 5-7%. This

agreement is remarkable since the 21 cm line and the PSPC are actually measuring the columns of different elements. Most of the soft X-ray absorption is due to He I or He II, rather than H I, and the H I column is indirectly inferred assuming the column ratio H I/He I= 10. The fact that the 21 cm line and the PSPC give the same H I column implies that the H I/He column ratio at high Galactic latitudes must indeed be close to 10. The dispersion in the H I/He column ratio is lower than 20% (based on typical quasars in our sample), and may even be lower than 5% (based on our highest S/N spectra). There is therefore no appreciable Galactic column at high Galactic latitudes where the ionized fraction of H differs significantly from the ionized fraction of He, as found for example in H II regions (e.g. Osterbrock 1989).

The consistency of the 21 cm and X-ray columns also indicates that the typical column of cold gas intrinsic to the quasars in our sample must be smaller than the X-ray $N_{\rm H}$ uncertainty, or about $3 \times 10^{19}(1+z)^3$ cm^{-2}. An additional indication for a lack of an intrinsic cold column in quasars comes from the fact the the strong correlations of α_x with the emission line parameters described above (§3.3) become weaker when we use α_x from the free $N_{\rm H}$ fit rather than α_x from the fit with $N_{\rm H\ I}^{\rm Gal}$. This indicates that $N_{\rm H\ I}^{\rm Gal}$ is closer to the true $N_{\rm H}$ than the free $N_{\rm H}$ (see discussion in Paper I). In our highest S/N spectra we can set an upper limit of $\sim 2 \times 10^{19}$ cm^{-2} on any intrinsic absorption. As discussed in Paper I, the lack of intrinsic X-ray column for most quasars is consistent with more stringent upper limits set by the lack of a Lyman limit edge, as well as the He I and the He II bound-free edges in a few very high z quasars.

Puchnarewicz et al. (1996) suggest that the strong α_x vs. α_{ox} correlation in their sample is due to absorption of the optical and soft X-ray emission by cold gas and dust. They show that the α_x vs. α_{ox} correlation for the 10 objects in Paper I can be explained by a universal spectral shape absorbed by a gas with a column of up to $N_{\rm H}= 3 \times 10^{20}$ cm^{-2} (see their Figure 16). As described above, such absorbing columns are clearly ruled out by our high S/N spectra.

The mean α_o in the Puchnarewicz et al. sample is -0.92 ± 0.07, which is significantly steeper than the mean α_o for optically selected quasars, e.g. a median of -0.2 for 105 PG quasars (Neugebauer et al. 1987), a median of -0.32 for 718 LBQS quasars (Francis et al. 1991), and $\langle \alpha_o \rangle = -0.36 \pm 0.05$, in our sample. Puchnarewicz et al. suggested that the much flatter α_o of the PG quasars is a selection bias since these quasars were selected by the strength of their UV excess. However, the PG sample was selected on the basis of the color criterion $U - B < -0.44$, which using the flux transformations of Allen (1973), corresponds to $\alpha_o \geq -1.8$. Thus, most of the red quasars discovered by Puchnarewicz et al. fit into the PG color criterion. The difference between the soft X-ray selected and optically selected quasars must reflect the true tendency of X-ray selected quasars to be significantly redder than optically selected quasars. These red quasars may very well be affected by a large absorbing column ($N_{\rm H}> 10^{21}$ cm^{-2}), as suggested by Puchnarewicz et al.

Intrinsic absorption is common in Seyfert 1 galaxies. About half of the Seyfert galaxies observed by Turner & Pounds (1989) using the *EXOSAT* LE+ME detectors, by Turner, George & Mushotzky (1993) using the *ROSAT* PSPC, and by Nandra & Pounds (1994) using the *GINGA* LAC, show low energy absorption, or spectral features inconsistent with the simple power-law typically observed above 2 keV. Quasars are very different, excess absorption produces significant spectral features only in one object (PG 1114+445, see paper I), i.e. $\sim 5\%$ (1/23) of the objects, and the absorbing gas is partially ionized ("warm"), rather than neutral. We cannot, however, rule out partial absorption, or complete absorption and scattering, by a very high column density ($N_{\rm H} > 10^{24}$ cm^{-2}) gas since such effects may only suppress the flux level without affecting the spectral shape, and without inducing significant spectral features. As described in §4.8, we suspect that such strong absorption may indeed be present in about $\sim 10\%$ (3/23) of the quasars in our sample (the X-ray weak quasars).

4.3 *Implications of the Continuum-Continuum Correlations*

The continuum-continuum luminosity correlations found here are all weaker than found in Paper I. This is mostly due to the three X-ray weak quasars which were not present in Paper I. For example, in Paper I we found that $f_{0.3\ \rm keV}$ can be predicted to within a factor of two, once $f_{1.69\ \mu m}$ is given. This statement is still valid if the 4 extreme objects labeled in Fig.3 middle panel are excluded. The implications of the near IR versus X-ray luminosity correlation on the X-ray variability power spectrum were discussed in Paper I.

In Paper I we noted the similarity $\langle \alpha_{ox} \rangle = \langle \alpha_x \rangle = -1.50$, which was also noted by Brunner *et al.* (1992) and Turner, George & Mushotzky (1993). However, we argued there that this similarity is only fortuitous, and that it does not imply that the X-ray power law can be extrapolated into the UV since the optical slope is significantly different. Here we find that the relation $\langle \alpha_{ox} \rangle \simeq \langle \alpha_x \rangle$ holds only roughly for the complete sample where $\langle \alpha_{ox} \rangle = -1.55 \pm 0.24$, and $\langle \alpha_x \rangle = -1.62 \pm 0.45$. This relation does not hold when the sample is broken to the RQQ where $\langle \alpha_{ox} \rangle = -1.56 \pm 0.26$, and $\langle \alpha_x \rangle = -1.72 \pm 0.41$, and to the RLQ where $\langle \alpha_{ox} \rangle = -1.51 \pm 0.16$, and $\langle \alpha_x \rangle = -1.15 \pm 0.27$.

A significantly flatter $\langle \alpha_{ox} \rangle$ is obtained when the three X-ray weak quasars, and the absorbed quasar PG 1114+445 are excluded. Thus, "normal" RQQ quasars in our sample have $\langle \alpha_{ox} \rangle = -1.48 \pm 0.10$, $\langle \alpha_x \rangle = -1.69 \pm 0.27$, while for the RLQ $\langle \alpha_{ox} \rangle = -1.44 \pm 0.12$, $\langle \alpha_x \rangle = -1.22 \pm 0.28$, where the $\pm$ denotes here and above the dispersion about the mean, rather than the error in the mean.

The α_x versus α_{ox} correlation found here is weaker than in Paper I due to the presence of the X-ray weak quasars. However, the other 20 quasars appear to follow a trend of increasing α_x with increasing α_{ox} (Fig.5e), indicating as discussed in Paper I that a steep α_x is generally

associated with a weak hard X-ray component (at 2 keV), rather than a strong soft excess. The only object which clearly violates this trend is PG 1626+554 (Fig.3), which has both a steep α_x and a strong soft excess. Puchnarewicz, Mason & Cordova (1994) and Puchnarewicz et al. (1995a; 1995b) present PSPC spectra of three AGNs with extremely strong soft excess, where $L_{0.2\ \mathrm{keV}} > L_{3000\ \mathring{\mathrm{A}}}$. Our sample suggests that such objects are most likely rare, as can also be inferred from the selection criteria of Puchnarewicz et al. who selected their three objects from the *ROSAT* WFC all sky survey, in which only five AGNs were detected. This selection criterion implies that these AGNs must have a very high far UV flux.

The soft X-ray selected quasars in the Puchnarewicz et al. (1996) sample have $\langle \alpha_{ox} \rangle = -1.14 \pm 0.02$, and none of their quasars is "X-ray weak", i.e with $\alpha_{ox} < -1.6$. The absence of X-ray weak quasars in their sample is clearly a selection effect. The small survey area implies that most quasars in their sample are optically rather faint ($m_B \sim$ 18-19). "Normal" α_{ox} quasars in their sample produce a few hundred PSPC counts, but "X-ray weak" quasars are below their detection limit. The abundance of "X-ray loud" quasars (i.e $\alpha_{ox} > -1$) in the Puchnarewicz et al. sample is consistent with their rarity in optically selected samples. For example, quasars with $\alpha_{ox} = -1$ are about 20 times fainter at 3000Å than quasars with $\alpha_{ox} = -1.5$, for the same L_x. Since the space density of quasars increases as $\sim L_{\mathrm{opt}}^{-2.5}$ (§4.5) there are about 2,000 times more of these fainter quasars per unit volume in space. Thus, even if only 0.1% of quasars at a given $\sim L_{\mathrm{opt}}$ have $\alpha_{ox} = -1$, there would still be twice as many quasars with $\alpha_{ox} = -1$ than $\alpha_{ox} = -1.5$ per unit volume in space, at a given L_x.

4.4 *Implications of The Continuum-Line Correlations*

The presence of the strong correlations of α_x with the Hβ FWHM, with $L_{[\mathrm{O\ III}]}$, and with the Fe II/Hβ ratio described in Paper I is verified here. The correlation coefficients for the complete sample are comparable or somewhat smaller than those found in Paper I, but since the sample is larger the significance level is now much higher (Fig.5). We also report here an additional strong correlation of α_x with the ratio of [O III] peak flux to the Hβ peak flux, which is one of the emission line parameters measured by Boroson & Green. The α_x versus Hβ FWHM correlations is the strongest correlation we find between any of the X-ray continuum emission parameters and any of the emission line parameters reported by Boroson & Green (with the addition of lines luminosities reported in Table 5).

The α_x versus Hβ FWHM correlation is much stronger than the well known α_x correlation with radio loudness ($r_S = 0.26$, Pr=0.23 in our sample, but see Wilkes & Elvis 1987 and Shastri et al. 1993 for stronger correlations). Thus, the fact that the average α_x in RLQ is significantly flatter than in RQQ (§4.1) may actually be completely unrelated to the presence of radio emission,

it may just reflect the fact that RLQ tend to have broader lines than RQQ (e.g. Tables 3 and 5 in Boroson & Green). This appears to be the case in our sample, where the RLQ follow the same α_x versus Hβ FWHM distribution defined by the RQQ (Fig.5a). This intriguing suggestion can be clearly tested by comparing α_x for RLQ and RQQ of similar Hβ FWHM.

Boller, Brandt & Fink studied in detail narrow line Seyfert 1 galaxies (NLS1) and they also find an apparently significant trend of increasing α_x with increasing Hβ FWHM. However, the scatter in their sample is significantly larger than what we find here. In particular they find a large range of α_x for Hβ FWHM$<$ 2000 km s^{-1}, where only a few objects are available in our sample. The overall larger scatter in the Boller, Brandt & Fink data is probably due in part to the generally larger statistical errors in their α_x determinations. Large systematic errors may also be induced by the use of Hβ FWHM from a variety of sources. The measured Hβ FWHM can be sensitive to the exact measuring procedure, such as continuum placement, subtraction of Fe II blends, and subtraction of the narrow component of the line (produced in the narrow line region) which may not be well resolved in low resolution spectra. For example, Shastri et al. 1993 and Boroson & Green measured the Hβ FWHM independently for 13 overlapping objects, in 8 of which their values differ by more than 1000 km s^{-1}. Other than these technical reasons the increased scatter may represent a real drop in the strength of the correlation when the luminosity decreases from the quasar level studied here to the Seyfert level studied by Boller, Brandt & Fink. One should also note that intrinsic absorption is probably common in Seyfert 1 galaxies (Turner & Pounds, 1989; Turner, George & Mushotzky, 1993), and such an absorption may lead to a large systematic error in α_x unless a high S/N spectrum is available indicating that features are present.

Wang, Brinkmann & Bergeron (1996) analyzed PSPC spectra of 86 AGNs, including 22 of the 23 quasars from our sample. Their sample is more heterogeneous than ours and includes some high z quasars and a number of AGNs selected by their strong Fe II emission. The various correlations found by Wang et al. are typically similar, or somewhat weaker than found here. For example, their(our) values are $r_S = -0.73(-0.79)$ for α_x versus Hβ FWHM, and $r_S = 0.65(0.714)$ for α_x versus Fe II/Hβ. The somewhat smaller values found by Wang et al. may result from their inclusion of $z > 0.4$ quasars, where α_x measures a higher energy slope than measured here, and from their use of a free $N_{\rm H}$ fit (limited from below by $N_{\rm H\ I}^{\rm Gal}$), which increases the random error in α_x (see Paper I).

We verify the strong correlation between $L_{\rm H\beta}$ and $L_{2\ \rm keV}$ found in Paper I. The correlations of the other lines with X-ray luminosity are significantly weaker than found in Paper I, and they are only marginally significant. Corbin (1993) found significant correlations of $L_{2\ \rm keV}$ with Fe II/Hβ ($r_S = -0.474$), and of $L_{2\ \rm keV}$ with the Hβ asymmetry ($r_S = -0.471$). We find that neither correlation is significant in our sample ($r_S = -0.288$, Pr=0.19, and $r_S = -0.106$, Pr=0.63).

Since we can only test for correlation with $r_S > 0.64$, we cannot securely exclude the presence of the correlations reported by Corbin.

As discussed in Paper I, the α_x versus $L_{[\mathrm{O\ III}]}$ correlation can be used to place a limit on the α_x variability on timescales shorter than a few years. Given the scatter in this correlation we estimate that α_x should not vary by significantly more than 0.3 on these timescales.

It is hard to interpret the α_x versus [O III] to Hβ peak flux ratio correlation since the physical meaning of the [O III] to Hβ peak flux ratio parameter defined by Boroson & Green is rather obscure. The [O III] peak flux is related to the width of [O III], and the [O III] to Hβ peak flux ratio may thus partly reflect the FWHM ratio of these lines. Thus, this correlation may represent a correlation of the [O III] FWHM with α_x. High spectral resolution measurements of the [O III] line profile are required to test this possibility.

4.5 *Inconsistency with Thin Accretion Disk Models*

Figure 7 presents the continuum emission from two thin accretion disk models. The models are for a disk around a rotating black hole, and viscous stress which scales like the $\sqrt{P_{\mathrm{gas}}P_{\mathrm{rad}}}$, where P_{rad} is the radiation pressure and P_{gas} is the gas pressure (Laor & Netzer 1989). Significant soft X-ray emission is obtained for disks with a high accretion rate and a small inclination. However, as discussed by Fiore et al. (1995), the observed soft X-ray spectral slope is always much flatter than the one produced by a thin 'bare' accretion disk model. As noted above there is no indication in the 0.2-2 keV band for a very steep and soft "accretion disk" component.

Although thin disks cannot reproduce the 0.2-2 keV spectral shape, they may still be able to contribute a significant fraction of the flux at the lowest observed energy, i.e. 0.2-0.3 keV, above which a non thermal power-law component sets in. As noted by Walter et al. (1994) and in Paper I, accretion disk models predict a large dispersion in the optical/soft X-ray flux ratio, and the strong correlation between these fluxes argues against the idea that a thin disk produces both the optical and soft X-ray emission. The arguments put by Walter et al. and in Paper I were only qualitative, and were not based on actual disk models. Furthermore, the objects in the small sample of Walter et al. were selected from known optically bright AGNs, and they also had to be bright soft X-ray sources since most spectra were obtained from the *ROSAT* all sky survey. Thus, these objects were a priori selected to be bright at both optical-UV and at soft X-rays, and the absence of a large scatter in the UV/soft X-ray flux ratio may just reflect the sample selection criteria. Such selection effects are not present in our sample since the sample was defined independently of the X-ray properties, and X-ray spectra were obtained for all objects.

Below we describe a detailed calculation of the expected distribution of optical/soft X-ray flux ratio for a complete optically selected sample based on the thin disk models of Laor &

Netzer (1989), and show that such models cannot be reconciled with the observed distribution of optical/soft X-ray flux ratio in our complete sample.

The optical/soft X-ray flux ratio, α_{os}, of a given disk model depends on the black hole mass, accretion rate $\dot{m}$, and inclination angle $\theta = \cos^{-1}\mu$. We now need to determine what distributions of these parameters which will be consistent with the observed luminosity function in a complete optically selected sample. The intrinsic distribution of disk inclinations must be random. However, the observed distribution depends on the shape of the luminosity function of quasars, and possible obscuration effects, as described below.

The luminosity function of quasars is parametrized using the number density of quasars per unit volume per magnitude $\Phi \equiv d^2N/dMdV$, and it is well fit by a power-law over a restricted range of magnitude, M. Using Figure 2 in Hartwick & Schade (1990) we find $\log\Phi = 0.55M + c$ for $z < 0.2$ and $\log\Phi = 0.66M + c$ for $0.4 < z < 0.7$, where c is a constant. Since our sample is restricted to $z < 0.4$ we assume $\log\Phi = 0.6M + c$. Using the relation $M = -2.5\log L + c$ we get that $dn/dL \propto L^{-2.5}$, where $n \equiv dN/dV$.

The apparent luminosity of a flat disk $L_{\rm app}$ is related to its intrinsic luminosity through $L_{\rm app} = 2\mu L$, neglecting limb darkening effects which steepen the μ dependence, and relativistic effects which flatten the μ dependence. This provides a reasonable approximation in the optical-near UV regime (see Laor, Netzer, & Piran 1990). Assuming $dN/d\mu = const$, i.e. a uniform distribution of inclination angles for the intrinsic quasar population, we would like to find $dn/d\mu$ for a given $L_{\rm app}$. When $L_{\rm app}$ is fixed, $\mu \propto L^{-1}$, and substituting μ in the expression for dn/dL we get $dn/d\mu \propto \mu^{0.5}$. Thus although the disks are assumed to have a uniform distribution of inclination angles the observed distribution at a given $L_{\rm app}$ is biased towards face on disks.

To reproduce the observed luminosity function we choose two values of $\dot{m} = 0.1, 0.3$, where $\dot{m}$ is measured in units of the Eddington accretion rate. Since $L \propto m_9\dot{m}$, where m_9 is the black hole mass in units of $10^9 M_\odot$ the required mass distribution is $dn/dm_9 \propto m_9^{-2.5}$. The observed number of objects in a flux limited sample is $dN_{\rm ob}/dL \propto dn/dL \times V(L)$, where $V(L) \propto L^{3/2}$ is the observable volume for a flux limited sample, such as the BQS sample. We therefore select a mass distribution of $dN_{\rm ob}/dm_9 \propto m_9^{-1}$.

Figure 8 compares the observed distribution of α_{os}, as a function of νL_ν at 3000Å, with the one expected from thin accretion disk models with the parameter distribution described above. Thin disk models cannot account for the very small scatter in α_{os}.

The range of observed disk inclinations may actually be smaller than assumed here. For example, for a certain range of inclinations the disk may be completely obscured by an optically thick torus, as suggested in unification schemes for RQQ (e.g. Antonucci 1993). However, even if μ is fixed at a given value for all AGNs (say $\mu = 1$ which corresponds to the points extending from $\alpha_{os} = -1.5$ on the left axis to $\log\nu L_\nu = 46.5$ on the bottom axis of Fig.8), the range in m_9

and $\dot{m}$ will stil produce a range in α_{os} which is much larger than observed.

The X-ray power-law emission is most likely produced by Comptonization of the thermal disk emission in a hot corona above the disk (e.g. Czerny & Elvis 1987). The slope and normalization of the power-law component are determined by the temperature and electron scattering optical depth in the corona (e.g. Sunyaev & Titarchuk 1985; Titarchuk & Lyubarskij 1995). The small range in α_{os} implies that some physical mechanism which connects the optical and soft X-ray emission processes must be operating, e.g. through a feedback which regulates both the temperature (see Haardt & Maraschi 1993) and the optical depth of the corona.

As pointed out by various authors (Ross, Fabian & Mineshige, 1992; Shimura & Takahara 1995; Dorrer et al. 1996), and shown in Fig.7, simple thin accretion disks with no corona can produce a significant flux below 1 keV. For various disk model parameters α_{os} can in fact be significantly flatter than observed (Fig.8), yet such extreme flat optical-soft X-ray spectra are only rarely observed (e.g. Puchnarewicz 1995a). The flattest spectra are expected for disks which are close to edge on (e.g. Laor, Netzer & Piran 1990), and one therefore needs to assume that such disks are not observable. This is indeed expected in AGNs unification schemes which invoke obscuring material close to the disk plane. Alternatively, the accreted material may form a geometrically thick, rather than a thin, configuration close to the center, which would display a smaller inclination dependence.

4.6 *Inconsistency with Optically Thin Free-Free Emission Models*

As was clearly demonstrated by Fiore et al. (1995) for 6 low redshift quasars with a high S/N PSPC spectra, and by Siemiginowska et al. (1995) using *EINSTEIN* data for 47 quasars from Elvis et al. (1994), isothermal optically thin pure free-free emission models (Barvainis 1993) cannot fit the observed UV to soft X-ray energy distribution in AGNs. Furthermore, as was pointed out by Kriss (1995), and Hamman et al. (1995), optically thin free-free emission can also be ruled out based on the observed UV line emission.

4.7 *On the origin of the α_x versus Hβ FWHM correlation*

What is the physical process behind the α_x versus Hβ FWHM correlation? In Paper I we speculated that this may either be an inclination effect, or that it could be an $L/L_{\rm Edd}$ effect. More recently, Fiore & Elvis (1995) and Pounds, Done & Osborne (1995) raised the very interesting suggestion that steep α_x quasars may be analogous to 'high'-state Galactic black hole candidates, which display a steep slope in the soft and the hard X-ray bands when their brightness increases. The physical interpretation for this effect described by Pounds et al. is that the hard X-ray power-law is produced by Comptonization in a hot corona and that as the object becomes brighter in the

optical-UV, Compton cooling of the corona increases, the corona becomes colder, thus producing a steeper X-ray power-law. This is obviously far from being a predictive model since the corona heating mechanism is not specified, and it is implicitly assumed that the coronal heating does not increase much as the quasar becomes brighter. However, the narrow Hβ line profiles provide independent evidence that steep α_x quasars may indeed have a higher $L/L_{\rm Edd}$, as further described below.

The $L/L_{\rm Edd}$ of quasars can be estimated under two assumption: 1. The bulk motion of the gas in the broad line region is virialized, i.e. $\Delta v \simeq \sqrt{GM/r}$, where Δv=Hβ FWHM. This gives

$$\Delta v_{3000} = 2.19 m_9^{1/2} R_{0.1}^{-1/2},$$

where $\Delta v_{3000} = \Delta v/3000$ km s^{-1}, $m_9 = M/10^9\ M_\odot$, and $R_{0.1} = R/0.1$ pc. 2. The size of the broad line region is determined uniquely by the luminosity, $R_{0.1} = L_{46}^{1/2}$ pc, where $L_{46} = L_{\rm Bolometric}/10^{46}$. This scaling is consistent with reverberation line mapping of AGNs (Peterson 1993; Maoz 1995), and is theoretically expected if the gas in quasars is dusty (Laor & Draine 1993, Netzer & Laor 1994). Combining assumptions 1 and 2 gives

$$\Delta v_{3000} = 2.19 m_9^{1/2} L_{46}^{-1/4},$$

and thus the mass of the central black hole is

$$m_9 = 0.21 \Delta v_{3000}^2 L_{46}^{1/2}.$$

Using $L_{\rm Edd,46} = 12.5 m_9$ one gets

$$L/L_{\rm Edd} = 0.38 \Delta v_{3000}^{-2} L_{46}^{1/2}.$$

Thus, given the two assumptions made above, narrow line quasars should indeed have a high $L/L_{\rm Edd}$, as Fiore & Elvis and Pounds et al. suggested based only on their steep α_x, and analogy to Galactic black hole candidates.

To test whether $L/L_{\rm Edd}$ is indeed the underlying parameter which determines α_x, rather than just the Hβ FWHM, we looked at the correlation of α_x versus $\Delta v_{3000}^{-2} L_{46}^{1/2}$ displayed in Fig.5f, where we used the 1.7 μm luminosity and the relation $L_{\rm Bolometric} = 15 L_{14.25}$ (see Fig.7 in Laor & Draine). This correlation is not as strong as the α_x versus Hβ FWHM correlation, but it certainly appears suggestive. Note that $L/L_{\rm Edd} > 1$ for some of the objects in the sample. These values are well above the thin accretion disk limit ($L/L_{\rm Edd} = 0.3$, Laor & Netzer 1989) and suggest a thick disk configuration. However, the assumption used above to infer $L/L_{\rm Edd}$ are more qualitative than quantitative since both the luminosity and the velocity field in the broad line region may not be isotropic and therefore the presence of $L/L_{\rm Edd} > 1$ cannot be securely deduced.

The Pounds et al. mechanism implies that a steep α_x is associated with a weak hard X-ray component, and as described in §3.2, this indeed appears to be the trend in our sample. If the Pounds et al. mechanism is true then steep α_x AGNs should also have a steep hard X-ray power-law. We are currently persuing this line of research using ASCA and SAX observations of our sample.

An additional hint that a steep α_x may indeed be associated with a high $L/L_{\rm Edd}$ comes from the anecdotal evidence described by Brandt, Pounds & Fink (1995), Brandt et al. (1995), Grupe et al. (1995), and Forster & Halpern (1996) where a number of Seyfert galaxies with a steep α_x display rapid, large amplitude, soft X-ray variability, which as Boller, Brandt, & Fink discuss may imply a low mass black hole, and thus a high $L/L_{\rm Edd}$. We are currently persuing a more systematic study of the soft X-ray variability properties of broad versus narrow line quasars using the *ROSAT* HRI.

The Pounds et al. suggestion is very appealing since it allows a physical explanation for the tight correlation of apparently completely unrelated quantities. Although it is a priori not clear that α_x must steepen with increasing $L/L_{\rm Edd}$, it appears that this is indeed what happens in Galactic black hole candidates.

Wang et al. also suggested that steep α_x objects have a high $L/L_{\rm Edd}$ based on the fact that the fraction of luminosity emitted in the X-ray regime in thin accretion disk models increases with $L/L_{\rm Edd}$, as discussed above in §4.5. However, if this were indeed the physical process behind the α_x versus Hβ FWHM correlation then one would expect high $L/L_{\rm Edd}$ objects to have a high soft X-ray to optical flux ratio, while we find no correlation between Hβ FWHM and α_{os} ($r_S = -0.079$, Table 5).

We note in passing that one does not need to eliminate the normal broad line region in narrow line AGNs, as suggested by Boller et al., and Pounds et al. The lines are narrow simply because of the lower black hole mass. The broad line emitting gas does not extend much closer to the center in narrow line AGNs, as it does not extend much closer to the center in other AGNs, simply because of the effects of a higher ionization parameter, and a higher gas density, each of which quenches line emission.

4.8 *The X-ray Weak Quasars*

Two of the quasars in our sample, the RQQ PG 1001+054 and PG 1411+442, and possibly also the RLQ PG 1425+267 appear to form a distinct group which we term here "X-ray weak" quasars, where the normalized X-ray luminosity is a factor of 10-30 smaller than the sample median. The position of these quasars as outliers can be noticed in the near IR normalized flux distribution (Fig.3), in the α_x versus α_{ox} correlation (Fig.5e), and in the Hβ versus 2 keV and

0.3 keV luminosity correlations (Fig.4). The first two indicators are based on the spectral shape, but the last one is independent of the spectral shape, and it also suggests a deficiency of the X-ray luminosity by a factor of 10-30 relative to the one expected based on the Hβ luminosity. An apparently bimodal distribution in α_{ox} can also be seen in Figure.5b of Wang et al. where 6 of their 86 quasars appear to form a distinct group with $\alpha_{ox} < -2$.

Although the three X-ray weak quasars in our sample stand out in luminosity correlations, they conform well to the α_x correlations (Figs.5a-d). They thus have the "right" slope but the "wrong" flux level. Why are these quasars different? A simple answer is that for some unknown reason the X-ray emission mechanism, most likely Comptonization by $T \geq 10^8$ K electrons, tends to be bimodal, and in about 10% of quasars the X-ray flux level is strongly suppressed, while the spectral slope is not affected. Another option is that these are just normal quasars where the direct X-ray flux happens to be obscured. In this case what we see is only the scattered X-ray flux. Photoionization calculations indicate that a few percent of the direct flux will be scattered (depending on the covering factor of the absorber and the ionization parameter), and if the ionization parameter is large enough then the scattering will be mostly by free electrons which preserves the spectral shape (see Netzer 1993, and by Krolik & Kriss 1995). Such scattering will explain why the flux level is strongly reduced, while the spectral shape is not affected.

Additional hints towards this interpretation come from the fact that PG 1411+442 is a broad absorption line quasar (BALQSO, Malkan Green & Hutchings, 1987), and the UV absorbing gas may also produce soft X-ray absorption, as may also be the case in PHL 5200 (Mathur Elvis & Singh, 1995). In addition, Green & Mathur (1996) find that BALQSO observed by *ROSAT* have $\alpha_{ox} \lesssim -1.8$, i.e. as observed here in the X-ray weak RQQ. Another hint is provided by the fact the PG 1114+445 is also somewhat underluminous at 0.3 keV (Fig.3b), and this quasar is most likely seen through a warm absorber. The X-ray weak quasars could therefore be more extreme cases of PG 1114+445 and have an absorbing column which is large enough to completely absorb the direct soft X-ray emission.

Note that PG 1425+267 is a RLQ, while all BALQSO are known to be RQQ (Stocke et al. 1992). It would thus seem implausible to suggest that PG 1425+267 is a BAL. However, PG 1425+267 has about the same relatively steep α_{ox}, compared to other RLQ, as in 3C 351 (Fiore et al. 1993), where X-ray absorption is observed together with resonance UV absorption lines (Mathur et al. 1994) which are narrower than in 'proper' BALQSO.

Forthcoming HST spectra of all 23 quasars in our sample will allow us to test if there is a one to one correspondence between X-ray weakness and broad absorption lines, i.e. if all X-ray weak quasars are BALQSO, and not just that all BALQSO are X-ray weak, as strongly suggested by the Green & Mathur, and the Green et al. (1996) results.

A simple test on whether these are truly "X-ray weak quasars", or just normal highly absorbed

quasars, can be done by looking at their hard X-ray emission. If the X-ray column is below 10^{24} cm^{-2} then the obscuring material would become transparent at $E < 10$ keV, and the observed hard X-ray emission will rise steeply above the cutoff energy, as seen in various highly absorbed AGNs, such as Mkn 3 (Iwasawa et al. 1994), NGC 5506 (Nandra & Pounds 1994), NGC 6552 (Reynolds et al. 1994), and NGC 7582 (Schachter et al. 1996). Forthcoming ASCA observations of PG 1411+442 and PG 1425+267 will allow us to test this scenario.

Another prediction is that the X-ray weak quasars should show lower variability compared with other quasars of similar X-ray luminosity. This is because: 1). they are intrinsically more X-ray luminous, and variability tends to drop with increasing luminosity (e.g. Fig.9 in Boller, Brandt & Fink). 2). the scattering medium must be significantly larger than the X-ray source, and short time scale variability will be averaged out.

5 SUMMARY

We defined a complete sample of 23 optically selected quasars which includes all the PG quasars at $z \leq 0.400$, and $N_{\rm H\,I}^{\rm Gal} < 1.9 \times 10^{20}$ cm^{-2}. Pointed *ROSAT* PSPC observations were made for all quasars, yielding high S/N spectra for most objects. The high quality of the *ROSAT* spectra allows one to determine the best fitting α_x with about an order of magnitude higher precision compared with previously available X-ray spectra. In this paper we report the observations of 13 quasars not described in Paper I, analyze the correlation of the X-ray properties of the complete sample with other emission properties, determine the mean X-ray spectra of low z quasars, discuss the possible origin of the α_x versus Hβ FWHM correlation, the nature of X-ray weak quasars, and the physical origin of the soft X-ray emission. Our major results are the following:

1. The spectra of 22 of the 23 quasars are consistent, to within $\sim 10-30\%$, with a single power-law model over the rest frame range $0.2 - 2$ keV. There is no evidence for significant soft excess emission with respect to the best fit power-law. We place a limit of $\sim 5 \times 10^{19}$ cm^{-2} on the amount of excess foreground absorption by cold gas in most of our quasars. The limits are $\sim 1 \times 10^{19}$ cm^{-2} in the two highest S/N spectra.

2. X-ray absorption by partially ionized gas ("warm absorber") in quasars is rather rare, occurring for $\lesssim 5\%$ of the population, which is in sharp contrast to lower luminosity AGNs, where absorption probably occurs for $\sim 50\%$ of the population.

3. The average soft X-ray spectral slope for RQQ is $\langle \alpha_x \rangle = -1.72 \pm 0.09$, which is significantly steeper than the mean for RLQ $\langle \alpha_x \rangle = -1.15 \pm 0.16$.

4. Extensive correlation analysis of the X-ray continuum emission parameters with optical emission line parameters indicates that the strongest correlation is between α_x, and the Hβ

FWHM. A possible explanation for this remarkably strong correlation is a dependence of α_x on $L/L_{\rm Edd}$, as observed in Galactic black hole candidates.

5. There appears to be a distinct class of "X-ray weak" quasars, which form $\sim$ 10% of the population, where the X-ray emission is smaller by a factor of 10-30 than expected based on their luminosity at other bands, and on their Hβ luminosity.

6. Thin accretion disk models cannot reproduce the observed 0.2-2 keV spectral shape, and they also cannot reproduce the tight correlation between the optical and soft X-ray emission.

7. The H I/He I ratio in the ISM at high Galactic latitudes must be within 20%, and possibly within 5%, of the total H/He ratio.

The main questions raised by this study are:

1. What is the true nature of X-ray quiet quasars? Are these quasars indeed intrinsically X-ray weak, or are they just highly absorbed but otherwise normal quasars?

2. What physical mechanism is maintaining the strong correlation between the optical-UV and the soft X-ray continuum emission, or equivalently, maintaining a very small dispersion in the maximum possible far UV cutoff temperature?

3. What is the physical origin for the strong correlations between α_x, and $L_{[\rm O\ III]}$, Fe II/Hβ, and the peak [O III] to Hβ flux ratio?

4. Is the soft X-ray emission indeed related to the presence of radio emission, or is it just a spurious relation and the primary effect is related to the Hβ line width? Or, put differently, do RLQ and RQQ of similar Hβ FWHM have similar α_x?

Extensions of the *ROSAT* PSPC survey described in this paper to the hard X-ray regime with ASCA and SAX, to the UV with HST, and soft X-ray variability monitoring with the *ROSAT* HRI, which are currently being carried out, may provide answers to some of the questions raised above. These studies will also allow us to: 1) Test if steep α_x quasars have a steep 2-10 keV slope, as expected based on the Pounds et al. $L/L_{\rm Edd}$ interpretations. 2) Test if soft X-ray variability is indeed strongly tied to the Hβ FWHM, as expected if the Hβ FWHM is an indicator of $L/L_{\rm Edd}$. 3) Explore the relation of the UV line emission properties to the ionizing spectral shape.

This work was supported in part by NASA grants NAG 5-2087, NAG 5-1618, NAG 5-30934, NAGW 2201 (LTSA), and NASA contract NAS 8-30751. A. L. acknowledges support by NSF grant PHY 92-45317.

REFERENCES

Allen, C. W. 1973, Astrophysical quantities, third edition. University of London, Athlone Press, London

Antonucci, R., 1993, ARAA, 31, 473

Barvainis, R. 1993, ApJ, 412, 513

Bevington, P. R. 1969, Data Reduction and Error Analysis for the Physical Sciences (NY: McGraw-Hill)

Boller, Th, Brandt, W. N., & Fink, H. 1996, A&A, 305, 53

Boroson, T. A. & Green, R. F., 1992, ApJS, 80, 109

Brandt, W. N., Fabian, A. C., Nandra, K., Reynolds, C. S., & Brinkmann, W., 1994, MNRAS, 271, 958

Brandt, W. N., Pounds, K. A., & Fink, H., 1995, MNRAS, 273, L47

Brunner, H., Friedrich, P., Zimmermann, H.-U., & Staubert, R. 1992, in X-Ray Emission from Active Galactic Nuclei and the Cosmic X-Ray Background, ed. W. Brinkmann & J. Trümper, (MPI: Garching), 198

Canizares, C. R. & White, J. L. 1989, ApJ, 339, 27

Comastri, A., Setti, G., Zamorani, G., Elvis, M., Giommi, P., Wilkes, B. J., & McDowell, J. C. 1992, ApJ, 384, 62

Corbin, M. R. 1993, ApJ, 403, L9

Czerny, B. & Elvis, M. 1987, ApJ, 321, 305

Dickey, J. M. & Lockman, F. J. 1990, ARAA, 28, 215

Dorrer, T., Riffert, H., Staubert, R., & Ruder, H., 1996, A&A, in press

Elvis, M., Lockman, F. J. & Wilkes, B. J. 1989, AJ, 97, 777

Elvis, M., Wilkes, B. J., McDowell, J. C., Green, R. F., Bechtold, J., Willner, S. P., Polomski, E., & Cutri, R. 1994, ApJS, 95, 1

Ferland, G. F., Korista, K. T. & Peterson, B. M. 1990, ApJ, 363, L21

Fiore, F., Elvis, M., Mathur, S., Wilkes, B. J., & McDowell, J. C. 1993, ApJ, 415, 129

Fiore, F. & Elvis, M., 1995, in proceedings of the 30th COSPAR meeting "High energy radiation from Galactic and extragalactic black holes", in press

Fiore, F., Elvis, M., McDowell, J. C., Siemiginowska, A., & Wilkes, B. J., 1994, ApJ, 431, 515

Fiore, F., Elvis, M., Siemiginowska, A., Wilkes, B. J., McDowell, J. C., & Mathur, S., 1995, ApJ, 449, 74

Forster, K. & Halpern, J. P. 1996, ApJ, submitted

Francis, P. J., Hewett, P. C., Foltz, C. B., Chaffee, F. H., Weymann, R. J., & Morris, S. 1991, ApJ, 373, 465

Gondhalekar, P. M., Kellett, B. J., Pounds, K. A., Metthews, L., & Quenby, J. J. 1994, MNRAS, 268, 973

Green, P. J. & Mathur, S. 1996, ApJ, in press
Green, P. J. et al. 1996, ApJ, in press
Grupe, D., Beuermann, K., Mannheim, K., Thomas, H.-C., Fink, H. H., & de Martino, D., 1995, A&A, 300, L21
Haardt, F. & Maraschi, L. 1993, ApJ, 413, 507
Hamann, F., Shields, J. C., Ferland, G. J., & Korista, K. T., 1995, ApJ, 454, 688
Hartwick, F. D. A. & Schade, D., 1990, ARAA, 28, 437
Iwasawa, K., Yaqoob, T., Awaki, H., & Ogasaka, Y., 1995, PASJ, 46, L167
Kellerman, K. I., Saramek, R., Schmidt, M., Shaffer, D. B. & Green, R. 1989, AJ, 98, 1195
Kriss, G. 1995, in The Analysis of Emission Lines, STScI Symp. Series 8, eds. R. E. Williams & M. Livio (CUP: Cambridge)
Krolik, J. H. & Kriss, G. A., 1995, ApJ, 447, 512
Kruper, J. S., Urry, C. M., & Canizares, C. R. 1990, ApJS, 74, 347
Laor A., 1990, MNRAS, 246, 369
Laor, A., & Draine, B. T. 1993, ApJ, 402, 441
Laor, A. & Netzer, H. 1989, MNRAS, 238, 897
Laor, A. Netzer, H., & Piran, T., 1990, MNRAS, 242, 560
Lawson, A. J., Turner, M. J. L., Williams, O. R., Stewart, G. C., & Saxton, R. D. 1992, MNRAS, 259, 743
Lockman, F. J., Jahoda, K., & McCammon, D. 1986, ApJ, 302, 432
Lockman, F. J. & Savage, B. D. 1995, ApJS, 97, 1
Malkan, M. A., Green, R. F., & Hutchings, J. B., 1987, ApJ, 322, 729
Maoz, D., 1995, in: Reverberation Mapping of the BLR of AGN, eds. P. M. Gondhalekar, K. Horne, B. M. Peterson, (SF: Astronomical Society of the Pacific), p.95
Marshall, H. L., Carone, T. E., Shull, J. M., Malkan, M. A., & Elvis, M. 1995, ApJ, 457, 169
Masnou, J-L, Wilkes, B. J., Elvis, M., Arnaud, K. A. & McDowell, J. C. 1992, A&A, 253, 35.
Mathews, W. G. & Ferland, G. J. 1987, ApJ, 323, 456
Mathur, S., Wilkes, B., Elvis, M., & Fiore, F., 1994, ApJ, 434, 493
Mathur, S., Elvis, M., & Singh, K. P., 1995, ApJ, 455, L9
Morrison, R. & McCammon, D. 1983, ApJ, 270, 119
Mushotzky, R. F. 1984, Adv. Space Res., 3, No. 10, 157
Mushotzky, R. F., Done, C., & Pounds, K. A. 1993, ARAA, 31, 717
Murphy, E. M., Lockman, F. J., Laor, A., & Elvis, M. 1996, ApJS, in press
Nandra, K. & Pounds, K. A. 1994, MNRAS, 268, 405
Netzer, H. 1993, ApJ, 411, 594
Netzer, H., & Laor, A. 1993, ApJ, 404, L51

Neugebauer, G., Green, R. F., Mathews, K., Schmidt, M., Soifer, B. T. & Bennet, J. 1987, ApJS, 63, 615

Osterbrock, D. E. 1989, Astrophysics of Gaseous Nebulae and Active Galactic Nuclei, (California: University Science Books)

Peterson, B., 1993, PASP, 105, 247

Pounds, K. A., Done, C., & Osborne, J. P., 1995, MNRAS, 277, L5

Press, W. H., Flannery, B. P., Teukolsky, S. A., & Vetterling, W. T. 1989, "Numerical Recipes: The Art of Scientific Computing", (Cambridge: Cambridge University Press)

Puchnarewicz, E. M., Mason, K. O., & Cordóva, F. A. 1994, MNRAS, 270, 663

Puchnarewicz, E. M., Mason, K. O., Siemiginowska, A., & Pounds, K. A., 1995, MNRAS, 276, 20

Puchnarewicz, E. M., Branduardi-Raymont, G., Mason, K. O., & Sekiguchi, K., 1995, MNRAS, 276, 1281

Puchnarewicz, E. M. et al., 1996, MNRAS, submitted

Rachen, J. P., Mannheim, K., & Biermann, P. L. 1996, A&A, in press

Reynolds, C. S., Fabian, A. C., Makishima, K., Fukazawa, Y., & Tamura, T., 1994, MNRAS, 268, L55

Ross, R. R., Fabian, A. C., & Mineshige, s., 1993, MNRAS, 258, 189

Sanders, D. B., Phinney, E. S., Neugebauer, G., Soifer, B. T. & Mathews, K., 1989, ApJ, 347, 29

Savage, B. D. *et al.* 1993, ApJ, 413, 116

Saxton, R. D., Turner, M. J. L., Williams, O. R., Stewart, G. C., Ohashi, T., & Kii, T. 1993, MNRAS, 262, 63

Schachter et al. 1996, in preparation

Schartel, N., et al. 1996, ApJ, in press

Schmidt, M. & Green, R. F. 1983, ApJ, 269, 352

Shastri, P., Wilkes, B. J., Elvis, M., & McDowell, J. 1993, ApJ, 410, 29

Shimura, T. & Takahara, F., 1995, ApJ, 440, 610

Siemiginowska, A., Kuhn, O., Elvis, M., Fiore, F., McDowell, J. C., & Wilkes, B. J., 1995, ApJ, 454, 77

Stark, A. A., Gammie, C. F., Wilson, R. W., Bally, J., Linke, R. A., Heiles, C., & Hurwitz, M., 1992, ApJS, 79, 77

Stocke, J. T. Morris, S. L., Weymann, R. J., & Foltz, C. B., 1992, ApJ, 396, 487

Sunyaev, R. A. & Titarchuk, L., A&A, 143, 374

Titarchuk, L. & Lyubarskij, Y., 1995, ApJ, 450, 876

Turner, T. J., George, I. M., & Mushotzky, R. F. 1993, ApJ, 412, 72

Turner, T. J., Nandra, K., George, I. M., Fabian, A. C., & Pounds, K. A. 1993, ApJ, 419, 127

Turner, T. J. & Pounds, K. A. 1989, MNRAS, 240, 833

Ulrich, M.-H. & Molendi, S. 1996, ApJ, in press

Véron-Cetty, M. P., Véron, P. 1991, "A catalogue of Quasars and Active Nuclei (5th Edition)" (Munich: European Southern Observatory)

Walter, R. & Fink, H. H. 1993, A&A, 274, 105

Walter, R., Orr, A., Courvoisier, T. J.-L., Fink, H. H., Makino, F., Otani, C., & Wamsteker, W. 1994, A&A, 285, 119

Wang, T., Brinkmann, W., & Bergeron, J. 1996, A&A, in press

Wilkes, B. J. & Elvis, M. 1987, ApJ, 323, 243

Williams, O. R. *et al.*, 1992, ApJ, 389, 157

FIGURE CAPTIONS

Figure 1. The observed vs. single power-law fit PSPC spectra of the 13 quasars not reported in paper I. The upper panel for each object shows the observed count rate (points with error bars), and the expected count rate using the best fit single power-law model with a free $N_{\rm H}$ (solid line histogram). The middle panel shows the observed minus expected flux in units of standard deviations, and the lower panel for each object shows the fractional deviations from the expected flux. The best fit α_x, the fit χ^2, and the number of degrees of freedom (dof) are indicated for each object. The spectra of all quasars are consistent with a simple power-law. Note in particular the high S/N spectrum of PG 1116+215 where intrinsic features below 1 keV must have an amplitude of less than $\simeq$ 10%.

Figure 2. The H I column determined by 21 cm measurements versus the best fit H I column determined by a power-law fit to the quasars PSPC spectrum. The assumption that both values are equal, indicated by the straight line, is acceptable at the 8% level. Note, in particular, the two highest S/N objects, which deviate from the straight line by less than 1×10^{19} cm^{-2}. The agreement between the two measures of $N_{\rm H}$ indicates a lack of intrinsic cold gas absorption in quasars, and that H I/He I$\simeq$H/He in the ISM at high Galactic latitudes.

Figure 3. Comparison of the spectral energy distribution of all 23 quasars. Upper panel, the absolute luminosity. Middle panel, the luminosity of the 19 RQQ normalized to unity at $\log \nu = 14.25$ (the longest wavelength available for all objects). Note that PG 1626+554 is the only quasar where a steep α_x is associated with a strong soft excess, in all other objects a steep α_x is associated with a low 2 keV flux. Note also the two lowest spectra (PG 1001+054 and PG 1411+442), which appear to form a distinct group of "X-ray weak" quasars. Lower panel, as in middle panel for the four RLQ. PG 1425+267 may also be an "X-ray weak" quasar.

Figure 4. Correlations of line luminosity vs. X-ray luminosity. Open symbols are for radio-loud quasars. The Spearman rank-order correlation coefficient (r_S) and the two sided significance level (P_r) are indicated above each panel. The strongest correlation is displayed by the Hβ luminosity (which correlates even better with the optical and near IR luminosity). Note the position of the X-ray weak quasars. These appear to be fainter by factors of 10-30 in the X-ray than expected based on their $L_{\rm H\beta}$. This factor is similar to the deficiency seen in Fig.3.

Figure 5. Various correlations with α_x. Figs.5a-d: the emission line parameters which correlate strongly with α_x. Open symbols are for radio-loud quasars. The α_x versus Hβ FWHM corre-

lation is the strongest in our sample. Note that the X-ray weak quasars do not stand out in these correlations, they thus have the "right" spectral slope, but the "wrong" luminosity. Fig.5e: note the trend of increasing α_{ox} with increasing α_x, which indicates that a steep α_x tends to be associated with a weak 2 keV flux, rather than a strong 0.3 keV flux. The position of the x-ray weak quasars are marked. Fig.5f: the Y axis is a measure of $L/L_{\rm Edd}$ under some simplified assumptions, as described in §4.5.1

Figure 6. A composite optical-soft X-ray spectrum for the RQQ and RLQ in our sample. The three X-ray weak quasars, and PG 1114+445 which is affected by a warm absorber, were excluded from the composite. The composite uses $\langle\alpha_{ox}\rangle = 1.482$ (± 0.025) and $\langle\alpha_x\rangle = 1.69$ (± 0.07) for the RQQ, and $\langle\alpha_{ox}\rangle = 1.445$ (± 0.07) and $\langle\alpha_x\rangle = 1.22$ (± 0.16) for the RLQ. Note that despite the fact that RLQ are brighter at 2 keV, they are fainter at 0.3 keV. The Mathews & Ferland spectral shape assumes a hard X-ray power-law down to 0.3 keV and a very steep component below 0.3 keV. This spectral shape is inconsistent with the PSPC results. The far UV emission can be parameterized as a cutoff power-law. The spectrum shown here has $T_{\rm cut} = 5 \times 10^5$ K, which is close to the upper limit on $T_{\rm cut}$.

Figure 7. The observed energy distribution of some of the quasars in our sample versus two accretion disk spectra. The disk models are for a rotating black hole, $\alpha = 0.1$, and viscous stress $\propto \sqrt{P_{\rm gas} P_{\rm rad}}$ (the other parameters are indicated). Note that although significant soft X-ray flux can be produced by the thin disk models, the spectral slope is always much steeper than observed.

Figure 8. The observed α_{os} versus luminosity distribution, and the one expected from a distribution of accretion disks which conforms to the observed luminosity function. The observed range in α_{os} is much smaller than the expected range, indicating that the UV and soft X-ray emission mechanism are much better correlated than expected from thin disk models.

X-ray Spectral Survey of WGACAT Quasars, I: Spectral Evolution & Low Energy Cut-offs

Fabrizio Fiore[1,2,3], Martin Elvis[1], Paolo Giommi[3],
Paolo Padovani[4]
[1] Harvard-Smithsonian Center for Astrophysics
60 Garden St, Cambridge MA 02138
[2]Osservatorio Astronomico di Roma, Monteporzio (Rm), Italy
[3]BeppoSAX Science Data Center, Roma, Italy
[4]Dipartimento di Fisica, II Università di Roma

version: 1pm June 24 1997

ABSTRACT

We have used the WGA catalog of ROSAT PSPC X-ray sources to study the X-ray spectrum of about 500 quasars in the redshift interval 0.1–4.1, detected with a signal to noise better than 7. We have parameterized the PSPC spectrum in terms of two 'effective energy spectral indices', α_S (0.1-0.8 keV), and α_H (0.4-2.4 keV), which allows for the different Galactic N_H along the quasars line of sight. We have used these data to explore the questions raised by the initial PSPC high redshift quasar studies, and in particular the occurrence of low X-ray energy cut-offs in high redshift radio-loud quasars. We have also studied the emission spectra of a large sample of radio-loud and radio-quiet quasars and studied their differences.

We find that low energy X-ray cut-offs are more commonly (and perhaps exclusively) found in radio-loud quasars. Therefore the low energy X-ray cut-offs are physically associated with the quasars, and not with intervening systems, since those would affect radio-quiet and radio-loud equally. We suggest that photoelectric absorption is a likely origin of the these cut-offs.

The number of 'cut-offs' in radio-loud quasars significantly increases with redshift, rather than with luminosity. A partial correlation analysis confirms that α_S is truly anti-correlated with redshift at the 99.9% confidence level, indicating evolution with cosmic epoch, and not a luminosity effect. Conversely, for α_H the observed anti-correlation with redshift is mostly due to a strong dependence on luminosity.

We find marginal evidence for a flattening of α_H (P=4.5 %) going from z<1 to z=2, in radio-quiet quasars, in agreement with previous studies. On the other

hand, radio-loud quasars at z<2.2 show a 'concave' spectrum ($\alpha_H < \alpha_S$ by $\sim$0.2). This new result is consistent with the widespread suggestion that the X-ray spectrum of radio-loud quasars may be due to an additional component above that seen in radio-quiet quasars. However, it might also imply different processes at work in radio-loud and radio-quiet sources. At $z \gtrsim 2$ the average soft and hard indices are similar and both significantly smaller than at lower redshifts. This can be due to the soft component of radio-loud quasars being completely shifted out of the PSPC band at z> 2.

Subject headings: quasars — absorption, quasar — evolution, X-rays

1. Introduction

The ability of ROSAT to study fainter X-ray sources than ever before opened up the range of quasars that could be reached to span virtually the whole of their properties. High redshift objects (up to $z \approx 4$) became accessible in X-rays, and their spectrum was measured for the first time between 0.4 and 10 keV (in the quasar frame, Elvis et al 1994a). Unexpected low energy cut-offs, far larger than those expected due to absorption by our galaxy, were detected in several high-z radio-loud quasars (Wilkes et al. 1993, Elvis et al. 1994a). The obvious possibility was that these were caused by photoelectric absorption, either along the line of sight, or at the quasar. If the absorber were at the quasar, then the material could be nuclear, as in low redshift low luminosity objects (e.g. Elvis & Lawrence, 1985, and Elvis, Mathur & Wilkes 1995) or could be on the larger scale of the host galaxy or proto-galaxy. A tentative link with the highly compact 'GigaHertz Peaked' (GPS) radio sources suggested the latter and hence that X-ray astronomy offered a new probe of early galaxy conditions.

Targeted ROSAT studies of high redshift quasar X-ray spectra are, however, limited to a dozen or so objects. Within the more than 3000 ROSAT PSPC pointings (covering about 10 % of the sky) lie more than 50,000 sources (White, Giommi & Angelini 1995, Voges et al 1994). Out of these, a sample of several hundred quasar X-ray spectra can be readily compiled for the first time, thanks to the release of the two source catalogs, WGACAT (White, Giommi & Angelini 1995) and ROSATSRC (Voges et al 1994). We have used these data to explore the questions raised by the initial PSPC high redshift quasar studies. As an additional benefit of this program we are able to study the emission spectra of a large sample of radio-loud and radio-quiet quasars and study their differences.

We investigate the connection between low energy X-ray cut-offs and the radio and optical spectra of these quasars in a companion paper (Elvis et al. 1997, Paper II). A

later paper (Nicastro et al. 1997) will discuss a sub-sample of quasars selected to have the typical colors produced by absorption features imprinted on the X-ray spectrum by an ionized absorber along the line of sight.

We use a Friedman cosmology with H_0=50 km s^{-1} Mpc^{-1} and $\Omega = 0$ throughout this paper.

2. The Sample

Quasars were selected by cross-correlating the first revision of the WGA catalog (White, Giommi & Angelini 1995) with a variety of optical and radio catalogs, including the Veron-Cetty & Veron (1993) and Hewitt & Burbidge (1993) quasar catalogs, and the 1 Jy (Stickel et al. 1994) and S4 (Stickel & Kühr 1994) radio catalogs. Uncertain classifications and border line objects have been also checked in the Nasa Extragalactic Database (NED). [1] All the objects selected have optical spectra dominated by nonstellar emission and all show broad emission lines.

The maximum radius adopted for identifying cross-correlation candidates was one arcminute. The resulting distribution of X-ray/optical offsets is shown in Figure 1. The mean offset is $\simeq$ 18 arcsec, while the median one is $\simeq$ 13 arcsec, in agreement with the estimated errors on the positions of the WGA sources (White et al. 1995). Potential misidentifications through chance co-incidences were addressed by shifting the X-ray positions by various amounts several times, and repeating the cross-correlations. Using these randomized X-ray positions establishes the chance co-incidence rate to be small. The number of spurious X-ray/optical associations is at maximum 2, i.e. less than 0.5% of the whole sample (see below).

We excluded from the sample:

1. observations of sources with a quality flag in the WGA catalog < 5 (corresponding to problematic detections);

2. observations of sources with a signal to noise ratio in the 0.1-2.4 keV energy band less than 7 (to ensure reasonable X-ray color determinations);

---

[1]The NASA/IPAC Extragalactic Database (NED) is operated by the Jet Propulsion Laboratory, California Institute of Technology, under contract with the National Aeronautics and Space Administration.

3. observations of quasars located at an off-axis angle larger than 45 arcmin, (to avoid large systematic errors due to the uncertainties in the PSPC calibration near the edge of the field of view);

4. fields with a Galactic N_H along the line of sight higher than 6×10^{20} cm^{-2} (to ensure good low energy signal to noise);

5. quasars with z< 0.1 (to eliminate the low luminosity Seyfert galaxies in which absorption is common, e.g. Lawrence & Elvis 1982).

We are then left with 453 quasars for which fluxes in three bands, and so two X-ray colors ("soft" and "hard"), can be derived. This is the largest sample of quasars for which homogeneous X-ray spectral information is available. We used only one observation for each quasar. When more than one observation was available for a quasar we chose the one with the highest signal to noise ratio.

Of these quasars 202 have a radio measurement in the literature, and 167 of those are radio-loud according to the usually adopted definition $R_L = log(f_r/f_B) > 1$, with f_r radio flux at 5 GHz and f_B the B-band flux (Wilkes & Elvis 1987; Kellermann et al. 1989; Stocke et al. 1992). This translates into a (rest-frame) value of the radio to optical spectral index, $\alpha_{ro} > 0.19$. The sample includes 87 Flat Spectrum Radio Quasars ($\alpha_r < 0.5$), the majority of which are discussed by Padovani et al (1997). Steep Spectrum Radio Quasars account for 62 sources. Note that this flat/steep classification is based mostly on the radio spectrum at only 2 or 3 frequencies. Quasars with complex radio spectra (e.g. GigaHertz Peaked Spectrum (GPS) Sources) could appear in either class. This classification also does not distinguish compact steep spectrum (CSS) radio sources from extended ones. For 18 radio-loud quasars we could find radio measurements at one frequency only, and therefore their radio spectral index is unknown. We assumed $\alpha_R = 0.5$ in calculating α_{ro}. Most of the quasars without radio measurement are likely to be radio-quiet (e.g. Ciliegi et al., 1995) so we include them in the radio-quiet sample, making for 286 radio-quiet quasars in the sample.

In the WGACAT there are another 35 quasars with Galactic $N_H > 6 \times 10^{20}$ but passing all other above points, for which we derive a "hard" color only. Of these 28 are radio-loud.

The redshift distributions for radio-quiet quasars and radio-loud quasars is shown in figure 2. At $z \lesssim 1$ the number of radio-quiet objects is higher than that of radio-loud, due to the higher volume density of radio-quiet quasars. By $z \gtrsim 2$ however, the number of radio-loud objects is higher than that of the radio-quiet objects, due to the higher L_X/L_{opt} of radio-loud quasars.

3. Effective X-ray Spectral Indices

The WGA catalog provides raw count rates in three energy bands: 0.1-0.4 keV (soft band, S), 0.40-0.86 keV (mid band, M) and 0.87-2 keV (hard band, H) for each entry. The count rates can be combined to form a 'softness ratio' (SR=S/M) and a 'hardness ratio' (HR=H/M). To allow for the effect of the varying Galactic absorption from source to source these softness and hardness ratios can be converted to 'effective spectral energy indices', α_S (0.1-0.8 keV), and α_H (0.4-2.4 keV), assuming the Galactic N_H as derived from 21 cm measurements (Stark et al 1992, Shafer et al, private communication, Heiles & Cleary 1979),"Wisconsin" cross-sections (Morrison & McCammon (1983) and solar abundances (Anders & Ebihara 1982), and using the PSPC calibration.

3.1. Correction for the instrumental point spread function

In converting the three count rates into effective spectral indices, corrections must be applied for the instrumental point spread function (PSF), to take into account the different fraction of counts lost outside the detection region in each energy band. The total PSPC PSF includes two main components: the mirror PSF and the PSPC detector PSF (Hasinger et al 1992a). The mirror PSF is energy independent, and dominates the total PSF at off-axis angles greater than about 20 arcmin. At these large off-axis angles a small detection region loses flux but does not significantly alter the spectral shape.

The detector PSF is, instead, highly energy dependent, and dominates the total PSF at small off-axis angles. Using a small detection region for an off-axis angle < 20 arcmin can strongly alter the spectral shape, predominantly at low energies. (The detector FWHM$\propto E^{-0.5}$). The method used in the WGA catalog to estimate the source count rates uses the counts detected in a box whose size optimizes the signal to noise ratio for each source. For relatively weak sources near the field center, this optimum box size is small, and the number of soft photons lost is greater than that of medium or hard energy photons, giving rise to an artificial reduction of the spectrum at low energies, which in turn can lead to an underestimation of α_S of up to 0.2-0.3.

We corrected the count rates in the three bands for both mirror and PSPC PSF effects. We used the analytical approximations for the energy and off-axis angle dependence of the PSF provided by Hasinger et al (1992b).

This method of estimating spectral indices is similar to the de-reddening procedure used in optical photometry, and is quite robust, with typical systematic uncertainties on

α_H smaller than 0.1 (as shown, for example, by Padovani & Giommi 1996 or Ciliegi & Maccacaro 1996). It is particularly suitable for handling large samples of objects (Giommi et al., in preparation) e.g. for the determination of the X-ray spectral index distributions.

However, a systematic uncertainty is present in the spectral indices estimates, because the magnitude of the PSF correction depends on the intrinsic source spectrum. To estimate the magnitude of this uncertainty we calculated five series of α_S and α_H for a grid of assumed source spectra: for the average value for high Galactic latitude line of sight ($N_H = 3 \times 10^{20}$ cm^{-2}) we used $\alpha_E = 1$, $\alpha_E = 1.5$ and $\alpha_E = 2.5$; for the mean value of energy spectral index (α_E=1.5) we used low ($N_H = 10^{20}$ cm^{-2}) and high ($N_H = 10^{21}$ cm^{-2}) absorption values. We then calculated the differences between the α_S and α_H calculated for each pair of α_E and N_H and those calculated for $\alpha_E = 1.5$ and $N_H = 3 \times 10^{20}$ cm^{-2}. The differences in α_H were always smaller than 0.05 and those in α_S were always smaller than 0.15. We therefore use these values as systematic uncertainties in the evaluation of these parameters.

3.2. PSPC background

The WGACAT count rates are not background subtracted. Therefore, another possible source of error in the evaluation of the PSPC spectral indices is the PSPC background in the three WGACAT bands. The PSPC background has been studied in great detail by Snowden et al (1992, 1994, noncosmic background, and 1995, 1997 diffuse, cosmic X-ray background) using ROSAT All Sky Survey (RASS) data and pointed observation data. The energy band which shows, by far, the highest background at high Galactic latitude is the 0.1-0.28 keV range, which spans most of the SOFT band defined in WGACAT (0.1-0.4 keV). We now analyze the effect that a wrong or absent background subtraction in the SOFT band can have on the soft energy index α_S.

The cosmic background in the SOFT band is highly spatially variable, with large regions of maxima of about 0.0015 counts s^{-1} arcmin^{-2} at high Galactic latitudes ($|b| > 30$) and minima of 0.0003 counts s^{-1} arcmin^{-2}. Long-Term enhancements are difficult to identify and model in pointed observations. They mainly affect the low frequency part of the spectrum, E< 0.28 keV, where their contribution can even be as high as 0.001 counts s^{-1} arcmin^{-2}. We adpot a conservative value for the total SOFT band background of 0.003 counts s^{-1} arcmin^{-2}.

The typical box-side of the WGACAT extraction regions is 0.3-0.8 arcmin for off-axis angles smaller than 20 arcmin and 1-3 arcmin for off-axis angles between 20 and 45 arcmin, where the lower limits apply to the faintest sources. Such extraction regions, together with the above background rate would give a few counts in the low energy band in typical exposures of 1000-10000 sec for sources detected in the central 20 arcmin, and a few tens of

counts for sources detected in the outer PSPC region.

Let us assume the case of a faint (close to our limit of 7 in signal to noise ratio) and strongly cutoff source, whose counts in the SOFT band are a few, comparable with the background contribution, and 15-30 in the MEDIUM band. In this case the upper limit on the slope between the SOFT and MEDIUM energy bands differs from the slope we would measure neglecting background subtraction by ~ 0.5. This compares with a typical statistical error in α_S of 0.5-0.7 for such faint sources and with a systematic uncertainty of 0.15. We conclude that the small extraction regions used in the WGACAT means that background is not a significant problem, even for the SOFT band count rate of our faint sources. As a result we did not subtract background in the evaluation of the effective spectral indices α_S and α_H.

To investigate the robustnes of this assumption, we searched for correlations between the soft and hard effective spectral indices and (1) the size of the extraction region, (2) the off-axis angle, and (3) the source count rate. Any correlations could be evidence that neglecting the background was causing problems. In no case did we find significant correlations. We conclude that neglecting the background subtraction does not strongly affect or bias our results.

There are other two sources of uncertainties in the spectral indices estimates: first, quasars located near the PSPC rib structures can suffer a preferential loss of soft photons. We inspected the original ROSAT images for each source that appeared to have unusually low soft band counts and rejected those that might have been so affected. Second, the spectral indices estimates from hardness ratios may be significantly different from the results of a proper spectral fit to the full PHA spectrum, in presence of a curvature in the intrinsic spectrum, because of the skewness induced in the broad energy bands used to construct the hardness ratios. For all these reasons the effective spectral indices α_S and α_H should not be regarded as a measure of the true emission spectral indices. They should rather be regarded as a rough estimation of the "average" soft and hard spectral shapes. They are the soft X-ray analogs of (U-B), (B-V) colors, for which multiple physical interpretations are possible. We will use α_S as an indicator of a possible low energy cut-off.

3.3. Effective Spectral Indices and Quasar Properties

The radio-quiet and radio-loud quasars α_S and α_H are plotted against each other in figure 3a,b. In the radio-loud plot flat spectrum radio sources are identified by circles, and steep spectrum sources by squares. High redshift quasars (z>2.2) are shown with filled symbols. The range of α_S and α_H are large and so the different parts of the diagram

correspond to radically different spectral shapes. These are illustrated with three-point spectra in figure 3. For the purpose of this paper we are most interested in those for which a low energy cut-off is indicated (lower center of figure 3).

To study these features more closely we divided the quasars into four redshift bins: 0.1-0.5; 0.5-1; 1-2.2; and z> 2.2. Table 1 gives the average spectral indices (α_S, α_H) and their dispersions $(\sigma(\alpha_S), \sigma(\alpha_H))$ in these four redshift bins for both radio-quiet and radio-loud quasars. The typical statistical uncertainties on α_S and α_H are ± 0.2, the systematic uncertainty is at most ± 0.15 for α_S and ± 0.05 for α_H, so the measured dispersions are not strongly affected by these uncertainties.

Table 1: **Quasars Average Spectral Indices & Cut-off statistics**

z bin	N	α_S	$\sigma(\alpha_S)$	N	α_H	$\sigma(\alpha_H)$	no. cut-off	fraction
Radio-Quiet Quasars								
0.1–0.5	136	1.73	0.48	141	1.62	0.51	7	0.051
0.5–1.0	66	1.68	0.36	67	1.67	0.51	3	0.045
1.0–2.2	72	1.67	0.38	72	1.51	0.49	1	0.014
>2.2	12	1.54	0.26	13	1.32	0.69	0	0
Radio-Loud Quasars								
0.1–0.5	34	1.49	0.52	41	1.20	0.63	1	0.029
0.5–1.0	45	1.30	0.62	51	1.18	0.48	2	0.044
1.0–2.2	70	1.37	0.52	78	1.13	0.51	4	0.057
>2.2	18	0.89	0.71	25	0.89	0.60	7	0.389
Flat Spectrum Radio Quasars								
0.1–0.5	9	1.38	0.30	14	1.32	0.38		
0.5–1.0	26	1.24	0.73	30	1.11	0.51		
1.0–2.2	40	1.35	0.50	43	0.99	0.46		
>2.2	12	0.74	0.75	17	0.78	0.60		
>0.1	87	1.24	0.63	104	1.04	0.51		
Steep Spectrum Radio Quasars								
0.1–0.5	19	1.52	0.62	21	0.96	0.65		
0.5–1.0	14	1.29	0.44	16	1.23	0.39		
1.0–2.2	24	1.40	0.58	28	1.12	0.46		
>2.2	5	1.15	0.58	7	1.33	0.60		
>0.1	62	1.37	0.56	72	1.14	0.56		

3.3.1. Radio-Loud vs. Radio-Quiet

The mean and dispersion of α_H and α_S for the radio-quiet quasars are $(1.59, 0.52)$ and $(1.69, 0.41)$; those of radio-loud quasars are $(1.13, 0.55)$ and $(1.32, 0.59)$. The difference of $\sim$0.5 in α_H agrees with the widespread finding that radio-loud quasars have flatter X-ray spectra than radio-quiet quasars (e.g. Elvis & Wilkes 1987, Laor et al., 1994, Laor et al., 1997, Schartel et al., 1996a).

For radio-quiet quasars the distribution of α_S is consistent with that of α_H in all redshift bins. In the last redshift bin there are only 12 quasars (see Table 1), and only three at z> 2.5, and therefore the test is not very stringent for this redshift interval. This uniformity suggests a single emission mechanism dominating the whole ROSAT band (c.f. Laor et al., 1997), at least for redshifts smaller than about 2.

Radio-loud quasars, instead, have α_H smaller than α_S by $\sim$0.2 (i.e. a concave spectrum) in the low redshift bins (z<2.2). The Kolmogorov-Smirnov probability of α_S being drawn from the same distribution function as α_H, is 5.0 % for redshifts 0.1−0.5, 22 % for redshifts 0.5−1.0 and 0.14 % for redshifts 1.0−2.2. This new result could be interpreted in terms of an additional component in the spectrum of radio-loud quasars above that seen in radio-quiet quasars (as suggested earlier by e.g. Wilkes & Elvis 1987). However, it may also imply different processes at work in radio-loud and radio-quiet quasars, (as also suggested by Laor et al., 1997). To disentangle these two possibilities a careful analysis of the optical to X-ray Spectral Energy Distribution of WGACAT quasars is needed. This is beyond the scope of this paper and will be addressed in a forthcoming paper.

We have computed the mean α_S and α_H for the two samples of flat and steep radio spectrum quasars. These are reported in Table 1. Although both distributions of α_S and α_H for the steep and flat radio quasars are consistent with being drawn from the same distribution function (using a K-S test), the mean α_S of steep radio spectrum quasars is steeper than that of flat radio spectrum quasars (at the 90 % confidence level). The mean α_H of the two samples of quasars is on the other hand very similar. Redshift bins 0.1-0.5 and z> 2.2 are populated by too small a number of flat radio spectrum and steep radio spectrum quasars respectively to allow a statistically significant comparison. In the other two redshift bins the distributions of α_H and α_S of the two samples are consistent with each other.

The dispersion in α_H and α_S is large for both radio-quiet and radio-loud quasars. The radio-loud dispersion in α_S is larger than that of radio-quiet quasar at a confidence level of 96 %. Emission or absorption mechanisms that produce more varied outputs seems to be needed for radio-loud quasars.

From figure 3 it appears that the number of radio-loud quasars with $\alpha_S < 0.5$ is much larger than the number of radio-quiet with $\alpha_S < 0.5$, especially at high z (solid symbols).

This is the sense of the change in α_S to produce low energy cut-offs, as would be produced by photoelectric absorption.

We compare the distribution of radio-loud and radio-quiet indices about their respective mean α_S (figure 4). By offsetting from the mean of each group we remove the difference in the group means discussed above. Figure 4 shows the broader dispersion of α_S for radio-loud quasars. It also shows a population of radio-loud quasars with smaller α_S, i.e. quasars that show low energy cut-offs. This tells us with high confidence that the cut-offs are not due to intervening material. Intervening material would not 'know' whether a background quasar was radio-loud or radio-quiet. The cause of the cut-offs must be physically associated with the quasar in some way.

3.3.2. Dependence on Redshift

To quantify the differences with redshift and study their evolution we plot α_H and α_S versus redshift for radio-quiet and radio-loud quasars in figures 5a,b and 6a,b respectively. There is no strong evidence of evolution of either α_H or α_S with redshift for radio-quiet quasars. Again the small number of radio-quiet quasars with z>2 does not allow us a strong conclusion to be drawn for high redshift objects. For the bins 0.5<z<1 and 1<z<2.2 the probability that the two distributions of α_H are draw from the same distribution function is marginally unacceptable (P=4.5%), in agreement with previous studies (Schartel et al 1996b).

On the other hand radio-loud quasars show strong changes in both α_S and α_H for $z > 2.2$, in the sense that both indices are smaller than in lower redshift bins. We ran a Kolmogorov-Smirnov test between the distributions of spectral indices in each possible pair formed with the four redshift bins. The distributions of α_S and α_H at z< 2.2 are all consistent with each other. Only the $z > 2.2$ bin shows significant differences from the others, for both α_S and α_H. Table 2 gives the percentage probability that the spectral index distributions of α_S and α_H in two redshift bins are drawn from the same distribution function.

Table 2: **Kolmogorov-Smirnov test for Radio Loud Quasars**

		α_S		
	0.1–0.5	0.5–1.0	1.0–2.2	> 2.2
>2.2	3.0	5.8	2.1	–
		α_H		
>2.2	0.10	4.1	0.16	–

Some caution is required however. In flux limited samples redshift and luminosity are often degenerate, so that it is hard to distinguish the effects of one from the other. The apparent trend with redshift discussed above may thus be induced by a correlation with luminosity (figure 7a). We tested for this degeneracy by selecting a sub-sample of only the high $\log(L_{opt})$ (>32) quasars. The correlation between α_S and z for this sample is still very good (figure 7b, linear correlation coefficient $r = -0.46$, which, for 43 points, corresponds to a probability of 99.8%). On the other hand, the correlation between α_H and z for the high luminosity, high redshift quasar is not significant, $r = -0.17$ (probability of 72%).

To better disentangle the luminosity/redshift dependence of α_S and α_H we also performed a partial correlation analysis (e.g., Kendall & Stuart 1979) on the whole radio-loud sample. While α_S is anti-correlated with redshift even subtracting the effect of the optical luminosity ($P \simeq 99.9\%$), in the case of α_H no correlation with redshift is left once the luminosity dependence is subtracted out ($\simeq 48\%$). On the other hand, excluding the redshift dependence, we find that α_H is anti-correlated with luminosity at the 99.2% level.

We conclude that the flat α_S, unlike α_H, are truly more common at high redshifts, and so are an evolutionary, or cosmological, effect.

3.3.3. Low Energy Cut-offs

The high incidence of low energy cut-offs at high redshifts can be made clearer by defining a sample of 'candidate cut-off' objects using α_S and then examining the fraction that occur among both radio-loud and radio-quiet quasars as a function of redshift.

The change in index of radio-loud quasars can be seen in figure 6b as due to a population of radio-loud quasars with a soft spectral index significatively smaller than the average and smaller than the hard spectral index. (Although there are also a few radio-quiet quasars with exceptionally flat α_S, figure 5b). These small α_S quasars are 'cut off' in their low energy spectrum compared with an extrapolation of the hard spectrum.

We select 'candidate' low energy cut-off quasars using three criteria. (1) $\alpha_S < \alpha_H$; (2) $\alpha_S < 0.5$ selects all the high redshift radio-loud candidates apparent in figure 6b. (3) Lower redshift radio-loud and all radio-quiet candidates require a more careful selection since their mean α_S are different. We use the criterion that they have α_S smaller than the average by at least 0.75. For radio loud quasars the average α_S at z< 2.2 is 1.32 and therefore we selected quasars with $\alpha_S < 0.58$ in this redshift interval. For radio-quiet quasars there is no evidence for a change in the average α_S with z and therefore we selected the quasars with $\alpha_S < 0.94$ (the average α_S is 1.69). These criteria select 10 radio-quiet and 14 radio-loud 'candidate'

cut-off quasars. Table 3 gives the optical or radio names, redshift and optical luminosity of these objects.

The distribution of 'candidate' cut-offs is striking. Table 1 gives the total number of quasars, the number of "candidate" cut-off quasars and its fraction in each redshift bin, while figure 8 shows the fraction of 'candidate' cut-off quasars as a function of z for both quasar samples. The fraction of "candidate" cut-off quasars among the 18 radio-loud objects at z> 2.2 is significantly different from that at z< 2.2 (probability of 0.002 %, using the binomial distribution). For radio-quiet objects the absence of cut-offs among the 12 quasars at z> 2.2 is consistent with the cut-offs distribution at lower redshift (probability of 50 %). In turn, the probability of finding zero 'candidate' cut-off quasars among the n=12 radio quiet quasars at z> 2.2, assuming a frequency of cut-offs similar to that of radio loud quasars at the same redshift, is 0.3 %.

This strongly suggests a difference in the 'candidate' cut-off quasar distribution with z between radio loud and radio quiet objects. We calculated, using the Fisher exact probability test (e.g. Siegel 1956), the probability that the two "candidate" cut-off samples differ in the proportion with which they are distributed in redshift, e.g. below and above a given redshift. For z=2.2 the difference is significant at the 98.4% level.

4. X-ray Spectra

A flatter α_S at high redshift than at low redshift can be due to at least three effects: (a) the redshifting of a soft component contributing at the emission below $\approx 1-3$ keV (quasar frame) out of the observed energy range for $z \gtrsim 2$; (b) evolution of the emission spectrum; (c) a cut-off due to low energy absorption becoming more frequent at $z \gtrsim 2$. A simple color analysis cannot distinguish between these three possibilities. A two parameter spectral fit can discriminate more strongly, and is possible for the quasars with a few hundreds detected PSPC counts. This section investigates such fits.

Most of the quasars in the sample do not have published PSPC spectral fits. We extracted the full pulse height spectrum for each of the quasars in the sample from the appropriate event files in the ROSAT archive. We used standard extraction criteria (see e.g. Fiore et al. 1994, Elvis et al 1994a). Table 4 gives the total counts in the 0.1-2.4 keV energy band, the exposure and the off-axis angle for these quasars. All the radio-loud quasars were observed on-axis and were the target of their observation. All the radio-quiet quasars (except RXJ16331+4157) are instead serendipitous sources in ROSAT fields. With one exception (SBS0945+495) the radio-quiet quasars all lay within the inner PSPC rib ($r = 18$ arcmin), where the calibration is most accurate.

We then fitted the spectra with a power law model with low energy absorption (at z=0). We made four fits for each quasar: We first let the column density be free to vary, and then kept it fixed to the Galactic (21 cm) value along the line of sight. Similarly, we let the power law spectral index be free to vary, and then kept it fixed to the mean value of α_H at the redshift of the quasar (Table 1). The results are given in Tables 5 and 6 for each quasar sample. Listed are: the best fit parameters, the χ^2, and the probability that the improvement in χ^2 between the fits with free N_H and N_H fixed to the Galactic value is significant (calculated using the χ^2 distribution with 1 dof for the $\Delta\chi^2$).

From Tables 5,6 we see that the evidence of a cut-off is very robust ('Class A') for four radio-loud quasars (PKS2126−158, PKS0438−436, 3C 212, and 3C 207), Probability $\gtrsim$99.9%. For another four radio-loud quasars (S4 1745+624, PKS2351−154, S4 0917+449 and PKS1334−127) the probability of a cut-off is $\gtrsim$95% ('Class B'). For S4 0917+624 the probability for a cut-off is $\gtrsim$92% ('Class C'). Furthermore three quasars (3C219, PKS0537-286 and S4 0636+680) have very flat energy index, much flatter than the average for radio loud quasars at those redshifts, if we insist on only Galactic absorption (we also call these 'Class C'). Excess absorption, similar to that required in the better spectra, readily produces a normal energy index. Two radio-loud quasars do not show any evidence for a cut-off (4C71.07 and PKS1442+101). The first is a famous blazar, detected by EGRET in the GeV energies (e.g. von Montigny et al 1995) and therefore beaming is important. The second is often classified as a Compact Steep Radio Spectrum quasar (e.g. DallaCasa et al 1995). The total number of cut-off radio loud quasars is therefore eight, with three more objects likely to be cut-off quasars.

By contrast, in radio-quiet quasars we have a strong evidence for a cut-off in only one case out of 289 (PHL6625, Probability > 99.9%). PHL6625 lies just 4.6 arcmin from the position of the low redshift galaxy NGC 247. The cut-off in PHL6625 may well be due to absorption in gas associated to NGC247 (Elvis et al., 1997). Two other radio quiet quasars MS03363-2546, US3333) have a probability for a cut-off $\gtrsim$95%. US3333 is included in the area of the sky already surveyed by the NVSS (Condon et al., in preparation) but has not been detected. The upper limit on the radio flux ($f_r < 2.5$ mJy) puts an upper limit of 0.2 on α_{ro}, very close to the threshold of 0.19 that we use to divide radio-loud and radio-quiet quasars. More sensitive optical and radio observation are then needed to assess the nature of this source. MS03363-2546 is not detected in radio by Stocke et al 1992. The limit on the radio flux assures that this quasar is a truly radio-quiet source. The origin of the cut-offs of MS03363-2546 and US3333 is unknown and deserves follow-up studies. The probability of finding by chance the detected number of cut-off radio quiet quasar at z< 2.2, assuming a frequency of cut-offs similar to that of radio loud quasars is 1.3 %.

5. Comparison with previous results

Results on the ROSAT pointed observations of the quasars in Table 3 have been published by Elvis et al (1994a, PKS0438-436, PKS2126-158, S40636+680), Elvis et al (1994b 3C212), Maraschi et al (1995, PKS1334-127), Brunner et al (1994, 4C71.07), Buhler et al. (PKS0537-286), Bechtold et al. (1994, PKS1442+101 and S41745+624).

The spectral fitting results in Table 6 generally agree well with the results presented in the above papers. Maraschi et al (1995) use a Galactic N_H higher than the one we adopted (from Stark et al 1992) by about 1.6×10^{20} cm^{-2}, and as a result conclude that there is little evidence for absorption in this source.

Some of the quasars in Table 3 have also been observed by ASCA (Siebert et al., 1996 PKS0537-286, Cappi et al., 1997, PKS0438-436, PKS0537-286, 4C71.07, PKS2126-158). The results found by these authors are consistent with those obtained from the ROSAT observations with the exception of 4C71.07, for which Cappi et al. (1997) report significant intrinsic absorption (of about 8×10^{20} cm^{-2}). The comparison between the ROSAT and the ASCA data implies a variation in the absorber column density on a time-scale of less than 2.6 years in this source. Cappi et al. (1997) discuss in detail the possibility that low energy absorption in addition to the 21 cm value in their sample of high redshift quasars may be due to molecular gas. For the four quasars in common between their and our sample they find no strong evidence for Galactic molecular gas absorption. We note here that our limit on the Galactic (21cm) N_H effectively excludes low Galactic latitude sources from our sample, thus minimizing the probability for a contamination from Galactic molecular clouds, which are strongly concentrated toward the Galactic plane. The CO survey by Blitz, Magnani & Mundy (1984) finds that molecular gas is uncommon at high Galactic latitudes. The only quasar known to be affected by molecular gas absorption (NRAO140, Marscher 1988, Turner et al., 1995) lies at low Galactic latitude, and was excluded from our sample because it has a Galactic (21 cm) N_H of 1.4×10^{21} cm^{-2}. Furthermore, de Vries, Heithausen & Thaddeus (1987) found that high Galactic latitude molecular clouds differ from the Galactic plane clouds so that their CO-to-H_2 conversion factor is significantly smaller: $\sim 0.5 \times 10^{20}$ instead of $\sim 2 - 4 \times 10^{20}$ molecules cm^{-2}(K^{-1} km^{-1}s)$^{-1}$ (Combes, 1991). This would reduce the additional hydrogen column density implied by any CO emission by a factor $\sim$6.

The evolution of the quasar X-ray spectrum has also been studied by three groups: Schartel et al (1996a) who used a sample drawn from the RASS containing all quasars with $M_V < -23$ and more than 80 RASS counts; Schartel et al (1996b) used the Large Bright Quasar Sample (LBQS) quasars observed during the RASS (using both detections and non-detections); Puchnarewicz et al (1996) used AGNs identified in the ROSAT International

X-ray/Optical Survey (RIXOS).

All the radio-quiet objects in Schartel et al (1996a) are at z< 0.5, while radio-loud objects are detected up to z=2.5. The indices of the radio-quiet objects are fully consistent with those of the WGACAT quasars. The PSPC spectral indices of radio-loud objects show a significant flattening above z$\sim$ 1, which is interpreted by Schartel et al in terms of a selection effect and/or a redshift effect, if quasar spectra are not simple power laws (but rather have a concave shape). In the WGACAT quasars we see little change in both α_S and α_H from 0.1<z<2, most of the evolution being confined at redshifts higher than $\sim$ 2.

On the other hand most of the LBQS objects studied by Schartel et al (1996b) are radio-quiet quasars. Schartel et al (1996b) find a marginal (2 sigma) evidence for a flattening of LBQS spectra at z$\gtrsim$1.5. This result is consistent with our findings (see Section 3.1.2 above) based on WGACAT quasars. In particular the slopes reported by Schartel et al (1996b) agree well with those in Table 1. Again, the study of the evolution of the spectrum of radio-quiet quasars is limited by the fact that high redshift radio-quiet quasars are faint and not easy to observe with ROSAT.

Puchnarewicz et al (1996) find a mean energy index significant flatter than those obtained from the WGACAT quasars. They also find no evidence for a change in α_X with z. The flat average slope reported by Puchnarewicz et al could be due to the selection criteria used to define the sample (a flux limit of 3×10^{-14} erg cm^{-2} s^{-1} in the ROSAT 0.4-2 keV 'hard band') which favors the inclusion in the sample of flatter AGN. Furthermore, the correlation between the optical to X-ray index with the X-ray spectral index (like the one found in Seyfert galaxies and low redshift quasars, see eg. Walter & Fink 1993, Fiore et al. 1995) can select preferentially flat X-ray quasars when considering a strictly X-ray selected sample (low optical to X-ray index). We also note (from their figure 3) that in their sample there are a few quasars with a very flat spectral index, possibly due to absorption, which tend to lower the average index. These quasars have a red optical continuum, strengthening the evidence for absorption in these cases.

Also the fraction of radio-loud AGN in the RIXOS is unknown. The energy index Puchnarewicz et al (1996) find at 2<z<3 is similar to the index we find in the same redshift interval for radio-loud objects. At low redshift the radio quiet population should dominate in number (because of its much larger volume density). However, we note that a similar X-ray flux limited survey (Schartel et al 1996a) is completely dominated by radio loud objects at z$\gtrsim$0.5, since radio-loud objects are brighter in X-rays than radio quiet (e.g Zamorani et al 1981, Green et al 1996). Therefore the RIXOS indices, at least at high redshift, could be dominated by the radio-loud population.

6. Conclusions

We have studied the 2 color X-ray spectra of a sample of about 167 radio-loud quasars and 286 'bona fide' radio-quiet quasars. Radio-loud quasars cover the whole redshift space from 0.1 to 4 rather uniformly, while there are only three radio-quiet quasars at z> 2.5, against 12 radio-loud quasars at the same redshifts. Any conclusion on radio-quiet quasars then apply to $z \lesssim 2$ only.

Concerning the low energy cut-off we have established:

1. Low energy X-ray cut-offs are more commonly (and perhaps exclusively) associated with radio-loud quasars. Detailed spectral fits allow us to add, with some confidence, that photoelectric absorption is a likely origin of the 'low energy cut-offs'. The conclusion is that *low energy X-ray cut-offs are associated with the quasars*, and not with intervening systems, since those would affect radio-quiet and radio-loud quasars equally.

2. Among radio-loud quasars those at high redshift have a lower mean α_S than those at low z (P=0.04%), with many lying in the X-ray 'cut-off' zone. Detailed spectral analysis of all candidate cut-off quasars show four robust cut-off detections at redshift higher than 2.2. The probability that the fraction of cut-off quasars among the 18 objects at z> 2.2 is similar to that of radio-loud quasars at z< 2.2 is very small, about 0.002 % (using the binomial distribution). This indicates that cut-offs were more common in the past than they are now. I.e. *the X-ray cut-offs show evolution with cosmic epoch.*

3. The degeneracy between redshift and luminosity found in flux limited samples of quasars was tested by using a partial correlation analysis. We found that while α_S is truly anti-correlated with redshift at the 99.9% confidence level, in the case of α_H the observed anti-correlation with redshift is mostly due to a strong dependence on luminosity. Therefore, the cut-offs are an evolutionary, not a luminosity, effect.

Concerning the emitted X-ray spectra of quasars we have established:

4. The distribution of α_S of radio-quiet quasars is consistent with that of α_H for $z \lesssim 2$. This uniformity suggests a single emission mechanism dominating the whole ROSAT band (c.f. Laor et al., 1997) up to a redshift of about 2. We find a marginal evidence for a flattening of α_H (P=4.5 %) going from z<1 to z=2, in agreement with previous studies (Schartel et al 1996b). This can be due to a selection effect even if quasar X-ray spectra are simple power laws, because at high redshift the steepest (and therefore

faintest) sources would not be detected. However, it is well known that ROSAT PSPC 0.1-2 keV spectral indices of Seyfert 1 galaxies and low redshift radio-quiet quasars are much steeper than those observed above 2 keV (e.g. Walter & Fink 1993, Fiore et al 1994, Laor et al 1997). If the spectrum of these AGN is made up of two distinct components that are equal at a typical energy E_0, the flattening of α_H at z> 1 would suggest that E_0 lies in the range 2-4 keV (quasar frame).

5. Radio-loud quasars at z<2.2 show a 'concave' spectrum ($\alpha_H < \alpha_S$ by $\sim$0.2). Both indices are much flatter than those of radio-quiet quasars. This new result is in line with the suggestion of Wilkes & Elvis (1987) that the X-ray spectrum of radio-loud quasars may be due to an additional component above that seen in radio-quiet quasars. However, it may also imply different processes at work in radio-loud and radio-quiet sources (as recently suggested by Laor et al., 1997).

   At $z \gtrsim 2$ the average soft and hard indices are similar and both significatively smaller than at lower redshifts. This could be due to the soft component of radio-loud quasars being completely shifted out of the PSPC band at z> 2. Most z> 2 radio-loud quasars in our sample have flat radio spectra. Padovani et al. (1997) suggested that these quasars are analogs to LBL BL Lacs, that is BL Lac objects with maximum energy emission in the IR-Optical band. Their high energy radiation should then be dominated by inverse Compton emission. At z> 2 we are then likely seeing pure inverse Compton emission. At lower redshift the ROSAT PSPC band could sample a mixture of inverse Compton emission, the tail of the Synchrotron component peaking in the infrared and thermal emission from the hypothesized accretion disk.

The radio and optical properties of the quasars with low energy X-ray cut-offs will be discussed in more detail in a companion paper (Elvis et al. 1997).

This research has made us of the BROWSE program developed by the ESA/EXOSAT Observatory, NASA/HEASARC, and the NASA/IPAC Extragalactic Database (NED) which is operated by the Jet Propulsion Laboratory, California Institute of Technology, under contract with the National Aeronautics and Space Administration.

REFERENCES

Anders, E., Ebihara, M. 1982, Geochim. Cosmochim. Acta, 46, 2363

Bechtold, J., Elvis, M., Fiore, F., Kuhn, O., Cutri, R.M., McDowell, J.C., Riecke, M., Siemiginowska, A., Wilkes, B.J. 1994, AJ, 108, 374

Blitz, L., Magnani, K., Mundy, L. 1984, ApJL, 282, L9

Brunner, H., Lamer, G., Worrall, D.M., Staubert, R. 1994, A&A, 287, 436

Buhler, P, Courvoisier, T.J.-L., Staubert, R., Brunner, H., Lamer, G. 1995, A&A 295, 309

Cappi, M. et al. 1997, ApJ, in press

Ciliegi, P., Maccacaro, T. 1996, MNRAS, 282. 477

Combes, F. 1991, ARAA, 29, 195

Dalla Casa, D, Fanti, C., Schilizzi, R.T., Spencer, R.E. 1995, A&A, 295, 27

de Vries, H.W. Heithausen, A., Thaddeus, P. 1987, ApJ 319 723

Elvis, M., Lawrence, A. 1985, in "Astrophysics of Active Galaxies and Quasi-Stellar Objects", ed. J.Miller [Univ.Science Press: Mill Valley CA]

Elvis, M., Fiore, F., Wilkes, B.J., McDowell, J., Bechtold, J. 1994a, ApJ, 422, 60

Elvis, M., Fiore, F., Mathur, S., Wilkes, B. 1994b, ApJ, 425, 103

Elvis, M., Mathur, S., Wilkes, B. 1995, ApJ, 452, 230

Elvis, M., Fiore, F., Giommi, P., Padovani, P. 1997, ApJ, in preparation (Paper II)

Fiore, F., Elvis, M., McDowell, J. C., Siemiginowska, A., Wilkes, B.J., 1994, ApJ, 431, 515

Fiore, F., Elvis, M., Siemiginowska, A., Wilkes, B.J., McDowell, J.C., Mathur, S. 1995, ApJ, 449, 74

Giommi, P. et al. 1997, in preparation

Green, P.J., et al. 1995, ApJ, 450, 51

Hasinger, G. et al 1992, Legacy, 2, 77, OGIP MEMO, CAL/ROS/92-001

Heiles C. and Cleary M.N., 1979, Aust. J. Phys. Suppl., 47, 1

Hewitt, A., Burbidge, G. 1993, ApJS, 87, 451

Hill, G.J., Goodrich, R.W., DePoy, D.L., 1996, ApJ, 462, 163

Kellermann, K. I., Sramek, R., Schmidt, M., Shaffer, D. B., Green, R. 1989, AJ, 98, 1195

Kendall, M., Stuart, A. 1979, The Advanced Theory of Statistics, MacMillan, New York

Lawrence, A., Elvis, M. 1982, ApJ, 256 410

Laor, A, Fiore, F. Elvis, M., Wilkes, B.J. McDowell, J.C.M. 1997, ApJ, 477, 93

Laor, A, Fiore, F. Elvis, M., Wilkes, B.J. McDowell, J.C.M. 1994, ApJ, 435, 611

Maraschi, L., Fossati, G., Tagliaferri, G., Treves, A. 1995, ApJ, 443, 478

Marscher 1988, ApJ, 334, 552

Morrison, R., McCammon, D. 1983, ApJ, 270, 119

Nicastro, F. et al. 1997, ApJ, in preparation

Padovani P., Giommi P. 1996, MNRAS, 279, 526

Padovani, P., Giommi, P., Fiore, F. 1997, MNRAS, 284, 569

Pfefferman, E., et al 1987, Proc SPIE, 733, 519

Puchnarewicz, E.M. et al. 1996, MNRAS, 281, 1243

Schartel, N., Walter, R. Fink, H.H., Trümper, J. 1996a, A&A, 307, 33

Schartel, N., et al. 1996b, MNRAS, 283, 101

Siebert, J., Matsuoka, M., Brinkmann, W., Cappi, M., Mihara, T. Takahashi, T., 1996, A&A, 307, 8

Siegel, S. 1956 'Non Parametric Statistics', New York: McGraw-Hill

Snowden, S.L., Plucinsky, P.P., Briel, U., Hasinger, G., Pfefferman, E. 1992, ApJ, 393, 819

Snowden, S.L., McCammon, D., Burrows, D.N., Mendenhall. J.A. 1994, ApJ, 424 714

Snowden, S.L., Freyberg, M.J., Schmitt, J.H.M.M., Voges, W., Trümper, J., Edgar, R.J., McCammon, D., Plucinsky, P.P., Sanders, W.T. 1995, ApJ, 454, 643

Snowden, S.L., Egger, R., Freyberg, M.J., McCammon, D., Plucinsky, P.P., Sanders, W.T., Schmitt, J.H.M.M., Trümper, J., Voges, W. 1997, ApJ, 485, in press

Stark, A. A., Gammie, C. F., Wilson, R. W., Bally, J., Linke, R. A., Heiles, C., Hurwitz, M., 1992, ApJS, 77

Stickel, M., Kühr, H., 1994, A&AS, 103, 349

Stickel, M., Meisenheimer, K., Kühr, H., 1994, A&AS, 105, 211

Stocke, J. T., Morris, S. L., Weymann, R. J., Foltz, C. B. 1992, ApJ, 396, 487

Trümper, J. 1983, Adv. Space Res., 2, No. 4, 241

Turner, T.J. et al. 1995, ApJ, 445, 660

Véron-Cetty, M.-P., Véron, P., 1993, A Catalogue of Quasars and Active Nuclei, 6th ed. ESO Scientific Report No. 13

von Montigny, C. et al. 1995, ApJ, 440, 525

Walter, R., Fink, H.H. 1993, A&A, 274, 105

Wilkes, B.J., Elvis, M. 1987, ApJ, 323, 243

Wilkes B.J., Elvis M., Fiore F., McDowell J.C., Tananbaum H. Lawrence A. 1992, ApJL, 393, L1

White, N. E., Giommi, P., Angelini, L., 1995,
http://lheawww.gsfc.nasa.gov/users/white/wgacat/wgacat.html

Zamorani, G. et al, 1981, ApJ, 245, 357

This preprint was prepared with the AAS LaTeX macros v3.0.

Table 3: **'Candidate' Cut-off Quasars**

Quasar	z	$logL_O$ erg s^{-1}
	Radio Quiet	
RXJ16331+4157	0.136	29.14
MS02388-2314	0.284	29.92
Q0335-350	0.321	29.68
MS03363-2546	0.334	30.20
US3333	0.354	30.55
PHL6625[a].	0.38	29.98
MS12186+7522	0.645	30.77
Q1234+1217	0.664	30.67
MS21340+0018	0.805	30.31
SBS0954+495	1.687	31.32
	Radio Loud	
3C219	0.174	29.93
PKS1334-127	0.539	31.08
3C207	0.684	30.98
3C212	1.043	30.91
S4 0917+624	1.446	31.29
S4 0917+449	2.18	32.01
4C71.07[b]	2.19	33.04
PKS2351-154	2.665	32.33
PKS0438-43	2.852	32.46
PKS0537-286	3.119	32.16
S4 0636+680	3.174	33.04
PKS2126-158	3.266	33.25
PKS1442+101	3.53	32.7
S41745+624	3.886	32.97

a. 4.6' from NGC247 nucleus

b. Blazar, EGRET $\gamma-$ray

Table 4: **"Candidate" Cut-off Quasars: PSPC Observations**

Quasar	Counts	exposure sec	off-axis angle arcmin
	Radio Quiet		
RXJ16331+4157	281	13636	on
MS02388-2314	223	8008	16.4
Q0335-350	744	17957	13.0
MS03363-2546	938	50058	18.7
US3333	416	11863	13.2
PHL6625	328	19072	3.0
MS12186+7522	321	6484	14.6
Q1234+1217	114	9426	13.5
MS21340+0018	86	5201	11.6
SBS0954+495	182	3669	35
	Radio Loud		
3C219	509	4386	on
PKS1334-127	516	3614	on
3C207	452	7017	on
3C212	770	21565	on
S4 0917+624	366	19465	on
S4 0917+449	640	3367	on
4C71.07	5254	6993	on
PKS2351-154	419	6335	on
PKS0438-43	163	21231	on
PKS0537-286	555	9487	on
S40636+680	68	5342	on
PKS2126-158	1262	7392	on
PKS1442+101	655	15433	on
S41745+624	506	16141	on

Table 5: **"Candidate" Cut-off Radio Quiet Quasars: Spectral Fits**

Quasar	N_{HGal} 10^{20} cm^{-2}	N_H 10^{20} cm^{-2}	α_E	χ^2/dof	prob.($\Delta\chi^2$
	Radio Quiet				
RXJ16331+4157	1.05	$1.1^{+2.1}_{-1.1}$	$0.87^{+0.80}_{-0.60}$	7.0/13	
		$2.7^{+0.8}_{-0.4}$	1.6 FIXED	9.2/14	–
MS02388-2314	2.29	$5.5^{+7.3}_{-3.1}$	1.0 ± 0.8	4.8/14	
		2.29 FIXED	0.32 ± 0.25	5.9/15	–
		$8.2^{+3.8}_{-3.0}$	1.6 FIXED	5.9/15	–
Q0335-350	1.26	$2.1^{+1.0}_{-0.8}$	1.18 ± 0.35	14.8/23	
		1.26 FIXED	0.86 ± 0.08	17.2/24	–
		3.1 ± 0.3	1.6 FIXED	17.6/24	–
MS03363-2546	1.05	$2.1^{+1.8}_{-0.8}$	1.28 ± 0.30	72.6/67	
		1.05 FIXED	0.89 ± 0.06	77.4/68	97.2 %
		2.9 ± 0.2	1.6 FIXED	74.3/68	
US3333	4.36	$7.7^{+5.1}_{-2.5}$	1.36 ± 0.55	8.2/15	
		4.36 FIXED	0.77 ± 0.14	12.8/16	96.8 %
		9.0 ± 0.2	1.6 FIXED	8.7/16	–
PHL6625	1.47	$7.7^{+3.0}_{-2.8}$	1.88 ± 0.6	2.5/12	
		1.47 FIXED	0.32 ± 0.14	19.3/12	99.995 %
MS12186+7522	3.02	3.0 FIXED	0.7 ± 0.5	5.7/11	
		$6.5^{+1.7}_{-1.0}$	1.6 FIXED	9.5/12	–
Q1234+1217	2.51	$4.5^{+9.1}_{-3.1}$	$1.5^{+1.6}_{-0.5}$	3.4/6	
		2.51 FIXED	0.93 ± 0.33	3.8/7	–
MS21340+0018	4.00	$2.7^{+18.3}_{-2.7}$	$0.6^{+1.5}_{-0.3}$	0.71/5	
		4.0 FIXED	0.90 ± 0.45	0.81/6	–
		$6.2^{+6.4}_{-1.7}$	1.6 FIXED	1.62/6	–
SBS0954+495	0.87	$5.2^{+6.8}_{-5.2}$	2.0 ± 2.0	6.5/7	
		0.87 FIXED	0.57 ± 0.30	7.9/8	–
		$4.0^{+1.4}_{-1.0}$	1.6 FIXED	6.6/8	–

Table 6: **"Candidate" Cut-off Radio Loud Quasars: Spectral Fits**

Quasar	N_{HGal} 10^{20} cm^{-2}	N_H 10^{20} cm^{-2}	α_E	χ^2/dof	prob.($\Delta\chi^2$
3C219	1.48	$2.1^{+0.8}_{-1.2}$	0.22 ± 0.40	6.3/22	
		1.48 FIXED	0.05 ± 0.10	6.8/23	–
		$5.7^{+0.7}_{-0.5}$	1.34 FIXED	23.0/23	
PKS1334-127	4.41	$7.1^{+3.0}_{-2.0}$	1.2 ± 0.4	11.0/20	
		4.41 FIXED	0.66 ± 0.13	15.3/21	96.2 %
3C207	4.07	$29^{+30}_{-21.5}$	2.3 ± 1.4	13.6/17	
		4.07 FIXED	0.34 ± 0.16	24.9/18	99.92 %
3C212	3.70	32^{+18}_{-16}	1.9 ± 1.0	14.4/21	
		3.70 FIXED	0.14 ± 0.09	32.0/22	99.997 %
S4 0917+624	3.55	$11.9^{+32}_{-7.9}$	0.46 ± 0.30	5.0/14	
		3.55 FIXED	0.76 ± 0.21	8.25/15	92.6
S4 0917+449	1.51	$2.9^{+1.2}_{-1.0}$	0.79 ± 0.33	17.6/22	
		1.51 FIXED	0.37 ± 0.08	22.1/23	96.6%
4C71.07	2.95	3.3 ± 0.3	0.52 ± 0.09	26.4/29	
		2.95 FIXED	0.43 ± 0.03	28.9/30	–
PKS2351-154	2.39	$5.4^{+3.5}_{-1.2}$	0.87 ± 0.49	12.6/19	
		2.39 FIXED	0.25 ± 0.14	17.3/20	97.0 %
PKS0438-43	1.50	$6.9^{+3.5}_{-1.8}$	$0.70^{+0.27}_{-0.22}$	10.3/22	
		1.5 FIXED	-0.16 ± 0.06	55.4/23	> 99.999
PKS0537-286	2.06	$2.7^{+1.7}_{-1.4}$	0.38 ± 38	16.2/22	
		2.06 FIXED	0.22 ± 0.11	16.8/23	–
		3.8 ± 0.5	0.7 FIXED	17.8/23	–
S40636+680	5.7	5.7 FIXED	-0.1 ± 0.4	10.64/15	
		20^{+10}_{-8}	1.7 FIXED	9.52/15	
PKS2126-158	4.85	$12.9^{+7.2}_{-3.8}$	$0.70^{+0.41}_{-0.29}$	20.6/20	
		4.85 FIXED	-0.03 ± 0.03	49.56/20	> 99.999
PKS1442+101	1.70	$1.9^{+1.2}_{-0.9}$	0.46 ± 0.35	23.2/24	
		1.70 FIXED	0.41 ± 0.10	23.4/23	–
S41745+624	3.31	$6.8^{+0.30}_{-3.0}$	$0.78^{+1.0}_{-0.44}$	14.5/16	
		3.31 FIXED	0.26 ± 0.13	19.1/17	96.8 %

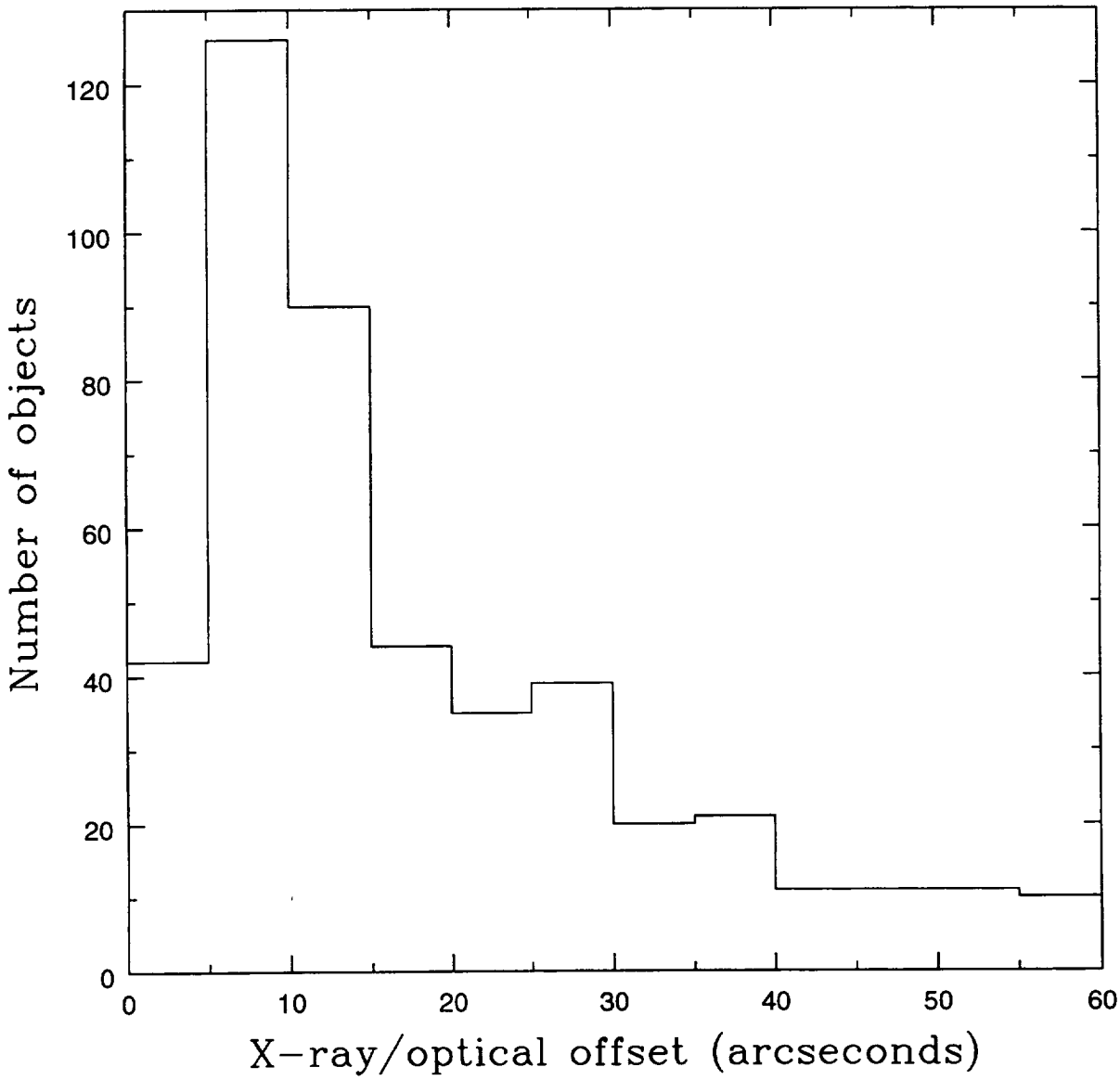

Fig. 1.— **Figure 1** The distribution of X-ray/optical offsets for our sources, obtained by cross-correlating the WGA catalog with various optical and radio catalogs with a correlation radius of one arcminute. The mean offset is $\simeq$ 18 arcsec. The number of spurious associations is $\lesssim 2$ (see text for details).

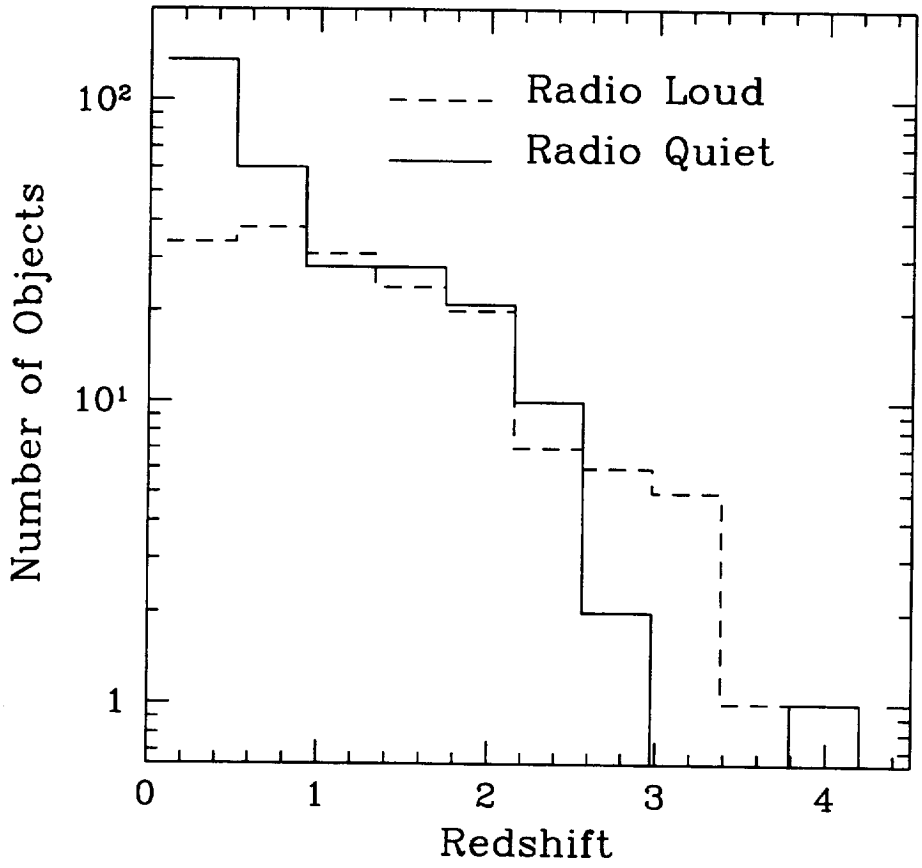

Fig. 2.— **Figure 2** The redshift distribution of WGACAT radio-quiet quasars (solid line) and radio-loud quasars (dashed line), used in this paper.

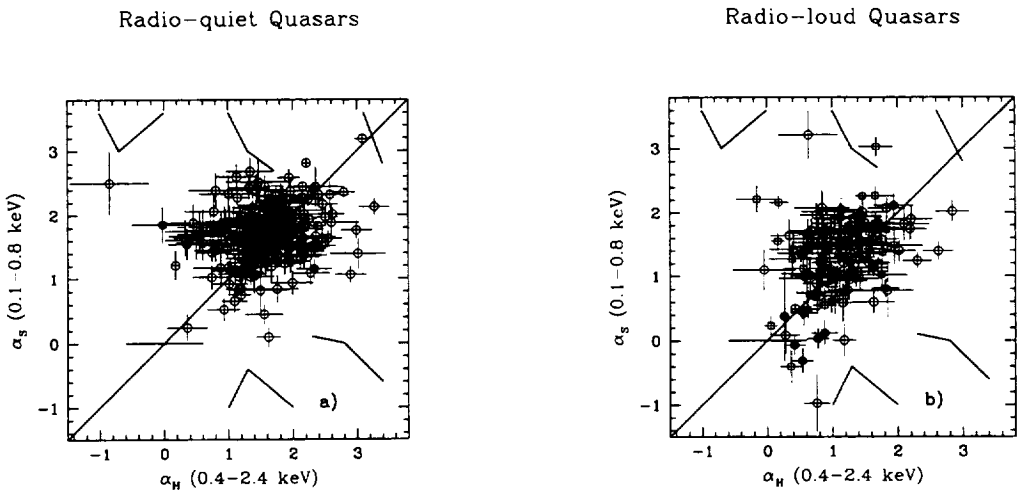

Fig. 3.— **Figure 3** The 'soft' effective spectral index (α_S) of (a) radio-loud quasars, and (b) radio-quiet quasars plotted against the 'hard' effective spectral index (α_H). Radio-loud flat spectrum radio sources are identified by circles, steep radio spectrum sources by squares. High redshift quasars (z>2.2) are shown with filled symbols. Three-point spectra illustrate the radically different spectral shapes in different parts of the diagrams.

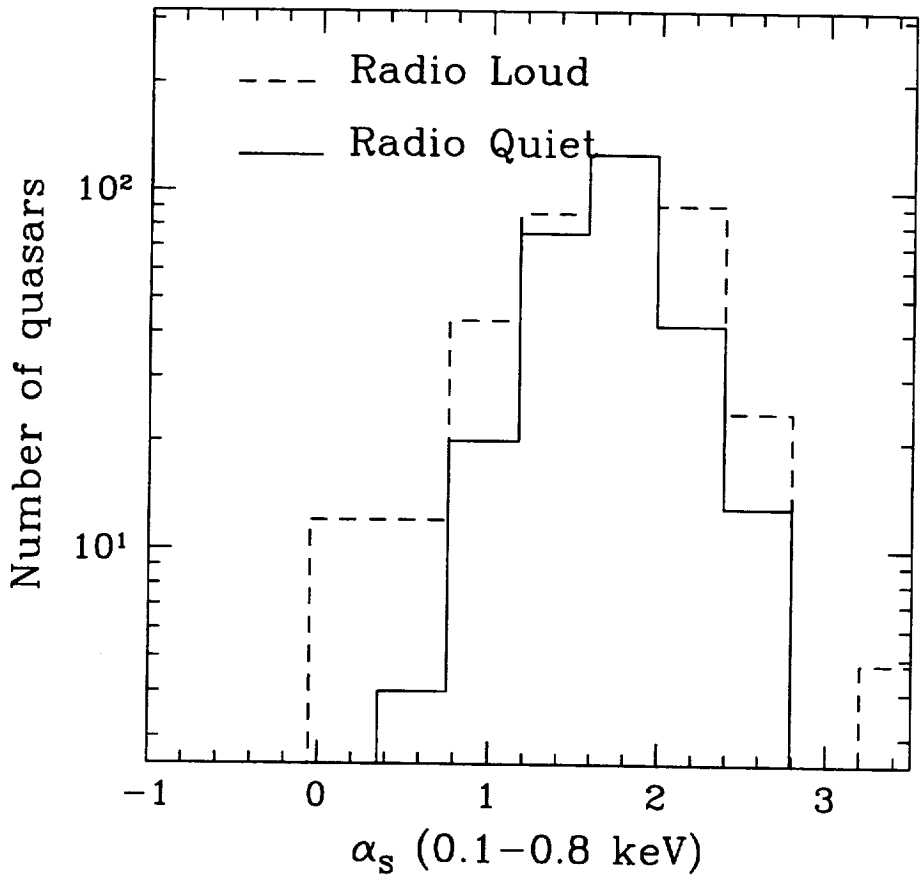

Fig. 4.— **Figure 4** The distribution of radio-loud (dashed line) and radio-quiet (solid line) indices about their respective mean α_S. The mean of radio-loud quasars has been offset to coincide at $\alpha_S = 1.7$ with that of radio-quiet quasars. The radio-loud distribution has been normalized to the maximum of the radio-quiet distribution.

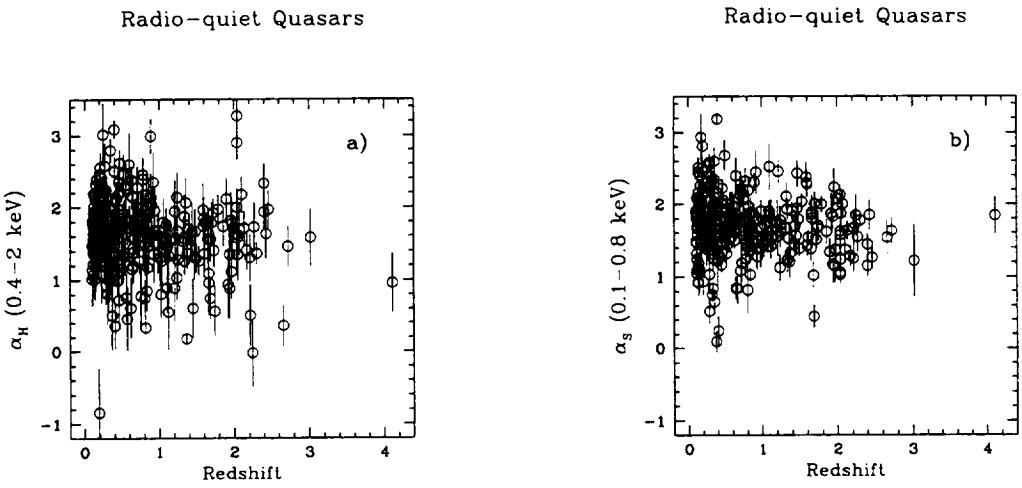

Fig. 5.— **Figure 5** α_H (a) and α_S (b) plotted against the redshift for radio-quiet quasars.

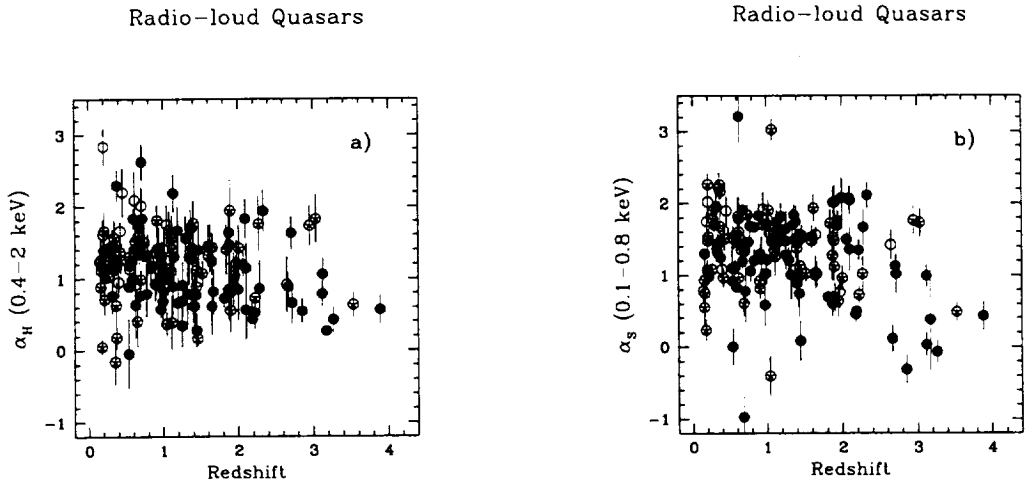

Fig. 6.— **Figure 6** α_H (a) and α_S (b) plotted against the redshift for radio-loud quasars. Filled circles identify flat radio spectrum quasars. Starred circles identify steep radio spectrum quasars.

X-ray Spectral Survey of WGACAT Quasars, II: Optical and Radio Properties of Quasars with Low Energy X-ray Cut-offs

Martin Elvis[1], Fabrizio Fiore[1,2,3], Paolo Giommi[3],
Paolo Padovani[4]
[1] Harvard-Smithsonian Center for Astrophysics
60 Garden St, Cambridge MA 02138, USA
[2]Osservatorio Astronomico di Roma, Monteporzio (Rm), Italy
[3]BeppoSAX Science Data Center, Roma, Italy
[4]Dipartimento di Fisica, II Università di Roma "Tor Vergata", Via della Ricerca Scientifica 1, I-00133 Roma, Italy

(version: 11:45m, 2 June 1997, post-referee)
re-submitted 6/3/97

ABSTRACT

We have selected quasars with X-ray colors suggestive of a low energy cut-off, from the ROSAT PSPC pointed archive. We examine the radio and optical properties of these 13 quasars. Five out of the seven quasars with good optical spectra show associated optical absorption lines, with two having high Δv candidate systems. Two other cut-off quasars show reddening associated with the quasar. We conclude that absorption is highly likely to be the cause of the X-ray cut-offs, and that the absorbing material associated with the quasars, not intervening along the line-of-sight. The suggestion that Gigahertz Peaked Sources are associated with X-ray cut-offs remains unclear with this expanded sample.

Ionized Absorbers in AGN: the role of collisional ionization and time-evolving photoionization

Fabrizio Nicastro[1,2], Fabrizio Fiore[1,2,3], G. Cesare Perola[4], Martin Elvis[1]
[1] Harvard-Smithsonian Center for Astrophysics
60 Garden St, Cambridge MA 02138
[2] Osservatorio Astronomico di Roma
via Osservatorio, Monteporzio-Catone (RM), I00040 Italy
[3] SAX Science Data Center
via Corcolle 19, Roma I00100 Italy
[4] Dipartimento di Fisica, Università degli studi "Roma Tre"
Via della Vasca Navale 84, Roma, I00146 Italy

version: 5:00pm, 12 September 1997

ABSTRACT

In this paper we explore collisional ionization and time-evolving photoionization in the, X-ray discovered, ionized absorbers in Seyfert galaxies. These absorbers show temporal changes inconsistent with simple equilibrium models. We develop a simple code to follow the temporal evolution of non-equilibrium photoionized gas. As a result seceral effects appear that are easily observable; and which, in fact, may explain otherwise paradoxical behavior.

Specifically we find that:

1. In many important astrophysical conditions (OVII, OVIII dominant; and high ($\gtrsim 10^{22.5}\mathrm{cm}^{-2}$) column density) pure collisional and photoionization equilibria can be distinguished with moderate spectral resolution observations, due to a strong absorption structure between 1 and 3 keV. This feature is due mainly to iron L XVII-XIX and Neon K IX-X absorption, which is much stronger in collisional models. This absorption structure may be misinterpreted as a flattening of the intrinsic emission spectrum above $\sim$ 1 keV in low resolution data.
2. In time-evolving non-equilibrium photoionization models the response of the ionization state of the gas to sudden changes of the ionizing continuum is smoothed and delayed at low gas densities (usually up to 10^8 cm^{-3}), even when the luminosity increases. The recombination time can be much longer (up to orders of magnitude) than the photoionization timescale. Hence a photoionized absorber subject to frequent, quick, and consistent changes of ionizing luminosity is likely to be overionized with respect to the equilibrium ionization state.
3. If the changes of the ionizing luminosity are not instantaneous, and the electron density is low enough (the limit depends on the average ionization state of the gas, but is usually $\sim 10^7$ cm^{-3} to $\sim 10^8$ cm^{-3}), the ionization state of the gas can continue to increase while the source luminosity decreases, so a maximum in the ionization state of a given element may occur during a minimum of the ionizing intensity (the opposite of the prediction of equilibrium models).
4. Different ions of different elements reach their equilibrium configuration on different timescales, so models in which all ions of all elements are in photoionization equilibrium so often fail to describe AGN spectral evolution.

These properties are similar to those seen in several ionized absorbers in AGN, properties which had hitherto been puzzling. We applied these models to a high S/N ROSAT PSPC observation of the Seyfert 1 galaxy NGC 4051. The compressed dynamical range of variation of the ionization parameter U and the ionization delays seen in the ROSAT observations of NGC 4051 may be simply explained by non-equilibrium photoionization model, giving well constrained parameters: $n_e = (1.0^{+1.2}_{-0.5}) \times 10^8$ cm^{-3}, and R= $(0.74^{+0.80}_{-0.40}) \times 10^{16}$ cm ($\sim$ 3 light days).

1. INTRODUCTION

The detection and the study of ionized absorbers is more difficult than that of cold neutral absorbers, but can yield much more detailed information about the nature of the absorbers and the state and geometry of the nuclear regions of AGN. If photoionization applies then the electron density of the gas and its distance from the ionizing source can be estimated.

Absorption features from ionized gas, are common in the X-ray spectra of Seyfert Galaxies and some quasars [1]. Deep oxygen VII and VIII absorption edges at 0.74 keV and 0.87 keV (rest) have been detected by the ROSAT PSPC and the ASCA SIS in quite a large number of Seyfert 1 galaxies (Reynolds, 1997).

We do not know yet what is the origin of the gas ionization. Models to date have assumed the simplest equilibrium photoionization case (e.g. Fiore et al., 1993; Guainazzi et al., 1996; Reynolds et al., 1995). In this case, if the gas is confined in a single cloud of constant density, and if the recombination time is smaller than the typical variability timescale, then the ionization parameter, and hence the ionization state of the gas, should follow closely the intensity of the ionizing continuum. This is not always observed. In two ASCA observations of MGC-6-30-15 (Fabian et al. 1994, Reynolds et al. 1995) the best fit ionization parameter is higher when the ionizing flux is lower, in contrast with the expectations of the simplest equilibrium photoionization model; the ASCA observations of MR2251-178 show a roughly constant ionization parameter despite large variation in the 2-10 keV flux (Reynolds & Fabian, 1995); finally, in a ROSAT observation of NGC 4051 (McHardy et al., 1995), the ionization parameter does not linearly track the luminosity, but shows changes that are smoothed and delayed with respect to the luminosity changes. It seems clear that, at least in the above three cases (which are also the best studied), the simplest photoionization equilibrium model is inadequate. We clearly need more complete and consistent models to interpret the available data. The gas could well be distributed in an irregular region with varying density. Different ionization states would then apply to different region of this gas. Other authors have adopted such multi-zone models (Otani et al. 1996, Kriss et al. 1996). In those models the authors assume that absorption features from different ions of the same element are imprinted on the spectrum by the transmission of the ionizing radiation through multiple distinct clouds of gas with different geometrical configurations, ionization states and densities. This is of course a possibility, but to us it seems rather 'ad hoc'.

In this paper instead we discuss the additional physics of collisional ionization, and of time-evolving photoionization ..... in a single zone model. We then apply these models to the Seyfert 1 galaxy NGC 4051.

2. Ionization Models

The innermost regions of an AGN are likely to be 'active', in the sense that the gas there confined is expected to be involved in significant bulk motion, as in strong outflows (Arav et al., 1995) or inflows. In particular the evidence for ionized outflows from the central regions of AGN is strong (Mathur et al. 1994, 1995, 1997). Hence sources of mechanical heating of the gas (for example adiabatic compression by

[1] NGC 4051: Mc Hardy et al. 1995; Guainazzi et al., 1996; MGC-6-30-15: Nandra & Pounds, 1992, Reynolds et al. 1995, MNRAS; NGC 3783: Turner et al. 1993, George et al., 1996; NGC 985, Brandt et al. 1994; NGC 5548: Done et al. 1995, Mathur et al. 1995; NGC 3227, Ptak et al. 1994; NGC 3516, Kriss et al. 1996; IC 4329A, Cappi et al. 1996 PG 1114+445, Laor et al. (1997); MR 2251−178, Halpern (1984), Pan, Stewart and Pounds (1990); 3C 351, Fiore et al. (1993); see also Reynolds (1997)

shock waves) may well be at work in the high density clouds, making collisional ionization the dominant ionization mechanism. In the low density clouds the gas could be far from photoionization equilibrium, because the recombination timescales have become greater than the X-ray continuum variability timescales. Hereinafter, by *photoionization time* (t_{ph}) and *recombination time* (t_{rec}) we mean the time necessary for the gas to reach photoionization equilibrium with the ionizing luminosity during increasing and decreasing phases respectively. We discuss in turn the possible importance of collisional ionization and time-evolving photoionization, in determining the final transmitted spectrum that we observe in AGN.

2.1. Collisional Ionization Models

To study collisional ionization we constructed a series of pure collisional ionization models and compared them with the equilibrium photoionization models. The models were created using CLOUDY (version 90.01, Ferland, 1996), fixing the ionization parameter (i.e. the dimensionless ratio between the number of Hydrogen ionizing photons and the electron density of the gas) U to 10^{-5} and calculating the spectra transmitted through clouds with a total column density, $N_H = 10^{22.5}$ cm^{-2}, constant density and temperature (the calculation of the physical condition of clouds in coronal or collisional equilibrium is one of the options of CLOUDY; Ferland, 1996). The distribution of fractional abundances for the most important ions is essentially independent of the electron density value: for $10 < n_e < 10^{12}$ cm^{-3}; the variation is smaller than 13% for ions with fractional abundances greater than 0.01.

For temperatures T_e in the range $10^5 - 10^{7.1}$ the main edges imprinted on the spectra are roughly the same as those in the spectra from photoionized gas with $-1 < log(U) < 1.5$. However, the distribution of the different ionic species is very different in the two cases, and so the relative optical depth of the edges differ markedly. High quality X-ray spectra, where more than one edge is visible, could then discriminate between the two cases.

The different ionic abundances in the collisional and photoionized cases can be seen in Figs. 1a,b and 2a,b. Here we plot the fractional abundances of NeVIII-NeXI and OVI-OIX (Fig. 1) and FeXIV-FeXXV (Fig. 2), computed in the case of photoionization and collisional ionization respectively as a function of U and T_e. As Fiore et al (1993) and Mathur et al. (1994) have shown, the photo-ionization state of the gas depends strongly on the spectral energy distribution (SED) of the ionizing continuum, from radio to hard X-rays. To simplify the comparison between photoionization models and the data, we therefore used an ionizing continuum similar to the SED of NGC 4051 (Done et al 1990).

Firstly we note that the fractional abundances in photoionized gas are more smoothly distributed than those of collisionally ionized gas. Let us consider the regime in which the OVII and OVIII fractions are higher than ≈ 0.2, so that both OVII and OVIII edges are present in the emerging spectrum, as sometimes found in Seyfert galaxies spectra (e.g. Otani et al. 1996, Guainazzi et al. 1996). In the photoionization case the range of U where this occurs is 1.2–3.6, a factor 3. This is twice as wide as the corresponding range of T_e: $1.5 \times 10^6 - 2.4 \times 10^6$ K (a factor of 1.6: dotted lines in panels *a* and *b* of Fig. 1). Moreover, NeIX is abundant and Carbon is almost fully stripped in the collisional case, but not in the photoionized case.

The difference in the resulting spectra is shown in Fig. 3a. Here we show the ratio between two power law spectra emerging respectively from clouds of collisionallly ionized ($T_e = 1.8 \times 10^6$ K) gas, and photoionized (U=2) gas with solar abundances (the choices of T_e and U were made by looking for similar OVII-OVIII abundances: see Fig. 1a). Below 1 keV there is a large feature due to the deep CVI K absorption edge in the photoionization case. The most important feature above 1 keV is the NeIX absorption edge in the collisional

case, but this feature is smoothed by the presence, in both cases, of deep OVII and OVIII absorption edges. Reynolds (1997), fitted both a simple OVII and OVIII K-edges model and a physical photoionization model to ASCA SIS spectra of a sample of Seyfert 1 known to host a warm absorber. Comparing the results he found that in some cases, the best fit 2-edges model continue to show residuals at the energy of CVI K edge, while residuals to physical photoionization model do not. This may point to photoionization as ionizing mechanism. Spectra with higher resolution from 0.4 keV to 3 keV should therefore allow one to diagnose absorption by collisionally ionized or photoionized gas that has significant OVII and/or OVIII abundances (e.g. Otani et al. 1996, Guainazzi et al. 1996).

The other important feature of collisional models is the inertia of the heavy elements (from Ne to Fe) against becoming highly ionized, even when the oxygen is almost fully stripped. In Fig. 1a and 1b we have marked the range of U for which OIX is by far the dominant ion ($n_{OIX} \gtrsim 0.8$) and OVIII is the only oxygen edge in the emergent spectrum ($\tau \lesssim 0.8$, for an N_H of $10^{22.5}$ cm^{-2} and solar abundances). These same intervals of U and T_e are also shown in Fig 2a and 2b. In the photoionization case Neon is almost fully stripped (NeXI), and the dominant ions of the iron are FeXVIII to FeXXIII. Instead in the collisional case there is a range of temperature for which Neon and Iron are much less ionized, with the dominant ions being NeIX-NeX, and FeXVI to FeXX. In particular we note the large abundance of FeXVII (FeXVII and FeXXV are respectively Ne-like and He-like, and so very stable). The different ionization level of Neon and Iron implies a very different emergent spectrum between 1 and 3 keV.

This is illustrated in Fig. 3b which shows the ratio between spectra transmitted from collisionally ionized gas with $T_e = 3.9 \times 10^6$ K, and photoionized gas with U=10 (both with $N_H = 10^{22.5}$ cm^{-2}). With these values of T_e and U, $n_{OIX} \sim 0.8$ in both collisional ionization and photoionization models (see Fig. 1a). The ratio does not show any significant feature at E< 1 keV (implying similar ionization states of Carbon, Nitrogen and Oxygen), but between 1 and 3 keV, the spectrum from collisionally ionized gas shows a large and complicated absorption structure due mainly to iron L XVII-XIX and Neon K IX-X absorption (Fig. 3b). This absorption structure may be mis-interpreted in moderate quality spectra as a flattening above ~ 1 keV. Again, higher spectral resolution data with good S/N can distinguish between photoionization or collisional equilibrium.

That the NeIX and FeXVII edges are of similar depth is due to a coincidence of cross-sections and abundances. The photoelectric cross section of the iron L shell atoms ranges from $\sim 2 \times 10^{-19}$ cm^2 for the Lp levels of FeXVI-FeXIX ($E \sim (1.17 - 1.47)$ keV), to $\sim 3 \times 10^{-20}$ cm^2 for the Lp level of FeXXII (E=1.78 keV) (Kallman & Krolik, 1995). [2] Furthermore in the collisional case the relative abundance of FeXVII is in the range 0.2–0.7, compared to $\lesssim 0.25$ in the analogous photoionization case. The relative abundance of the NeX, in the collisional case, is greater than 0.25, but NeX $\lesssim 0.4$ in the analogous photoionization case, while $0.05 \lesssim$ (NeIX)$_{Coll}$ $\lesssim 0.40$ and (NeIX)$_{Phot}$ $\lesssim 0.05$ (Fig. 1 a,b). The K-edge energy of NeX is 1.36 keV the same of that of the FeXVIII Lp-edge. While the photoelectric cross-section of Neon is about a factor 4 lower than Iron, the solar abundance of the Neon is about a factor 4 greater than that of Iron (Grevesse & Anders 1989). Furthermore the cross-section of NeIX is about a factor 3 higher than NeX. As a result, spectra from a cloud of collisional ionized gas at $T_e \sim 4 - 6 \times 10^6$ K, will show a very deep ($\tau_{Fe^{L_P}XVII} \sim 1.0 \times N_{H_{23}}$) edge at the FeXVII Lp-edge energy (1.26 keV), a deep ($\tau_{Fe^{L_P}XVIII + Ne^{K}X} \sim 0.7 \times N_{H_{23}}$) edge at 1.36 keV due to the comparable contributions of the NeX K-edge and the FeXVIII Lp-edge, and a similarly deep absorption edge at the NeIX K-edge energy ($E^K(NeIX) = 1.196$ keV, $\tau_{Ne^{K}IX} \sim 0.6 \times N_{H_{23}}$). In the corresponding

[2] The photoelectric cross section of the Ls levels of the iron ions, is about one order of magnitude lower than the correponding Lp cross sections, and the Lp levels of the ions FeXXIII-FeXXVI are not populated in ordinary conditions.

photoionization case, the relative abundances of both NeIX-X and FeXVII-XVIII are too low (Fig. 1a,b, 2a,b) to imprint similar features on the spectrum.

When collisions are the dominant ionization process, ($U \lesssim 0.01$) we can estimate the minimum distance, R, between the ionized gas cloud and the central source. For an ionizing luminosity L_{ion}, we find: $R > 1.6 \times 10^{16} (n_{e_{10}})^{-0.5} (Q_{52})^{0.5}$ (with $n_{e_{10}}$ being the electron density in units of 10^{10} cm^{-3}, and Q_{52} the rate of photons ionizing hydrogen in units of 10^{52} ph s^{-1}: $Q = \int_{E_{Ly}}^{\infty} dE(L_{ion}(E)/E)$). For typical AGN ionizing continuum shapes and luminosities ($L_{ion} = 10^{42}$, 10^{45} erg s^{-1}), and assuming $n_{e_{10}} = 1$, we find $R > 6.2 \times 10^{16}$ cm, 2×10^{18} cm, respectively, similar to the size of the BLR for such AGN (Peterson et al., 19??).

2.2. Mixed Collisional and Photoionization Models

The above discussion concerns gas in pure collisional equilibrium. If the gas density is low enough and/or if the gas is close enough to the central X-ray source then photoionization can be important too. We examined a number of models with a varying mixture of collisional ionization and photoionization. For $T_e = 2.5 \times 10^6$ we find that for values of U $\lesssim 0.1$ the main features of the fractional abundance distribution are still those of pure collisional ionized gas. Increasing U to 0.3 causes a sharp change in the ionization structure. For $0.3 <$ U $\lesssim 100$ (the exact value of the upper limit depending on the equilibrium temperature determined by collisional mechanisms) the ionization structure is determined by *both* processes, and the transmitted spectra resemble those from pure photoionized gas of *much higher* ionization parameter. This is shown in Fig. 4 where we plot in the lower panel three spectra from purely photoionized gas (column density logN_H=22.5 and log(U)=0.7, 1.1 and 1.4), and in the upper panel 5 spectra from gas in which both mechanisms are at work (logN_H=22.5, $T_e = 2.5 \times 10^6$ and log(U)=-2, -1, 0.3, 0, 0.4). The pure photoionization spectra with log(U)=0.7, 1 (lower panel) are very similar to the mixed collisional and photoionization spectra with a factor 4-10 times lower U (log(U)=-0.3, 0.4; upper panel). Fitting the mixed spectra with pure photoionation models would give a much more compressed range of U than the real one, as found by McHardy et al. in NGC4051. The above spectra in the two panels of Fig. 5 are practically undistinguishable even at high resolution, because the shape of the fractional abundance distributions when both processes are working, closely resemble those of a purely photoionized gas (see upper panels of Fig. 1 and 2). Fortunately the two models predict quite different delay properties (§2.3).

2.3. Time-evolving Photoionization Models

If photoionization is the dominant process (the gas being purely photoionized, or the density enough low to give U $\gtrsim 0.1$) the main features of the fractional abundance distribution are those of photoionized gas. However, if the X-ray source is variable, photoionization equilibrium will apply only if the density is high enough to make the ion recombination timescales shorter than the variability timescales. There are regimes where photoionization equilibrium does not apply at all. Here we investigate the low density case in some detail, beginning with a discussion of the relevant physics.

2.3.1. Equilibrium photoionization

Let us suppose that a single cloud of optically thin gas is illuminated by an intense flux of ionizing radiation emitted by a variable source located at a distance R from the cloud.

We can calculate the equilibrium distibution of the ionic species in the cloud, by setting the photoionization rate equal to the radiative recombination rate [3] (see, e.g., Netzer, 1990).

$$\left(\frac{n_{X^{i+1}}}{n_{X^i}}\right)^{eq} = \frac{F_{X^i}}{\alpha_{rec}(X^i, T_e) n_e}, \tag{1}$$

and adding the condition for charge conservation $\sum_i n_{X^i} = 1$. Here $\alpha_{rec}(X^i, T_e)$ is the radiative recombination coefficient (in cm^3 s^{-1}), which includes recombination to all levels, and F_{X^i} is the photoionization rate of the ion X^i, which, for optically thin gas clouds, can be written (see, eg., Netzer, 1990):

$$F_{X^i} = \frac{1}{4\pi R^2} \int_{\nu_{X^i}}^{\infty} d\nu \frac{L_\nu}{h\nu} \sigma_\nu(X^i). \tag{2}$$

The lower limit of the integral is the threshold ionization frequency of the ion X^i. $\sigma_\nu(X^i)$ is the photoelectric absorption differential cross section of the ion X^i.

In this simple scheme the ionization state of the gas is completely determined, at equilibrium, by the value of the ionization parameter $U = F_{HI}/n_e c$. [4]

With these approximations the ionization parameter U can be written as a function of the ratio between any two consecutive ionic species of the generic element X:

$$U = \left(\frac{n_{X^{i+1}}}{n_{X^i}}\right) \left(\frac{F_{HI}}{F_{X^i}}\right) \frac{\alpha_{rec}(X^i, T_e)}{c}. \tag{5}$$

2.3.2. Time-evolving photoionization: Equations

If the gas is not in equilibrium eq. 5 is of course meaningless. However, it is still possible to use it formally by introducing an ionization parameter $U^{X^i, X^{i+1}}(t)$ which depends both on time *and* on the specific ionic species under consideration.

The time evolution of the relative density of the ion i of the element X, considering only radiative recombination and photoionization, is then given by (Krolik and Kriss, 1995):

$$\frac{dn_{X^i}}{dt} = -\left[F_{X^i} + \alpha_{rec}(X^{i-1}, T_e) n_e\right] n_{X^i} + F_{X^{i-1}} n_{X^{i-1}} + \alpha_{rec}(X^i, T_e) n_e n_{X^{i+1}}. \tag{6}$$

---

[3] Neglecting the normally small effects of Auger ionization, collisional ionization and three body recombination.

[4] The inverse of the photoionization and radiative recombination rates are usually referred in the literature as the photoionization and recombination times:

$$t_1^{X^i} = \frac{1}{F_{X^i}}, \qquad t_2^{X^i} = \frac{1}{\alpha_{rec}(X^i, T_e) n_e}. \tag{3),(4)}$$

Instead in this paper we refer to different quantities as *photoionization* time and *recombination* time: see eq. 7.

The first term on the right of eq. 6, is the *destruction rate* of the ion X^i, both by photoionization $X^i \rightarrow X^{i+1}$ and radiative recombination $X^i \rightarrow X^{i-1}$, while the other two terms indicate the *formation rate* of the ion X^i by photoionization of the ion X^{i-1} and radiative recombination of the ion X^{i+1} respectively.

The solution of eq. 6 is a system of N coupled integral equations in the N unknowns n_{X^i}, which is analytically solvable only for N=2, with the addition of the charge conservation condition. These solutions define the time scale t_{eq}, that measures the time necessary for the gas to reach photoionization equilibrium with the ionizing continuum. This time is given at any point of the light curve of the ionizing continuum by the inverse of the destruction rate of the ion X^i (following Krolik & Kriss 1995) A useful analytical approximation for t_{eq} (valid if the ionic abundances of a given element are distributed mainly between just two ionic species), is:

$$(7) \qquad t_{eq}^{X^i,X^{i+1}}(t \rightarrow t+dt) \sim \left[\frac{1}{\alpha_{rec}(X^i,T_e)_{eq} n_e}\right]\left[\frac{1}{1+\left(\frac{n_{X^{i+1}}}{n_{X^i}}\right)_{eq,t+dt}}\right],$$

where *eq* indicates the equilibrium quantities. During increasing ionization flux phases we call $t_{eq}^{X^i,X^{i+1}}$ *photoionization time*, t_{ph}; during decreasing ionization flux phases we call $t_{eq}^{X^i,X^{i+1}}$ *recombination time*, t_{rec}. These times are generally different from t_1 and t_2 in eq. 3 and 4.

Equation 7 shows that the time $t_{eq}^{X^i,X^{i+1}}(t \rightarrow t+dt)$ necessary for the gas to reach equilibrium depends explicitly on the electron density n_e in the cloud, and on the equilibrium ratio between two consecutive ionic species calculated at the time t+dt. This is the key result of this work, which has major consequences:

1. the time scale on which the gas reaches equilibrium with the ionizing continuum depends on the electron density, *even when the continuum increases* (Fig. 5);
2. different ions reach their equilibrium relative abundances at different points of the light curve (Fig. 6);
3. if changes of intensity are not instantaneous (dL/dt$< \infty$), the time behavior of the relative abundance of a given ion can be opposite to that of the ionizing source (Fig. 6).

All of these effetcs have been seen in ionized absorbers in AGN. Using these effects non-equilibrium photoionization models can strongly constrain the physical state of the absorber.

2.3.3. Time-evolving Photoionization: Calculations

We created a program to solve the first order differential equation system of eq. 6 for all the ions of the elements H, He, Li, C, N, O. The program uses an iterative method (see Gallavotti, 1983), that permits the solution of any system of N first order differential equations in the N unknowns x_i, of the form $\dot{\mathbf{x}}(\tau) = \mathbf{f}(\mathbf{x}(\tau))$, $(\forall \tau > 0)$, with the only conditions being that $f_i \in C^\infty$ and a limited ensemble Ω exists, such that $x_i \in \Omega$.

We consider the photoionization from the K-shell of each element, and radiative recombination to all levels for each ion.

We use the recombination rates tabulated by Shull and Van Steenberg (1982) for the metals. We take the values of the recombination rate of hydrogen from Ferland (1996); we get the total recombination rate by

summing over levels n=1,20. We calculate the photoionization rate from the K-shell of each ion, carrying out the integrals in eq. 2, using for the spectral shape of the ionizing continuum, from the Lyman limit to γ-rays, a simple power law with $\alpha = 1.3$ (similar to the observed SED of NGC 4051). We use the photoelectric K-shell cross section tabulated by Kallman and Krolik (1995).

We do not carry out the calculation of the heating-cooling balance self-consistently. We calculate with CLOUDY (Ferland, 1996) a grid of models for 300 values of U (from 0.01 to 100), and build the curve U=U(T_e), using the technique described in Kallman and Krolik (1995). We then interpolate on these, to obtain the initial equilibrium electron temperature of the gas. The time evolution of the temperature in the cloud is carried out performing an iterative calculation of the time dependent photoionization equations, using the definition of $U^{X^i,X^{i+1}}(t)$ given above. This technique is only an approximation to the correct self-consistent time-evolving heating-cooling calculation. By comparing the equilibrium relative abundances of the main ions obtained with our method with that obtained using CLOUDY we estimate that for U in the range 0.1-50 the method works with a precision better than 10%. Furthermore, for all the cases in which the gas is far enough from equilibrium, the instantaneous temperature value of the gas is not critical, because of the weak dependence of the recombination rates on T_e (see Shull and Van Steenberg, 1982).

The inputs the program needs are: (a) the initial equilibrium value of the ionization parameter U; (b) the spectral shape of the ionizing continuum; (c) the light curve of the ionizing continuum; (d) the electron density n_e; (e) the ratio, P, between the source intensity and the intensity the source should have in order to produce the observed degree of ionization, assuming equilibrium at the beginning of the light curve.

The output of the program is a list of the relative ionic abundances of the chosen element, and the source flux at the illuminated face of the cloud as a function of time.

2.3.4. The Step Function Light Curve

The simplest case is that of a two state light curve. Let us suppose that the ionizing continuum intensity goes ***instantaneously*** from a "low" to a "high" state and comes back to the "low" state after a time t_{var} (Fig. 5a). The time behaviour of the ionization state of the gas irradiated by this continuum depends on the value of the ratio $t_{var}/t_{eq}^{X^i,X^{i+1}}(t \rightarrow t+dt)$, and the amplitude of the flux variation (here we adopt an unusual factor 100 change in flux to make the effects particularly clear).

We considered the case of an optically thin cloud of gas with an initial ionization such that the most relevant ionic species of the oxygen are OVIII and OIX (corresponding to equilibrium value of U$\gtrsim$10 with the adopted SED).

The time behavior of the relative density of n_{OIX} is shown in Fig. 5b. In both panels different lines identify different values of the electron density, $n_e = 5 \times 10^6$, 10^7, 10^8, 10^9 cm^{-3}. In the upper panel different n_e imply four values of the distance of the cloud from the ionizing source.

The photoionization time $t_{ph}^{OVIII,OIX}$ (eq. 7) of the gas becomes progressively longer as the density decreases: from about 10^3 s for $n_e = 10^8$ cm^{-3}, to 2×10^4 s for $n_e = 10^7$ cm^{-3} to even longer timescales for $n_e = 5 \times 10^6$ cm^{-3} (for $n_e \lesssim 10^5$ cm^{-3} the changes of n_{OIX} during the firt 10^4 s are < 10 %). Note that this is not true for t_1 in eq. 3, which is the definition of photoionization time usually found in litterature.

Formally the dependence of t_{ph} on n_e is introduced by the choice of a particular set of boundary conditions when solving eq. 6, and hence defining $t_{eq}^{X^i,X^{i+1}}(t \rightarrow t+dt)$. Physically, fixing the boundary

conditions of the system means to choose a particular initial ionic distribution in the gas, and hence its initial ionization state. Different values of n_e, given the initial ionization state of the gas (and hence the ratio between the flux of ionizing photons at the illuminated face of the cloud and the electron density), imply different distances of the gas from the X-ray source. This is clear in the upper panels of Fig. 5 where the ionizing flux at the illuminated face of the cloud is plotted for different values of n_e.

Recombination times are generally longer ($t_{rec}^{OIX,OVIII} > t_{var}$), and can be order of magnitude longer. Neither at the highest density tested ($n_e = 10^9$ cm^{-3}) the ionization state of the gas is able to relax to the initial equilibrium state in less than 2×10^4 s after the source switch off. Recombination time scales for $n_e \leq 10^8$ cm^{-3} are long, the order of many times 2×10^4 s. Since the source switch off is instantaneous the relative density of OIX never increases after the switch off.

This example illustrates how photoionization recombination timescales can have a strong effect on the changes observed in ionized absorbers.

2.3.5. The gradual rise & decay light curve: $dL/dt < \infty$

We now consider a more realistic light curve. In this case the source intensity goes from a low state to a high state in a finite time (4,000 s), and after 2,000 s comes back to the initial low state with the same absolute gradient (Fig. 6a). The entire up & down cycle lasts 10,000 s. The change in flux is a more common factor 10. The corresponding light curves of the relative abundances of the fully stripped ions of three different elements, CVII, NVIII and OIX, are shown in Fig. 6b. In both panels different lines correspond to different values of the electron density, $n_e = 10^8, 10^9$ cm^{-3}.

The gradual changes of the ionizing continuum produce time delays between the source light curve and the relative ion abundance light curves. In the lower density case ($n_e = 10^8$ cm^{-3} solid lines), n_{OIX} reaches its maximum value (well below the equilibrium value ~ 1) around the minimum of the luminosity intensity (at $\sim 10,000$ s). During the whole decreasing luminosity phase n_{OIX} is slightly increasing or constant. X-ray spectra taken during the high luminosity phase and the decreasing luminosity phase would show an OVIII absorption edge correlated with the intensity of the ionizing continuum, as seen in MGC-6-30-15 (Fabian et al., 1994, Reynolds et al., 1995). At this density CVII is able to reach its maximum equilibrium value (Fig. 6b), but even this ion does not relax to its initial equilibrium value for many times up and down cycle time. Fig. 6b also shows that the ions reach their maximum values at different times. n_{CVII} reach its maximum value about 4,000 s before n_{OIX}.

At higher densities ($n_e = 10^9$ cm^{-3}, dashed lines), the fractional abundance of each of the three ions reaches its maximum equilibrium value during the first 6,000 s, and relaxes to its minimum equilibrium value during the following 2.4×10^4 s, but with different times-scales: OIX reaches its minimum equilibrium value after a time corresponding to two cycles, about one cycle after CVII. This could help to explain why models in which all ions of all elements are in photoionization equilibrium, so often fail to describe AGN spectral evolution. Spectra accumulated immediately after a very steep decreasing intensity phase could contain no significant absorption features at the energies of OVII–OVIII K-edge (the oxygen being completely ionized), but still show a deep absorption edge at E$\sim$ 0.5 keV, due to the presence of a large amount of recombined CVI-CVII in the absorbing gas. High quality spectra would allow powerful tests of non-equilibrium photoionization models.

A general result is that the observation of any delays in the response of the absorber to flux changes on

time scales of $\sim 5000 - 1000$ s, immediately implies photoionization with a density in a reasonably restricted range, $10^6 \lesssim n_e \lesssim 10^9$ cm^{-3} (depending on the average ionization state).

3. Modeling the ROSAT data of NGC4051

NGC 4051 is an object with particulary good S/N (195 σ, 44620 counts) in the ROSAT PSPC, which exhibits behavior in its ionized absorber that is in conflict with simple photoionization equilibrium models (McHardy et al., 1995). NGC 4051 is a low luminosity, rapidly variable Seyfert 1 galaxy: both its soft and hard X-ray flux vary by large factors (up to 20) on a time scale of hours, and smaller variations have been detected on shorter time scales (e.g. Lawrence et al., 1985, Guainazzi et al., 1996). NGC4051 also exhibits a marked X-ray spectral variability, roughly correlated with intensity. The presence of an ionized absorber in this source, was first proposed on the basis of variations of the GINGA softness ratio correlated with the flux (Fiore et al. 1992). Subsequently a ROSAT PSPC observation performed during the All Sky Survey (Pounds et al. 1994), also suggested the presence of a high column density, highly ionized absorber. More sensitive ROSAT pointed observations (Mc Hardy et al. 1995), and ASCA observations (Mihara et al. 1994, and Guainazzi et al. 1996), confirm the presence of a deep absorption edge at 0.8-0.9 keV. In these papers the authors fit both continuum+edge and complete ionized absorber models to spectra accumulated in time intervals short enough (600-3000 s) to avoid large flux variations. McHardy et al. (1995), find that a simple single zone equilibrium photoionization model can provide a reasonably good representation of individual spectra, but the best fit ionization parameter does not track the source intensity, as required by the model. Guainazzi et al. (1996), analyzing an ASCA observation when the source intensity was on average a factor of 2 higher than during the 1991 ROSAT observation, find that while the depth of the OVII edge is correlated with source variations, the depth of the OVIII edge is consistent with a constant value during the whole observation.

This behaviour cannot be explained in a single zone ionization equilibrium model. For all these reasons NGC4051 is a good target to test our time-evolving photoionization and collisional ionization models. We therefore decided to compare our models to the ROSAT PSPC data aquired on 1991 November 16, and reported by McHardy et al. (1995), when the source count rate showed large and rapid variations (up to a factor of 6 in a few thousand sec., see figure 5 of McHardy et al., 1995).

The data reduction and the timing analysis were performed using the PROS package in IRAF. The observation spanned 77 ksec and contained 28.7 ksec of exposure time. NGC 4051 gave a mean count rate of 1.6 s^{-1}. We accumulated eight spectra ($a - h$), using a 3' radius extraction region, accumulating contiguous data with similar count rates. Background counts and spectra were accumulated from an annulus of internal and external radius of 3'.5 and 6' respectively.

3.1. Hardness ratio analysis: the absorber is not in photoionization equilibrium

Independent of any spectral fit the behavior of the main physical properties of the absorber can be seen in a color-color diagram. In Fig. 7 we plot the hardness ratios HR=H/M against the softness ratio SR=S/M from the count rates in three bands (S=0.1-0.6 keV, M=0.9-1.5 keV, and H=1.7-2.5 keV) for theoretical curves (for $\log(N_H)$=22, 22.5 and 23) obtained by folding the equilibrium photoionization models (for log(U) in the range -0.3 to $+1.5$, and Galactic N_H: 1.31×10^{20} cm^{-2}, Elvis et al. 1989) with the response matrix of the PSPC. We also plot the colors of the source in the eight spectra (a - h). All the data points lie in a region

of this diagram corresponding to the high U ends of the photoionization theoretical curves where both SR and HR decrease, as U increases, until all the ions in the gas are full stripped and the gas is completely transparent to radiation of any energy. The colors of NGC 4051 are all consistent with the OVIII-OIX ions being dominant. Filled circles on the $\log N_H$=22.5 curve mark values of U in the range 4.0–7. All the data points are between the two extreme values of U, a factor ~ 1.5 change, while the source intensity varies up to a factor ~ 6 in the eight spectra. The gas is clearly not responding to the continuum variations, a conclusion equivalent to that obtained by McHardy et al. (1995) using spectral fits with equilibrium photoionization models (see their figure 5). In the framework of the models discussed in this paper this behavior suggests three different possibilities (we do not take in account pure collisional ionization in this case because the observed spectral variations should be attributed to 'ad-hoc' changes of T_e or N_H on time scales as short as 2000-4000 s):

1. the gas is far from ionization equilibrium;
2. the gas has a distribution of densities;
3. both collisional and photoionization processes are comparably important in the same physical region.

We investigated these possibilities in turn using detailed spectral fits.

3.2. Time-evolving photoionization

From Fig. 1 we see that a given ionization state can be roughly determined by the measure of at least two consecutive ion abundances, e.g. OVII and OVIII. The measure of a single edge in fact would not distinguish between 'low' and 'high' ionization solutions. The same measured feature could be produced by a lower N_H, lower mean ionization gas, or by an higher N_H, higher mean ionization state gas.

The best derived quantities to compare observed spectra with our several physical models are atomic edge strengths. Here we are mainly interested in the OVII and OVIII because they are the strongest and therefore the easiest to detect and measure. However, with the PSPC OVII and OVIII edges are not individually discernable, and we must resort to model fits with multiple components. Our choice is to use the components that can ensure an estimate of the OVII and OVIII τ as unbiased as possible.

3.2.1. A 3-edge 'Model Independent' Spectral Fit

We fitted the eight spectra with a model consisting of a power law reduced at low energy by the Galactic column density, the OVII and OVIII edges and another edge at 1.36 keV to account for possible spectral complexity in the 1-2 keV region (in particular the NeIX-X K and Fe XV-XX Lp absorption discussed in §2.1). Five parameters were at first allowed to be free to vary: the spectral index α_E, the OVII and OVIII edges τ, the 1.36 keV edge τ and the model normalization. The results are presented in Table 3. The fits with the 3 edges model are acceptable in all cases. We stress that τ(1.36 keV) in Table 3 should not be regarded as a true measure of the optical depth of Ne K and Fe L ions. This feature provides only one of the possible parameterizations of the spectrum in the 1-2 keV range, a band in which a change in the continuum spectral index could also be present (the 2-10 keV Ginga and ASCA spectra of this source are typically flatter by ≈ 0.5 than the PSPC 0.1-2 keV spectra). As discussed in §2.1 is difficult to discriminate between

Ne absorption and a real spectral flattening above 1 keV with instruments of moderate spectral resolution like the PSPC. We have performed a series of fit using a broken power law with break energy in the 1-2 keV band and the two oxygen edges, obtaining τ similar to those reported in Table 3. We are therefore confident that the estimation of the oxygen edge τ is robust, within the rather large uncertainties given in Table 3. In principle, a way to reduce the uncertainties is to fix the continuum spectral index to a common value. The results of this series of fits are again given in Table 3. The uncertainies on τ(OVII) and τ(1.36 keV) are indeed smaller than in the previous case but this is not true for the τ(OVIII) uncertainties. The reason is that there is a strong anti-correlation between α_E and τ_{OVII}. A similar anti-correlation is present between α_E and $\tau(1.36keV)$. In contrast no correlation is present between α_E and τ(OVIII). This is illustrated in Fig. 8 where we show the χ^2 contours of these parameters for spectrum *g*. Since the τ(OVII) values could be biased in the fit with fixed α_E by the τ(OVII)-α_E correlation, we prefer to compare our time-evolving models to the OVII and OVIII optical depths obtained leaving α_E free to vary.

In all but one case (spectrum *d*) the depth of the OVIII edge is higher or comparable to that of OVII, suggesting a 'high' ionization solution (U>4, see Fig. 1), consistent with the hardness ratio analysis of Fig. 7.

3.2.2. Comparison between models and the oxygen edge depths: evidence for a non-equilibrium photoionization absorber?

We converted the best fit τ into OVII and OVIII relative abundances assuming a solar oxygen abundance and a total hydrogen column density N_H. An indication of N_H comes from the color-color diagram of Fig. 7. Although calculated using a photoionization equilibrium model, the theoretical curves in this diagram suggest a value for logN_H between 22 and 23, and so we adopt logN_H=22.5. The three panels of Fig. 9 show the light curves of the source count rate (upper panel) and of the OVIII and OVII abundances (middle and lower panels respectively).

The time evolution of the ionization structure of a cloud of gas photoionized by a variable source is complex and its behaviour sometime counter-intuitive. We then discuss first the simplest case: high electron density, for which each ion is close to its equilibrium state. We examine next the case of lower densities and hence non-equilibrium solutions.

The dotted curves on the middle and lower panels of Fig. 9 show the $n_e = 10^{10}$ cm^{-3}, P=1 (the ratio of the incident flux to that needed to produce the initial ionization distribution assuming photoionization equilibrium) curves, when the gas is close to equilibrium. While the equilibrium OVII curve tracks the count rate variations (it is strictly anticorrelated with the count rate light curve), the OVIII curve does not. The different OVIII behaviour is due to the different balance in the destruction rates of OIX and OVIII. When the ionizing flux is at its maximum most of the oxygen is OIX. When the flux decreases from the maximum (from point *b* to *d*) OIX recombines to OVIII increasing the OVIII abundance. When the flux decreases from point *e* to point *f* at first OVIII increases again because of the high destruction rate of OIX, but after a certain point the amount of OVIII recombining to OVII start to be higher than the amount of OIX recombining to OVIII, and so the total OVIII abundance start to decrease. Instead, the amount of OVIII recombining to OVII is always higher than the amount of OVII recombining to OVI. This gives rise to a different behaviour of the OVIII and OVII curves in response to the same ionizing flux variations. It is interesting to note that in this case while the dynamical range of variation of the OVII curve is larger than that of the ionizing flux, the OVIII equilibrium curve shows a more compressed range of variations (when the

Table 1: **NGC 4051: 3-Edge Model Fits**

Spectrum	τ(0.74 keV)	τ(0.87 keV)	τ(1.36 keV)	α_E	χ^2(d.o.f.)
a	$0.5^{+0.5}_{-0.4}$	$0.84^{+0.32}_{-0.33}$	1.0±0.4	1.3±0.1	0.84(21)
	$0.34^{+0.29}_{-0.23}$	$0.84^{+0.31}_{-0.32}$	$0.81^{+0.28}_{-0.23}$	1.34 (fixed)	0.82(22)
b	< 0.5	0.66±0.21	0.7±0.3	1.3±0.1	1.19(23)
	$0.23^{+0.19}_{-0.16}$	0.66±0.21	$0.71^{+0.18}_{-0.16}$	1.34 (fixed)	1.14(24)
c	$0.5^{+0.5}_{-0.4}$	$0.41^{+0.31}_{-0.34}$	< 0.6	1.3±0.1	0.85(22)
	$0.38^{+0.33}_{-0.26}$	$0.41^{+0.31}_{-0.34}$	< 0.42	1.34 (fixed)	0.82(23)
d	< 0.7	< 0.3	$1.1^{+0.8}_{-0.6}$	$1.6^{+0.1}_{-0.2}$	0.95(18)
	$0.99^{+0.22}_{-0.35}$	< 0.32	$1.95^{+0.81}_{-0.54}$	1.34 (fixed)	1.08(19)
e	$0.5^{+0.4}_{-0.3}$	0.86±0.28	0.5±0.3	1.4±0.1	1.30(22)
	$0.62^{+0.28}_{-0.22}$	$0.86^{+0.28}_{-0.30}$	0.65±0.19	1.34 (fixed)	1.25(23)
f	< 0.6	$1.01^{+0.24}_{-0.23}$	< 0.5	1.4±0.1	1.41(23)
	$0.54^{+0.20}_{-0.18}$	$1.02^{+0.23}_{-0.25}$	0.44±0.14	1.34 (fixed)	1.42(24)
g	< 0.5	1.47±0.29	< 0.5	1.3±0.1	0.65(22)
	< 0.18	$1.42^{+0.16}_{-0.24}$	< 0.21	1.34 (fixed)	0.67(23)
h	$1.2^{+0.6}_{-0.5}$	$0.79^{+0.35}_{-0.42}$	$0.9^{+0.4}_{-0.3}$	1.2±0.1	0.72(22)
	$0.63^{+0.33}_{-0.25}$	$0.86^{+0.33}_{-0.35}$	$0.45^{+0.20}_{-0.19}$	1.34 (fixed)	0.82(23)

ionizing flux varies by a factor of 6 the OVIII and OVII abundances vary by a factor of 3 and 30 respectively, see Fig. 9). Therefore variations of OVIII would be much more difficult to detect than variations of OVII, at least at these regimes of ionization. We re-emphasize: *the behaviour of a single edge does not provide a unique interpretation of the data.*

As explained in §2.3.3, a grid of theoretical OVII and OVIII light curves was generated using our time-evolving photoionization code for 28 values of n_e from 5×10^6 cm^{-3} to 10^9 cm^{-3} and 15 values of P from 0.5 to 2.

We compared these curves with the measured relative abundances of OVII and OVIII and found the best fit model using a χ^2 technique. The thick solid lines in the lower and middle panels of Fig. 9 represent the best fit non-equilibrium OVII and OVIII curves. The agreement between the best fit model and the observed OVII and OVIII abundances is good: $\chi^2 = 1.17$ for 14 dof. The best fitting values for n_e and P are tightly constrained: $n_e = (1.0^{+1.2}_{-0.5}) \times 10^8$ cm^{-3}, P$= 1.5^{+0.4}_{-0.3}$. From the best fit n_e we can estimate the distance of the absorbing cloud from the central source. We obtain R$= (0.74^{+0.80}_{-0.40}) \times 10^{16}$ cm (3 light days).

The dashed lines represent the solutions obtained using the 1 σ confidence interval on n_e and P. The best fit curves (and the 1 σ confidence intervals curves) show a compressed dynamical range of OVIII and OVII abundances variations and a delay between the source maxima and the ion abundance minima of 3000-6000 sec. The compressed dynamical range is due to a mean over-ionization of the gas. While the best fit P shows that the gas in the initial point *a* is near to equilibrium, it departs strongly from equilibrium during the later low intensity states (spectra *d* to *h*). So, despite the fact that the source spends more time in low states than in high states, the gas density is sufficiently low that the gas does not have time to fully recombine after the few events when it suffers high illumination and becomes highly ionized.

The above results were obtained assuming a total hydrogen column density of log(N_H)=22.5. Assuming an higher (lower) column would imply a mean lower (higher) OVII and OVIII relative ion abundance. Therefore, in principle the accurate measure of both edges would constrain also the total warm column density. The uncertainties on the PSPC determinations however preclude this possibility, and better resolution measurements are therefore needed. The energy resolution of the ASCA SIS, for example, is just sufficient to separate the OVII and OVIII absorption edges. A quantitative test of non-equilibrium photoionization model using the ASCA data and a comparison between ROSAT PSPC and ASCA data of NGC 4051 is in progress and will be part of a forthcoming paper. A much better separation, and therefore characterization, of the absorption features will be possible with the high resolution (factor of 10-30 better than ASCA SIS) gratings on AXAF and XMM.

3.3. Other models

Despite the success of time-evolving photoionization models, alternatives exist and should be considered on these .....

3.3.1. Large density variations in the absorbing gas

If the gas is not confined to a single cloud with constant density but rather is distributed in a region with, say, an increasing density, then different ionization equilibria could apply to different regions in the cloud. Two extreme regions may exist: in the region with higher density, lower U, collisional ionization

will be the dominant ionization mechanism and the spectra transmitted by this region would show always the same features, irrespective of the source intensity; the other region, with lower density and higher U, is completely ionized (for carbon, oxygen, neon and iron ions up to FeXXII) when the source is in the high state, but when the source is in a low state the abundances of OVIII are sizeble and imprint the edges in the spectrum seen in low intensity spectra. Here we are assuming that the density of the photoionized region is high enough for the gas to be in instantaneous equilibrium with the ionizing intensity. If not, the average ionization degree of the gas would be very high during the whole observation, and the gas would be always almost transparent at the energies of the relevant absorption edges.

We tested this hypothesis by fitting the highest intensity spectrum (b) with a simple power law model plus a collisionally ionized absorber, using the method of Fiore et al. (1993). The best fit temperature and N_H are $1.5^{+0.7}_{-0.5} \times 10^{22}\mathrm{cm}^{-2}$ and $2.8 \pm 0.1 \times 10^6$ K respectively. We then used the same model (with fixed continuum parameters, fixed temperature and N_H but variable normalization) with the inclusion of an additional OVIII edge to mimic a variable ionization state, equilibrium photoionization absorber. The fits are all acceptable. The worst fit is that of spectrum (d) ($\chi 2 = 1.4$, 21 dof, probability of 10.4 %). In Fig. 10 we plot $\tau(OVIII)$ as a function of the time. The dynamic range of variations of τ is here larger than that on n_{OVIII} in Fig. 9 but is still more compressed than that predicted by equilibrium photoionization model (solid line). We can therefore exclude the possibility that a major part of this absorber could be in pure photoionization equilibrium with the ionizing intensity.

3.4. A "hot" photoionized absorber

The other possibility is that both collisional and photoionization processes are important in the same physical region. In this case the transmitted spectra are very similar to those transmitted from purely photoionized clouds of gas which much higher ionization parameter (§2.1, Fig. 4). The electron temperature of the gas is mainly determined by collisions, and is higher than that expected in pure photoionization equilibrium. The ionization parameter U is no longer linearly correlated with the ionizing intensity, and then its dynamical range of variations is compressed by a factor > 2 compared to the pure photoionization case.

This could in principle explain the compression observed in the measured dynamical range of variation of n_{OVIII}, but could not account for the delays observed on the response of the ionization state of the gas to source intensity variation. Unfortunately there is no way to distinguish between 'hot' photoionized absorber models and simple pure photoionization models on the only basis of the spectral analysis. Nevertheless the delay observed in the response of the ionization degree of the gas between spectrum (b) and (c) suggests that a non-equilibrium photoionization component is mainly required by data.

4. Conclusion

We have investigated ionization models for AGN in different regimes of gas volume densities and photoionization states. In particular we focussed on 'high gas density, low photoionization parameter' gas clouds, where collisional ionization is likely to play a significant role in the gas ionization, and on low gas densities, where the photoionization may be far from equilibrium.

We presented detailed model calculations in both regimes. While the time-evolving photoionization

models in §2.3 are far from being complete or exhaustive they are nevertheless instructive, and reveal the main features of these kinds of models.

Our main findings can be summarized as follows:

1. In many important astrophysical conditions (OVII, OVIII regime) the fractional abundances of the most important ions of O and Ne in photoionized gas are more broadly distributed in U than those of collisionally ionized gas are in T.

2. In the collisional ionization case the heavy elements show a strong inertia against becoming highly ionized, even when lighter elements, like Oxygen, are almost fully stripped. In this case the transmitted spectrum shows a large and complicated absorption structure between 1 and 3 keV, mainly due to iron L XVII-XIX and Neon K IX-X absorption, which is much less visible in spectra emerging from photoionized gas with similar OVII and OVIII abundances. This absorption structure may be misinterpreted as a flattening of the spectra above $\sim$ 1 keV, when fitting low energy resolution data with a photoionization equilibrium model. Higher spectral resolution and good S/N observations are therefore needed to distinguish between collisional ionization and photoionization.

3. In non-equilibrium photoionization models the response of the ionization state of the gas to sudden changes of the ionizing continuum is delayed even during increasing luminosity phases. The delays increase for decreasing electron densities, as changes of n_e, require changes of the intensity of the ionizing flux, i.e. changes of the distance of the gas from the X-ray source (taking as fixed the initial ionization state of the gas).

4. The recombination timescale is generally much longer (up to orders of magnitudes) than the photoionization timescale, because of the dependence of $t_{eq}^{X^i,X^{i+1}}(t \rightarrow t+dt)$ on the equilibrium ratio $(n_{X^{i+1}}/n_{X^i})$, evaluated at the time $t+dt$. This means that a photoionized absorber undergoing frequent, quick, and consistent changes of ionizing luminosity is likely to be overionized with respect to the equilibrium ionization, a state that would be reached only after a sufficiently long low intensity phase.

5. If the changes of the ionizing luminosity are not instantaneous, and the electron density of the cloud is low enough, the ionization state of the gas could continue to increase during decreasing source luminosity phases. This means that we may measure a maximum in ionization state of a given element, when the ionizing flux is at a minimum (opposite to what is expected in equilibrium models).

6. Different ions of different elements reach their equilibrium abundance on different timescales. This is again because of the dependence of $t_{eq}^{X^i,X^{i+1}}(t \rightarrow t+dt)$ on the ratio $(n_{X^{i+1}}/n_{X^i})$. Therefore in the same cloud of gas carbon could be in equilibrium while oxygen could be very far from equilibrium. This may help in explaining why models where *all ions of all elements* are in photoionization equilibrium so often fails to provide a reasonable description of AGN spectra and spectra evolution

We have tested the above models in the case of the Seyfert 1 galaxy NGC4051. The ROSAT observations of NGC4051 are not consistent with a simple equilibrium model, but can be explained straightforwardly by our time-evolving photoionization models. The two main features in the non-equilibrium best fit models are: (a) the compressed range of variability of the measured OVII and OVIII relative abundances with respect to the amplitude of the source variations, and to the amplitude of the variations of the abundances of these ions expected in equilibrium photoionization models; (b) the 3000-6000 sec delay between the maximum

intensity state of the source (spectrum *b*) and the minimum of the best fit OVIII abundance curve, i.e. the maximum ionization state of the gas (spectrum *c*). As result we were able to estimate the gas electron density, $n_e = (1.0^{+1.2}_{-0.5}) \times 10^8$ cm^{-3} (assuming logN_H=22.5) and hence the distance of the ionized gas cloud from the X-ray source in R= $(0.74^{+0.80}_{-0.40}) \times 10^{16}$ cm (3 light days). We explored alternative models and we also explored alternatives which we find to be less likely; we discuss ways to distinguish between them conclusively.

We conclude that non-equilibrium photoionization and collisional models apply to wide zones of gas density and ionization, zones which are expected in AGN. These effects must be considered in understanding ionized absorbers, and seem likely to explain otherwise puzzling behavior, without resorting to ad hoc distributions of gas. Several clear diagnostics of these models exist so that decisive tests will soon be possible.

We thank Giorgio Matt for useful discussions. This work was supported in part by NASA grant NAG5-3066 (ADP). F.F. acknowledges support from NASA grant NAG5-2476. This work made use of the IRAS/PROS package and the ROSAT archive maintained at the HEASARC.

REFERENCES

Arav N., Korista K.T., Barlow T.A., Begelman M.C., 1995, Nature, 376, 576

Brandt W.N., Fabian A.C., Nandra K., Reynolds C.S., Brinkmann W. 1994, MNRAS, 271, 958

Cappi M., Mihara T., Matsuoka M., Hayashida K., Weaver K.A., Otani C. 1996, ApJ, 458, 149

Done C. et al. 1990, MNRAS, 243, 713

Done C., Pounds K.A., Nandra K., Fabian A.C. 1995, MNRAS, 275, 417

Elvis M., Wilkes B.J., Lockman F.J., 1989, A.J., 97, 777

Fabian A.C. et al. 1994, PASJ, 46, L59

Ferland G.J., 1996 CLOUDY: 90.01

Fiore F., Perola G.C., Matsuoka M., Yamauchi M., Piro L. 1992, A&A, 262, 37

Fiore F., Elvis M., Mathur S., Wilkes B.J., McDowell J.C. 1993, ApJ, 415, 192

Gallavotti G. 1983, "The elements of mechanics"

George I.M. et al. 1995, ApJ, 438, 120

Grevesse N., & Anders E. 1989, "Cosmic Abundances of Matter", AIP Conference Proceedings 183, ed. C.J. Waddington (New York: AIP).

Guainazzi M., Mihara T., Otani C., Matsuoka M. 1996, PASJ, 48, 781

Halpern J.P. 1984, ApJ, 281, 90

Kallman T.R. & Krolik J.H. 1995, XSTAR: 1.10

Kriss G.A. et al. 1996, ApJ, 467, 629

Krolik J.H. & Kriss G.A. 1995, ApJ, 447, 512

Laor, A, Fiore, F. Elvis, M., Wilkes, B.J. McDowell, J.C.M. 1997, ApJ, 477, 93

Lawrence A., Watson M.G., Pounds, K.A., Elvis M. 1985, MNRAS, 217, 685

Matsuoka M., Piro L., Yamauchi M., Murakami T. 1990, ApJ, 361, 440

Mathur S., Wilkes B.J., Elvis M., Fiore F. 1994, ApJ, 434, 493

Mathur S., Elvis M., Wilkes B.J. 1995, ApJ, 452, 230

Mathur S., Wilkes B.J., Aldcroft T. 1997, ApJ in press

McHardy I.M. et al. 1995, MNRAS, 273, 549

Mihara T. et al. 1994, P.A.S.J., 46, L137

Nandra K. & Pounds K.A. 1992, Nature, 359, 215

Netzer H. 1990, "Active Galactic Nuclei" ed. Springer-Verlag

Nicastro F., Fiore F., Perola G.C., Elvis M., 1997, ApJL, submitted

Otani C. et al. 1996, P.A.S.J., 48, 211

Pan H.C., Stewart G.C. & Pounds K.A. 1990, MNRAS, 242, 177

Peterson B. 19??

Pounds K.A., Nandra K., Fink H.H., Makino F. 1994, MNRAS, 267, 193

Ptak T., Yaqoob T., Serlemitsos P.J., Mushotzky R., Otani C. 1994, ApJ, 436, L31

Reynolds C.S. & Fabian A.C. 1995, MNRAS, 273, 1167

Reynolds C.S., Fabian A.C., Nandra K, Inoue H., Kunieda H, Iwasawa K. 1995, MNRAS, 277, 901

Reynolds C.S., 1997, MNRAS, 286, 513

Shastri P., Wilkes B.J., Elvis M., McDowell J. 1993, ApJ, 410, 29

Shull J.M. & Van Steenberg M. 1982, ApJS, 48, 95

Turner T.J., Nandra K., George I.M., Fabian A.C., Pounds K.A. 1993, ApJ, 419, 127

This preprint was prepared with the AAS LaTeX macros v3.0.

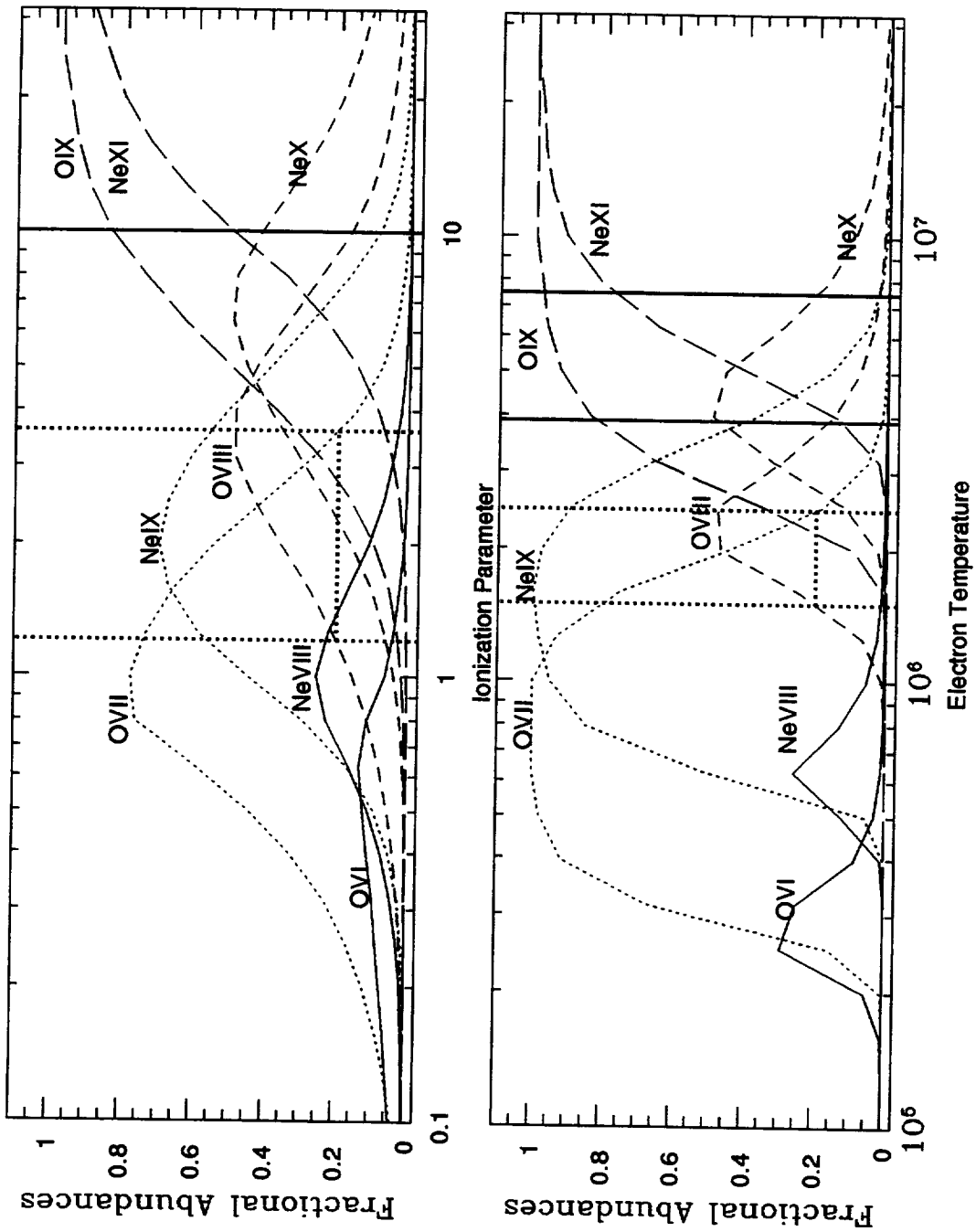

Fig. 1.— Fractional abundances of NeVIII-NeXI, and OVI-OVIX, calculated in the case of photoionization (Fig. 1a: upper panel), and collisional ionization (Fig. 1b: lower panel). The two intervals of U and T_e highlighted are: (a) the interval for which both OVII and OVIII abundances are greater than 0.2 (dotted lines), and (b) the one for which the OIX relative abundance is greater than 0.75.

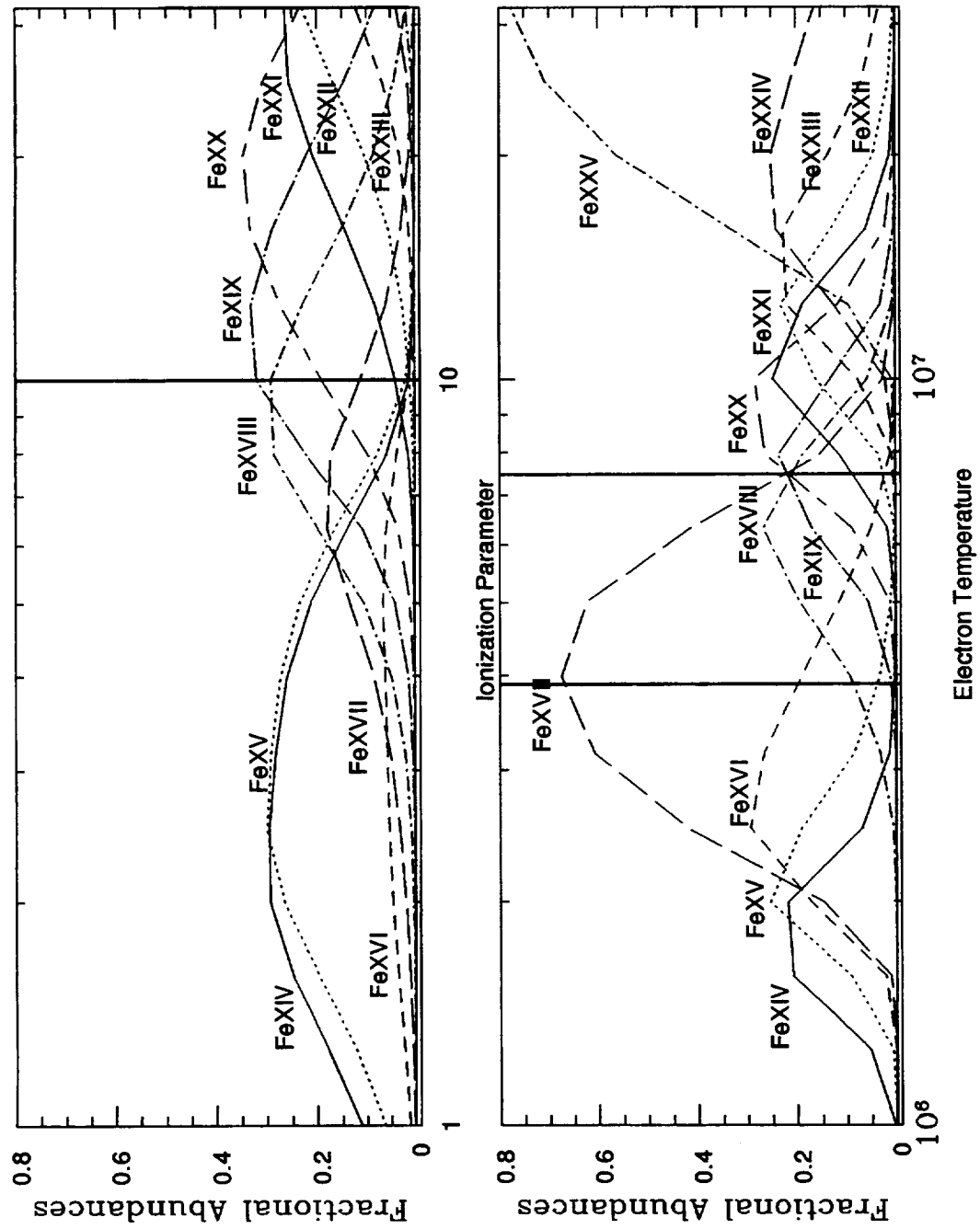

Fig. 2.— Like Fig. 1, for the relative abundances of the ions FeXIV-FeXXV.

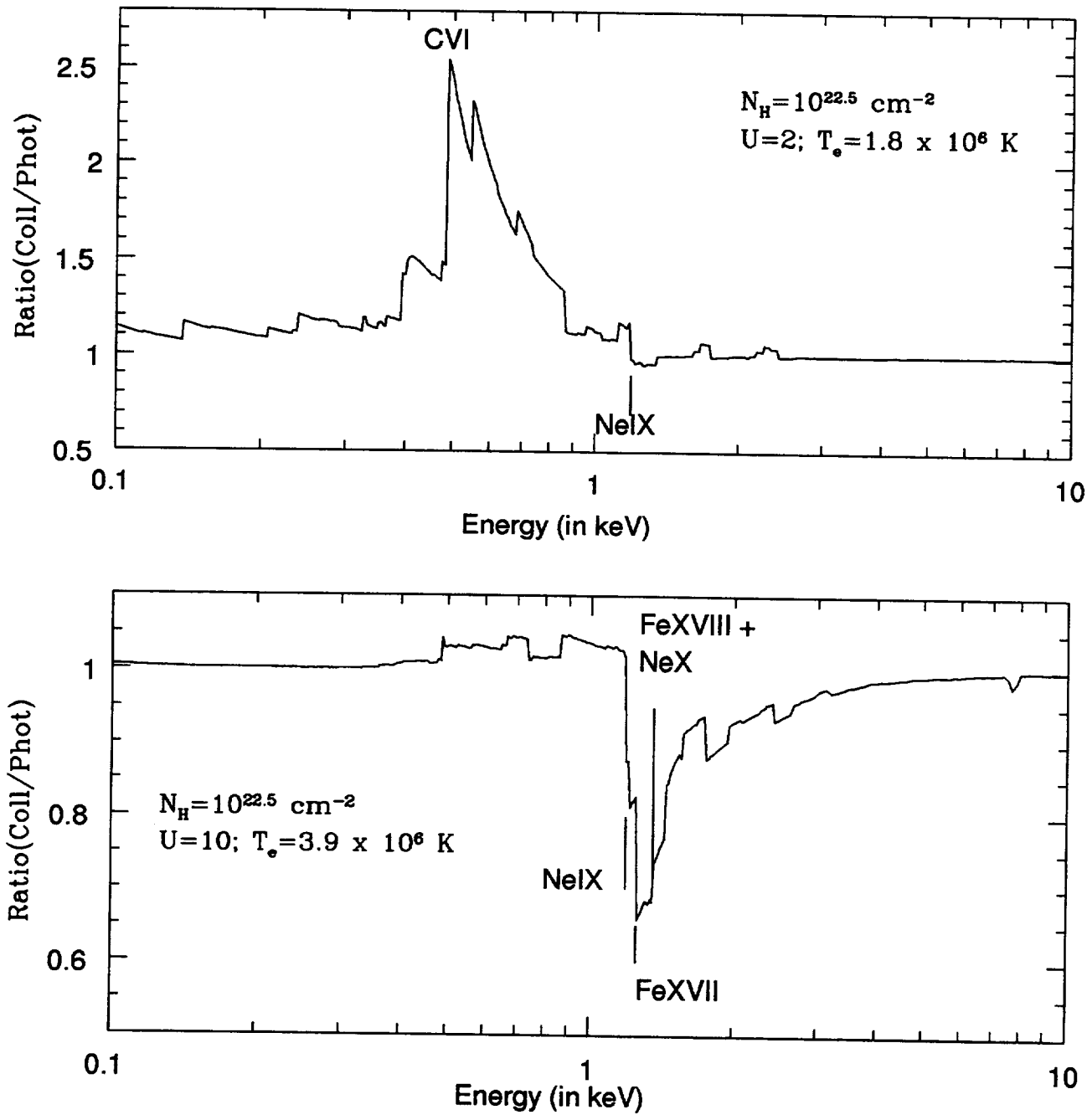

Fig. 3.— (a) The ratio between two power law spectra emerging from clouds of collisional ionized (T_e = 1.8 x 10^6 K) and photoionized (U=2) gas with solar abundances. (b) The ratio between two power law spectra emerging from clouds of collisionally ionized gas with $T_e = 3.9 \times 10^6$ K, and photoionized gas with U=10. The column density is $N_H = 10^{22.5}$ cm^{-2} in both cases.

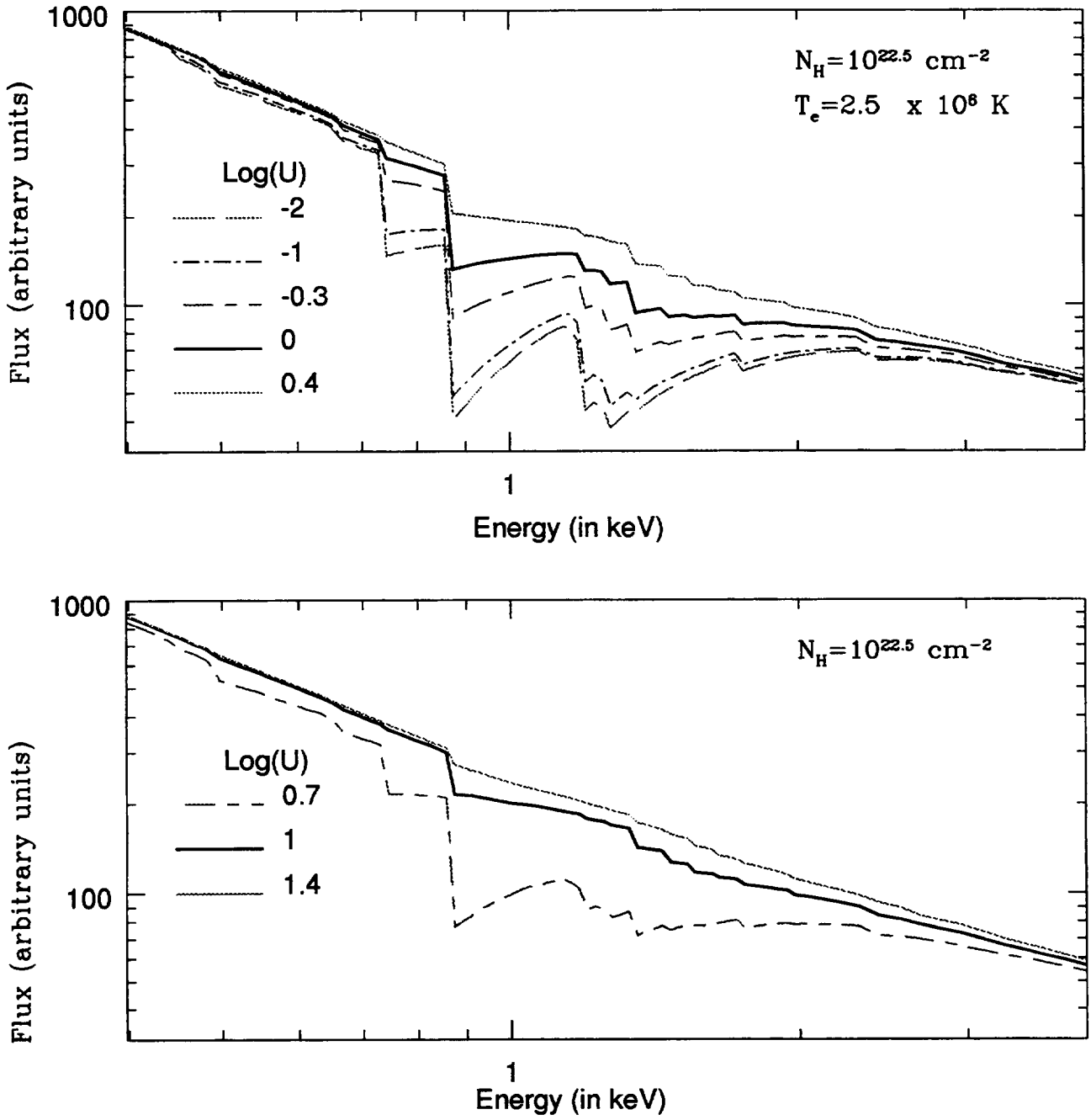

Fig. 4.— (a) Spectra from gas in which both collisional ionization and photoionization are important. The temperature of the gas is fixed at $T_e = 2.5 \times 10^6$ K, and log(U)=-1, -1, 0.3, 0. 0.4. (b) Spectra from gas in pure photoionization equilibrium., with log(U)=0.7, 1.1, 1.4. The column density is $N_H = 10^{22.5}$ cm^{-2} in both cases.

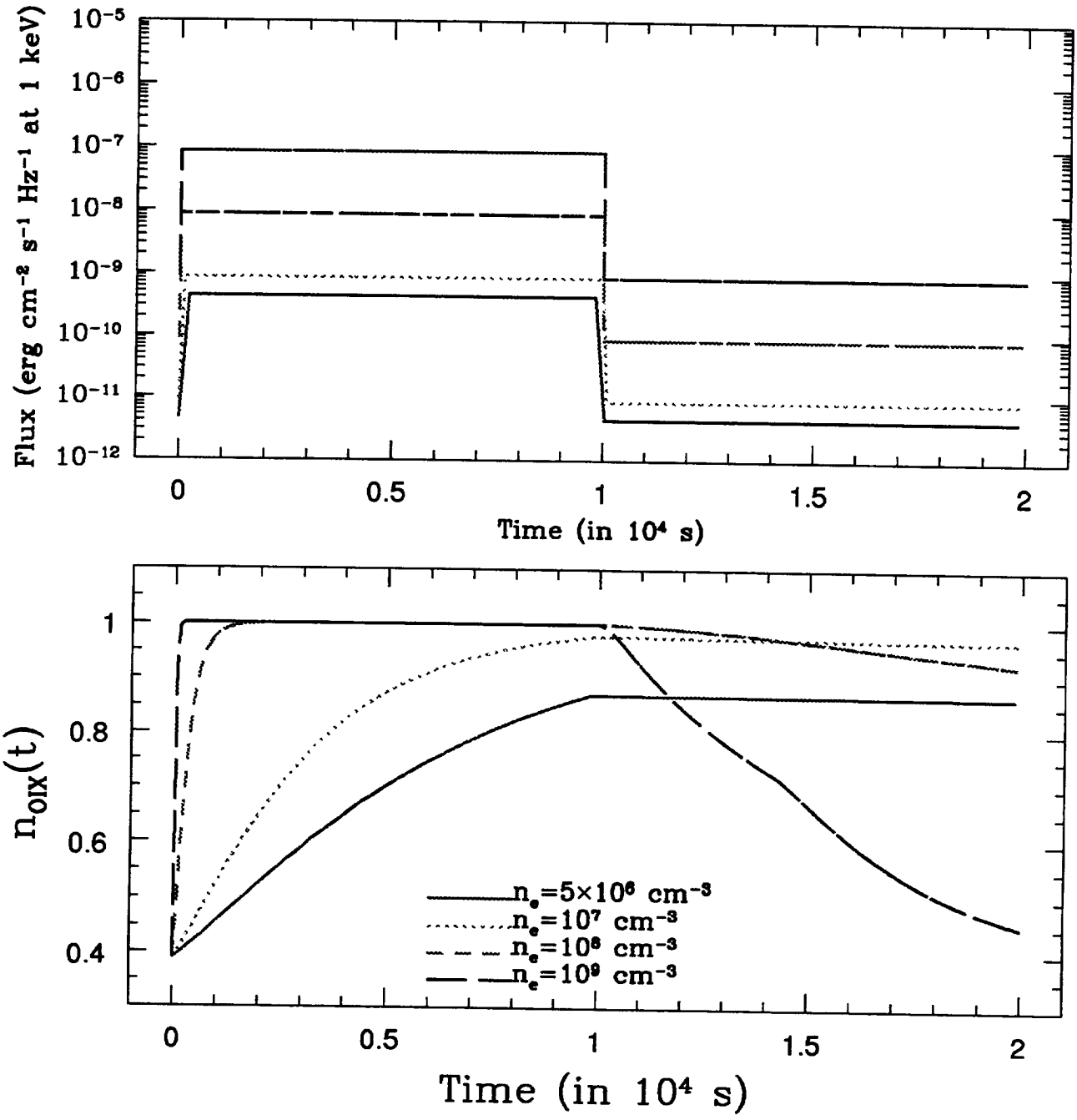

Fig. 5.— Upper panel: step light curve of the ionizing radiation, for four different values of the electron density ($n_e = 5 \times 10^6$, 10^7, 10^8, and 10^9 cm^{-3}, which correspond to four different values of the incident flux). Lower panel: time behaviour of the relative abundance of OIX, for the four values of n_e.

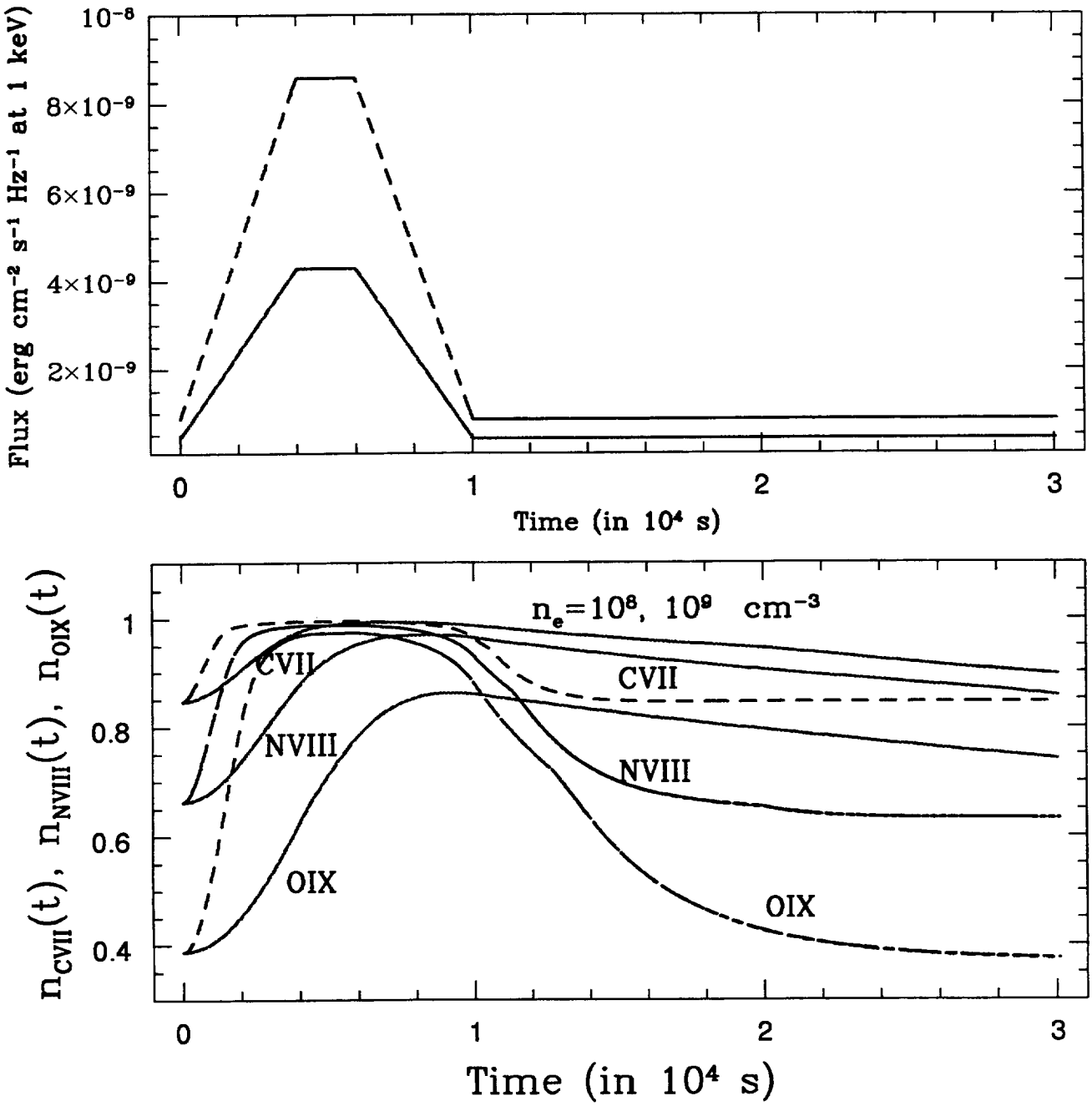

Fig. 6.— Upper panel: 2-phases light curve of the ionizing continuum. Lower panel: time behaviour of the relative abundances of the fully stripped ions of three elements: CVII, NVIII, OIX. In both panel different lines correspond to different values of the electron density, $n_e = 10^8$ (solid line), and 10^9 cm^{-3} (dashed line).

The variability properties of X-ray steep and X-ray flat quasars

Fabrizio Fiore[1,2,3], Ari Laor[4], Martin Elvis[1],
Fabrizio Nicastro[1,2], Emanuele Giallongo[2]
[1] Harvard-Smithsonian Center for Astrophysics, Cambridge MA 02138, USA
[2] Osservatorio Astronomico di Roma, Monteporzio (Rm) I00040 Italy
[3] SAX Science Data Center, Roma, Italy
[4] Physics Department, Technion, Haifa 32000, Israel

(version: 8pm 21 November 1997)

ABSTRACT

We have studied the variability of 6 low redshift, radio quiet 'PG' quasars on three timescales (days, weeks, and months) using the ROSAT HRI. The quasars were chosen to lie at the two extreme ends of the ROSAT PSPC spectral index distribution and hence of the Hβ FWHM distribution. The observation strategy has been carefully designed to provide even sampling on these three basic timescales and to provide a uniform sampling among the quasars

We have found clear evidence that the X-ray steep, narrow Hβ, quasars show larger amplitude variations than the X-ray flat broad Hβ quasars on timescales from 2 days to 20 days. On longer timescales we do not find significant differences between steep and flat quasars, although the statistics are poorer. We suggest that the above correlation between variability properties and spectral steepness can be explained in a scenario in which the X-ray steep, narrow optical line objects are in a higher L/L_{Edd} state with respect to the X-ray flat, broad optical line objects.

Subject headings: quasars — variability, X-rays, emission lines

1. Introduction

While X-ray variability in Seyfert galaxies has been the subject of intensive study (see review by Mushotzky, Done & Pounds 1993, and Green et al 1993, Nandra et al. 1997), the variability of quasars, being fainter, have received far less attention (the Zamorani et al. 1984 study remains the most extensive to date). Higher luminosity AGN had been expected

to be physically larger and so have slower, and most likely lower amplitude, variations. A typical quasar is 100–1000 times more luminous than the highly variable Seyferts, such as NGC 4051, and so would vary at a significantly lower rate, i.e. a minimum of several days. It was probably this expectation that deterred extensive observing campaigns. This is unfortunate since we show here that X-ray variability is common, rapid and of quite large amplitude. The variability most likely originates in the innermost regions of quasar, and so can help unravel the basic parameters of the quasar central engine (mass, geometry, radiation mechanisms, radiative transfer) none of which are yet well constrained.

These speculations are supported by compact galactic sources, for which the investigation of the "variability properties vs. spectral shape" and the "variability properties vs. luminosity" planes have brought a great improvement in our understanding (see e.g. van der Klis 1995). The same is likely to happen for quasars. Compact galactic sources are usually bright and variable on timescales as short as 1 ms, which means that their variability timescales can be probed by just a few observations of individual objects. For example, the Galactic black hole candidate (BHC) Cyg X-1 recently underwent to dramatic changes in its variability and spectral properties (see e.g. Cui et al. 1997), and it was possible to follow the whole cycle from the usual low and hard state, to a medium-high, softer state, and back to the low and hard state in the course of a few months. This is unlikely to happen in a luminous AGN, even if there were similiarities between AGN and black hole candidates, because the variability timescales (and the sizes and luminosities) are probably much longer (greater and higher) in AGN. Instead, if the analogy between quasars and BHC holds, we will observe a population of quasars some in a 'high and soft' state, and some in a 'low and hard' state.

Hence the analogous observational way forward quasars is to investigate the variability properties of samples of quasars, selected according to their spectral properties and luminosity.

The evidence for rapid, large amplitude, X-ray variability in a few AGN with unusually steep X-ray spectra and unusually narrow Balmer lines (mostly Narrow Line Seyfert 1 galaxies, NLSy1, given the strong correlation between these two quantities found by Laor et al., 1994, 1997, Boller, Brandt & Fink 1996) has recently grown:

1. NGC4051 shows large variations (50 %) on timescales of $\approx$ 100 seconds and has very narrow optical and UV emission lines and steep 0.1-2 keV X-ray spectrum. It is also highly variable in the EUV (a factor of factor of 20 in 8 hours, Fruscione et al 1997).

2. IRAS13224-3809 has a particularly steep 0.1-2 keV spectrum ($\alpha_X > 3$) narrow Hβ line, very strong FeII emission and shows X-ray variations of a factor 50 or more on

timescales of a few days (Otani 1995, Brandt et al. 1995, Boller et al 1997) and a factor of 2 in less than 800 seconds (Boller et al. 1996);

3. RE J 1237+264 showed one very large (factor of 50) variability event (Brandt, Pounds & Fink, 1995)

4. PHL1092 varied by a factor of 4 in 2 days (Forster & Halpern 1997, Lawrence et al. 1997). PHL1092 is a high luminosity (5×10^{46} erg s^{-1}) very steep 0.1-2 keV spectrum and narrow emission line quasar.

5. The relatively high luminosity quasar NAB0205+024 ($L_{0.5-10keV} = 8 \times 10^{44}$ erg s^{-1}) shows variations of a factor of 2 in less than 20 ks in an ASCA observation (Fiore et al. 1997).

6. Mark 478 (PG1440+356) shows factor of 7 variations in 1 day during a long EUVE monitoring (Marshall et al 1996)

7. The extremely soft NLSy1 WPVS007 ($\alpha_{0.1-2keV} = 7.3$) showed a huge variation (factor of 400) variation between the RASS observation and a follow-up PSPC pointed observation (Groupe et al. 1995).

8. The luminous quasar ($L_{2-10keV} = 6 \times 10^{44}$ erg s^{-1}) PKS0558-504 showed a factor of 70 % variation in 3 minutes during a Ginga observation, interpreted by Remillard et al. (1991) in terms of beaming.

At this point we believe that a systematic study of normal quasars with a range of properties is needed. A systematic study of the variability properties of AGNs is not an easy task, since it requires:

1. the selection of well defined and unbiased sample;

2. the availability of numerous repeated observations;

3. a carefully designed observational strategy. In particular, it is very important that the sampling time is regular and that it is similar for all objects in the sample, so that the results on each object can be easily compared with each other and differences in the observed variability would not be induced just by differences in sampling patterns.

Because of these stringent requirements systematic studies are still lacking (for example the Zamorani et al. 1984 study on quasars, and the Green et al. 1993 study on Seyfert

galaxies do not fulfill any of the three criteria above). To explore in a systematic manner the possible relation between line width, soft X-ray spectrum and X-ray variability properties, we initiated a pilot program using the ROSAT HRI. In the following we present the results from a campaign of observations of six PG quasars which addresses the above points.

2. The sample

Six quasars were chosen from a complete sample of 23 optically selected (PG) quasars, all studied with the ROSAT PSPC (Laor et al. 1994, 1997). To maximize the rest frame soft X-ray detectability in the whole 0.1-2 keV PSPC band the Laor et al. sample of PG quasars ($M_B < -23$) is limited to quasars with: low redshift (z<0.4) and low Galactic N_H ($< 1.9 \times 10^{20}\mathrm{cm}^{-2}$). This sample of AGN has the advantage that it is extracted from a complete sample of optically selected quasars, and should therefore be representative of such quasars. In particular, the Laor et al. sample selection criteria are independent of the X-ray properties, and thus the sample is free from X-ray selection biases.

The six quasars were chosen to lie at the two extreme ends of the PSPC spectral index distribution ($f_\nu \propto \nu^{-\alpha_X}$, $1.4 \lesssim \alpha_X \gtrsim 1.9$) and hence of the H$\beta$ FWHM distribution. Figure 1 show the Hβ FWHM as a function of α_X for the radio quiet quasars in the Laor et al sample. (We excluded the X-ray weak quasar PG1001+054 which is too faint for followup variability studies with the HRI). X-ray steep and flat quasars discussed in this paper are identified by filled squares and open circles respectively. The quasar with $\alpha_X < 1$ and large errors is PG1114+445, which has an ionized absorber along the line of sight (Laor et al. 1997, George et al. 1997).

Extreme conditions should help to highlight the basic correlations which may provide important hints for the underlying physical processes. Table 1 gives the redshift, the PSPC energy index, the 2 keV and 3000 Å luminosities (for $H_0 = 50$ km s^{-1} Mpc^{-1}, $q_0 = 0.5$) and the H_β FWHM for the six quasars. All the chosen quasars are radio-quiet.

3. The observational strategy

The observational strategy was designed to: a) provide even sampling on three basic timescales (days, weeks, and months), b) provide a uniform sampling among the quasars, and c) keep the total integration time reasonably small. These constraints result in a quasi-logarithmic observation plan: one $\sim$ 2000 s exposure a day for one week; one $\sim$ 2000 s exposure each week for one month; two $\sim$ 2000 s exposures a month apart, 6 months after

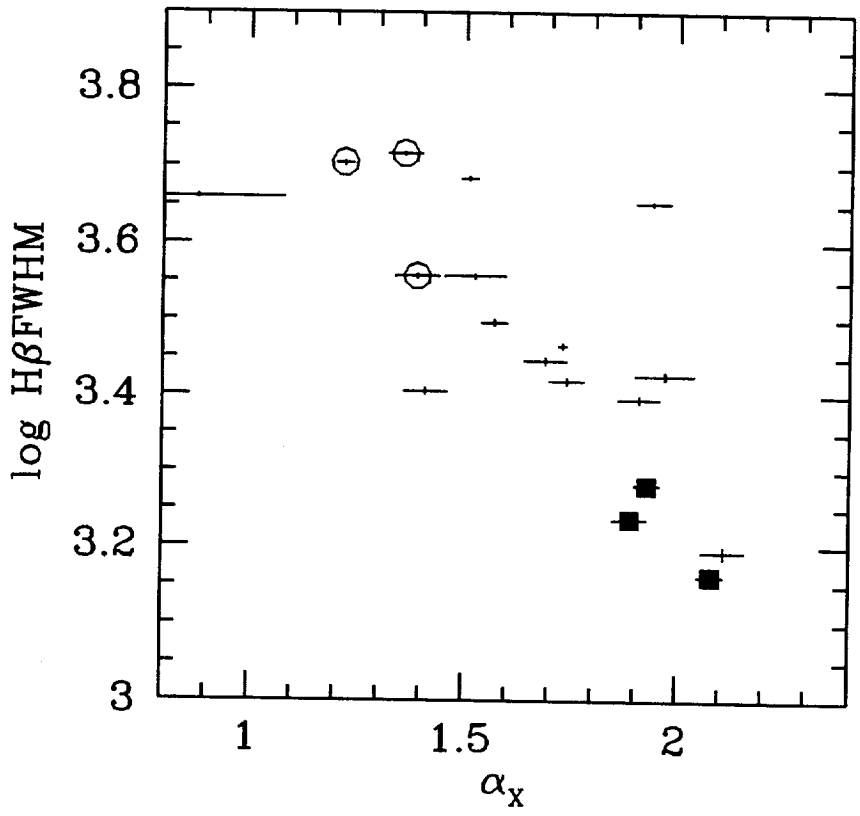

Fig. 1.— Hβ FWHM as a function of α_X for the quasars in the Laor et al sample. Filled squares and open circles identify the three X-ray steep and the three X-ray flat quasars discussed in this paper.

Table 1: Continuum and Line Parameters

name	z	α_X	$\nu L_\nu(2keV)$ erg s^{-1}	$\nu L_\nu(3000\AA)$ erg s^{-1}	HβFWHM km s^{-1}
		Steep X-ray quasars			
PG1115+407	0.154	1.9	43.61	44.96	1720
PG1402+261	0.164	1.9	44.08	45.45	1910
PG1440+356	0.077	2.1	43.64	44.91	1450
		Flat X-Ray quasars			
PG1048+342	0.167	1.4	43.85	45.14	3600
PG1202+281	0.165	1.2	44.25	45.00	5050
PG1216+069	0.334	1.4	44.78	45.94	5190

the main campaign, i.e. 6-7 points with an *even* spacing of 1 day; 4-5 points with an *even* spacing of 1 week 2 points with a spacing of 1 month and 2 points with a spacing of 6 months. The S/N obtained allows the 3σ detection of $\sim 30\%$ variability in the faintest source of the sample.

4. Results

Tables 2 and 3, respectively, give the observation date, the net HRI exposure and the background subtracted HRI count rate for the X–ray steep and flat quasars. Counts were extracted from a region of 60 arcsec radius. Since $\sim 90\%$ of the counts from a point source fall within the same extraction region (David et al. 1996) no correction has been made for lost flux. Background was extracted from two 60 arcsec radius regions straddling the source region. The background is small in all cases (< 10 counts ks^{-1} in a 60 arcsec radius regions).

We have also looked at longer variability timescales (of the order of 2000 days) by comparing the HRI fluxes with the PSPC fluxes obtained during the Rosat All Sky Survey (RASS) and the pointed ROSAT PSPC observations reported in Laor et. (1997). We converted the PSPC count rates to effective HRI count rates by assuming the spectral shape observed in the ROSAT pointed observations (Laor et al. 1997). RASS and pointed PSPC observations 'converted' count rates are given in Table 4.

4.1. Logarithmic normalized light curves

Figure 2 shows the logarithm of the light curves of the six quasars, each normalized to the mean flux, spanning about one month each, while figure 3 shows the observations performed six months later compared with the average flux and the dispersion observed on timescales shorther than one month. Figure 4 shows the normalized RASS and PSPC pointed observation points, the dispersion as in Figure 2 and the normalized HRI observation performed 6 months later.

The steep α_X quasars show large variations (up to a factor of 2) on all the timescales investigated. Conversely, the flat α_X quasars show little variability on short timescales. Factor of 2 variations with respect to the average flux seem to be allowed for both X–ray steep and X–ray flat quasars on 200-2000 days timescales, although the statistics on these timescales are poorer.

4.2. Structure function

To compare the variability of the quasar groups more quantitatively we computed the logarithm of the ratio between each pair of flux measurements (at two times t_i and t_j in the quasar rest frame). We then computed the median and the mean in 9 time bins for both flat and steep X-ray quasar samples:

$$(1) \qquad < \Delta m >= median\ or\ mean(|2.5 * log(f(t_j)/f(t(i)))|).$$

The function using the mean is similar to the so called 'average structure function' (see e.g. Di Clemente et al. 1996).

We have verified that no single quasar dominates the median and mean in eq. (1).

$< \Delta m >$ for the median is shown in figure 5. Error bars represent here the semi interquartile range. $< \Delta m >$ for the mean is shown in figure 6. Error bars represent here the error on the mean and are therefore less conservative.

It is clear that the $< \Delta m >$ (both mean and median) for X-ray steep quasars is significantly higher than that of X-ray flat quasars on timescales from 2 days to 20 days. On the longest timescale (200 days) the two $< \Delta m >$ are consistent with each other, with large errorbars. The point at about 2000 days in figures 5 and 6 compares the HRI monitoring results with the RASS results. The point at about 1000 days compares the HRI monitoring

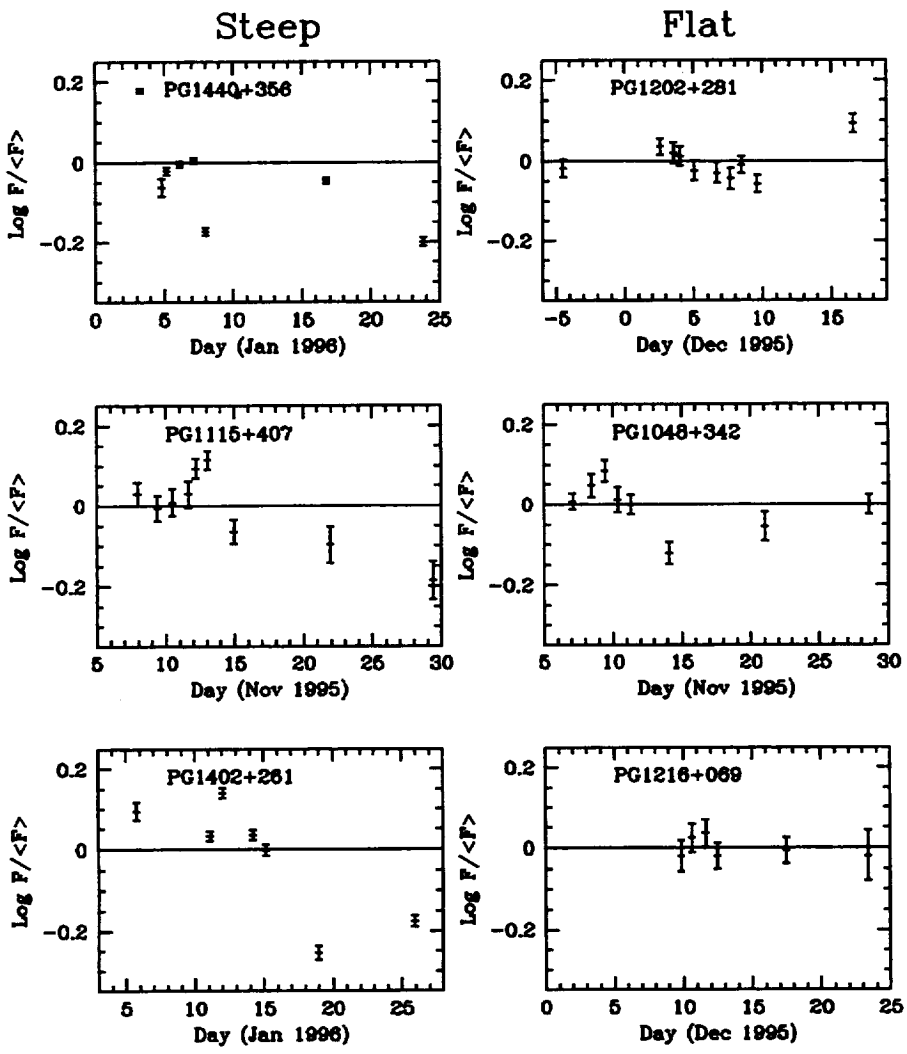

Fig. 2.— The ROSAT HRI light curves (plotted as logarithm of the ratio of the flux to the average flux) of the six quasars on a 2-20 day timescale.

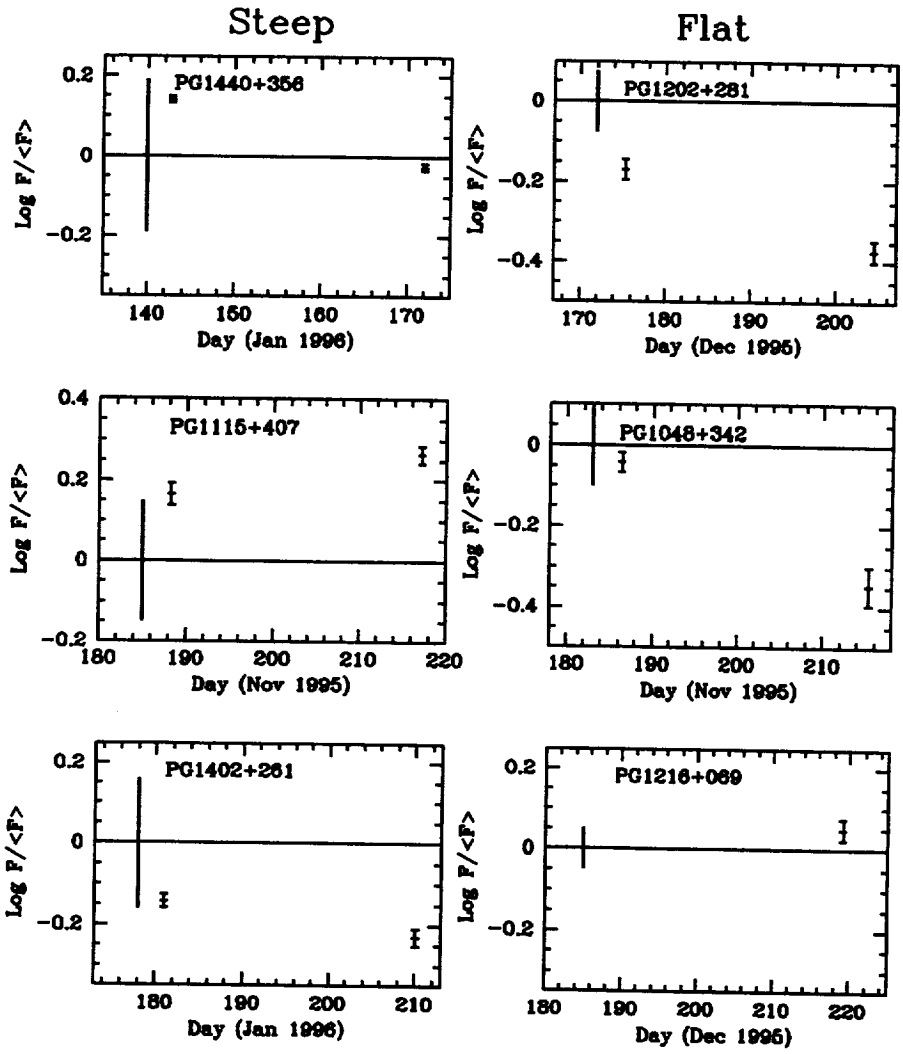

Fig. 3.— The HRI observations of the six quasars performed six months later compared with the average flux and the dispersion observed on timescales shorther than one month (20-200 days timescale).

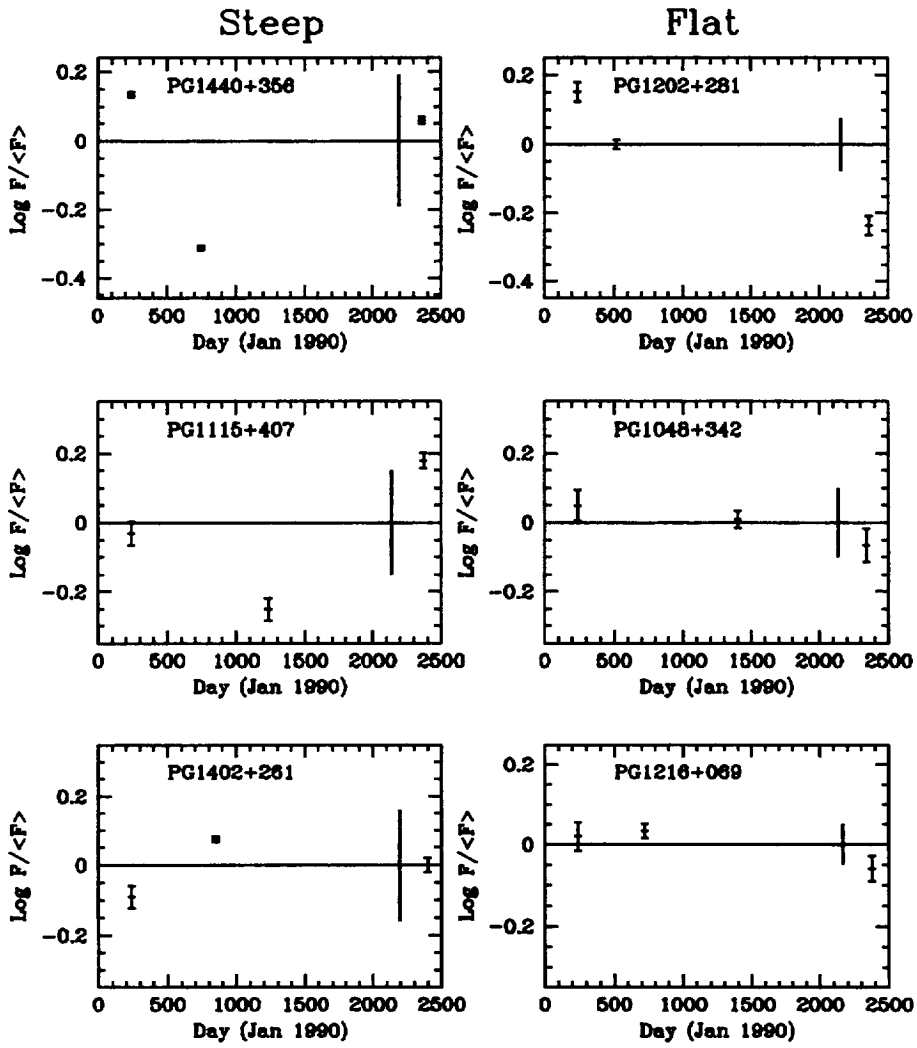

Fig. 4.— The HRI observations of the six quasars compared with the RASS and with the PSPC pointed observations (200-2000 days timescale).

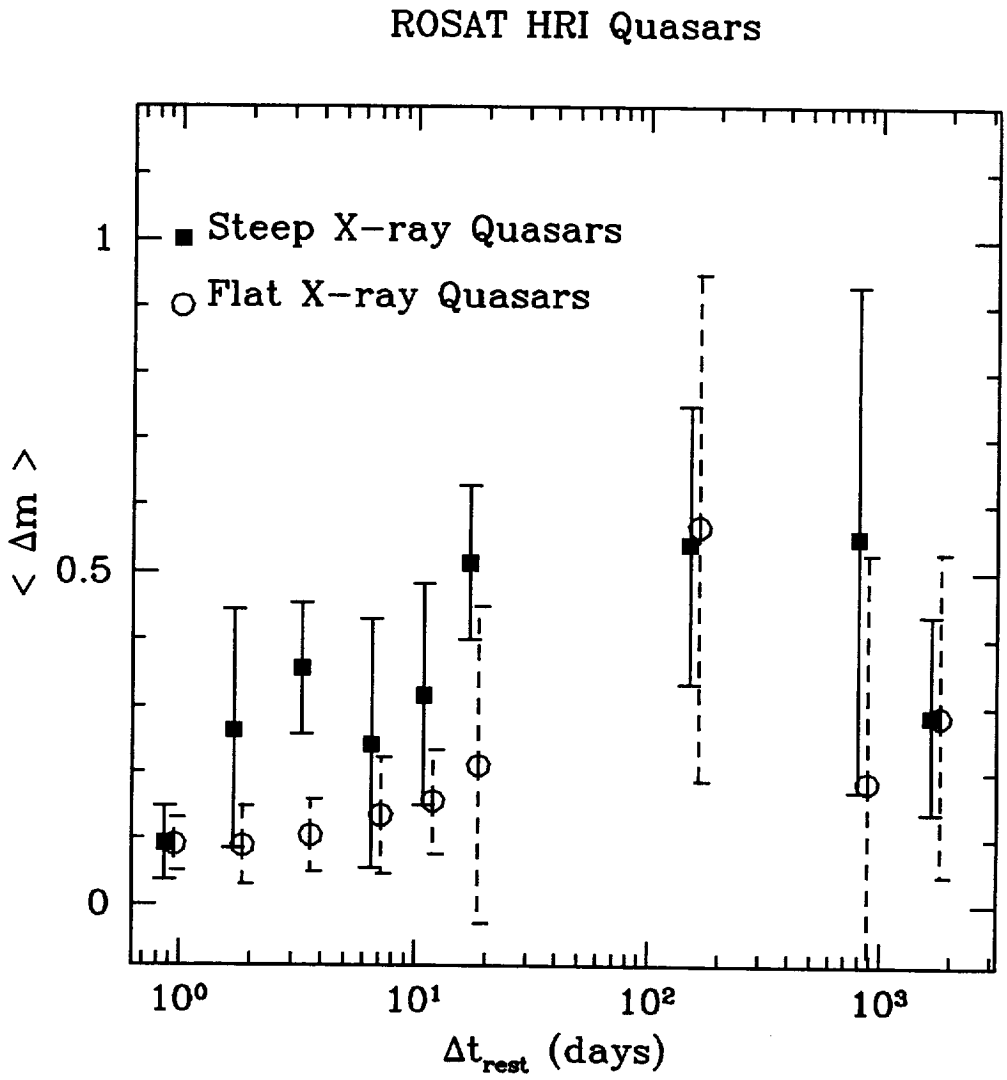

Fig. 5.— "Median" Structure Function ($< \Delta m >$, see eq. 1) for the X-ray steep (filled squares) and flat (open circles). X-ray flat quasars points have been slightly shifted from real Δt for a sake of clarity.

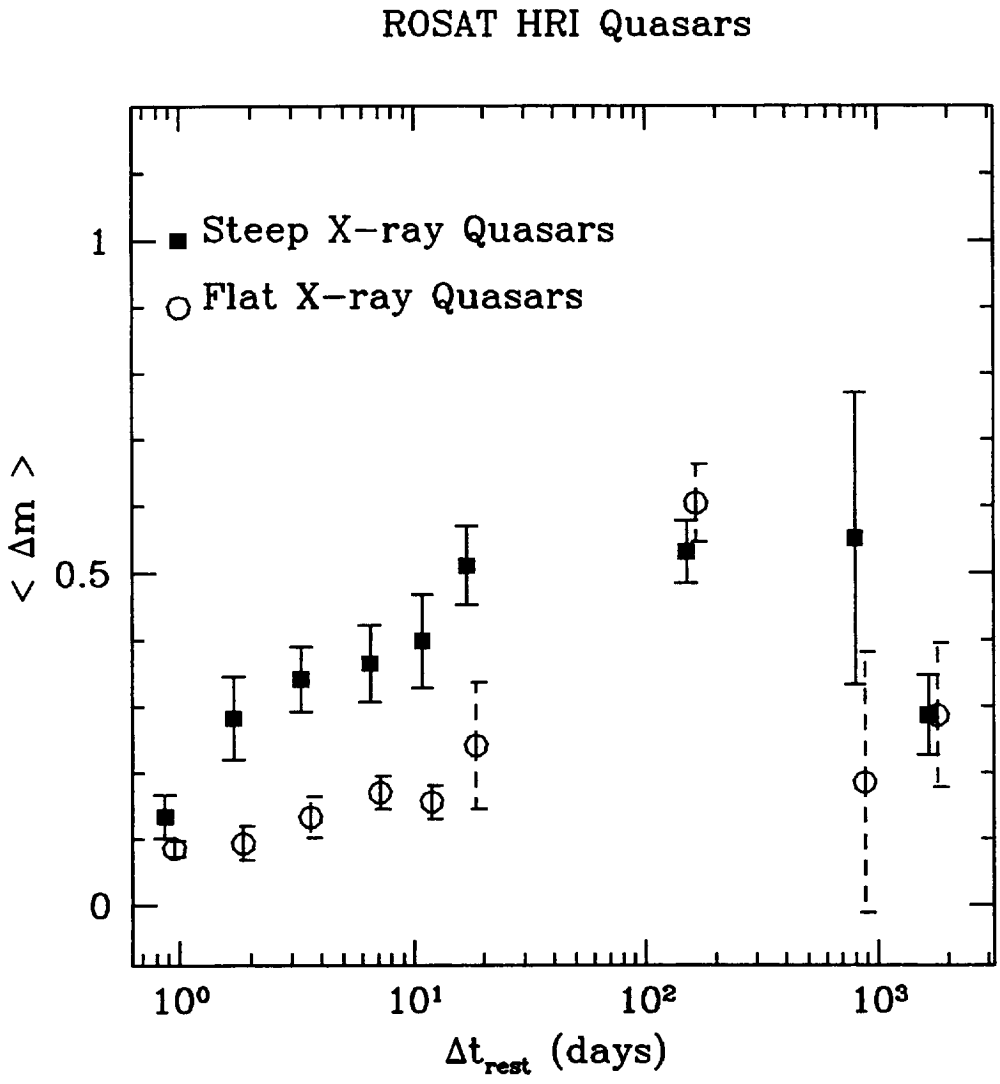

Fig. 6.— Mean Structure Function ($< \Delta m >$, see eq. 1) for the X-ray steep (filled squares) and flat (open circles). X-ray flat quasars points have been slightly shifted from real Δt for a sake of clarity.

and the RASS results with the ROSAT PSPC pointed observations. The error bars here are larger because of the different sampling times used.

4.3. Power spectrum of PG1440+356

For the brightest quasar in our sample (PG1440+356) it is possible to investigate timescales shorter than the duration of each single HRI exposure. Analysis of the HRI light curves of each single OBI reveals significant variability down to a time scale of a few hundred seconds. To quantify the amplitude of this variability we have computed a power spectrum for each of the single HRI exposures and, to improve the statistics, we have added together the 12 power spectra. The resulting coadded power spectrum is shown in figure 7, along with the lower frequency power spectrum calculated at six reasonably well sampled frequencies using the full HRI monitoring. The error bars represent the dispersion of the power in each bin.

The power spectrum above 10^{-3} Hz is flat, and thus consistent with white noise. Excess power is detected at $\sim 5 \times 10^{-4}$ Hz, which is a factor ~ 100 smaller than that detected at $\sim 5 \times 10^{-6}$ Hz, a mean 1/f distribution. Unfortunately we do not have information on the power in the decade between 10^{-5} and 10^{-4} Hz and therefore we cannot tell whether the power spectrum decreases smoothly as 1/f above $\sim 5 \times 10^{-6}$ Hz or rather if it breaks at an intermediate frequency. Continuous monitoring up to several days is needed to answer to this question.

5. Comparison with other work

Nandra et al. (1997) used the source root mean square variation σ^2_{rms} from ASCA SIS data for a sample of (X-ray bright) AGN to suggest an inverse relation between variability and X-ray luminosity. Our sample of high luminosity, optically selected objects allows us to test this suggestion. We have calculated σ^2_{rms} separating it from that of the noise according to the method of Nandra et al (1997). These are reported in Table 5 for two different time scales: days and months-to-years. (We do not show errors on σ^2_{rms} because the analytic formula provided by Nandra et al (1997) is not valid in the limit of small number of points.) Since the light curves of the flat X-ray quasars in figure 2 are consistent with a constant value we can take the value of σ^2_{rms} calculated in these cases (≈ 0.01) as an upper limit on its uncertainty.

Figure 8 shows σ^2_{rms} as a function of the X-ray luminosity and of the soft (0.1-2 keV)

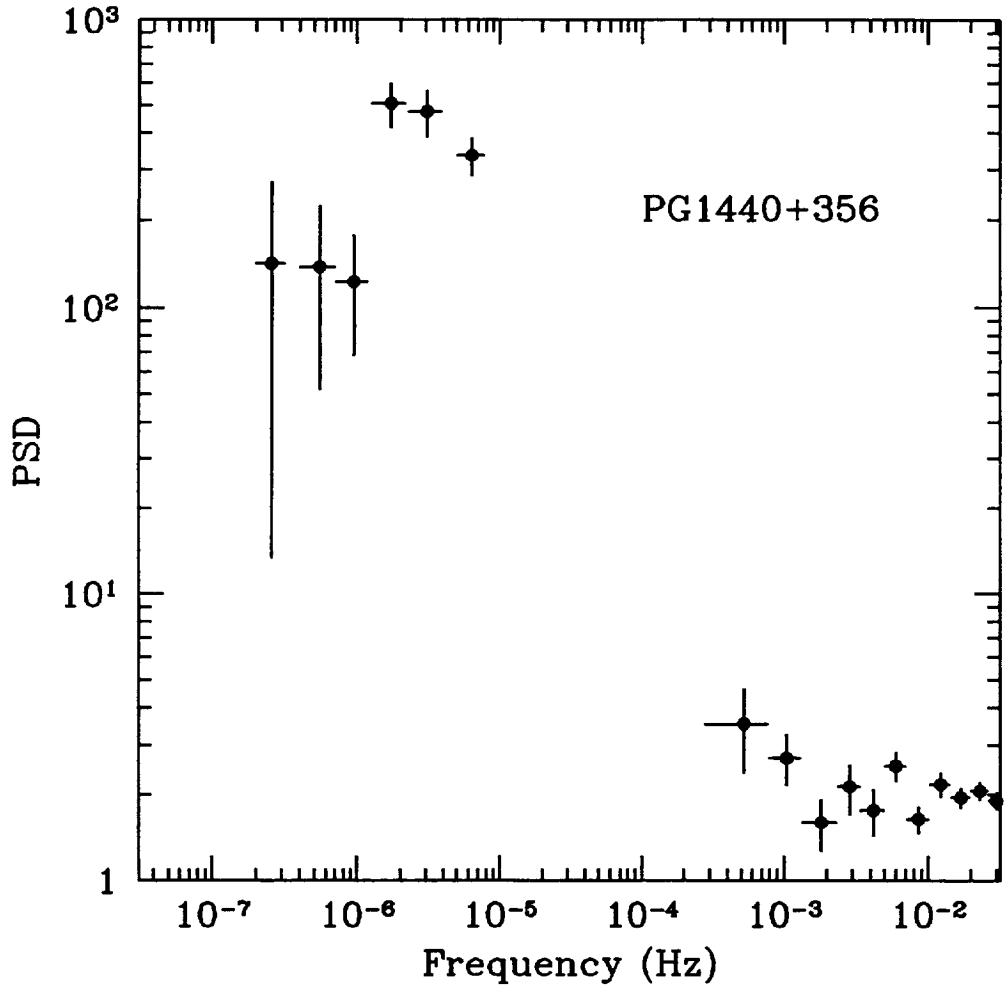

Fig. 7.— The power spectrum of PG1440+356 from 0.03 to 2×10^{-7} Hz. The power spectrum is normalized such that the level of the noise is 2.

X-ray spectral index for the six quasars in our study and for the sources in Nandra et al (1997) with no strong low energy absorption (to provide a low energy X-ray spectral index). For this figure we used the σ^2_{rms} SIS 0.5-2 keV in Nandra et al (1997). This band overlaps quite well with the HRI band (the HRI has some response in the 'carbon' band, below 0.3 keV, but this is much smaller than in the 0.5-2 keV band). PSPC spectral indices are taken from Walter & Fink (1993) and Laor et al (1997) or are calculated from WGACAT hardness ratios when not available in these papers.

The addition of the six quasars makes a substantial difference. For the Nandra et al. sample alone the σ^2_{rms} vs L_{1keV} linear correlation coefficient is r=–0.82 (probability of 99.9 %), while with the quasars it is reduced to r=–0.54. This is still significant (probability of 95 %), although it depends entirely on one point (the low luminosity Seyfert 1 galaxy NGC4051). Instead, σ^2_{rms} and α_X were uncorrelated for the Nandra et al. sample alone (r=+0.37, probability of 15%); adding the quasars brings r=+0.55, a 95 % probability correlation. The spread of the ASCA 2-10 keV indices is significantly smaller than that of the PSPC spectral indices (Brandt et al 1997). Therefore, both the relatively small spread of ASCA 2-10 keV indices and the absence in the Nandra et al. sample of very steep soft X-ray quasars reduced the chance to detect a correlation between σ^2_{rms} and the soft X-ray spectral shape in previous works.

At a given luminosity the three x-ray 'steep' quasars from our sample all have σ^2_{rms} higher than both the 'flat' X-ray quasars in our sample and all the other objects in the Nandra et al. (1997) sample by a factor of 10 to 100. While σ^2_{rms} for the Nandra et al. (1997) sample refers to a factor of ten smaller timescale, even if the power spectrum of the steep X-ray spectrum quasars falls like $\approx 1/f$ (as suggested for PG1440+356, see §4.3), only part of the difference in σ^2_{rms} could be explained. Instead the power spectrum stays more or less constant on these timescales then this difference is highly significant. A comparison between variability rms in this frequency range between broad and narrow line Seyfert galaxies using ASCA and BeppoSAX light curves of similar sampling and length is in progress and will be part of a forthcoming paper (Fiore et al. 1998, in preparation).

Finally we note that the 1 keV X-ray luminosity and the spectral index are slightly anti-correlated (r=–0.20) in the sense that steeper objects tend to have lower 1 keV luminosities. The correlation is not significant here, but Laor et al. (1997) find a more significant correlation between α_X and the 2 keV luminosity in their sample of PG quasars ($r_s = 0.482$, probability of 98 %). Thus, low luminosity AGNs tend to be more variable because of the luminosity-variability correlation, but they also tend to have flatter spectra, which tends to diminish their variability due to the spectral index-variability correlation. To remove the effect of the α_X-luminosity correlation from the σ^2_{rms}–luminosity and σ^2_{rms}–α_X correlations

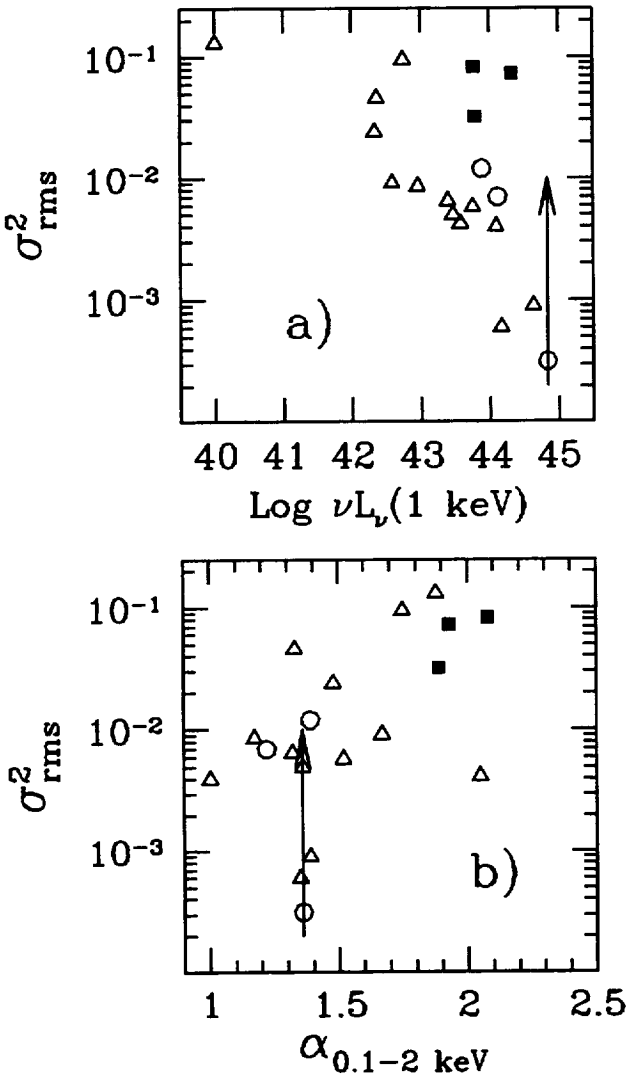

Fig. 8.— The 'excess' variance as a function of the 1 keV luminosity (in erg s^{-1} Hz^{-1}) and of the 0.1-2 PSPC spectral index. Open triangles show quasars and Seyfert galaxies from Nandra et al. 1997, filled squares identify steep X-ray spectrum quasars, open circles identify flat X-ray spectrum quasars.

we performed a partial correlation analysis (e.g., Kendall & Stuart 1979). The correlation coefficients turns out to be very similar to the previous ones (-0.53 and 0.54), giving a probability for a correlation again of 95 %. This is still a marginal result, which could be highly strengthened or weakened by adding just a few more points at low and high luminosities and at flat and steep α_X.

A correlation between variability and spectral shape, similar to that discussed in this paper, has been reported also by Green et al. (1993) and König, Staubert and Timmer (1997) in two different analyses of EXOSAT lightcurves of AGN.

Di Clemente et al. (1996) studied the variability of 30 PG quasars in the red band and compared it with that of a sample of 21 PG quasars observed by IUE. Their full sample contains 39 quasars, the majority of which (24) at $z < 0.4$, as the quasars discussed in this paper. Three of the six quasars discussed in this paper are also part of the Di Clemente et al sample (the three X-ray flat quasars). Di Clemente et al. found that the variability amplitude increases with the rest frame frequency on both 0.3 and 2 years timescales. Extrapolating their correlation in the X-ray band one would predict a $< m >$ of 0.75 and 0.83 for the 2 timescales. This is somewhat surprisingly close to the measured $< m >$ on these timescales, given that variability in the red band, UV and X-ray may well have a completely different origin.

6. Discussion

In our sample of six PG quasars we found clear evidence that X-ray steep quasars show larger amplitude variations than X-ray flat quasars on timescales from 2 days to 20 days. On longer timescales we do not find significant differences between steep and flat quasars, although the statistics are poorer. While the sample in this pilot study is small (and expanded monitoring of a larger sample of quasars surely needed), the distinction is so clean cut that we feel justified in speculating on its origin.

Large narrow band flux variability in sources with a steep spectrum could be induced by changes in the spectral index without big variations of the spectrum normalization. If this is the case each source should show large spectral variability, with α_X anti-correlated (correlated) with the observed flux if the pivot is at energies lower (higher) than the observed band. Spectral variability of this kind has not been observed in the PSPC observations of these and other quasars (Laor et al. 1997, Fiore et al. 1994) and in NLSy1 (Boller et al 1997, Fiore et al. 1997, Brandt et al. 1995). Although our HRI observations cannot directly rule out this possibility, we therefore conclude that the observed temporal variability pattern is

not likely the result of complex spectral variability.

Laor et al (1997) suggest that a possible explanation for the remarkably strong α_X–H_β FWHM correlation is a dependence of α_X on $L/L_{\rm Edd}$. The line width is inversely proportional to $\sqrt{L}/L_{\rm Edd}$ if the broad line region is virialized and if its size is determined by the central source luminosity (see Laor et al. 1997, §4.7). So narrow-line, steep (0.1-2 keV) spectrum AGNs emit close to the Eddington luminosity and have a relatively low mass black hole. A similar dependence between spectral shape and $L/L_{\rm Edd}$ is seen in Galactic black hole candidates (BHC) in the "high and soft" state.

A physical interpretation for this effect, as described by Pounds et al. (1995), is that the hard X-ray power-law is produced by Comptonization in a hot corona and that as the object becomes more luminous in the optical-UV, Compton cooling of the corona increases, the corona becomes colder, thus producing a steeper X-ray power-law. If the Pounds et al mechanism is operating, then steep α_X(PSPC) quasars should also have a steep hard X-ray power-law. In a sample of quasars with similar luminosities, those emitting closer to the Eddington luminosity will also be those with the smallest black hole and hence smaller X-ray emission region. Thus light travel time effects would smear intrinsic X-ray variability up to shorter time scales in high L/L_{Edd} objects, compared with low L/L_{Edd} objects. From figures 5 and 6 it appears that the the emission region of the steep soft X-ray quasars is a factor of $\approx$ 10 smaller than that of flat soft X-ray quasars (about $\approx 10^{16}$ cm and 10^{17} cm respectively). It is interesting to note that a completely different analysis, based on the interpretation of the optical to X-ray spectral energy distribution in terms of emission from accretion disks also suggest a small black hole mass and an high arretion rate in two NLSy1 (Siemiginowska et al. 1998).

It is interesting to note that Cyg X-1 in the "high and soft" state (Cui et al. 1997) shows a total root mean square variability higher than that measured during periods of transitions and in the "low and hard" state. This is due to strong 1/f noise, extending down to at least a few 10^{-3} Hz, when the source is the "high and soft" state (Cui et al. 1997). When the source is in the "low and hard" state this 1/f noise is not present (see e.g. the review of van der Klis 1995).

Ebisawa (1991) in a systematic study of Ginga observations of 6 BHC found that the time scales of variability for the soft and hard components are often different. The soft component is usually roughly stable on time scales of 1 day or less, while the hard component exhibits large variations down to msec time scales. If the time scales of BHC and quasars scale with the mass of the compact object the above two time scales translate to 10^4 years and 0.1 day respectively for our quasar sample. For a sample of quasars with similar redshifts and luminosities this predicts a rather small scatter in the soft component and a bigger scatter

in the hard component. ROSAT results go in this direction. Laor et al. (1994, 1997) find that (for their sample of 23 low–z PG quasars) the scatter in the PSPC 2 keV luminosity is significantly larger than that in the 0.3 keV luminosity.

We conclude that the analogy between AGN and Galactic BHC seems to hold qualitatively for their X-ray variability properties.

An alternative and intriguing possibility to explain the correlation between X-ray variability amplitude and spectral shape is that a component generated closer to the black hole dominates the emission of steep α_X quasars, as in the spherically converging optically thick flow proposed by Chakrabarti and Titarchuk (1995) to characterize BHC in the high and soft state. If this is the case then we would again expect that the spectrum of the steep α_X quasars remain steep above 2 keV (and up to $m_e c^2$ according to Chakrabarti and Titarchuk). Observations with the ASCA and BeppoSAX satellites instruments, which are sensitive up to 10 keV, (Brandt et al 1997, Fiore et al 1997, Comastri et al 1997) suggest that this is indeed the case.

Variability on short timescale (a few hundred seconds) is also evident in the steep α_X quasars. The HRI sensitivity allows to study the variability of these object down to a few hundred seconds. To investigate shorter timescale we will have to await missions with high throughput like AXAF and XMM.

F.F. acknowledge support from grant NAG5-3039. M.E. and F.N. acknowledge support from ADP grant NAG5-3066. A.L. acknowledges support from the Technion research promotion fund. F.F. thanks Lev Titarchuk for useful discussions.

REFERENCES

Boller T., Brandt W.N., Fink H. 1996, A&A, 305, 53

Boller T., Brandt W.N., Fabian A.C., Fink H. 1997, MNRAS, 289, 393

Brandt W.N., Pounds K.A., Fink H., 1995, MNRAS, 273, L47

Brandt W.N., Mathur S., Elvis M. 1997, MNRAS 285L25

Chakrabarti S.K., Titarchuk L. 1995, ApJ, 455, 623

Comastri A. et al. 1997, A&A, in press

Cui W., Heindl W.A., Rothshild R.E., Zhang S.N. Jahoda K., Focke W. 1997, ApJL, 474, L57

David L.P., Harnden F.R., Kearns K.E., Zombeck M.V. 1993 "The ROSAT High Resolution Imager", Technical Rep. US ROSAT Science Data Center/SAO

Di Clemente A., Giallongo E., Natali G., Trevese D., Vagnetti F. 1996, ApJ, 463, 466

Fiore F., et al. 1992, A&A, 262, 37

Fiore F., Elvis M., McDowell J.C., Siemiginowska A., Wilkes B.J. 1994, ApJ, 431, 515

Fiore F., et al. 1997, A&A, submitted

Fruscione A., Cagnoni I., Papadakis 1997, ApJ, in preparation

Forster K., Halpern J.P. 1997, ApJ, in press

Kendall M., Stuart A. 1979, The Advanced Theory of Statistics, MacMillan, New York

König M., Staubert R., Timmer J. 1997, proc. of the conference "Astronomical Time Series", Tel Aviv 1-3 Jan 1997

George I. et al. 1997, ApJL in press

Green A.R., McHardy I.M., Letho H.J. 1993, MNRAS, 265, 664

Groupe D., Beuermann K., Mannheim K., Thomas H.-C. Fink H.H., de Martino D. 1995, A&A, 300, L21

Laor A., Fiore F., Elvis M., Wilkes B.J., McDowell J.C. 1994, ApJ, 435, 611

Laor A., Fiore F., Elvis M., Wilkes B.J., McDowell J.C. 1997, ApJ, 477, 93

Lawrence A. et al. 1997, MNRAS, 285, 879

Marshall H.L., Carone T.T., Shull J.M. Malkan M.A., Elvis M. 1996, ApJ 457 169

Mushotzky R., Done C., Pounds K. 1993, Ann. Rev. A&A, 31, 717

Nandra K., George I.M., Mushotzky R.F., Turner T.J., Yaqoob T., 1997, ApJ, 476, 70

Remillard R.A., Grossan B., Bradt H. V., Ohashi, Hayashida K., Makino F., Tanaka Y., 1991, Nat, 350, 589

Siemiginowska A., Fiore F., Comastri A. et al. 1998, ApJ, in preparation

van der Klis, M. 1995, in "X-ray Binaries", ed. W.H.G. Lewin, J. van Paradijs, E.P.J. van den Heuvel, Cambridge Un. press, p. 252

Zamorani G., et al. 1984, ApJ, 278, 28

This preprint was prepared with the AAS LaTeX macros v4.0.

Table 2: HRI Monitoring of 3 X-ray Steep Quasars

Source	Observation Date	Exposure[a]	HRI Count-rate[b]
PG 1115+407	07/Nov/95	3.14	87 ± 6
	09/Nov/95	2.39	80 ± 6
	10/Nov/95	2.23	83 ± 7
	11/Nov/95	2.29	87 ± 7
	12/Nov/95	2.91	101 ± 6
	13/Nov/95	3.53	106 ± 6
	14/Nov/95	3.62	70 ± 5
	21/Nov/95	1.71	65 ± 7
	29/Nov/95	2.06	53 ± 6
	05/May/96	2.00	139 ± 9
PG 1402+261	05/Jan/96	1.10	380 ± 20
	11/Jan/96	4.40	329 ± 9
	12/Jan/96	3.30	422 ± 12
	14/Jan/96	4.33	331 ± 9
	15/Jan/96	3.24	304 ± 10
	18/Jan/96	3.84	170 ± 7
	25/Jan/96	4.80	204 ± 7
	20-21/Jun/96	3.86	201 ± 8
PG 1440+356	03/Jan/96	3.69	1339 ± 19
	04/Jan/96	0.56	770 ± 40
	05/Jan/96	2.66	847 ± 18
	06/Jan/96	4.02	880 ± 15
	07/Jan/96	4.35	900 ± 15
	08/Jan/96	3.99	596 ± 13
	10/Jan/96	5.51	1304 ± 16
	16/Jan/96	3.51	800 ± 15
	23/Jan/96	3.50	561 ± 13
	20/Jun/96	2.72	1276 ± 22

[a] in ks; [b] in ks^{-1}

Table 3: HRI Monitoring of 3 X-ray Flat Quasars

Source	Date Obs	Exposure[a]	HRI Count-rate[b]
	07/Nov/95	4.13	105 ± 5
	08/Nov/95	2.08	115 ± 8
	09/Nov/95	2.06	125 ± 8
	10/Nov/95	2.14	106 ± 8
PG 1048+342	11/Nov/95	3.30	103 ± 6
	14/Nov/95	3.40	78 ± 5
	21/Nov/95	1.86	91 ± 8
	28-29/Nov/95	3.02	103 ± 6
	04/May/96	4.31	87 ± 5
	02/Jun/96	2.54	43 ± 5
	25/Nov/95	2.59	153 ± 8
	02/Dec/95	3.51	173 ± 8
	03/Dec/95	2.19	167 ± 10
	03-04/Dec/95	2.37	164 ± 9
PG 1202+281	04-05/Dec/95	2.32	151 ± 9
	06/Dec/95	2.09	149 ± 9
	07/Dec/95	2.33	144 ± 9
	08/Dec/95	2.84	156 ± 8
	09/Dec/95	3.03	140 ± 7
	16/Dec/95	2.10	197 ± 11
	23/May/96	3.50	99 ± 6
	21/Jun/96	4.56	62 ± 4
	09/Dec/95	2.46	67 ± 6
	10/Dec/95	2.33	74 ± 6
PG 1216+069	11/Dec/95	2.65	76 ± 6
	12/Dec/95	3.16	67 ± 5
	17/Dec/95	3.80	69 ± 5
	23/Dec/95	0.88	67 ± 10
	06/Jul/96	3.79	80 ± 5

[a] in ks; [b] in ks^{-1}

Table 4: RASS and PSPC pointed observation

Source	RASS	PSPC pointed
Count-rate[a]	Date Obs	Count-rate[a]
PG1115+407	108±9	65±5
PG1402+261	133±10	195±4
PG1440+356	1028±18	367±6
PG1048+342	56±6	51±3
PG1202+281	152±10	107±3
PG1216+069	96±8	99±4

[a] 'converted' (see text) PSPC count rates in ks^{-1}

Table 5: Source root mean square variation

name	σ^2_{rms}(2-20 days)	σ^2_{rms}(200-2000 days)
	10^{-2}	10^{-2}
	Steep X-ray quasars	
PG1115+407	3.2	13.8
PG1402+261	7.3	19.1
PG1440+356	8.3	15.2
	Flat X-Ray quasars	
PG1048+342	1.2	13.9
PG1202+281	0.7	9.7
PG1216+069	0.0	1.8

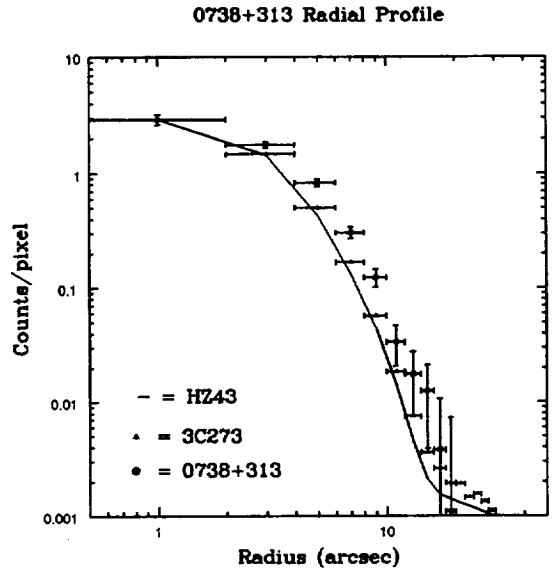

Fig. 1. The 0738+313 radial profile compared with that of 3C273 and the HRI psf

and then restacked into a single image. To check for residual spurious broadening of the HRI psf we analyzed the observation of the bright quasar 3C273. In figure we show the radial profile of 0738+313 compared with that of 3C273 (after removing the jet region) and with the HRI psf, as parameterized by David et al (1993). The profile of 3C273 differs from the HRI psf above about 5 arcsec. The excess of counts in 3C273 with respect to the psf is $\sim$ 20% between 5 and 10 arcsec and $\sim$ 45% between 10 and 20 arcsec. On the other hand in 0738+313 the excess of counts with respect to the psf is $110\pm15\%$ between 5 and 10 arcsec and $190\pm70\%$ between 10 and 20 arcsec. We therefore conclude that significant extended emission is present in 0738+313 on scales from 5 to about 20 arcsec, where the source starts to become fainter than the background. To quantify this emission is however difficult because of the presence on the uncertainty in the satellite aspect reconstruction and therefore on the true HRI psf.

References

David, L.P. et al.: 1993, "The ROSAT HRI" (Tech. Rep. US ROSAT SDC/SAO).
Ellingson, E., Yee, H.K., and Green, R.F. 1991, *Astrophys. J.* **371**, 49.
Elvis, M., et al.: 1994, *Astrophys. J.* **422**, 60.
Fabian, A.C. and Crawford, C.S., 1990, *Mon. Not. R. Astr. Soc.* **247**, 439.
White D.A., et al.: 1991, *Mon. Not. R. Astr. Soc.* **252**, 72.
Yee, H.K., and Green R.F. 1987, *Astrophys. J.* **319**, 28.

Mon. Not. R. Astron. Soc. 000, 000–000 (0000) Printed 10 September 1997

The ASCA view of steep soft X-ray quasars

F. Fiore[1,2,3], G. Matt[4], M. Cappi[5,6], M. Elvis[3], K. M. Leighly[6,7], F. Nicastro[8], L. Piro[8], A. Siemiginowska[3], B. J. Wilkes[3]

[1] *Osservatorio Astronomico di Roma, Via dell'Osservatorio, I–00044 Monteporzio Catone, Italy*
[2] *SAX Science Data Center, Via Corcolle 19, I–00131 Roma, Italy*
[3] *Harvard-Smithsonian Center fo Astrophysics, 60 Garden Street, Cambridge MA 02138 USA*
[4] *Dipartimento di Fisica, Università degli Studi "Roma Tre", Via della Vasca Navale 84, I–00146 Roma, Italy*
[5] *Istituto per le Tecnologie e Studio Radiazioni Extraterrestri (ITESRE), CNR, via Gobetti 101, I–40129 Bologna, Italy*
[6] *Cosmic Radiation Laboratory, RIKEN, Hirosawa 2-1, Wako-shi, Saitama, 351, Japan*
[7] *Columbia Astrophysics Laboratory, Columbia University, 538 West 120th Street, New York, NY 10027, USA*
[8] *Istituto di Astrofisica Spaziale (IAS), CNR, Via E. Fermi 21, I00044 Frascati, Italy*

10 September 1997

ABSTRACT

Steep soft X-ray (0.1-2 keV) quasars share several unusual properties: narrow Balmer lines, strong FeII emission, large and fast X-ray variability, rather steep 2-10 keV spectrum. These intriguing objects have been suggested to be the analogs of Galactic black hole candidates in the high, soft state. We present here results from ASCA observations of two of these quasars: NAB0205+024 and PG1244+026.
Both objects show similar variations (factor of ~ 2 in 10 ks), despite a factor of about ten difference in the 0.5-10 keV luminosity (7.3×10^{43} erg s^{-1} for PG1244+026 and 6.4×10^{44} erg s^{-1} for NAB0205+024, assuming isotropic emission, $H_0 = 50.0$ and $q_0 = 0.0$).
The X-ray continuum of the two quasars flattens by 0.5-1 going from the 0.1-2 keV band toward higher energies. Similar results have been recently obtained on an other half a dozen steep soft X-ray quasars.
PG1244+026 shows a significant feature in the '1 keV' region, which can be described by either a broad emission line centered at 0.95 keV (quasar frame) or edge (or line) absorption at 1.17 (1.22) keV. The line emission could be due to reflection from an highly ionized accretion disk, in line with the view that steep soft X-ray quasars are emitting close to the Eddington luminosity. Photoelectric edge absorption or resonant line absorption could be produced by gas outflowing at a large velocity (0.3-0.6 c).

Key words: Galaxies: Seyfert – Galaxies: individual: PG1244+026, NAB0205+024 — X–rays: galaxies — Line: formation — Line: identification

1 INTRODUCTION

The ROSAT PSPC has found a large spread in the energy spectral indices of low-z quasars*: $0.5 < \alpha_{0.1-2keV} < 3.5$; in about 10% of the cases $\alpha_{0.1-2keV} \gtrsim 2$ (e.g. Laor et al. 1994, 1997, Walter & Fink 1993, Fiore et al. 1994). The large spread in $\alpha_{0.1-2keV}$ favoured the discovery of its correlation with the Hβ FWHM and FeII equivalent width, the variability properties and the X-ray to UV luminosity ratio (Walter & Fink 1993, Laor et al 1994, 1997, Fiore et al. 1995, 1997, Boller et al. 1995, 1997, Lawrence et al. 1997).

In fact, the steep soft X-ray quasars have then been realized to share a cluster of unusual properties:

- Narrow balmer lines; †
- strong FeII emission;
- Somewhat steep hard X-ray spectra ($2 > \alpha_{2-10keV} > 0.6$, Pounds et al. 1995, Brandt et al., 1997);

* We indicate as "quasars" all Seyfert 1 type of objects, regardless of their luminosity.

† the permitted lines have FWHM $\lesssim 2000$ km s^{-1}, yet still are clearly broader than the forbidden lines.

The Equilibrium Photoionized Absorber in 3C351

Fabrizio Nicastro[1,2], Fabrizio Fiore[1,2,3], G. Cesare Perola[4], Martin Elvis[1]

Abstract

We present two ROSAT PSPC observations of the radio-loud, lobe-dominated quasar 3C 351, which shows an 'ionized absorber' in its X-ray spectrum. The factor 1.7 change in flux in the ~2 years between the observations allows a test of models for this ionized absorber.

The absorption feature at ~ 0.7 keV (quasar frame) is present in both spectra but with a lower optical depth when the source intensity - and hence ionizing flux at the absorber - is higher, in accordance with a simple, single-zone, equilibrium photoionization model. Detailed modeling confirms this agrement quantitatively. The maximum response time of 2 years allows us to limit the gas density: $n_e > 2 \times 10^4$ cm^{-3}; and the distance of the ionized gas from the central source R < 19 pc. This produces a strong test for a photoionized absorber in 3C 351: a factor 2 flux change in ~1 week in this source *must* show non-equilibrium effects in the ionized absorber.

3c351_2_1297.tex

[1] Harvard-Smithsonian Center for Astrophysics, 60 Garden St, Cambridge MA 02138
[2] Osservatorio Astronomico di Roma, via Osservatorio, Monteporzio-Catone (RM), I00040 Italy
[3] SAX Science Data Center, via Corcolle 19, Roma I00100 Italy
[4] Dipartimento di Fisica, Università degli studi "Roma Tre", Via della Vasca Navale 84, Roma, I00146 Italy

1 INTRODUCTION

An ionized absorber was discovered in the quasar 3C351 (z=0.371) by Fiore et al (1993). The main absorption feature in the ROSAT PSPC X-ray spectrum is a deep edge at $\sim$ 0.7 keV (quasar frame), which is likely to be due to OVII-OVIII. Mathur et al. (1994) built a simple one-zone model of this absorber that also explained the OVI, CIV and Lyα UV absorption lines seen in a nearly simultaneous HST FOS spectrum. Such simple models, although elegant, have come under criticism. Ionized absorbers in some Seyfert galaxies show different variability behavior in different absorption features, some of which are not as predicted for gas in photoionization equilibrium. Multiple absorbing zones have been introduced to explain these effects (e.g. Reynolds 1997 ??). In another paper (Nicastro et al., 1997, submitted) we instead explore additional physics (non-equilibrium photonionization models and collisional models) while retaining a single zone of absorbing gas. Here we show that in 3C 351 at least the simplest photoionization equilibrium, single zone model continues to be sufficient.

3C351 was observed twice by ROSAT, on 1991 October and 1993 August. The first observation was reported by Fiore et al. (1993). The second observation was then proposed in order to search for time variability that could test photoionization models. Fortunately a factor 1.7 decrease in the PSPC count rate was seen, providing just such a test. Here we present the second data and compare the results with predictions.

2 Observations and Data Analysis

We considered the two PSPC observations of 3C351 taken roughly two years apart, in 1991 October and 1993 August. Table 1 gives, for each observation, the observation date, its duration, the net exposure time, the net source counts, the count rate, and the signal to noise ratio. The data reduction and the timing analysis were performed using XSELECT.

We reduced the second PSPC observation of 3C351 following the procedures used in Fiore et al. (1993) for the first observation. For the first observation we used the spectrum and light curve obtained by Fiore et al. (1993). The source intensity was consistent with a constant value during both PSPC observations, but the mean count rate dropped by a factor $\sim$ 1.7 during the 22 months between the observations (see Fig. 1 and Table 1). Hereinafter we shall call these the 'High' and 'Low' states, respectively.

Table 1: ROSAT PSPC observations of 3C 351

Start Date	Duration (ksec)	Exposure (ksec)	Net Counts	Count Rate ct s^{-1}	S/N	State
91 Oct 28	168	13.1X	1390	0.110	31.0	High
93 Aug 23	1143	15.41	980	0.064	26.0	Low

3 Ionization Models

We produced equilibrium photoionization models and pure collisional ionization models using CLOUDY (version 90.01, Ferland 1996) to fit to the PSPC spectra of 3C 351. We use a Friedman cosmology with $H_0 = 50$ km s^{-1} Mpc^{-1} and $q_0 = 0.1$ to derive a luminosity of

$L_{2keV} \sim 4 \times 10^{44}$ erg s^{-1} for the quasar. This determines the distance scale in the absorber for a given value of the ionization parameter, U.

3C 351 is a radio-loud lobe-dominated quasar and, as Fiore et al (1993) and Mathur et al (1994) have shown, the ionization state of the gas strongly depends on the spectral energy distribution (SED) of the ionizing continuum, from radio to hard X-rays. We therefore made our photoionization models using the observed SEDs for 3C351 (Mathur et al 1994). We varied the ill-determined energy at which the X-ray spectrum turns up to meet the ultraviolet using a broken power-law with a break energy from the unobserved EUV range to well within or above the PSPC range, as in Mathur et al (1994). The low energy spectral index is fixed by the observed flux in the UV at one end, and the break energy at the other. The high energy spectral index above the break energy is fixed at 0.9. This is typical for lobe dominated radio loud quasars (Shastri et al., 1993). A model with a continuum break energy of 0.4 keV (rest frame) and UV-to-soft-X-ray index of 2.4 provides the best fits to both the PSPC spectra of 3C351.

3.1 Spectral Analysis

The spectral analysis was performed using XSPEC and the latest version of the 256 channels PSPC response matrix ("pspcb_gain2", relased on.....). We binned each spectrum in channels with at least 50 counts, to warrant the poissonian statistics to be used.

We first fitted the high and low state spectra with a simple power law model reduced at low energy by Galactic absorption (Model 1). Only 2 parameters were left free to vary: the photon spectral index Γ and the normalization F_0. Table 2 shows the best fit parameters along with the reduced χ^2 and degree of freedom (d.o.f.). (Errors for all fits represent the 90% confidence intervals for two interesting parameters). In both the cases the χ^2 is unacceptably high. Fig. 2 shows the ratio between data and best fit model for the spectra, fixing the spectral index to the mean of the best fit high and low state values. The deficit of counts at $\sim$ 0.6 keV (rest frame) is evident in both spectra. Following Fiore et al. (1993) we interpret these features as due to a blend of OVII-OVIII absorption K-edges caused by ionized gas along the line of sight.

Table 2: Fits with Simple Power Law[a] (Model 1)

Spectrum	Γ	[b]F_0	χ^2(dof)
High	2.29 ± 0.06	$2.67^{+0.06}_{-0.09}$	2.99(46)
Low	2.04 ± 0.07	1.87 ± 0.10	3.09(19)

[a] With N_H fixed to the Galactic value of 2.26×10^{20} cm^{-2} (Elvis et al., 1989).
[b] in 10^{-4} ph cm^{-2} s^{-1} keV^{-1}, at 1 keV.

We then fitted both spectra using the equilibrium photoionization models described in §3 (Model 2). Only three parameters were left free to vary in the fit: normalization (F_0), U and N_H. The soft and hard spectral index were fixed to the values of the ionizing continuum used to build the models (see §3). Table 3 gives the best fit parameters. While the best fit values of N_H are consistent with a constant value, there is marginal evidence (at the 2 σ level) of variation in U.

We then fitted the high and low state spectra simultaneously, fixing N_H to the best fit value found in the high state, since this has the best statistics. Table 3 gives again the best fit values for U and the F_0 in the two spectra (with the 90% confidence intervals for one interesting parameter). The best fit U and F_0 are linearly correlated with each other (Figure 3), in the manner expected if the gas is in photoionization equilibrium with the ionizing continuum . Table 3 also gives the best fit abundances of OVII and OVIII and their ratio. The change of U translates to a factor of three change in the OVII to OVIII ratio as the source intensity drops by about 70 %.

Table 3: Equilibrium Photoionization Model Fits

Spectrum	Log(N_H)	Log(U)	[a] F_0	χ^2(d.o.f.)	n_{OVIII}	n_{OVIII}	n_{OVIII}/n_{OVII}
High	$22.14^{+0.14}_{-0.17}$	$0.78^{+0.21}_{-0.13}$	8.9 ± 1.8	0.89(45)	0.783	0.168	0.03
Low	$21.89^{+0.22}_{-0.28}$	$0.49^{+0.23}_{-0.30}$	5.0 ± 0.1	0.89(18)	0.822	0.081	0.10
High+Low	22.14 (frozen)	$0.78^{+0.12}_{-0.09}, 0.63^{+0.10}_{-0.09}$	$8.7^{+0.9}_{-0.8}, 6.0^{+0.7}_{-0.5}$	0.99(62)			

[a] in 10^{-5} ph s^{-1} cm^{-2} keV^{-1} (at 1 keV).

Collisional ionization models fit the data equally well, as they should at low column densities (Nicastro et al., 1997). To do so they require arbitrary changes, by a factor 20 in temperature or a factor 2 in N_H. Instead photoionization equilibrium models predict the observed correlation with the ionizing continuum. To the authors this is a strong argument in favor of a photoionization model.

3.2 X-ray Colors of the warm absorbers in 3C 351

The behavior of the main physical properties of the absorber can be seen in a color-color diagram. In Fig. 4 we plot the hardness ratios HR=H/M against the softness ratio SR=S/M from the count rates in three bands (S=0.15-0.58 keV, M=0.88-1.47 keV, and H=1.69-3.40 keV, at z=0.371) for theoretical curves (for log(N_H)=21, 21.5, 22 and 22.14) obtained by folding the equilibrium photoionization models (for log(U) in the range -0.3-1.5, and Galactic N_H) with the response matrix of the PSPC.

The position of a point in this diagram readily gives the dominant ion in the gas. The rapid change of SR as U increase from 0.5 to 5.5 (on the curve corresponding to log(N_H)=22.14) corresponds to large increases of the transparency of the gas at E< 0.5 keV as H and He becomes rapidly fully ionized. As U further increases from 5.5 to 16.5 the SR color changes more slowly, and inverts its trend at U$\sim$ 11, with HR now changing more rapidly than SR. The inversion point indicates the switch from an ionization state dominated by OVII to that dominated by OIX. In the last part of the curve as U increases, SR and HR decrease until all the ions in the gas are fully stripped and the gas is completely transparent to radiation of any energy.

The two data points show the two 3C 351 observations. The best fit U in the High observation is marked on the log(N_H)=22.14 curve along with the value obtained by scaling by the intensity ratio between the two observations (a factor 1.7). The two points are consistent with the position of the observed colors of 3C351 in the two observations, so the predictions of the simple equilibrium photoionization model is consistent with the data.

4 Discussion

The as predicted change of the the ionization parameter in the 3C 351 absorber to a change in the ionizing continuum is strong evidence that photoionization is the dominant ionization mechanism. We also see that the absorber comes to ionization equilibrium within 22 months, and can use this to constrain the physical properties of the absorber.

The time t_{eq} measures the time the gas needs to reach equilibrium with the instantaneous ionizing flux (Nicastro et al, 1997). This time depends on the particular ionic species considered. The ionic abundances of Oxygen in the absorber in 3C 351 are distributed mainly between only two ionic species: OVII and OVIII. In this simple case a useful analytical approximation for t_{eq} is:

$$\mathrm{t}_{\mathrm{eq}}^{\mathrm{OVII,OVIII}}(\mathrm{t} \rightarrow \mathrm{t} + \Delta\mathrm{t}) \sim \frac{1}{\alpha_{rec}(OVII, T_e)_{eq} n_e} \frac{1}{1 + \left(\frac{n_{OVIII}}{n_{OVII}}\right)_{eq, t+\Delta t}} \quad (1)$$

where *eq* indicates the equilibrium quantities.

By requiring that t_{eq} for OVII and OVIII species is shorter than the 6×10^7 s elapsed between the two observations, we can find a lower limit to the electron density of the absorber: $n_e > 2 \times 10^4$ cm^{-3}. Since we know the values of U and F_0, this density limit translates into a limit on the distance of the ionized gas from the central source, R< 19 pc.

These limits are consistent with the upper limit of $n_e < 5 \times 10^7$ cm^{-3}, and R> 0.3 pc, found by Mathur et al. (1994) using a lower limit for the distance of the cloud from the central source, based on the absorber being outside the broad emission line region.

The relative closeness of these two limits (factor ~100) implies that a variation in shorter times ($\sim$ 1 month), would be likely to show non-equilibrium effects (Nicastro et al, 1997). If a factor 2 flux change in $\lesssim$1 week showed no such effects the simplest photoionization model would have to be abandoned.

5 Conclusion

We have tested ionization models for the ionized absorber in 3C 351. In particular, we tested a simple one zone photoionization equilibrium model on two PSPC spectra of 3C 351 that show a factor $\sim$ 2 decrease in flux. The model correctly predicts the sense and amplitude of the observed change in the ionization state of the absorber, correlated with the ionizing continuum flux.

Given that photoionization equilibrium applies we can derive a lower limit to the electron density of the absorber: $n_e > 2 \times 10^4$ cm^{-3}. This is consistent with the upper limit of $n_e < 5 \times 10^7$ cm^{-3} found by Mathur et al. (1994). The distance of the ionized gas from the central source is then 0.3 pc < R < 19 pc. The closeness of these two limits creates a strong test of photoionization models: factor 2 variations in 3C 351 on timescales of order a week *must* show non-equilibrium effects.

This work was supported in part by NASA grant NAG5-3066 (ADP).

References

Arav N., Korista K.T., Barlow T.A., Begelman M.C., 1995, Nature, 376, 576

Elvis M., Wilkes B.J., Lockman F.J., 1989, A.J., 97, 777

Fiore F., Elvis M., Mathur S., Wilkes B.J., McDowell J.C. 1993, ApJ, 415, 192

Guainazzi M., Mihara T., Otani C., Matsuoka M. 1997, PASJ, in press

Laor, A, Fiore, F. Elvis, M., Wilkes, B.J. McDowell, J.C.M. 1997, ApJ, 477, 93

Mathur S., Wilkes B.J., Elvis M., Fiore F. 1994, ApJ, 434, 493

Mathur S., Elvis M., Wilkes B.J. 1995, ApJ, 452, 230

Mathur S., Wilkes B.J., Aldcroft T. 1997, ApJ in press

Nicastro F., Fiore F., Perola G.C., Elvis M., 1997, Apj submitted

Reynolds C.S., Fabian A.C., Nandra K, Inoue H., Kunieda H, Iwasawa K. 1995, MNRAS, 277, 901

Reynolds C.S., 1997, to appear in M.N.R.A.S.

Shastri P., Wilkes B.J., Elvis M., McDowell J. 1993, ApJ, 410, 29

Extended X-Ray Emission around GPS Quasars

LUCIO ANGELO ANTONELLI[1], FABRIZIO FIORE[1,2]
[1] *BeppoSAX Science Data Center, via Corcolle, 19 I-00131 Roma, Italy*
[2] *Osservatorio Astronomico di Roma, via dell'Osservatorio,5 I-00044 Monteporzio, Italy*

ABSTRACT. The dense cooling intracluster gas surrounding quasars at $z > 0.4$ could confine the radio source and therefore produce the low frequency cut-off observed in GigaHz peaked spectrum (GPS) sources through free free absorption or syncrotron self-absorption. We searched, by using the ROSAT HRI, for the extended X-ray emission from this cooling gas in three GPS quasars at $z \sim 0.6$. We report here the positive detection of extended emission on scales from 5 to 15 arcsec in one of the quasar: 0738+313.

1. Introduction

Radio-loud quasars and radio galaxies at $z > 0.4$ are preferably found in clusters (Ellingson, Yee and Green 1991) and so they are probably immersed in dense cooling intracluster gas. Emission from this gas is difficult to reveal in X-ray surveys because it will be outshone by the higher luminosity quasar within it However, Elvis et al. (1994) report significant absorption in high redshift quasars, similar to the absorption seen in cooling flows, lending strength to the above suggestion. A large fraction of the clusters show evidence of cooling flows and the gas pressure inferred in the cooling flow around quasars ($P \sim 10^8$ cm^{-3}, Fabian and Crawford 1990), could confine the radio source and produce the small sizes and low frequency cut-offs observed in GPS sources. GPS quasars could be extreme cases of quasars immersed in massive cooling flows. Since soft X-ray absorption is common in X-ray cooling flows (White et al. 1991) this could explain the detection of a significant absorbing column in the z=3.27 GPS quasar PKS 2126-158 (Elvis et al. 1994). We decided to search for the extended X-ray emission from the cooling gas by observing three radio loud quasars at $z \sim 0.5 - 1.0$ with the ROSAT HRI. This instrument, thanks to its good angular resolution and effective area, allows to search for extended emissions around quasars at $z > 0.4$. We have chosen the most promising cases for an initial study, i.e. those with: highly compact radio structures (to have a high chance for a dense and hot confining medium being present), moderate quasar luminosity (to maximize the cooling gas visibility against the glare of the quasar), and moderate redshifts (to give the most favorable spatial scale).

2. Data Analysis and Results

To minimize the broadening of the HRI psf due to the not perfect aspect reconstruction, images were extracted from contiguos groups of OBIs, translated to a common reference